2012

Hybrid spintronics and straintronics: An ultra-low-energy computing paradigm

Kuntal Roy
Virginia Commonwealth University

Virginia Commonwealth University

This is to certify that the dissertation prepared by Kuntal Roy entitled
"Hybrid spintronics and straintronics: An ultra-low-energy computing paradigm"
has been approved by his committee as satisfactory completion of the dissertation
requirement for the degree of Doctor of Philosophy.

Supriyo Bandyopadhyay, Ph.D., Department of Electrical and Computer Engineering (ECE) and Physics Department, ECE Graduate Program Director

---

Gary Atkinson, Ph.D., Department of Electrical and Computer Engineering

---

Jayasimha Atulasimha, Ph.D., Department of Mechanical and Nuclear Engineering

---

Puru Jena, Ph.D., Physics Department

Ümit Özgür, Ph.D., Department Electrical and Computer Engineering

---

Rosalyn Hobson, Ph.D., Associate Dean for Graduate Studies, School of Engineering

---

F. Douglas Boudinot, Ph.D., Dean of the School of Graduate Studies

July 24, 2012

Hybrid spintronics and straintronics: An ultra-low-energy computing paradigm

A dissertation submitted in partial fulfillment of the requirements for the degree of Doctor of Philosophy at Virginia Commonwealth University.

by

Kuntal Roy

MSc, Advanced Learning and Research Institute, Switzerland (2006-2008)

BE, Jadavpur University, India (1999-2003)

Director: Dr. Supriyo Bandyopadhyay

Professor, Electrical and Computer Engineering Department

and Physics Department

Virginia Commonwealth University

Richmond, Virginia

July, 2012

Contents

List of Figures

List of Tables

Abstract

Title: HYBRID SPINTRONICS AND STRAINTRONICS: AN ULTRA-LOW-ENERGY COMPUTING PARADIGM

By Kuntal Roy, MSc

A dissertation submitted in partial fulfillment of the requirements for the degree of Doctor of Philosophy at Virginia Commonwealth University.

Virginia Commonwealth University, 2012.

Director: Dr. Supriyo Bandyopadhyay, Professor, Dept. of Electrical and Computer Engg.

The primary obstacle to continued downscaling of charge-based electronic devices in accordance with Moore's law is the excessive energy dissipation that takes place in the device during switching of bits. Unlike charge-based devices, spin-based devices are switched by flipping spins without moving charge in space. Although some energy is still dissipated in flipping spins, it can be considerably less than the energy associated with current flow in charge-based devices. Unfortunately, this advantage will be squandered if the method adopted to switch the spin is so energy-inefficient that the energy dissipated in the switching circuit far exceeds the energy dissipated inside the system. Regrettably, this is often the case, e.g., switching spins with a magnetic field or with spin-transfer-torque mechanism. In this dissertation, it is shown theoretically that the magnetization of two-phase multiferroic single-domain nanomagnets can be switched very energy-efficiently, more so than any device currently extant, leading possibly to new magnetic logic and memory systems which might be an important contributor to Beyond-Moore's-Law technology.

A multiferroic composite structure consists of a layer of piezoelectric material in intimate contact with a magnetostrictive layer. When a tiny voltage of few millivolts is applied across the structure, it generates strain in the piezoelectric layer and the strain is transferred to the magnetostrictive nanomagnet. This strain generates magnetostrictive anisotropy in the nanomagnet and thus rotates its direction of magnetization, resulting in magnetization reversal

or 'bit-flip'. It is shown after detailed analysis that full 180° switching of magnetization can occur in the "symmetric" potential landscape of the magnetostrictive nanomagnet, even in the presence of room-temperature thermal fluctuations, which differs from the general perception on binary switching. With proper choice of materials, the energy dissipated in the bit-flip can be made as low as one attoJoule at room-temperature. Also, sub-nanosecond switching delay can be achieved so that the device is adequately fast for general-purpose computing.

The above idea, explored in this dissertation, has the potential to produce an extremely low-power, yet high-density and high-speed, non-volatile magnetic logic and memory system. Such processors would be well suited for embedded applications, e.g., implantable medical devices that could run on energy harvested from the patient's body motion.

Chapter 1

Introduction

In this chapter, we will first introduce the basics of a binary switch, which is the primitive device for digital information processing. We will discuss the deleterious effects of excessive energy dissipation that may take place when the switch toggles. This is a major impediment to continued downscaling of devices in accordance with Moore's law. Finally, we show how the use of a two-phase multiferroic structure, acting as a binary switch, may ameliorate the energy dissipation problem, leading to an ultra-low-energy computing paradigm.

1.1 A binary switch

The *binary* switch is at the heart of all digital computing and information processing. Its potential energy profile ideally consists of a double potential well with two degenerate minima and an energy barrier separating them. The minima act as the two stable states and the barrier prevents unwanted transitions between the two states (random switching). (See Fig. 1.1.) Transition from one stable state to another (switching) is effected by lowering the barrier with an external agent and then introducing an asymmetry in the potential landscape that prefers the desired state over the other [1, 2, 3, 4]. Once the switching is completed, the barrier is raised back up to its original height to prevent random switching. (See Fig. 1.1.) It should be emphasized here that introducing a large asymmetry in the barrier may be a sufficient condition to switch, but it is not necessary. Also, an *external* torque supplied from outside can make the particle *climbing up* the barrier and perform the switching too without *physically* removing

the barrier (e.g., spin-transfer torque induced by an externally supplied spin-polarized current, which we would discuss later in Subsection 1.7.2).

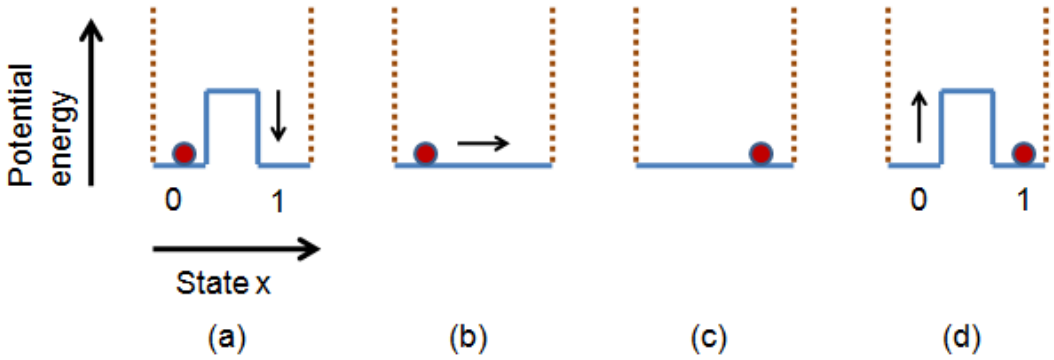

Figure 1.1: Switching in a bistable potential well. The state x is a generalized coordinate representing quantity which is switched. (a) Symmetric potential energy profile of a binary switch showing a double well with two minima corresponding to the two stable states. The current state is termed as *state 0*. (b) Switching is accomplished by lowering the barrier. A torque preferring the *state 1* over the *state 0* is conceptually assumed. Such torque is usually generated by tilting the potential landscape along the *state 1* but it can be also an internal torque generated due to the *non-equilibrium* dynamics of the particle, which is proposed in this dissertation. (c) The particle has reached its desired destination that is at *state 1*. (d) The barrier is raised back to its original position, however, the particle is now at the *state 1*.

The minimum energy that must be dissipated in a bit flip operation is technology-independent and is determined by the fundamental laws of thermodynamics. As long as the switch is in local thermodynamic equilibrium with its surroundings (at temperature T), the minimum energy dissipation needed to switch a binary device is $kT\,ln(2)$, which is the so-called Landauer-Shannon limit [1, 2, 5, 6, 7, 8, 9, 10, 11]. There are schemes of *dissipationless* switching [12, 13] whereby a switch can be toggled without dissipating any energy. They are at the core of conservative (or reversible) logic where logically reversible operations are performed without dissipating energy, but they require infinite storage capacity [14] and/or adiabatic switching at sluggish speeds [15, 16]. More importantly, these switching schemes are extremely error-prone. Thus, they are of academic interest, but not quite suitable for practical information processing.

1.2 Electronics and MOSFET scaling limits

Traditionally, the *charge* of an electron has been the state variable of choice for information processing. Charge-based devices (e.g., MOSFETs) are switched between logic levels 1 and 0 by injecting or extracting a certain amount of charge from the device's active region. (See

Fig. 1.2.) MOSFETs dissipate typically 2.5-5 fJ of energy per bit flip if the clock frequency is ∼2 GHz. The corresponding power dissipation is 5-10 μW. The Pentium IV chip of circa 2000 had a device density of 10^8 cm^{-2} and dissipated 50-100 Watt/cm^2 when 10% of the devices switched simultaneously.

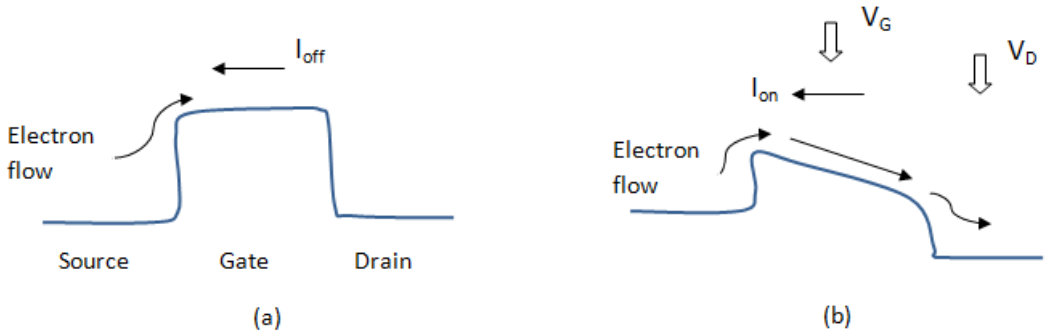

Figure 1.2: MOSFET as a binary switch. Charge is a scalar quantity and has no direction. Therefore the logic levels must be demarcated by a difference in the *magnitude* of charge. (a) When no gate voltage is applied, the barrier is high enough so the channel (gate) region is depleted of charge. Little amount of current I_{off} flows from drain to source even if a drain voltage is applied to lower the barrier at the drain terminal. Note that we are talking about an n-type MOSFET where negatively charged electrons are the carriers. (b) A gate voltage is applied to lower the barrier and thus a significant amount of charge carriers can topple the barrier. A drain voltage has to be applied too so that carriers flow continuously from source towards drain (hence a current I_{on} from drain to source).

Thermal management on a chip has so far kept abreast of dissipation. In 1981, it was demonstrated that 1 kW/cm^2 of heat could be removed from chip using standard heat sinking technology [17], which should more than suffice for thermal management on the Pentium IV. However, virtually no progress has been made in heat-sinking technology since then. There is little doubt that with increasing device density, heat dissipation will ultimately overwhelm heat sinking technologies, resulting in a catastrophic meltdown of chips. This is the primary threat to so-called Moore's law, propounded by Intel's founder Gordon Moore in 1965, which predicted that the device density on a chip will double every 18 months [18, 19, 20]. If Moore's law continues unabated, we will reach a density of 10^{11} transistors per cm^2 in the year 2017, provided technological advance in device processing permits it. However, the corresponding power dissipation can be exorbitant. Even if the energy dissipation per transistor decreases to 1 fJ and the clock frequency increases to 10 GHz, the power dissipation would be 100 kW/cm^2 assuming 10% switching activity level. This cannot be handled with any known heat sinking technology. The only solution is to decrease the energy dissipation during switching

per transistor by several orders of magnitude, e.g., to ∼1 attoJoule (aJ).

The semiconductor industry has focused on *multi-core* architecture to divide the heat dissipation in different cores as a survival methodology. However, it requires parallel programming to exploit this approach, which is not always viable [21].

1.3 Spintronics

Spintronics is a rapidly emerging field of electronics that exploits the quantum-mechanical spin of an electron to store, process, and communicate information [22]. The term "spintronics" was first introduced in 1996 to designate a program of the U.S. Defense Advanced Research Projects Agency (DARPA) [23]. Unlike charge, which is a scalar quantity, the quantum-mechanical spin of an electron is a vector quantity, which can be *roughly* thought of as a tiny magnetic moment attached to an electron [24]. Devices made of electron's spin as a state variable are switched by flipping spins without moving any charge in space and causing current flow. This eliminates the I^2R energy associated with switching.

Flipping spins incurs some energy dissipation as well, but it can be considerably less than the energy dissipated in charge-based devices [25, 26]. Moreover, spin couples very weakly to its surroundings (phonon baths) and only spin-flip scattering events can affect its state. Therefore, spins can be retained *out of equilibrium* for long durations. Spin relaxation time as long as one second at a temperature of 100 K has been demonstrated in some organic materials [27]. Such prolonged existence in non-equilibrium states can overcome the Landauer-Shannon's limit of energy dissipation $kT\,ln(2)$ per bit flip since this limit presupposes equilibrium statistics [28]. This gives "spin" an advantage over "charge" as a state variable and motivates research in spintronics [29, 22, 30, 31, 32].

1.4 Nanomagnets

Considerable progress has been achieved in the understanding of the behavior of ferromagnetic bodies since 1930 [33, 34]. However, it is the recent advances in nanofabrication technologies (e.g., electron-beam lithography) that have facilitated probing magnetism in small

length scales [35]. In this respect, perhaps the most intriguing theorem is stated by Brown [36], which says that magnetic domain formation should be limited to very small dimensions (∼100 nm) because of the competition between the magnetostatic energy and the quantum-mechanical exchange energy, causing nanomagnets to behave like single giant spins. There exist several experimental and theoretical investigations on single-domain states and phase transitions in magnetization distribution [35, 37, 38]. Such "single domain" particles are very promising for spintronic applications since they can be utilized as a binary switch [39, 40, 41]. Multi-domain nanomagnets formed into nanowires also have promising applications that we discuss in Section 1.8. Note that unlike transistors, magnets have *no leakage* and no standby power dissipation, which is an important additional benefit.

Recently, it has been shown that the *minimum* energy dissipated to switch a charge-based device like a transistor at a temperature T is $\sim NkTln(1/p)$, where N is the number of information carriers (electrons or holes) in the device and p is the bit error probability [42]. On the other hand, the minimum energy dissipated to switch a single-domain nanomagnet (which is a collection of M spins) can be only $\sim kTln(1/p)$ since the exchange interaction between spins makes M spins rotate together in unison like a giant classical spin [35, 42]. This gives a nanomagnet an inherent advantage over a transistor.

Unfortunately, the magnet's advantage is lost if the method adopted to switch it is so inefficient that the energy dissipated in the switching circuit far exceeds the energy dissipated in the magnet. Regrettably, this is often the case. So there is a need to identify an energy-efficient mechanism for switching a magnet, which we will discuss later in this chapter.

1.5 Magnetic anisotropy

The internal energy of a magnet depends on the direction of spontaneous magnetization. Hence, this energy is termed as magnetic anisotropy energy. Generally, in a magnet of isotropic shape (e.g. a sphere), the magnetic energy term possesses the crystal symmetry of the material and we call it *crystal magnetic anisotropy* or *magnetocrystalline anisotropy*. In a *polycrystalline* material, magnetocrystalline anisotropy can be neglected. Also, magnetic anisotropy energy can be generated by (1) modifying the shape of the particle, which is termed as *shape anisotropy*,

and (2) inducing strain, which is termed as *magnetostrictive anisotropy* [34, 33].

1.5.1 Shape anisotropy

Any deviation from the spherical shape of a nanomagnet generates anisotropy in the magnetization energy which favors aligning the magnetization in some preferred directions [34]. Consider an elliptical-shaped single-domain nanomagnet having major axis a, minor axis b, and thickness l with $a > b$, $a/b \sim 1$, and $a, b >> l$; the shape anisotropy energy is given by

$$E_{shape-anisotropy} = \frac{\mu_0}{2} M_s^2 \Omega \left[N_{d-xx} - N_{d-yy} \right] cos^2\theta \tag{1.1}$$

where M_s is the saturation magnetization of the magnet, Ω is the nanomagnet's volume, θ is the angle between the magnetization direction with the x-direction (see Fig. 1.3), and N_{d-mm} is the demagnetization factor in the m-direction, which is a function of the shape of the specimen [34]. For conceptual illustration of shape anisotropy we have not introduced the demagnetization factor along the out-of-plane direction of the magnet, i.e., N_{d-zz} in the expression of shape anisotropy. (See Chapter 2 for details.)

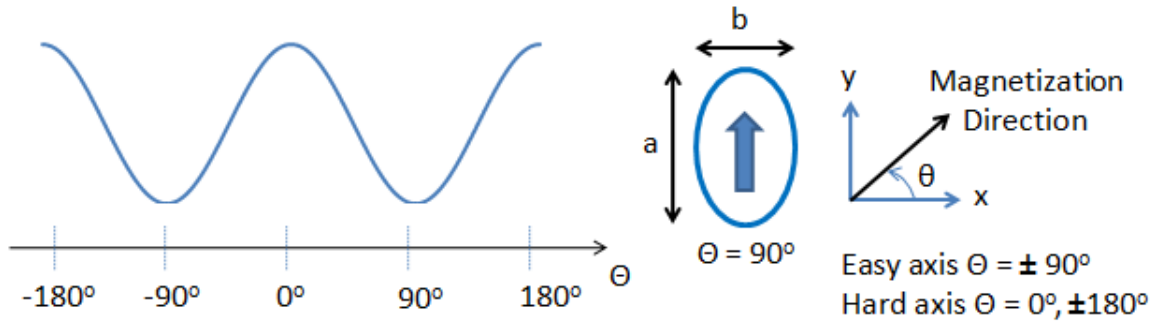

Figure 1.3: Potential landscape of a single-domain elliptical nanomagnet. Shape anisotropy has generated two stable minima in the potential energy landscape, which allows it to be used as a binary switch.

The potential energy landscape of the nanomagnet is shown in the Fig. 1.3. We can notice that the potential energy is minimum for $\theta = \pm 90°$ and maximum at $\theta = 0°, 180°$. Thus the magnetization favors aligning along the $\theta = \pm 90°$ direction, which is why we call each of them *easy axis*. These two directions can be thought of being two stable states in a binary switch. With a similar analogy, the two directions $\theta = 0°, 180°$ are termed as *hard axes*.

In general, we should consider full three-dimensional potential landscape of a nanomagnet, which allows us to consider full three-dimensional motion of magnetization too and that has important consequences on the binary switching between its two stable states. This will be prominent in the chapters onwards. Fig. 1.4 shows the magnetization in full three-dimensional space. Note that y-z plane ($\phi = \pm 90°$) is the magnet's plane and x direction is the out-of-plane direction, which is along the thickness of the nanomagnet. The two directions $\theta = 0°, 180°$ are the two stable axes (easy axes), which are along the $\pm z$-direction. We call the $\pm y$-direction as the *in-plane* hard axes and the $\pm x$-direction as the *out-of-plane* hard axes, which are *harder* than the in-plane ones due to the small thickness of the nanomagnet compared to the lateral dimension in $\pm y$-direction.

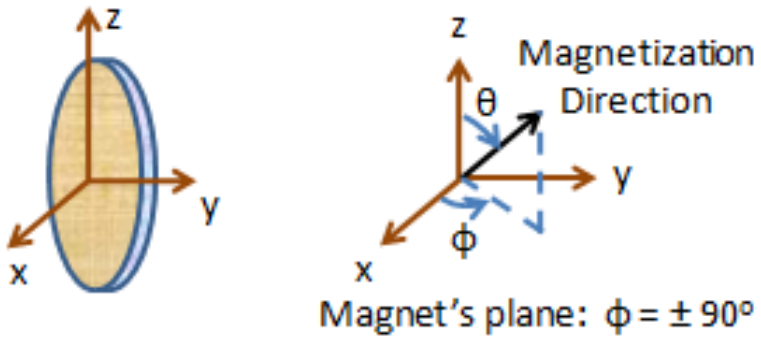

Figure 1.4: Magnetization in full three-dimensional space. Standard spherical coordinate system is used. (θ is the polar angle and ϕ is the azimuthal angle.)

Fig. 1.5 shows the full three-dimensional landscape of a nanomagnet with thickness around 10 times smaller than the lateral dimensions. The potential barrier goes higher along the out-of-plane direction compared to in-plane directions (i.e., $\phi = 90°, 270°$) due to small thickness of the nanomagnet along the out-of-plane direction. Note that we need to topple only the barrier along in-plane direction (i.e., $\phi = \pm 90°$) for binary switching, however, out-of-plane excursion of magnetization along the out-of-plane direction has very important and intriguing consequences, which would be prominent in the chapters onwards.

1.5.2 Magneostrictive anisotropy

Magnetostriction is a phenomenon wherein materials undergo a change in shape due to change in magnetization in the material. In the most common magnets (e.g., Iron, Cobalt, Nickel), the deformation $\delta l/l$ due to magnetostriction is as small as $\sim 10^{-5}$. However, giant

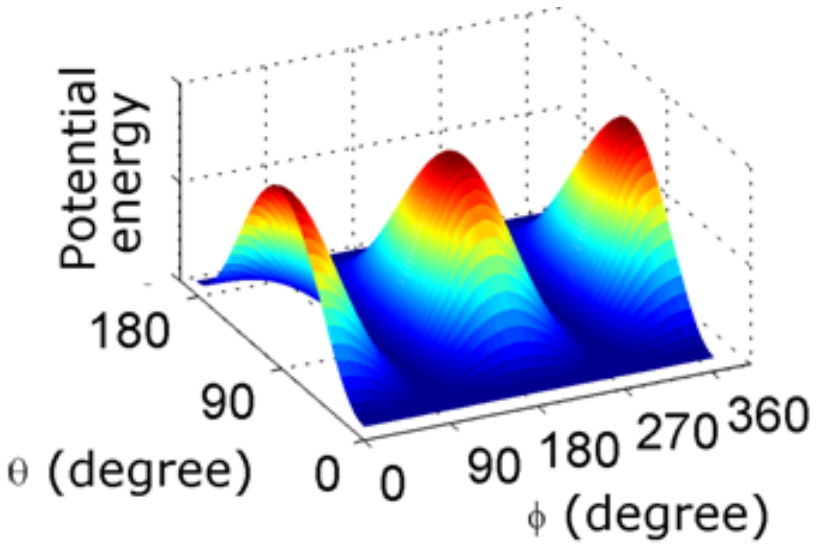

(a)

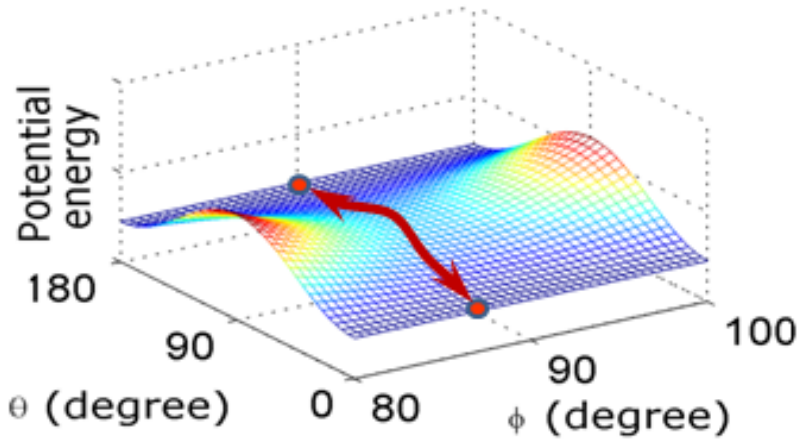

(b)

Figure 1.5: Potential landscape of a single-domain elliptical nanomagnet in full three-dimensional space. (a) Potential landscape for azimuthal angle $\phi = 0° - 360°$. (b) Potential landscape for azimuthal angle $\phi = 80° - 100°$. Even if we need to just topple the in-plane energy barrier to switch between the two stable states (as shown by the arrow), we will see later that magnetization dynamics is not that simple. The out-of-plane energy barrier and magnetization's out-of-plane motion have intriguing consequences.

magnetostriction of $\sim 10^{-3}$ at room temperature is possible in Terfenol-D (TbDyFe), a specially formulated alloy containing Iron (Fe) and rare earth materials Terbium (Tb) and Dysprosium (Dy) [43, 44].

Stress-induced magnetostrictive anisotropy is given by [34, 33].

$$E_{stress-anisotropy} = -\frac{3}{2}\,\lambda_s \sigma\, \Omega\, sin^2\theta \tag{1.2}$$

where $(3/2)\lambda_s$ is saturation magnetostriction, σ denotes stress, θ is the angle between the magnetization direction with the x-direction (see Fig. 1.6), and Ω is the nanomagnet's volume. The corresponding potential landscape is plotted in the Fig. 1.6. Note that we have assumed $\lambda_s \sigma$ as some negative value while generating the plot. It means that we assume a *compressive* (negative) stress for materials with positive magnetostriction coefficient (e.g., Terfenol-D), while a *tensile* (positive) stress for materials with negative magnetostriction coefficient (e.g., Iron, Cobalt, Nickel).

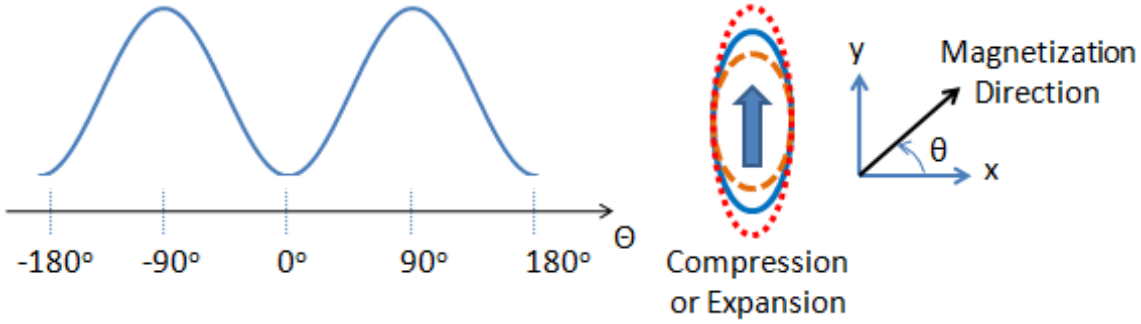

Figure 1.6: Potential landscape of a single-domain nanomagnet with stress-induced magnetostrictive anisotropy. Shape anisotropy is not considered in the plot. The nanomagnet is expanded or compressed depending on the sign of stress and subsequently a stress anisotropy is generated.

We notice that the potential landscapes in the Figs. 1.3 and 1.6 are complementary in nature, i.e., the minima and maxima positions are interchanged. Accordingly, magnetostrictive anisotropy can be exploited to *beat* the shape anisotropy, which will shift the nanomagnet's minimum energy position along its *hard* axis rather than along an easy axis. (See Fig. 1.7.) This is a useful mean to switch the magnetization of a magnetostrictive nanomagnet, which we will discuss in the Section 1.10. The minimum stress required to topple the shape anisotropy barrier by introducing magnetostrictive anisotropy can be determined by equating the shape

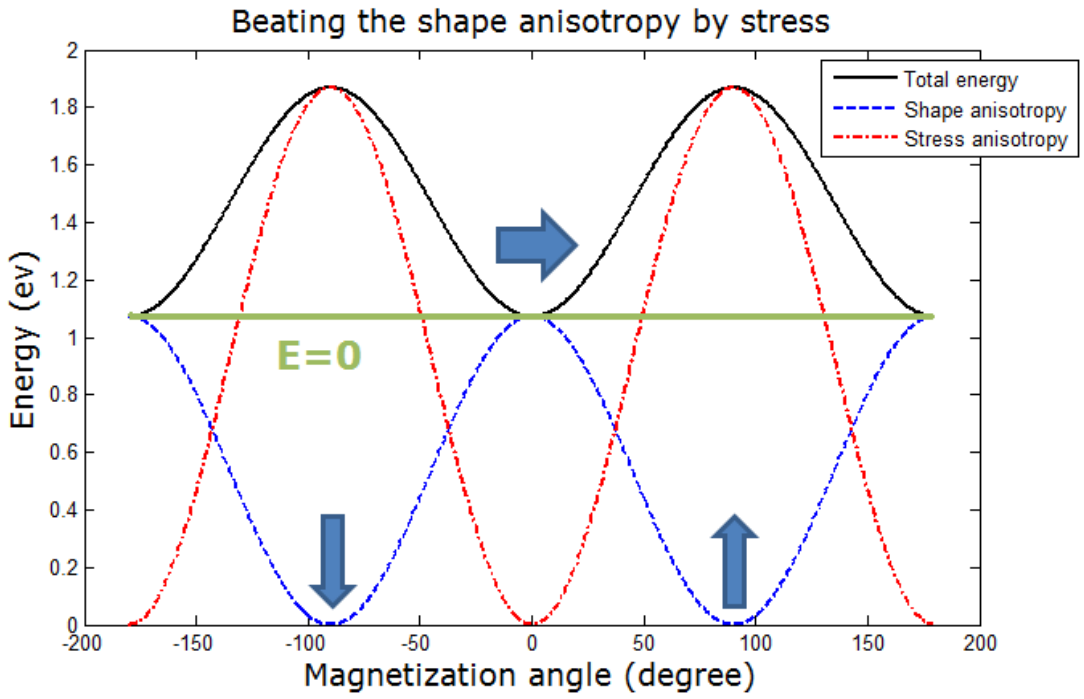

Figure 1.7: Magnetostrictive anisotropy is overcoming the shape anisotropy barrier, which makes the minimum energy position of the magnet along its hard axes rather than the easy axes.

anisotropy and the magnetostrictive anisotropy as follows.

$$\frac{\mu_0}{2} M_s^2 \Omega \left[N_{d-xx} - N_{d-yy}\right] = -\frac{3}{2} \lambda_s \sigma \, \Omega$$

$$\Rightarrow \quad \sigma_{E=0} = -\frac{1}{(3/2)\lambda_s} \frac{\mu_0}{2} M_s^2 \left[N_{d-xx} - N_{d-yy}\right]. \tag{1.3}$$

We notice that the required stress for magnetization switching is independent of the nanomagnet's volume, Ω provided $N_{d-xx} - N_{d-yy}$ remains constant, which is a function of the shape of the nanomagnet.

1.6 Magnetoresistance: Reading of states

Magnetoresistance is the change in electrical conductivity due to the presence of magnetic field. The so-called Giant Magnetoresistance (GMR) is a quantum-mechanical phenomenon that is observed in layered magnetic thin-film structures composed of alternating ferromagnetic and non-magnetic layers, which has earned the inventors Nobel prize in physics, 2007 [45,

46]. If the magnetic moments of the ferromagnetic layers are parallel, the spin-dependent scattering of the carriers is minimized so the resistance is minimum. Similarly, the antiparallel magnetic moments of the ferromagnetic layers produce a maximum resistance. (See Fig. 1.8.) Magnetoresistance (which is defined as the percentage change in between the minimum and maximum resistance) increases with a thinner nonmagnetic layer in between the ferromagnetic layers. Magnetic multilayers also show rich physical phenomena [47, 48, 49]. GMR had a major economic impact in producing read heads of the magnetic hard disk drives [39].

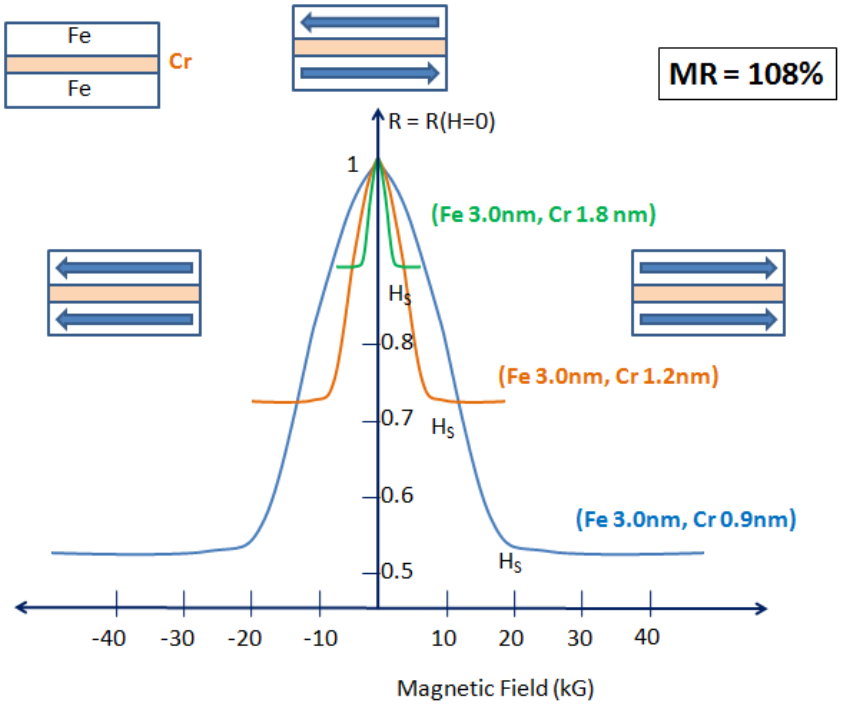

Figure 1.8: Giant magnetoresistance effect. Resistance is maximum when the magnetic moments in the ferromagnetic layers are antiparallel and minimum when the magnetic moments in the two layers are parallel. Magnetoresistance increases with a thinner non-magnetic spacer layer [50].

Tunneling magnetoresistance (TMR) is a similar phenomenon to the GMR, where the non-magnetic sandwiched layer is replaced by a thin (∼1 nm) insulator (e.g., Al_2O_3, MgO) [51, 52, 53, 54, 55]. Such structure is known as magnetic tunnel junctions (MTJs). The TMR is much higher (∼500%) than GMR because of tunneling phenomenon involved therein. MgO-based MTJ was predicted and analyzed first [56, 57, 58, 59, 60, 61, 62], and later that was experimentally demonstrated [63, 64]. Using half-metallic magnets, for which one-spin channel conducts while the other spin-channel does not conduct [65, 66, 67, 68, 69, 70, 71, 72, 73], we can have in principle infinite TMR, but spin-orbit interaction destroys such infinite nature,

however, still we can get very high TMR [74, 75].

TMR methodology is widely used for reading the magnetization states in a single-domain nanomagnet. By incorporating a hard nanomagnet (e.g., made of Iron-Platinum) whose magnetization direction is *fixed* and known, we can read the magnetization state of the *free* nanomagnet by TMR measurement mechanism. When the magnetization directions of the *fixed* and *free* layers are parallel, the resistance is low and when they are anti-parallel, the resistance is high. Thus, by measuring the resistance of an MTJ, one can ascertain the magnetization orientation of the magnetostrictive layer (relative to the fixed hard layer) and thus read the stored state. The resistance can be measured with a small sense current (of pA range), which dissipates very little power. Note that the reading of the states is *non-destructive*, i.e., a nanomagnet preserves its state after reading. Also a nanomagnet retains its state after the power supply is turned off, provided the shape anisotropy barrier is high enough to beat the thermal fluctuations with a very low probability of hold failure, which is why it is possible to build *non-volatile* memory and logic with nanomagnets. Therefore, nanomagnets have immense economic impact on future information processing technology [76, 77].

1.7 Conventional methodologies for switching spins: Writing of states

The writing of magnetization states in a single-domain nanomagnet is much more complex than that of reading. There are two traditional methodologies that came up in sequence are described in subsequent subsections. Both have the drawback that energy dissipation is excessively high with current technology.

1.7.1 External magnetic field

A magnetic field can switch the magnetization state of a nanomagnet. And we can sense the magnetization state in a magnetic tunnel junction (MTJ). This gave rise to magnetic random access memory (MRAM) technology, in which an MTJ is utilized as both storage device and storage sensing device [78]. A magnetic field modulates the potential landscape of

the nanomagnet depending on the magnitude and direction of the field. The potential energy term with an external magnetic field **H** is expressed as

$$E_{mag} = -\mathbf{M}.\mathbf{H} \tag{1.4}$$

where **M** is the magnetization. The basic operation of an MRAM is shown in Fig. 1.9. In principle, the operation is similar to a binary switch as in Fig. 1.1 [79]. A magnetic field H_x along the nanomagnet's hard axis removes the barrier and then another magnetic field H_y is applied along the *positive* y-direction to modulate the potential landscape in such a way that it prefers magnetization to be pointing *up* rather than pointing *down*, hence achieving a flip. The tilt in the potential profile that switches the magnetization along the pointing-up direction has to be sufficient enough so that it can beat the thermal fluctuations resulting in a sufficiently low error probability. If we want to switch the magnetization from pointing-up to pointing-down, the asymmetry-making field H_y has to be applied in the *negative* y-direction.

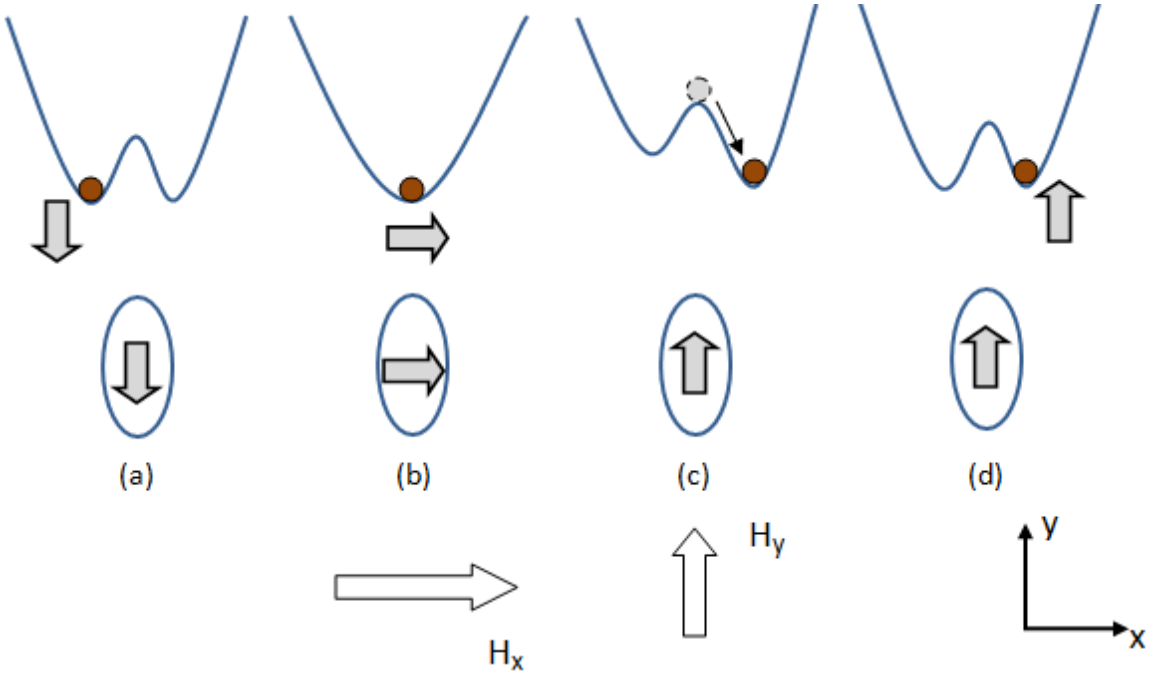

Figure 1.9: MRAM as a binary switch. (a) Magnetization is pointing down initially. Our task is to switch it to pointing-up direction. (b) A magnetic field H_x along the hard-axis of the nanomagnet is applied to remove the barrier and the potential landscape has become *monostable*. (c) An asymmetry-making field H_y is applied along the positive y-direction, while the field H_x has been withdrawn. The magnetization direction being pointing-up is preferred over the pointing-down direction because of the asymmetry in the potential profile. Thus the magnetization reaches to it desired state. (d) The field H_y is removed. Potential landscape is back to its original position as in (a) but the magnetization direction is switched.

Even if a binary switch utilizing the giant-spin of a nanomagnet can be materialized with magnetic fields as external agents, it is imperative to estimate the energy dissipation for generating the external magnetic fields for its possible wide application. Current-generated magnetic field was reported in Ref. [80] and energy dissipation is turned out to be 10^{11} - 10^{12} kT at room temperature (T = 300 K) with a switching delay in the order of 1 μs, which clearly makes it impractical [81, 82, 83, 84, 85, 86, 87, 88, 89, 90, 91]. In fact, it will make the magnet inferior to the transistor which can be switched in sub-nanosecond while dissipating 10^{7} - 10^{8} kT of energy in a circuit [92]. Such excessive energy dissipation has motivated the researchers in devising better technologies that possibly incur a reasonable energy dissipation. Moreover, magnetic field is difficult to confine in small space, which creates additional complexity and sacrifices chip-area.

1.7.2 Spin-transfer torque

Spin-angular-momentum-transfer or simply spin-transfer-torque (STT) mechanism is an electric current-induced magnetization switching (CIMS) mechanism that can rotate the magnetization axis of a nanomagnet by exerting a torque on it [93, 94, 95, 96]. This mode of magnetization rotation eliminates the need of applying cumbersome magnetic fields which are difficult to confine within small spaces [76] and require significant energy to generate. STT-induced switching has been unambiguously verified in magnets with ∼100 nm size [97] and has been demonstrated in numerous experiments involving both spin-valves [98] and magnetic tunnel junctions (MTJs) [99].

The magnetization switching in a nanomagnet using STT is principally different than that of using an external magnetic field. A magnetic field modifies the potential landscape of the nanomagnet and the torque is *generated* from the gradient of potential landscape. But, with spin-transfer torque (STT) mechanism, the torque is supplied by the spin-angular momentum transfer and thus it does not depend on the modification of potential barrier, i.e., the potential energy expression of the nanomagnet is not modified. However, the methodology of binary switching still can be conceived by assuming that the total energy of the magnetization has increased over the barrier energy, which can be thought of equivalent to the removal of the energy barrier in a binary switch. Once the barrier is toppled, the magnetization falls towards

its destination and the negative-gradient of the potential barrier facilitates the switching. (See Fig. 1.10.)

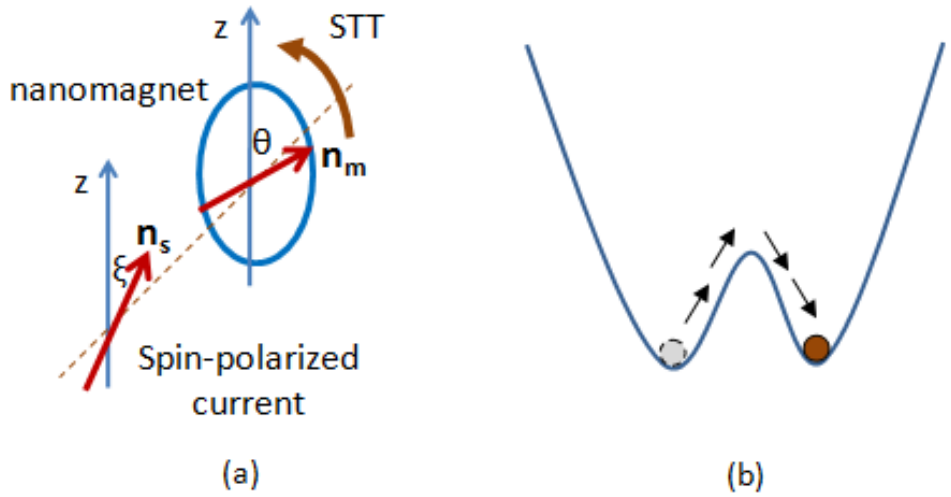

Figure 1.10: Magnetization switching using spin-transfer-torque (STT) mechanism. (a) A spin-polarized current is passed through the nanomagnet and the spin-angular momentum is transferred to the magnetization. This exerts a torque on the magnetization, rotating it towards the direction of spin polarization in the incident current. (b) Switching from one stable state to another takes place when an electrical current with spin-polarization having direction along the desired state is passed through the nanomagnet.

Following Fig 1.10(a), the torque due to STT can be expressed as

$$T_{STT} = s\,\mathbf{n_m} \times (\mathbf{n_s} \times \mathbf{n_m}) = sin(\xi - \theta)\hat{\mathbf{e}}_\theta$$

where $s = (\hbar/2e)\eta I$ is the spin angular momentum deposition per unit time, and $\eta = (I_\uparrow - I_\downarrow)/(I_\uparrow + I_\downarrow)$ is the spin-polarization factor of the incident current I. Note that by changing the direction of current, a torque in the opposite direction can be exerted.

Recent studies - both theoretical [100, 101, 102, 103, 104, 105, 106, 107, 108, 109] and experimental [110, 111, 112] have shown a significant amount of field-like torque in magnetic tunnel junctions producing voltage asymmetry in spin-transfer torque switching. However, the effect of this field-like torque in switching dynamics of a nanomagnet is yet to be understood properly. This field-like torque is the in-plane component of the effective field produced by the spin-transfer phenomenon and can be described by a pseudo magnetic field [107]. This is different from the conventional out-of-plane field component, which is responsible for the traditional 'Slonczewski' type switching [93] described above and is always non-conservative [93,

95].

Spin-transfer torque mechanism, although fascinating from physical point of view, had the drawback from beginning that it requires a very high current density of $\sim 10^7$ A/cm^2 [113] dissipating 10^7 - 10^8 kT at room temperature (T = 300 K). It also incurs additional dissipation in the *polarizer* magnet due to polarizing the spins in the incident current. There have been ideas on using nanomagnets with low-saturation magnetization [114, 115, 116], passing in-plane current rather than perpendicular-to-plane current [117, 116] etc., but still the energy dissipation remained high. Recently, magnetization switching via *spin-accumulation* technique with a *pure spin current* rather than a spin-polarized charge current has gained a lot of attention [118, 119]. However, the low-injection efficiency of the pure spin current and its feasibility to low energy dissipation are still in question.

There have been proposals of computing using both magnetic field and spin-torque mechanism [120, 121, 122, 123, 124, 125, 126, 127], but excessive energy dissipation limits their applications.

1.8 Multi-domain magnets and domain-wall motion

Domain-wall is the transition layer between two adjacent ferromagnetic domains and it has a finite thickness without abrupt change in the spin direction from one domain to the other [34]. Magnetic information can be encoded by manipulating the domain walls, in fact domain-wall motion was the mean of early investigation in magnets because of the unavailability of single-domain nanomagnets beyond the past decade [113].

However, in recent days, magnetization reversal through domain-wall switching [128, 129, 130, 131, 132] in dilute ferromagnetic semiconductor structures [e.g., (Ga,Mn)As [133], (Ga,Mn)N [134] etc.] has gained a lot of attention because the current density of switching can be reduced to 10^4 - 10^5 A/cm^2 [135, 136, 137], which is several orders of magnitude lower than the current density required to switch with spin-transfer-torque mechanism in single-domain nanomagnets. But the switching speed is not enough high ($<$ 100 MHz) and also the operational temperature is much below than the room temperature [135, 138].

On the positive side, ferromagnetic semiconductors has a significant advantage in that

they can be seamlessly integrated into the traditional semiconductor structures because of conductivity matching, however, the conductivity mismatch problem of spin-injection from a ferromagnet metal into a semiconductor has been addressed especially through tunnel contacts [139, 140, 141, 122].

We would now discuss briefly about the possibility of building memory with domain-wall motion. In a bulk ferromagnet, the magnetization direction in different domains may subtend different angles between them but in a nanowire due to strong shape anisotropy, the magnetization direction in the domains is either parallel or antiparallel to the wire axis. Exploiting this point, there has been demonstration of magnetic domain-wall *racetrack* memory [142, 143, 144, 145, 146]. Along the racetrack nanowire successive domain-walls alternate between head-to-head and tail-to-tail configurations. Writing domain walls can be carried out using a spin-momentum transfer torque generated from the current injected into the racetrack [142]. Racetrack memory can potentially be a three-dimensional technology by placing the nanowires *vertically* on a chip. Although fascinating, with the current technology, the switching current density is excessively high ($\sim 10^8$ A/cm^2) and the switching delay is 10-50 ns, which restrict its wide application in RAM technologies. Magnetic domain-wall logic has also gained a lot of attention [147, 148] but it is difficult to pipeline them, which restricts its wide application [31].

1.9 Polarization switching in ferroelectrics

Ferroelectrics possess a spontaneous polarization, which is electrically switchable [149]. The application of ferroelectric capacitors in non-volatile RAMs (FeRAMs) is due to its switchable polarization, however, the readout mechanism is destructive [149]. Ultrafast polarization switching in $\sim$50 ps is possible in thin-film ferroelectrics [150]. Ferroelectric tunnel junctions comprising of ferromagnetic electrodes with a ferroelectric layer sandwiched in between has been utilized to demonstrate non-volatile control of polarization by electrically switching the ferroelectric [151, 152]. While fast electric writing is an adorable advantage in ferroelectrics, which dissipates low energy, the *destructive* capacitive readout is a bottleneck for wide application of ferroelectric RAMs. Some research works are coming along that show *non-destructive* readout

of ferroelectric states [153, 151], however, the tunneling electroresistance is still $< 20\%$, which is not good enough for distinguishability of binary states in a binary switch in the presence of fluctuations and noise; hence it prevents FeRAM's wide application.

1.10 Multiferroic magnetoelectrics

The *magnetic writing*, whether it's by a magnetic field or via passing a spin-polarized current incurs an exorbitant energy dissipation, while *magnetic reading* via magnetoresistance measurement technique is non-destructive, the magnetoresistance itself is quite high and hence quite viable. On the other hand, *electric writing* in ferroelectrics dissipates less energy but the readout mechanism in ferroelectrics is destructive or the measured electroresistance is small. Accordingly, using *multiferroic* materials that are both ferroelectric and ferromagnetic would be attractive since it will exploit the best aspects while avoiding the issues of reading FeRAMs and magnetic writing, i.e., data is written electrically and read magnetically. In general, *multiferroics* are materials or composites where different ferroic orders such as ferroelectric, ferromagnetic/ferrimagnetic, ferroelastic coexist. For our discussion, we will assume the coexistence of ferroelectric and ferromagnetic orders to mean mutiferroism.

However, multiferroic materials are rare. Density functional theory (DFT) has shown that in general, transitional metal d electrons that are responsible for magnetism reduces the tendency of off-center ferroelectric distortion, hence, the magnetic ferroelectrics are rare [154]. Moreover, magnetoelectric responses of the multiferroic materials (e.g., $BiFeO_3$ [155, 156]) is very weak or occur at low temperatures so their technological applications are not viable at all, however, *hybrid improper ferroelectricity* is showing some promise recently [157, 158]. In contrast, multiferroic *composites* are built with a ferroelectric layer and a ferromagnetic layer with intimate contact to each other; their magnetoelectric responses are high enough at room temperature that they can be utilized for potential technological applications [159, 160, 161]. Multiferroic *materials* are termed as *single-phase* multiferroics, while the multiferroic *composites* are termed as *two-phase* multiferroics.

Enhanced magnetoelectric coupling in a two-phase multiferroic can be obtained by indirect coupling, via *strain* [162, 163, 164]. In that case the ferroelectric material has to be *piezoelectric*

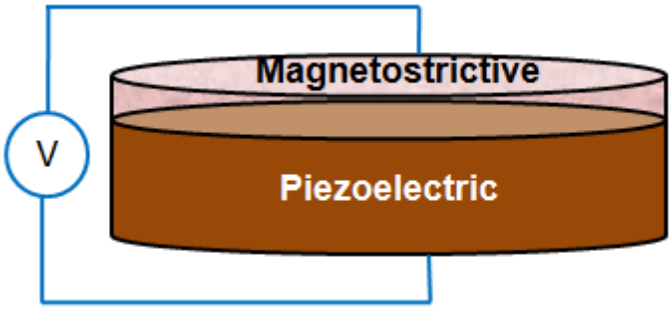

Figure 1.11: An elliptical two-phase multiferroic composite structure. Stress is generated on the magnetostrictive nanomagnet by applying a voltage across the structure.

and the ferromagnetic material has to be *magnetostrictive*. Fig. 1.11 shows such a structure.

A voltage applied across the structure generates a strain in the piezoelectric layer and the strain is elastically transferred to the magnetostrictive layer, which generates a stress in the magnetic layer. The procedure for determining the voltage required to generate a desired stress in a magnetostrictive layer is as follows. In order to generate a stress σ in a magnetostrictive layer, the strain in that material must be $\varepsilon = \sigma/Y$, where Y is the Young's modulus of the material. We will assume that a voltage applied to the PZT layer strains it and since the piezoelectric layer is much thicker than the magnetostrictive layer, all the strain generated in the piezoelectric layer is transferred completely to the magnetostrictive layer. Therefore, the strain in the piezoelectric layer must also be ε. The electric field needed to generate this strain is calculated from the piezoelectric coefficient d_{31} (that has unit of m/V) of the piezoelectric material and the corresponding voltage is found by multiplying this field with the thickness of the piezoelectric layer.

The generated stress in the magnetostrictive layer creates a magnetostrictive anisotropy (see Subsection 1.5.2) therein. It is experimentally shown that this magnetostrictive anisotropy can induce domain-wall motion for multi-domain magnetic layers [165]. There have been also experimental efforts for single-domain case [166, 167]. So the viability of magnetostrictive anisotropy is very prominent. In this dissertation, it is theoretically shown that the magnetization of a shape-anisotropic *single-domain* magnetostrictive nanomagnet can be *switched* with a small voltage applied to the piezoelectric layer [168, 169, 170, 171]. In this method, the electrostatic potential generates a *uniaxial* strain in the piezoelectric layer, and that is elastically transferred to the magnetostrictive layer if the latter is considerably thinner. The nanomag-

net is constrained along its hard axis so that the generated stress is along the easy axis of the nanomagnet. This makes the magnetization of the magnetostrictive layer rotate towards the nanomagnet's hard axis. However, magnetostrictive anisotropy cannot make a potential landscape asymmetric (which is usually required for binary switching, e.g., in MARM [see Subsection 1.7.1]) because of the square term in its expression [see Equation (1.2)]. But, it is shown that an asymmetry in potential landscape is *not necessary* for successful switching. Analysis of full three-dimensional motion of the magnetization reveals that there exists a *built-in* torque in the system that can switch the magnetization towards its destination without requiring the potential landscape to be asymmetric. We will discuss this mechanism in details bolstering with theoretical formulations and simulation results in the Chapters 2 and 3. There are proposals of using multiferroic structures in magnetic logic and memory [172, 173, 174, 175, 41]. There are proposals of utilizing the magnetocrystalline anisotropy instead of magnetostrictive anisotropy too [176, 177, 178, 179, 180, 181].

With a nanomagnet density of 10^{10} cm^{-2} in a memory or logic chip, the dissipated power density can be of the order of one mW/cm^2 if 10% of the magnets switch at any given time (i.e., 10% activity level). Also, sub-nanosecond switching speed can be achieved. Such *extremely low power*, yet *high density* and *high speed* magnetic logic and memory systems, composed of multiferroic nanomagnets, can be powered by existing energy harvesting systems [182, 183, 184, 185] that harvest energy from the environment without the need for an external battery. These processors are uniquely suitable for implantable medical devices, e.g. those implanted in a patient's brain that monitor brain signals to warn of impending epileptic seizures. They can run on energy harvested from the patient's body motion. These hybrid spintronic/straintronic processors can be also incorporated in "wrist-watch" computers powered by arm movement, buoy-mounted computers for tsunami monitoring (or naval applications) that harvest energy from sea waves, or structural health monitoring systems for bridges and buildings that are powered solely by mechanical vibrations due to wind or passing traffic.

1.11 Outline of the remaining chapters

The outline of the remaining chapters are as follows. Chapter 2 provides the theoretical formulations to solve the dynamics of a magnetostrictive nanomagnet. The well-known Landau-Lifshitz-Gilbert (LLG) equation for magnetization motion is solved analytically in spherical coordinate system to get a couple-dynamics of motion between the polar angle and the azimuthal angle of the magnetization vector. It is explained from the equations that the *built-in* dynamics can complete the switching without requiring the potential landscape to be asymmetric. Also, the equations for calculating energy dissipations both in the external switching circuitry and internally due to damping are given in this chapter. In Chapter 3, the coupled equations are solved numerically to get the switching dynamics of magnetization as well as the quantitative values of switching delay and energy dissipation during the period of switching. Simulation results pertaining to the dynamics of magnetization are described and explained from theoretical formulations. Chapter 4 presents the dynamics of magnetizations in a circuit of multiple nanomagnets based on the same model developed in Chapter 2, e.g., signal propagation in a horizontal wire via Bennett clocking mechanism. Preliminary experimental works on building single-domain nanomagnets are provided in Chapter 5. Finally, Chapter 6 discusses some important points pertaining to this dissertation and concludes on the ramification of present study towards our future nanoelectronics.

Chapter 2

Theoretical Formulations

In this chapter, we first introduce the Landau-Lifshitz-Gilbert (LLG) equation of magnetization motion. The LLG equation is solved for a magnetostrictive nanomagnet in spherical coordinate system. The magnetization motion in three-dimensional space produces a coupled set of analytical equations involving the polar angle and azimuthal angle of the magnetization, which demands numerical solution to proceed further. The solution of LLG equation provides us the understanding of magnetization dynamics as well as it permits us to extract the quantitative values switching delay and energy dissipation during the switching.

2.1 Landau-Lifshitz-Gilbert equation

Similar to the rotational motion of a rigid body in classical mechanics, the equation of motion for the magnetic moment $\mathbf{M}$ of a spin can be written as

$$\frac{\partial \mathbf{M}(\mathbf{r},t)}{\partial t} = -|\gamma|\,\mathbf{M}(\mathbf{r},t) \times \mathbf{H}(\mathbf{r},t), \tag{2.1}$$

where γ is the gyromagnetic ratio defined as the ratio between magnetic moment and angular momentum, and $\mathbf{H}(\mathbf{r},t)$ is the *effective field*. The effective field is defined by

$$\mathbf{H}(\mathbf{r},t) = -\frac{\delta U[\mathbf{M}(\mathbf{r},t)]}{\delta \mathbf{M}(\mathbf{r},t)}, \tag{2.2}$$

where $U[\mathbf{M}(\mathbf{r},t)]$ is the potential energy of $\mathbf{M}(\mathbf{r},t)$ and δ denotes the *functional* derivative.

For a *giant-spin* or *macrospin* of a nanomagnet, we have a single magnetic moment with its magnetization fixed in space (that is the *saturation* magnetization) and the equation of motion can be simplified as

$$\frac{d\mathbf{M}(t)}{dt} = -|\gamma|\,\mathbf{M}(t) \times \mathbf{H}(t). \tag{2.3}$$

The *macrospin assumption* may have some limitations in describing the dynamics in a *multi-spin* system, even in a *single-domain* nanomagnet [186, 187, 188, 189], but this does not hinder us in getting the insight behind the binary switching of magnetization. Moreover, multi-spin analysis is very simulation extensive. The assumption of *macrospin* is commonplace in *single-domain* nanomagnets. Therefore, we will use the *macrospin approximation* in this dissertation.

In the Equation (2.3), we have not considered *damping* of the magnetization. So magnetization just precesses around the effective field as depicted in Fig. 2.1(a) and thus cannot align to the effective field. Damping in a physical system causes a transfer of energy from macroscopic motion to microscopic thermal motion, which results in internal energy losses. Details of the mechanisms of this transfer process are complex. Thus the trend is to consider a *damping parameter* that takes into account the rate of energy transfer and can be determined experimentally without knowing the details of the transfer mechanisms [190, 191]. Damping generates a force that acts in opposition to the macroscopic driving force as depicted in the Fig. 2.1(b). The force due to damping tends to align the magnetization along the direction of the effective field. So the magnetization precesses the effective field in a spiral motion and ultimately aligns itself with the effective field; how fast it aligns is determined by the magnitude of damping parameter.

The damping term was first introduced by Landau and Lifshitz for ferromagnetic bodies [190]. The corresponding Landau-Lifshitz (LL) equation of magnetization dynamics can be written as follows.

$$\frac{d\mathbf{M}(t)}{dt} = -|\gamma|\,\mathbf{M}(t) \times \mathbf{H}(t) + \frac{\alpha|\gamma|}{M}\mathbf{M}(t) \times (\mathbf{M}(t) \times \mathbf{H}(t))\,. \tag{2.4}$$

But the theory could not match experimental results when damping is large, i.e., for *thin*

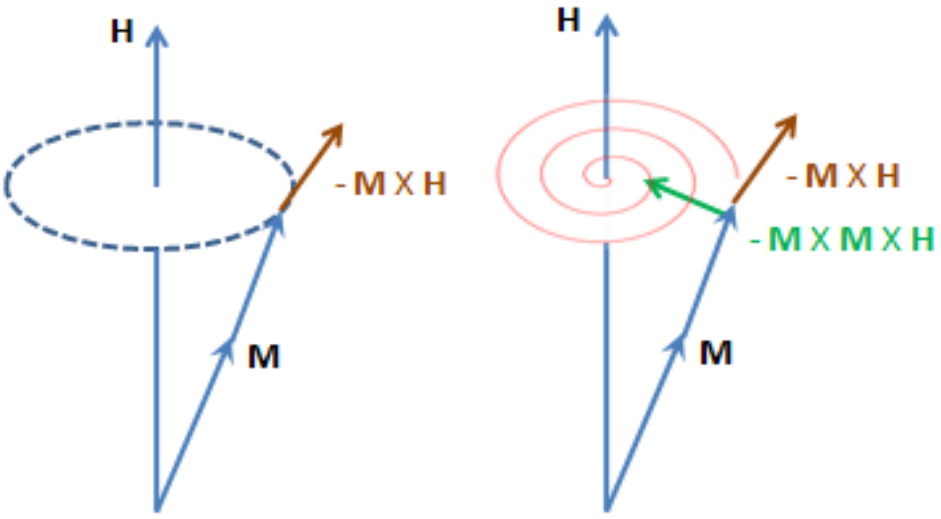

(a) (b)

Figure 2.1: Damping of a magnetic moment along the direction of the effective field as it precesses around the effective field. (a) Without considering damping, magnetization continues to precess around the effective field and thus it cannot align along the effective field. (b) Considering damping, magnetization aligns itself along the direction of effective field and how fast it would align itself depends on the magnitude of the damping, which is a material parameter.

ferromagnetic sheets. Gilbert came up with a phenomenological theory of damping that has been successfully able to take care of large damping [191]. The corresponding equation for damped motion of a magnetic moment is known as the Landau-Lifshitz-Gilbert (LLG) equation, which reads as follows [190].

$$\frac{d\mathbf{M}(t)}{dt} = -|\gamma|\,\mathbf{M}(t) \times \mathbf{H}(t) + \frac{\alpha}{M}\left(\mathbf{M}(t) \times \frac{d\mathbf{M}(t)}{dt}\right). \tag{2.5}$$

In standard form, with an analogy to Landau-Lifshitz (LL) equation, the LLG equation can be written after doing some vector algebra from the above equation as

$$(1+\alpha^2)\,\frac{d\mathbf{M}(t)}{dt} = -|\gamma|\,\mathbf{M}(t) \times \mathbf{H}(t) + \frac{\alpha|\gamma|}{M}\mathbf{M}(t) \times (\mathbf{M}(t) \times \mathbf{H}(t))\,. \tag{2.6}$$

Comparing the LL equation [Equation (2.4)] and LLG equation [Equation (2.6)], we see that there is a difference because of the factor $(1+\alpha^2)$ and it is not negligible if α is not $<< 1$.

2.2 Magnetization dynamics of a magnetostrictive single-domain nanomagnet

In this section, we derive the equations describing the time evolution of the polar angle $\theta(t)$ and the azimuthal angle $\phi(t)$ of the magnetization vector in spherical coordinate system for a magnetostrictive nanomagnet. We do this starting from the Landau-Lifshitz-Gilbert (LLG) equation as in Equation (2.5).

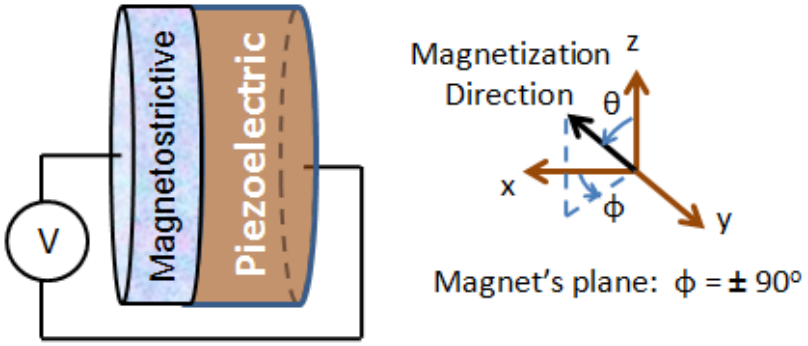

Figure 2.2: A two-phase multiferroic nanomagnet in the shape of an elliptical cylinder is stressed with an applied voltage via the d_{31} coupling in the piezoelectric. The multiferroic is prevented from expanding or contracting along the in-plane hard axis (y-axis), so that a uniaxial stress is generated along the easy axis (z-axis). The resulting stress in the magnetostrictive layer favors aligning the magnetization vector in the plane defined by the in-plane hard axis (y-direction) and the out-of-plane hard axis (x-direction) rather than along the easy axis (z-direction) [168].

Consider an isolated nanomagnet in the shape of an elliptical cylinder whose elliptical cross section lies in the y-z plane with its major axis aligned along the z-direction and minor axis along the y-direction. (See Fig. 2.2.) The dimension of the major axis is a, that of the minor axis is b, and the thickness is l. The volume of the nanomagnet is $\Omega = (\pi/4)abl$. Let $\theta(t)$ be the angle subtended by the magnetization axis with the $+z$-axis at any instant of time t and $\phi(t)$ be the angle between the $+x$-axis and the projection of the magnetization axis on the x-y plane. Thus, $\theta(t)$ is the polar angle and $\phi(t)$ is the azimuthal angle. Note that when $\phi = \pm 90°$, the magnetization vector lies in the plane of the magnet. Any deviation from $\phi = \pm 90°$ corresponds to out-of-plane excursion and we will see onwards that this out-of-plane dynamics has a very important role in switching the magnetization axis.

The total energy of the single-domain, magnetostrictive, polycrystalline (we assume it to be polycrystalline otherwise we would need to consider magnetocrystalline anisotropy) nano-

magnet, subjected to uniaxial stress along the easy axis (major axis of the ellipse) is the sum of the uniaxial shape anisotropy energy and the uniaxial stress (magnetostrictive) anisotropy energy [34]:

$$E(t) = E_{SHA}(t) + E_{STA}(t), \tag{2.7}$$

where $E_{SHA}(t)$ is the uniaxial shape anisotropy energy and $E_{STA}(t)$ is the uniaxial stress anisotropy energy at time t. The former is given by [34]

$$E_{SHA}(t) = (\mu_0/2) M_s^2 \Omega N_d(t) \tag{2.8}$$

where M_s is the saturation magnetization and $N_d(t)$ is the demagnetization factor expressed as [34]

$$N_d(t) = N_{d-zz} cos^2\theta(t) + N_{d-yy} sin^2\theta(t)\ sin^2\phi(t) + N_{d-xx} sin^2\theta(t)\, cos^2\phi(t) \tag{2.9}$$

with N_{d-zz}, N_{d-yy}, and N_{d-xx} being the components of the demagnetization factor along the z-axis, y-axis, and x-axis, respectively. The parameters N_{d-zz}, N_{d-yy}, and N_{d-xx} depend on the shape and dimensions of the nanomagnet. If $l \ll a, b$ and $a/b \sim 1$, then N_{d-zz}, N_{d-yy}, and N_{d-xx} can be approximated by [34]

$$N_{d-zz} = \frac{\pi}{4}\left(\frac{l}{a}\right)\left[1 - \frac{1}{4}\left(\frac{a-b}{a}\right) - \frac{3}{16}\left(\frac{a-b}{a}\right)^2\right] \tag{2.10a}$$

$$N_{d-yy} = \frac{\pi}{4}\left(\frac{l}{a}\right)\left[1 + \frac{5}{4}\left(\frac{a-b}{a}\right) + \frac{21}{16}\left(\frac{a-b}{a}\right)^2\right] \tag{2.10b}$$

$$N_{d-xx} = 1 - (N_{yy} + N_{zz}). \tag{2.10c}$$

Accurate and general expressions of N_{d-zz}, N_{d-yy}, and N_{d-xx} can be determined from the prescription in Ref. [192].

Note that uniaxial shape anisotropy will favor lining up the magnetization along the major axis (z-axis) by minimizing $E_{SHA}(t)$, which is why we will call the major axis the "easy axis" and the minor axis (y-axis) the "in-plane hard axis" of the magnet. The x-axis will therefore be the "out-of-plane hard axis" of the magnet and it is "harder" than the in-plane one since the thickness is much smaller than the magnet's lateral dimensions (i.e., $l << a, b$). By con-

straining the nanomagnet from expanding or contracting in the y-direction, we can generate uniaxial stress along the z-axis (easy axis). An appropriate way to do this is to attach the magnetostrictive layer to a piezoelectric layer to make a 2-phase multiferroic. By applying a potential across the piezoelectric layer, we generate a strain in it which is transferred to the magnetostrictive layer by elastic coupling. This generates uniaxial stress in the latter layer. It is the preferred technique for generating stress since it is electrical in nature and dissipates very little amount of energy [168].

The stress anisotropy energy is given by [34]

$$E_{STA}(t) = -(3/2)\lambda_s \sigma(t) \Omega \, cos^2\theta(t) \tag{2.11}$$

where $(3/2)\lambda_s$ is the magnetostriction coefficient of the single-domain nanomagnet and $\sigma(t)$ is the stress at an instant of time t. Note that a positive $\lambda_s\sigma(t)$ product will favor alignment of the magnetization along the major axis (z-axis), while a negative $\lambda_s\sigma(t)$ product will favor alignment along the minor axis (y-axis), because that will minimize $E_{STA}(t)$. In our convention, a compressive stress is negative and tensile stress is positive. Therefore, in a material like Terfenol-D that has positive λ_s, a compressive stress will favor alignment along the minor axis, and tensile along the major axis. The situation will be opposite with nickel and cobalt that have negative λ_s.

At any instant of time, the total energy of the nanomagnet can be expressed as

$$E(t) = E[\theta(t), \phi(t)] = B(\phi(t)) sin^2\theta(t) + C(t) \tag{2.12}$$

where

$$B_0(\phi(t)) = \frac{\mu_0}{2} M_s^2 \Omega \left[N_{d-xx} cos^2\phi(t) + N_{d-yy} sin^2\phi(t) - N_{d-zz} \right] \tag{2.13a}$$

$$B_{stress}(t) = (3/2)\lambda_s \sigma(t) \Omega \tag{2.13b}$$

$$B(\phi(t)) = B_0(\phi(t)) + B_{stress}(t) \tag{2.13c}$$

$$C(t) = \frac{\mu_0}{2} M_s^2 \Omega N_{zz} - (3/2)\lambda_s \sigma(t) \Omega. \tag{2.13d}$$

Note that $B_0(\phi(t))$ is always positive, but $B_{stress}(t)$ can be negative or positive according to the sign of the $\lambda_s\sigma(t)$ product. It will be negative if we use stress to rotate the magnetization from the easy axis (z-direction) to the plane defined by the in-plane hard axis (y-direction) and the out-of-plane hard axis (x-direction).

In the macrospin approximation, the magnetization $\mathbf{M}$(t) of the nanomagnet has a constant magnitude at any given temperature but a variable direction, so that we can represent it by the vector of unit norm $\mathbf{n_m}(t) = \mathbf{M}(t)/|\mathbf{M}| = \hat{\mathbf{e}}_\mathbf{r}$ where $\hat{\mathbf{e}}_\mathbf{r}$ is the unit vector in the radial direction in spherical coordinate system represented by (r,θ,ϕ). This means that the magnetization vector is in the radial direction, and the polar and azimuthal angles $(\theta(t), \phi(t))$ will specify its orientation at any given time t. The unit vectors in the θ- and ϕ-directions are denoted by $\hat{\mathbf{e}}_\theta$ and $\hat{\mathbf{e}}_\phi$, respectively.

The gradient of potential energy at any particular instant of time t is given by

$$\nabla E(t) = \nabla E(\theta(t), \phi(t)) = \frac{\partial E(t)}{\partial \theta(t)}\,\hat{\mathbf{e}}_\theta + \frac{1}{sin\theta(t)}\,\frac{\partial E(t)}{\partial \phi(t)}\,\hat{\mathbf{e}}_\phi \tag{2.14}$$

where

$$\frac{\partial E(t)}{\partial \theta(t)} = 2B(\phi(t))sin\theta(t)cos\theta(t) \tag{2.15}$$

and

$$\begin{aligned}\frac{\partial E(t)}{\partial \phi(t)} &= -\frac{\mu_0}{2}\,M_s^2\Omega(N_{d-xx} - N_{d-yy})sin(2\phi(t))sin^2\theta(t) \\ &= -B_{\phi e}(\phi(t))\,sin^2\theta(t).\end{aligned} \tag{2.16}$$

Here

$$B_{\phi e}(\phi(t)) = \frac{\mu_0}{2}\,M_s^2\Omega(N_{d-xx} - N_{d-yy})sin(2\phi(t)). \tag{2.17}$$

The effective field acting on the magnetization per unit volume due to shape and stress anisotropy is

$$\begin{aligned}\mathbf{H_{eff}}(t) &= -\nabla E(\theta(t), \phi(t)) \\ &= -\left[2B(\phi(t))sin\theta(t)cos\theta(t)\,\hat{\mathbf{e}}_\theta - B_{\phi e}(\phi(t))sin\theta(t)\,\hat{\mathbf{e}}_\phi\right].\end{aligned} \tag{2.18}$$

Accordingly, the torque acting on the magnetization per unit volume due to shape and stress anisotropy is

$$\begin{aligned}\mathbf{T_E}(t) &= \mathbf{n_m}(t) \times \mathbf{H_{eff}}(t) \\ &= -\hat{\mathbf{e}}_\mathbf{r} \times [2B(\phi(t))sin\theta(t)cos\theta(t)\,\hat{\mathbf{e}}_\theta - B_{0e}(\phi(t))sin\theta(t)\,\hat{\mathbf{e}}_\phi] \\ &= -2B(\phi(t))sin\theta(t)cos\theta(t)\,\hat{\mathbf{e}}_\phi - B_{\phi e}(\phi(t))sin\theta(t)\,\hat{\mathbf{e}}_\theta. \end{aligned} \tag{2.19}$$

Fig. 2.3 shows the potential landscape of a shape-anisotropic nanomagnet unperturbed by stress. According to the Equation (2.19), stress would rotate the magnetization in $\hat{\mathbf{e}}_\phi$ direction, so magnetization climbs up along the potential hill in ϕ-direction from its minimum energy position $\phi = \pm 90°$. This out-of-plane excursion triggered by stress has important consequences in switching the magnetization from one stable state to another. Note that the shape-anisotropic in-plane energy barrier height should be 32 kT at room temperature ($\sim$0.8 ev) or even more so that hold failure probability is less than e^{-32}, which is good for device applications. Keeping a higher barrier height makes the energy dissipation to write a bit more since the barrier has to be toppled to switch the magnetization states.

The magnetization dynamics of the single-domain magnet under the action of various torques is described by the Landau-Lifshitz-Gilbert (LLG) equation as follows.

$$\frac{d\mathbf{n_m}(t)}{dt} - \alpha \left(\mathbf{n_m}(t) \times \frac{d\mathbf{n_m}(t)}{dt} \right) = -\frac{|\gamma|}{M_V}\mathbf{T_E}(t) \tag{2.20}$$

where α is the dimensionless phenomenological Gilbert damping constant, $\gamma = 2\mu_B\mu_0/\hbar$ is the gyromagnetic ratio for electrons and is given by 2.21×10^5 (rad.m).(A.s)$^{-1}$, and $M_V = \mu_0 M_s \Omega$. In the spherical coordinate system with constant magnitude of magnetization,

$$\frac{d\mathbf{n_m}(t)}{dt} = \theta'(t)\,\hat{\mathbf{e}}_\theta + sin\theta(t)\,\phi'(t)\,\hat{\mathbf{e}}_\phi, \tag{2.21}$$

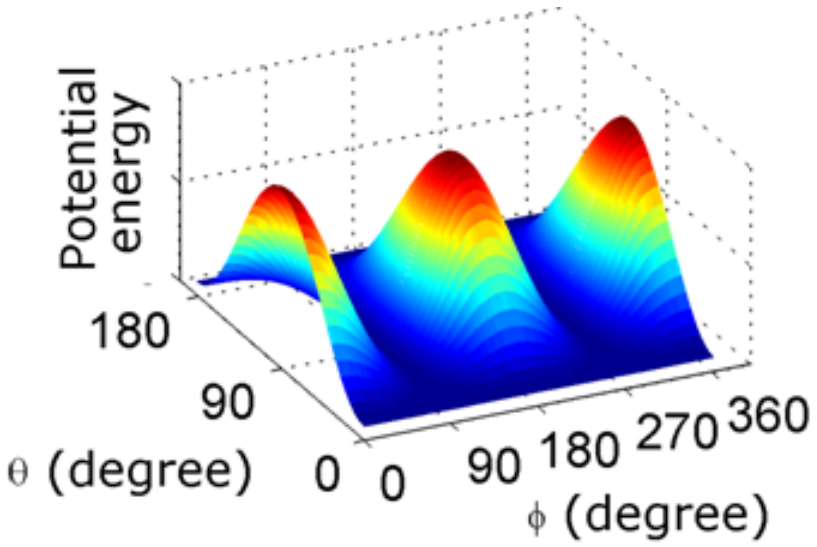

(a)

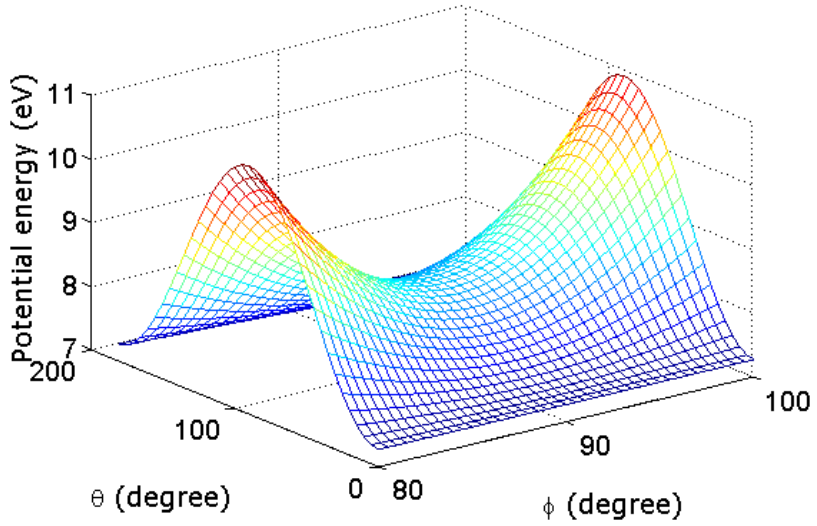

(b)

Figure 2.3: Potential landscape unperturbed by stress with torques acting both in θ- and ϕ-directions. (a) Potential landscape for azimuthal angle $\phi = 0° - 360°$. (b) Potential landscape for azimuthal angle $\phi = 80° - 100°$. Note that the potential energy barrier is minimum in ϕ-direction when $\phi = \pm 90°$. However, the torque due to stress [which is there in the $B(\phi(t))$ term in Equation (2.19)] would rotate the magnetization in ϕ-direction and thus magnetization is forced to climb up the potential hill along the ϕ-direction from in-plane minimum energy positions. This has a very important and intriguing consequence on the magnetization dynamics as we will see onwards.

where the prime denotes first derivative with respect to time. Accordingly,

$$\alpha \left(\mathbf{n_m}(t) \times \frac{d\mathbf{n_m}(t)}{dt} \right) = -\alpha sin\theta(t)\, \phi'(t)\, \hat{\mathbf{e}}_\theta + \alpha\theta'(t)\, \hat{\mathbf{e}}_\phi \tag{2.22}$$

and

$$\frac{d\mathbf{n_m}(t)}{dt} - \alpha \left(\mathbf{n_m}(t) \times \frac{d\mathbf{n_m}(t)}{dt} \right) = (\theta'(t) + \alpha sin\theta(t)\, \phi'(t))\, \hat{\mathbf{e}}_\theta + (sin\theta(t)\, \phi'(t) - \alpha\theta'(t))\, \hat{\mathbf{e}}_\phi. \tag{2.23}$$

Equating the $\hat{e}_\theta$ and $\hat{e}_\phi$ components in both sides of the Equation (2.20), we get

$$\theta'(t) + \alpha sin\theta(t)\, \phi'(t) = \frac{|\gamma|}{M_V} B_{\phi e}(\phi(t))\, sin\theta(t) \tag{2.24a}$$

$$sin\theta(t)\, \phi'(t) - \alpha\theta'(t) = \frac{|\gamma|}{M_V} 2B(\phi(t)) sin\theta(t) cos\theta(t). \tag{2.24b}$$

Simplifying the above, we get

$$\left(1 + \alpha^2\right) \theta'(t) = \frac{|\gamma|}{M_V} \left[B_{\phi e}(\phi(t)) sin\theta(t) - 2\alpha B(\phi(t)) sin\theta(t) cos\theta(t) \right], \tag{2.25}$$

$$\left(1 + \alpha^2\right) \phi'(t) = \frac{|\gamma|}{M_V} \left[\alpha B_{\phi e}(\phi(t)) + 2B(\phi(t)) cos\theta(t) \right]. \quad (sin\theta(t) \neq 0.) \tag{2.26}$$

We will assume that the initial orientation of the magnetization is aligned close to the negative z-axis so that $\theta_{initial} = 180° - \epsilon$. If $\epsilon = 0$ and the magnetization is exactly along the easy axis [$\theta = 0°, 180°$], then no amount of stress can budge it since the effective torque exerted on the magnetization by stress will be exactly zero [see Equation (2.19)]. Such locations are called "stagnation points". However, thermal fluctuations can deflect the magnetization out of its initial minima to enable switching, which we will consider in the next section. We will assume $\phi_{initial} = 90°$. Choosing the other in-plane angle $\phi_{initial} = -90°$ would not make any difference in the θ-dynamics and the ϕ-dynamics would be also equivalent. (See Fig. 3.42.) In general, in the presence of thermal fluctuations, we do need to take the distributions of $\theta_{initial}$ and $\phi_{initial}$ into account, which we will consider in the next section.

We should notice from Equation (2.25) that there is the possibility of one more stagnation

point at $\theta = 90°$ and $\phi = \pm 90°$ (in-plane hard axes, $\pm y$-axes) since there $\theta'(t) = 0$. At $\theta = 90°$, Equation (2.25) becomes

$$\left(1 + \alpha^2\right) \theta'(t) = \frac{|\gamma|}{M_V} B_{\phi e}(t) = -|\gamma| \frac{M_s}{2} \Omega (N_{d-xx} - N_{d-yy}) sin(2\phi(t)) \tag{2.27}$$

which indicates that as long as $\phi \in (90°, 180°)$ or $\phi \in (270°, 360°)$, the magnetization vector will continue to rotate towards the correct final state ($\theta \simeq 0°$) without backtracking or being stuck at $\theta = 90°$. We will describe such happenings pictorially and intuitively onwards. We will use the convention that magnetization's motion is in opposite direction to the torque exerted since the Landé g-factor for electrons is negative. This is taken care of by the factor $-|\gamma|$ in the LLG equation [Equation (2.20)].

At high enough stress, the out-of-plane excursion of the magnetization vector is significant and $\phi(t) > 90°$ in the quadrant $(90°, 180°)$ or $\phi(t) > 270°$ in the quadrant $(270°, 360°)$ is achieved so that stagnation is indeed avoided and the correct state is invariably reached. However, at low stress, the first term in Equation (2.26) will suppress out-of-plane excursion of the magnetization vector and try to constrain it to the magnet's plane, thereby making $\phi(t) = 90°$. This will result in stagnation when θ reaches 90° and switching will fail. Whether this happens or not depends on the relative strengths of the two terms in Equation (2.26) that counter each other. We need to avoid such low stresses to ensure successful switching. Thus, there is a minimum value of stress for which switching takes place. We will see later that the other two quadrants for ϕ [$(0°, 90°)$ and $(180°, 270°)$] would make magnetization to backtrack and we do need to consider such events in the presence of thermal fluctuations which we model in the next section.

First, we will describe the ϕ-motion of magnetization as derived in the Equation (2.26). Note the first term in Equation (2.25) containing the factor $B_{\phi e}(\phi(t))$, which is proportional to $sin(2\phi(t))$ and is given by the Equation (2.17). Mathematically, the effect of $sin(2\phi(t))$ dependence is to rotate the magnetization in a way to keep it in-plane of the magnet ($\phi = \pm 90°$), i.e., if the magnetization gets deflected from $\phi = \pm 90°$, this motion becomes active and tries to bring it back to magnet's plane. This is depicted in Fig. 2.4.

We will intuitively describe how magnetization is deflected from its plane ($\phi = \pm 90°$, i.e., y-z plane), and gets stabilized out-of-plane as depicted in Fig. 2.5. Dependence of shape-

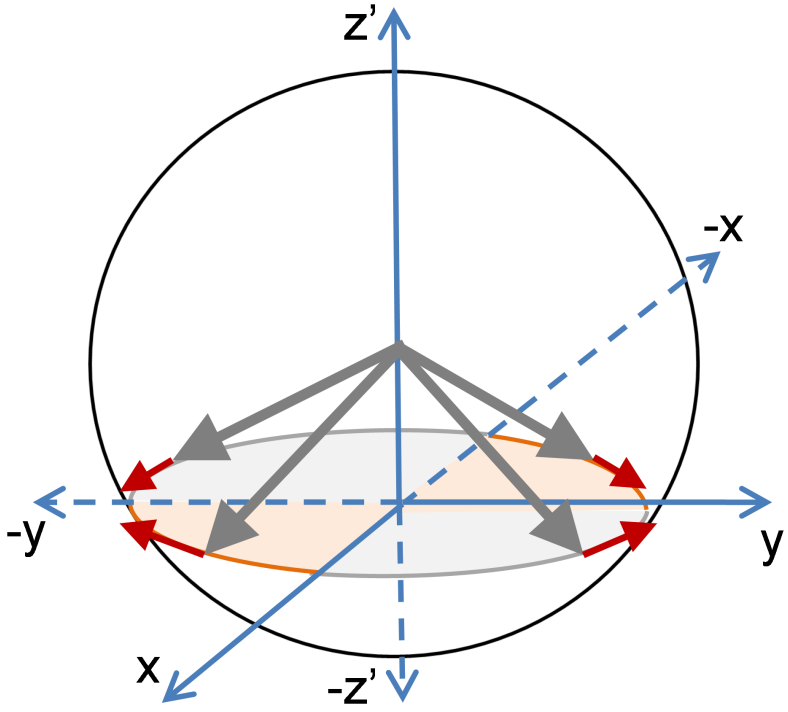

Figure 2.4: Magnetization comes back to magnet's plane as it gets deflected from its plane. If magnetization gets deflected from its plane ($\phi = \pm 90°$) due to applied stress, magnetization would try to come back to magnet's plane since $\phi = \pm 90°$ corresponds to the magnet's energy minima in its potential landscape. Mathematically, it can be tracked from its ϕ-motion that is proportional to $sin(2\phi(t))$ as described in the text.

anisotropy energy on azimuthal angle ϕ (rather than assuming $\phi = \pm 90°$) generates additional motions of magnetization in $\hat{\mathbf{e}}_\theta$ and $\hat{\mathbf{e}}_\phi$ directions (see the motions containing the term $B_{\phi e}(\phi)$ in Fig. 2.8 later); both the components are proportional to $sin(2\phi)$ and vanish when $\phi = \pm 90°$, but additionally the ϕ-component is proportional to the damping constant α [191]. As shown in the Fig. 2.5, the applied stress produces a torque that tries to rotate the magnetization anticlockwise and forces it to reside out-of-plane. As magnetization is deflected from the plane of the magnet ($\phi = \pm 90°$), the ϕ-component of the additional torque due to shape anisotropy as mentioned above [$\sim \alpha sin(2\phi)$] would try to bring the magnetization back to its plane. Because of such counteraction, out of the four quadrants for ϕ [i.e., (0°, 90°), (90°, 180°), (180°, 270°), and (270°, 360°)], the magnetization would be stable in the second quadrant or the fourth quadrant [i.e., (90°, 180°) or (270°, 360°)]. Note that $sin(2\phi)$ is *negative* in these two quadrants counteracting the precessional motion due to stress [see Fig. 2.5]. We would call these two quadrants "good" quadrants and the other two (first and third) quadrants "bad" quadrants, the reasoning behind which would be more prominent onwards. Consideration of the torques due to ϕ-dependence of

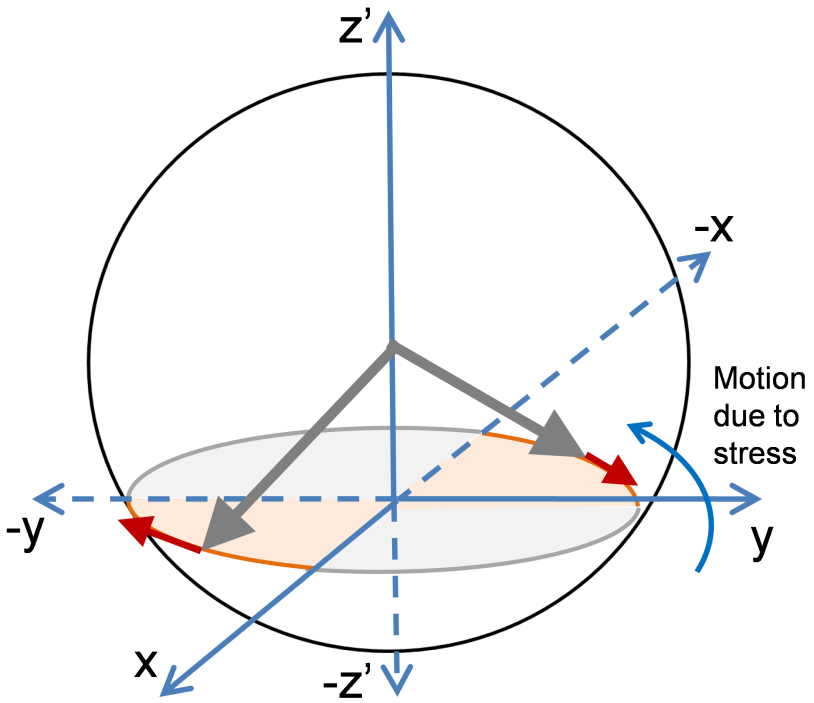

Figure 2.5: The applied stress tries to lift the magnetization vector out of the magnet's plane while the $\hat{\mathbf{e}}_\phi$-component of the shape anisotropy torque due to Gilbert damping [191] tries to bring it back to the plane ($\phi = \pm 90°$). This stabilizes the value of ϕ, but it happens only in the "good" quadrants $\phi \in (90°, 180°)$ and $\phi \in (270°, 360°)$. The terminology of "good" quadrants and "bad" quadrants would be more clear as we go on describing the dynamics onwards.

shape anisotropy energy is instrumental to the dynamics we present in this dissertation. The important lesson to take away is that ϕ is stable only in "good" quadrants, which is why ϕ is *much more likely* to be in a "good" quadrant during switching.

Figs. 2.6 and 2.7 show the LLG dynamics [Equations (2.26) and (2.25)] in ϕ- and θ-space, respectively. Note that the dependence of shape anisotropy energy on ϕ has generated two additional motions $-|B_{\phi e}(\phi)| sin\,\theta\, \hat{\mathbf{e}}_\theta$ and $-\alpha|B_{\phi e}(\phi)|\, \hat{\mathbf{e}}_\phi$. These two motions vanish when magnetization resides on magnet's plane ($\phi = \pm 90°$) since $B_{\phi e}(\phi) \sim sin(2\phi)$. However, as magnetization gets deflected from its plane due to applied stress, we *must* consider these two motions and consideration of these motions have very drastic consequences on the dynamics of magnetization as well as on reducing the switching delay to a couple of orders, with the realistic parameters.

We will now describe the motion of magnetization in the whole θ-ϕ space intuitively under various torques originating from shape and stress anisotropy as shown in the Fig. 2.8. We intend the motion of magnetization to be along the $-\hat{\mathbf{e}}_\theta$ direction since we are switching magnetization from $\theta \simeq 180°$ towards $\theta \simeq 0°$. The precessional motion of magnetization due to torque

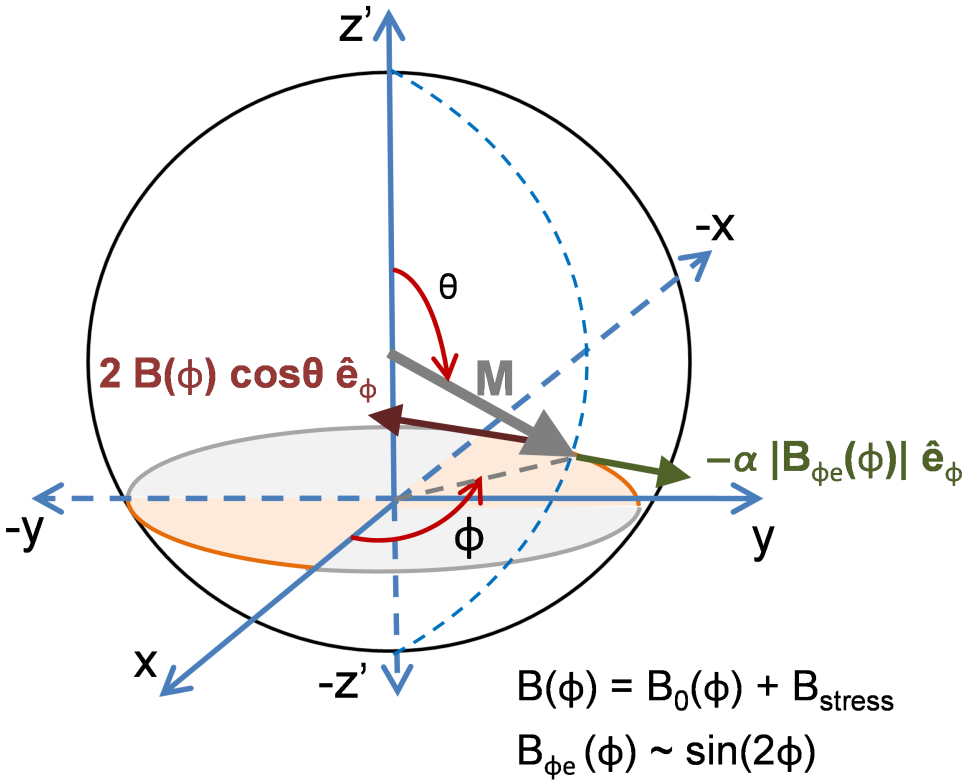

Figure 2.6: Stress rotates the magnetization out-of-plane of the magnet and the damping motion due to ϕ-dependence of magnetization tries to bring the magnetization in-plane ($\phi = \pm 90°$). Such counter-action is shown for the second quadrant of ϕ, i.e., $\phi \in (90°, 180°)$. Note that the term $B_{\phi e} \sim sin(2\phi)$ is negative in the second quadrant of ϕ. Choice of the fourth quadrant of ϕ, i.e., $\phi \in (270°, 360°)$ would have produced a similar picture.

generated by the applied stress is in the $+\hat{\mathbf{e}}_\phi$ direction, but the damping of magnetization generates an additional motion, which is perpendicular to both the direction of magnetization ($\hat{\mathbf{e}}_r$) and $+\hat{\mathbf{e}}_\phi$, i.e., in $-\hat{\mathbf{e}}_\theta$ direction. These two motions are depicted as $2B(\phi)cos\theta\,\hat{\mathbf{e}}_\phi$ and $-2\alpha B(\phi)sin\theta cos\theta\,\hat{\mathbf{e}}_\theta$, respectively in Fig. 2.8, where α is the damping constant and the quantity $B(\phi)$ includes a term due to in-plane shape anisotropy $B_0(\phi)$ too apart from the stress term B_{stress}. The quantity B_{stress} is negative and it must beat the in-plane shape anisotropy $B_0(\phi)$ for switching to get started. Mathematically, note that both the quantities $B(\phi)$ and $cos\,\theta$ are negative in the interval $180° \geq \theta \geq 90°$. Hence, magnetization switches towards its desired direction due to the applied stress. However, this damped motion in $-\hat{\mathbf{e}}_\theta$ direction is weak because of the multiplicative factor, α, which is usually much less than one (e.g., α=0.1 for Terfenol-D).

As magnetization rotates out-of-plane due to applied stress, and stays in the "good" quadrants for ϕ [i.e., (90°, 180°) or (270°, 360°)] as described earlier [see Fig. 2.5], it generates a

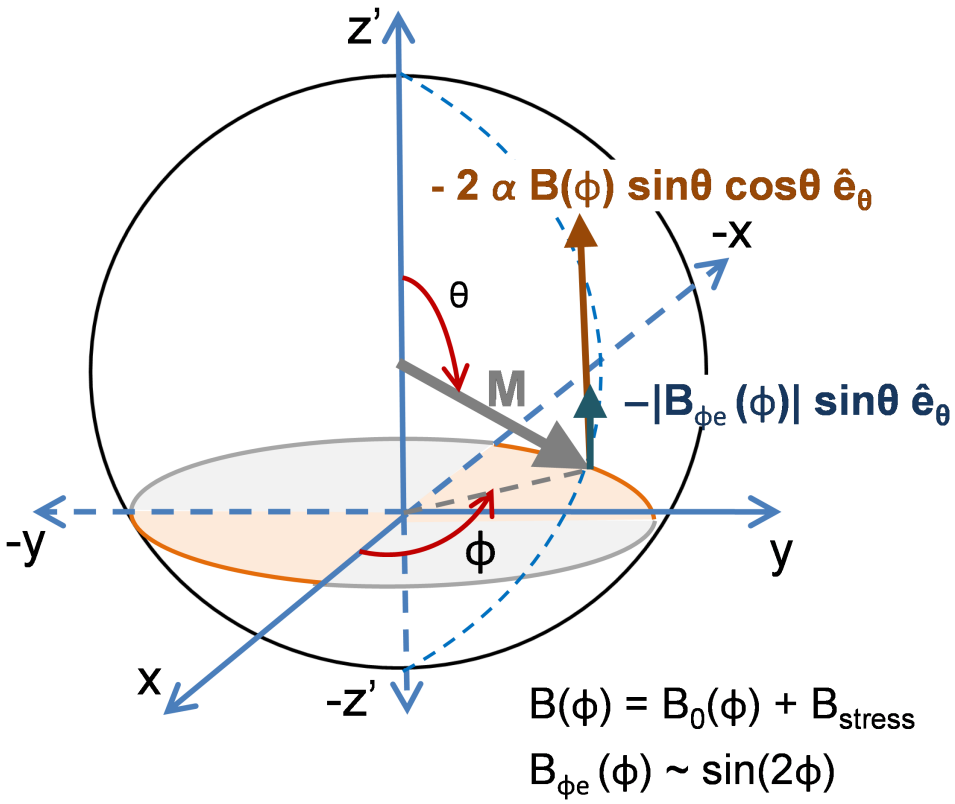

Figure 2.7: Magnetization's motion in θ-space. Note that the dependence of shape anisotropy energy on ϕ has generated an additional motion $-|B_{\phi e}(\phi)|sin\,\theta\,\hat{\mathbf{e}}_\theta$ and the term $B_{\phi e} \sim sin(2\phi)$ is negative in the second quadrant of ϕ as shown. Choice of the fourth quadrant of ϕ, i.e., $\phi \in (270°, 360°)$ would have produced a similar picture.

motion of magnetization in the $-\hat{\mathbf{e}}_\theta$ direction due to ϕ-dependence of shape anisotropy energy. Subsequently, a damped motion is generated too in the $-\hat{\mathbf{e}}_\phi$ direction. These two motions are depicted as $-|B_{\phi e}(\phi)|sin\theta\,\hat{\mathbf{e}}_\theta$ and $-\alpha|B_{\phi e}(\phi)|\,\hat{\mathbf{e}}_\phi$, respectively in Fig. 2.8, where $B_{\phi e}(\phi) \sim sin(2\phi)$. Note that in the "good" quadrants for ϕ, $B_{\phi e}(\phi)$ is negative. Thus, keeping the magnetization out-of-plane of the magnet in "good" quadrants is beneficial in switching the magnetization in its desired direction. In case the magnetization resides out-of-plane but in the "bad" quadrants, it would have resisted the motion of magnetization in its desired direction of switching. A higher magnitude of stress keeps the magnetization more out-of-plane in "good" quadrants due to precessional motion, however, the damped motion $-\alpha|B_{\phi e}(\phi)|\,\hat{\mathbf{e}}_\phi$ tries to bring magnetization back towards the magnet's plane. As these two motions counteract each other (see Fig. 2.8), magnetization keeps moving in the $-\hat{\mathbf{e}}_\theta$ direction and eventually reaches at the x-y plane defined by $\theta = 90°$. Note that without damping, such counteraction does not happen and magnetization precesses alternatingly through "good" quadrants and "bad" quadrants.

The stress-cycle alongwith the energy profiles and magnetization directions at different

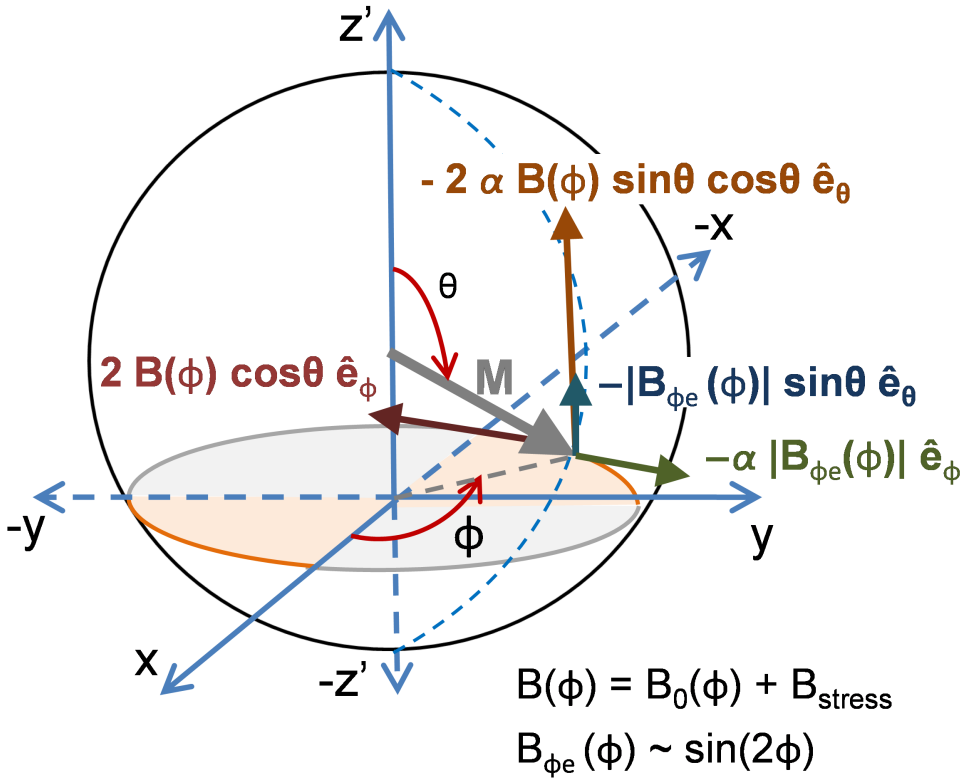

Figure 2.8: Illustration of magnetization's motion in full three-dimensional space under various torques generated due to shape and stress anisotropy alongwith considering the damping of magnetization (α is the phenomenological damping constant [191]). Note that the dependence of shape anisotropy energy on ϕ has generated two additional motions $-|B_{\phi e}(\phi)|sin\,\theta\,\hat{\mathbf{e}}_\theta$ and $-\alpha|B_{\phi e}(\phi)|\,\hat{\mathbf{e}}_\phi$. The quadrant $\phi \in (90°, 180°)$ is chosen for illustration; choice of the other "good" quadrant $\phi \in (270°, 360°)$ is analogous.

instants of time is shown in the Fig. 2.9. At time t_0, the magnetization direction is along the easy axis $\theta \simeq 180°$ and the potential landscape of the nanomagnet is unperturbed by stress. The potential profile of the magnet is symmetric in both θ- and ϕ-space with two degenerate minima at $\theta = 0°$, $180°$ and a maximum at $\theta = 90°$ in θ-space. The anisotropy in the barrier is due to shape anisotropy only, which is ∼44 kT at room-temperature using the magnet's dimensions and material parameters of Terfenol-D as in Table 3.2. Note that the barrier height separating the two stable states ($\theta = 0°$ and $180°$) is meant when the magnetization resides in-plane (i.e., $\phi = \pm 90°$) of the magnet. The barrier goes higher when the magnetization is deflected from $\phi = 90°$ as shown in the Fig. 2.9(c) [at time t_0]. The barrier is highest when the magnetization points along the out-of-plane direction ($\phi = 0°$ or $180°$), which is due to small thickness of the nanomagnet compared to the lateral dimensions. Magnetization can start from any angle $\phi_{initial} \in (0°, 360°)$ in the presence of thermal noise (see next section and Fig. 3.41(b)).

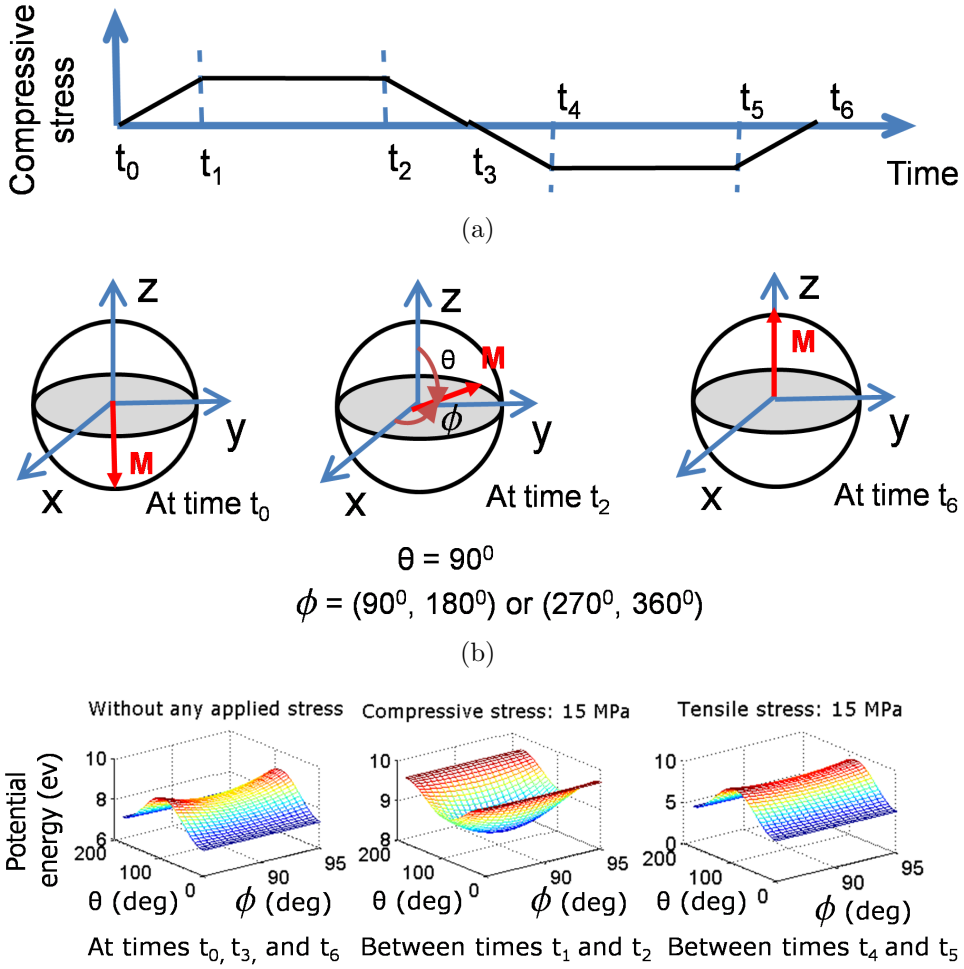

Figure 2.9: (a) Stress-cycle on the magnetostrictive nanomagnet, (b) Magnetization directions at different instants of time, and (c) Potential landscapes of the magnetostrictive nanomagnet in relaxed, compressively stressed, and expansively stressed conditions. Note that the three-dimensional potential landscape has never been made asymmetric to favor the final state during switching.

As a compressive stress is ramped up on the nanomagnet between time instants t_0 and t_1, the potential landscape in θ-space becomes monostable near $\phi = \pm 90°$ provided a sufficient stress is applied. The potential barrier near $\phi = 0°$ or $180°$ may not become monostable in θ-space since barrier height is high therein, however, that is not necessary for switching. Since application of stress rotates the magnetization in ϕ-direction, it can eventually come near $\phi = \pm 90°$ and starts switching from $\theta \simeq 180°$ towards $\theta = 90°$. The minimum energy position between time instants t_1 and t_2 is at ($\theta = 90°$, $\phi = \pm 90°$). From Fig. 2.9(c), we can see that the potential profile at time instant t_1 is still *symmetric*.

From Equations (2.18) and (2.19), at $\theta = 90°$, we can write the effective field and torque, respectively as

$$\mathbf{H_{eff}}(t) = B_{\phi e}(t)\,\hat{\mathbf{e}}_\phi = \frac{\mu_0}{2} M_s^2 \Omega (N_{d-xx} - N_{d-yy}) sin(2\phi(t))\,\hat{\mathbf{e}}_\phi \tag{2.28}$$

and

$$\mathbf{T_E}(t) = -B_{\phi e}(t)\,\hat{\mathbf{e}}_\theta = -\frac{\mu_0}{2} M_s^2 \Omega (N_{d-xx} - N_{d-yy}) sin(2\phi(t))\,\hat{\mathbf{e}}_\theta. \tag{2.29}$$

Accordingly, when $\phi(t)$ is in the quadrant $(0°, 90°)$, the direction of effective field $\mathbf{H_{eff}}(t)$ is along the $\hat{e}_\phi$ direction and the direction of torque $\mathbf{T_E}(t)$ is along the -$\hat{e}_\theta$ direction provided the condition $N_{d-xx} > N_{d-yy}$ is satisfied. The condition is true since it is a consequence of having $l < b$, i.e., the thickness of the magnet is smaller than the length of minor axis of the elliptical nanomagnet. So the magnetization can successfully traverse towards its destination $\theta \simeq 0°$. (See Fig. 2.10.) We can follow the same argument if $\phi(t)$ resides in the quadrant $(180°, 270°)$; the magnetization will go towards its destination ($\theta \simeq 0°$) too in that case. However, for the quadrants $(90°, 180°)$ and $(270°, 360°)$, the magnetization would backtrack towards $\theta \simeq 180°$, which follows from the same argument presented above. (See Fig. 2.10.) Note that if the magnetization would have started from $\theta \simeq 0°$ instead of $\theta \simeq 180°$, the aforesaid roles of the different quadrants would have just been opposite.

Upon reaching at $\theta = 90°$, if magnetization stays in the "good" quadrants for ϕ [i.e., $(90°, 180°)$ or $(270°, 360°)$], then the torque on the magnetization is in the correct direction so that it can traverse towards $\theta \simeq 0°$. (See Fig. 2.10.) This once again signifies the merit of

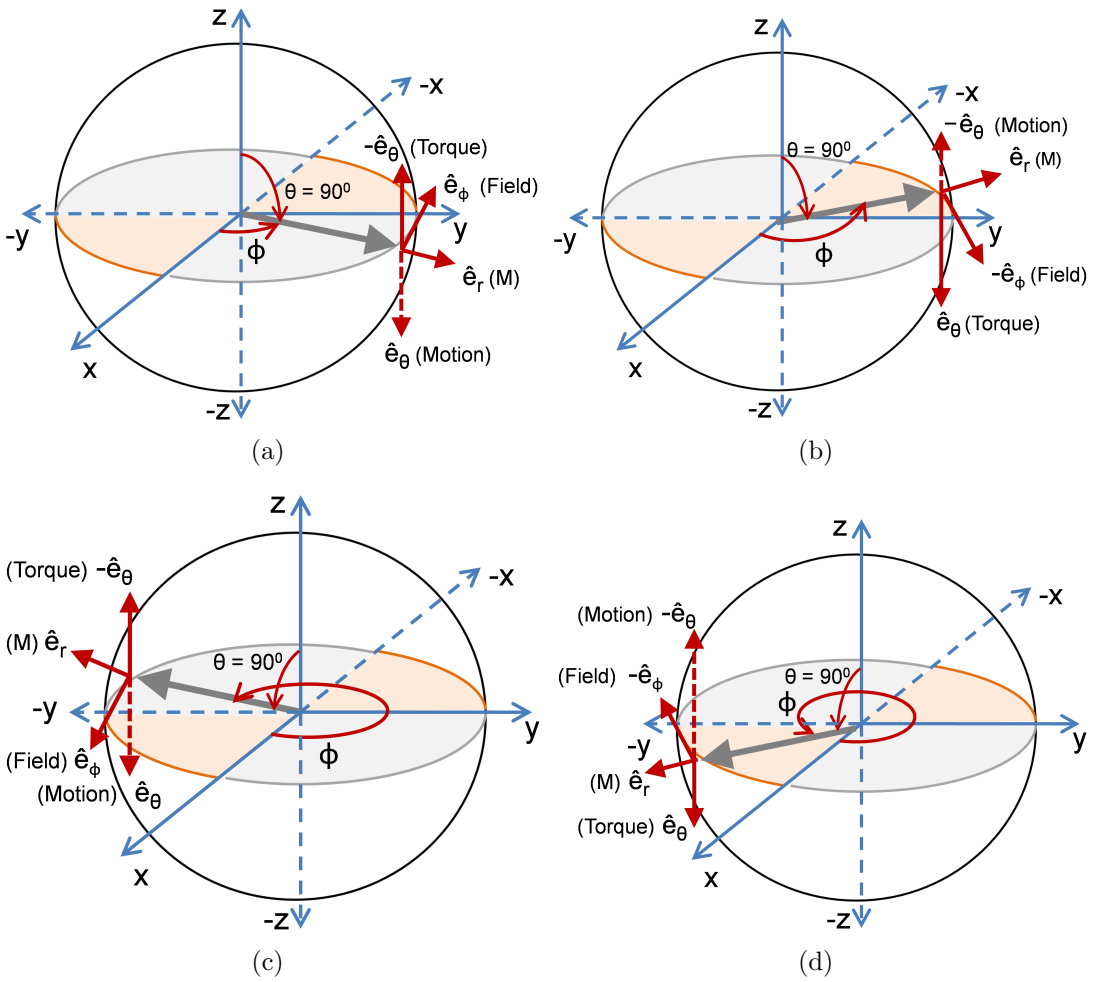

Figure 2.10: Field and torque on the magnetization, $\mathbf{M}$ when it comes on the x-y plane ($\theta = 90°$). The field always tries to keep the magnetization in-plane ($\phi = \pm 90°$) of the nanomagnet. Magnetization started from $\theta \simeq 180°$. (a) $\phi \in (0°, 90°)$, (b) $\phi \in (90°, 180°)$, (c) $\phi \in (180°, 270°)$, and (d) $\phi \in (270°, 360°)$. Magnetization can traverse towards its destination $\theta \simeq 0°$ for the cases (b) and (d), while it backtracks towards $\theta \simeq 180°$ for the cases (a) and (c). Note that the motion of magnetization is opposite to the direction of torque exerted on it since the Landé g-factor for electrons is negative. If magnetization starts from the other easy axis $\theta \simeq 0°$ towards $\theta \simeq 180°$, the role of the different quadrants would have been exactly opposite.

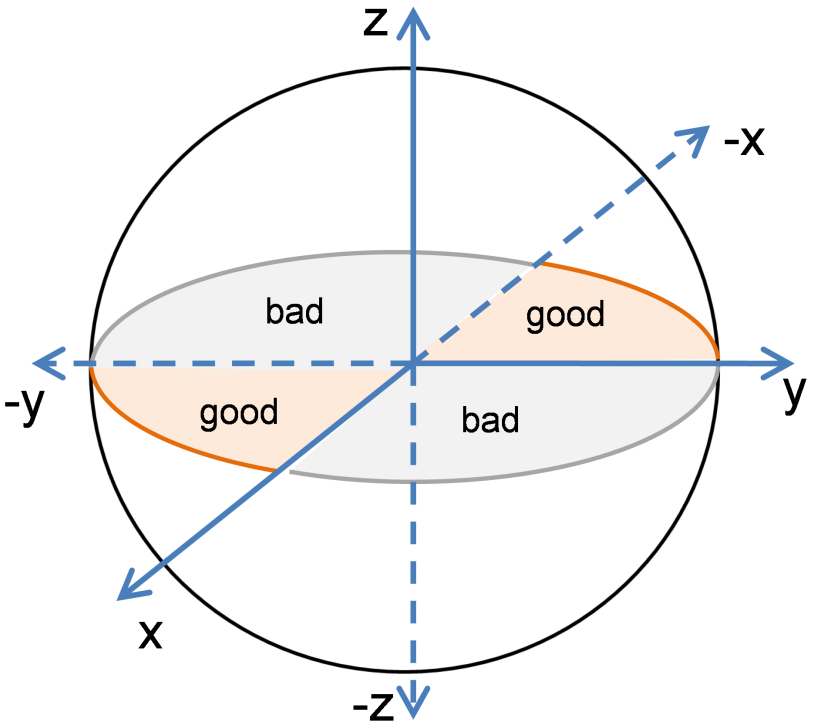

Figure 2.11: The "good" and "bad" quadrants for ϕ, when magnetization reaches $\theta = 90°$. Magnetization started from $\theta \simeq 180°$. If magnetization resides in a "good" quadrant, magnetization would be able to traverse towards $\theta \simeq 0°$. If magnetization starts from $\theta \simeq 0°$, the role of the quadrants would have been exactly opposite.

terminology ("good" or "bad") used for the four quadrants of ϕ. Note that at $\theta = 90°$ (i.e., $cos\,\theta = 0$), the effect of stress on the magnetization rotation has diminished completely. The only two motions that are active at that point are $-|B_{\phi e}(\phi)|sin\,\theta\,\hat{\mathbf{e}}_\theta$ and $-\alpha|B_{\phi e}(\phi)|\,\hat{\mathbf{e}}_\phi$ (see Fig. 2.8). Since $\alpha \ll 1$, magnetization quickly gets out of the $\theta = 90°$ position and as the magnetization vector gets deflected from $\theta = 90°$ towards $\theta = 0°$, the effect of stress comes into play.

We will see in Chapter 3 (where we provide the simulation results) that as long as the ramp rate of the applied stress is fast enough and we apply a sufficiently high stress, magnetization would reside in the "good" quadrants (see Fig. 2.11) and would keep moving towards $\theta \simeq 0°$. During this transition, as the stress is removed or reversed, the ϕ-motions of magnetization counteracts each other while still the θ-motions are in the correct direction so that magnetization can traverse towards $\theta \simeq 0°$. This is depicted in the Fig. 2.12.

Fig. 2.13 illustrates the summary of the magnetization's motion as discussed earlier. Magnetization's motion is coupled in θ-ϕ space; thus neither strictly in-plane motion nor strictly out-of-plane motion is viable. Since stress rotates magnetization in ϕ-direction, we must consider

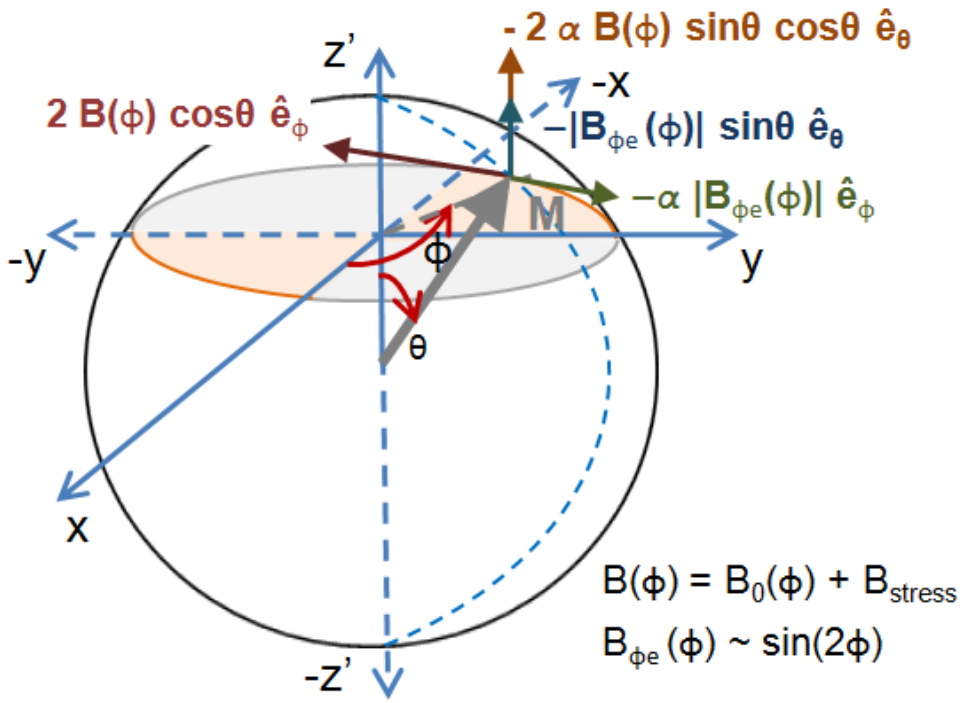

Figure 2.12: Illustration of magnetization's motion in full three-dimensional space under various torques generated due to shape and stress anisotropy when magnetization traverses from $\theta = 90°$ towards $\theta \simeq 0°$. The quadrant $\phi \in (90°, 180°)$ is chosen for illustration; choice of the other "good" quadrant $\phi \in (270°, 360°)$ is analogous.

full three-dimensional motion of magnetization in magnet's full three-dimensional potential landscape.

One other issue deserves mention. We have shown explicitly that we can switch from an initial state close to the $-z$-axis to a final state close to the +z-axis. Can we do the opposite and switch from $+z$-axis to $-z$-axis? For a single isolated magnet, this is always possible and the dynamics is identical. In magnetic random access memory (MRAM) systems, there will be a field acting on the *free* layer due to the fixed (pinned) layer. This can be avoided by replacing a simple pinned layer with a synthetic antiferromagnetic pinned layer, which consists of a pair of ferromagnetic layers antiferromagnetically coupled through a spacer layer [e.g., ruthenium (Ru)] and the layers need to be properly designed to nullify the net field acting on the free layer [78].

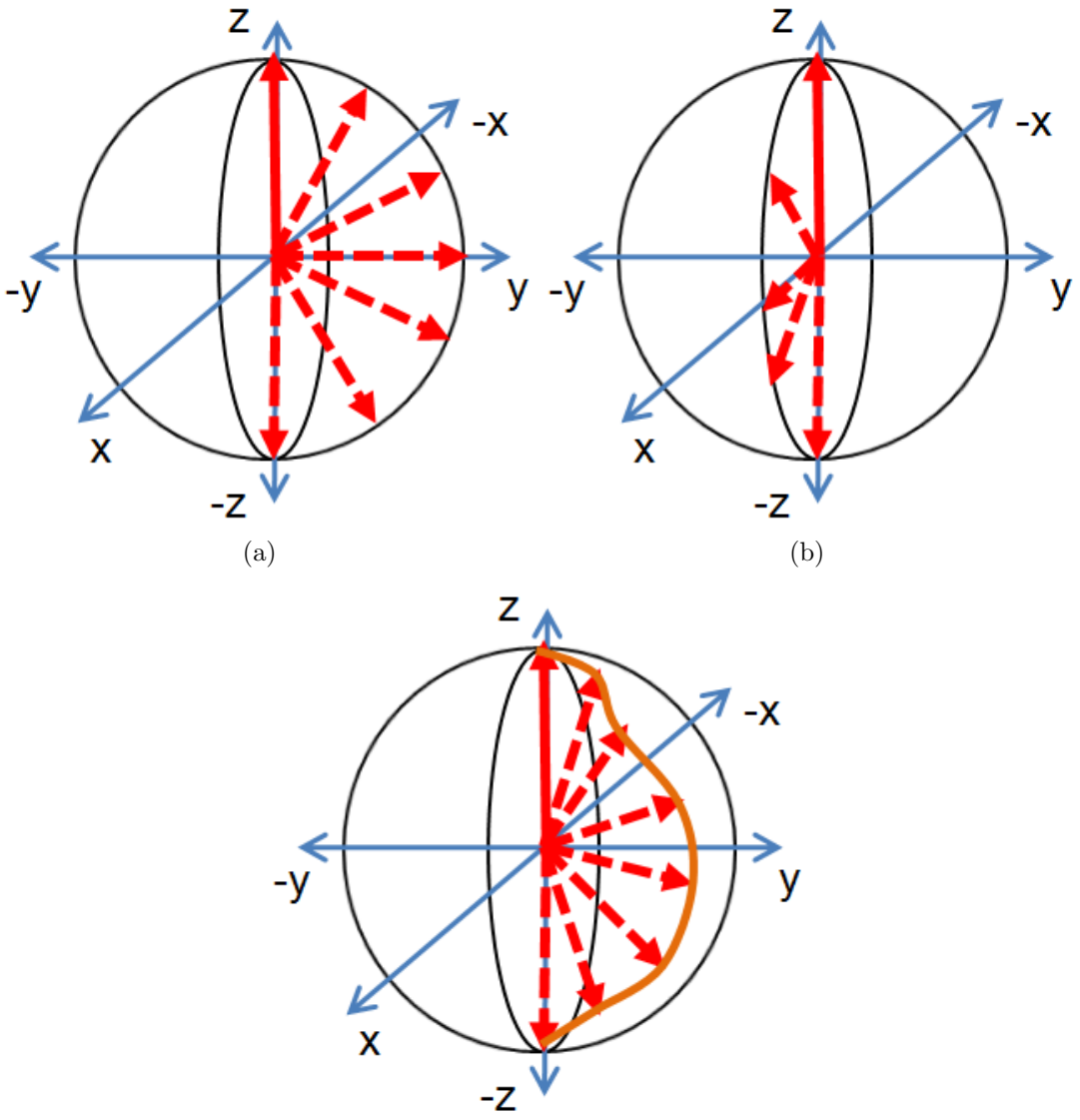

Figure 2.13: Illustration of magnetization's motion. (a) Since stress rotates magnetization out of magnet's plane, the motion in two-dimensional magnet's plane is not valid. (b) Completely out-of-plane motion is not possible since thickness of the nanomagnet is much smaller than the lateral dimensions. (c) Motion is neither in-plane nor out-of-plane of the magnet. An illustrative dynamics is shown.

2.3 Stochastic magnetization dynamics in the presence of thermal fluctuations

The torque due to thermal fluctuations is treated via a random magnetic field $\mathbf{h}(t)$ and is expressed as

$$\mathbf{h}(t) = h_x(t)\hat{\mathbf{e}}_\mathbf{x} + h_y(t)\hat{\mathbf{e}}_\mathbf{y} + h_z(t)\hat{\mathbf{e}}_\mathbf{z} \tag{2.30}$$

where $h_x(t)$, $h_y(t)$, and $h_z(t)$ are the three components of $\mathbf{h}(t)$ in x-, y-, and z-direction, respectively in Cartesian coordinates. We will assume the following properties of the random field, $\mathbf{h}(t)$ [193].

- The process $\mathbf{h}(t)$ is *stationary*.
- The distribution of the quantities $h_x(t)$, $h_y(t)$, and $h_z(t)$ is normal (Gaussian) with means equal to zero, i.e. $\langle h_i(t)\rangle = 0$ where $i = x, y, z$.
- The quantities $h_i(t)$ and $h_j(t')$ (where $t' - t = \pm\Delta$ and $i \neq j$) are correlated only for time intervals Δ, which is much shorter than the time it takes for the magnetization vector to rotate appreciably. Furthermore

$$\langle h_i(t)h_j(t)\rangle = U\delta_{ij}\delta(\Delta) \qquad (i, j = x, y, z) \tag{2.31}$$

  where $U = \frac{2\alpha kT}{|\gamma|(1+\alpha^2)M_V}$ [193, 187], α is the dimensionless phenomenological Gilbert damping constant, $\gamma = 2\mu_B\mu_0/\hbar$ is the gyromagnetic ratio for electrons and is equal to 2.21×10^5 (rad.m).(A.s)$^{-1}$, μ_B is the Bohr magneton, $M_V = \mu_0 M_s\Omega$, M_s is saturation magnetization, and Ω is magnet's volume.
- The statistical properties of the quantities $h_x(t)$, $h_y(t)$, and $h_z(t)$ are isotropic.

Accordingly, the random thermal field can be expressed as

$$h_i(t) = \sqrt{\frac{2\alpha kT}{|\gamma|(1+\alpha^2)M_V\Delta t}}\, G_{(0,1)}(t) \qquad (i = x, y, z) \tag{2.32}$$

where $1/\Delta t$ is proportional to the attempt frequency of the random thermal field. Consequently, Δt should be the simulation time-step used to solve the coupled LLG equations numerically

and $G_{(0,1)}(t)$ is a Gaussian distribution with zero mean and unit standard deviation [194]. The simulation time-step Δt should be selected small enough so that decreasing that step further does not make any significant difference in the results. Accordingly, the thermal torque can be written as

$$\mathbf{T_{TH}}(t) = M_V\, \mathbf{n_m}(t) \times \mathbf{h}(t) = P_\theta(t)\, \hat{\mathbf{e}}_\phi - P_\phi(t)\, \hat{\mathbf{e}}_\theta \tag{2.33}$$

where

$$P_\theta(t) = M_V \left[h_x(t)\, cos\theta(t)\, cos\phi(t) + h_y(t)\, cos\theta(t) sin\phi(t) - h_z(t)\, sin\theta(t)\right], \tag{2.34}$$

$$P_\phi(t) = M_V \left[h_y(t)\, cos\phi(t) - h_x(t)\, sin\phi(t)\right]. \tag{2.35}$$

To derive the thermal torque, we have used the following identities.

$$\hat{\mathbf{e}}_\mathbf{x} = sin\theta(t)\, cos\phi(t)\, \hat{\mathbf{e}}_\mathbf{r} + cos\theta(t)\, cos\phi(t)\, \hat{\mathbf{e}}_\theta - sin\phi(t)\, \hat{\mathbf{e}}_\phi, \tag{2.36a}$$

$$\hat{\mathbf{e}}_\mathbf{y} = sin\theta(t)\, sin\phi(t)\, \hat{\mathbf{e}}_\mathbf{r} + cos\theta(t)\, sin\phi(t)\, \hat{\mathbf{e}}_\theta + cos\phi(t)\, \hat{\mathbf{e}}_\phi, \tag{2.36b}$$

$$\hat{\mathbf{e}}_\mathbf{z} = cos\theta(t)\, \hat{\mathbf{e}}_\mathbf{r} - sin\theta(t)\, \hat{\mathbf{e}}_\theta. \tag{2.36c}$$

$$\hat{\mathbf{e}}_\mathbf{r} \times \hat{\mathbf{e}}_\mathbf{x} = cos\theta(t)\, cos\phi(t)\, \hat{\mathbf{e}}_\phi + sin\phi(t)\, \hat{\mathbf{e}}_\theta, \tag{2.37a}$$

$$\hat{\mathbf{e}}_\mathbf{r} \times \hat{\mathbf{e}}_\mathbf{y} = cos\theta(t)\, sin\phi(t)\, \hat{\mathbf{e}}_\phi - cos\phi(t)\, \hat{\mathbf{e}}_\theta, \tag{2.37b}$$

$$\hat{\mathbf{e}}_\mathbf{r} \times \hat{\mathbf{e}}_\mathbf{z} = -sin\theta(t)\, \hat{\mathbf{e}}_\phi. \tag{2.37c}$$

The magnetization dynamics under the action of the two torques $\mathbf{T_E}(t)$ and $\mathbf{T_{TH}}(t)$ is described by the stochastic Landau-Lifshitz-Gilbert (LLG) equation as follows.

$$\frac{d\mathbf{n_m}(t)}{dt} - \alpha \left(\mathbf{n_m}(t) \times \frac{d\mathbf{n_m}(t)}{dt} \right) = -\frac{|\gamma|}{M_V} [\mathbf{T_E}(t) + \mathbf{T_{TH}}(t)]\,. \tag{2.38}$$

Following the same procedure as of earlier in Equation (2.23) and equating the $\hat{e}_\theta$ and $\hat{e}_\phi$ components in both sides of Equation (2.38), we get

$$\theta'(t) + \alpha sin\theta(t)\,\phi'(t) = \frac{|\gamma|}{M_V}\left(B_{\phi e}(t) sin\theta(t) + P_\phi(t)\right), \tag{2.39}$$

$$sin\theta(t)\,\phi'(t) - \alpha\theta'(t) = \frac{|\gamma|}{M_V}\left(2B(t) sin\theta(t) cos\theta(t) - P_\theta(t)\right). \tag{2.40}$$

Solving the above equations, we get the following coupled equations for the dynamics of $\theta(t)$ and $\phi(t)$.

$$\begin{aligned}\left(1+\alpha^2\right)\frac{d\theta(t)}{dt} &= \frac{|\gamma|}{M_V}[B_{\phi e}(t) sin\theta(t) - 2\alpha B(t) sin\theta(t) cos\theta(t) \\ &\qquad + (\alpha P_\theta(t) + P_\phi(t))], \end{aligned}\tag{2.41}$$

$$\begin{aligned}\left(1+\alpha^2\right)\frac{d\phi(t)}{dt} &= \frac{|\gamma|}{M_V}\left[\alpha B_{\phi e}(t) + 2B(t) cos\theta(t) - \frac{1}{sin\theta(t)}\left(P_\theta(t) - \alpha P_\phi(t)\right)\right]. \\ &\qquad (sin\theta \neq 0.)\end{aligned}\tag{2.42}$$

2.3.1 Initial fluctuation due to thermal torque

We can see from Equation (2.8) that because $N_{d-zz} < N_{d-yy} \ll N_{d-xx}$, the shape anisotropy energy is minimum when $\theta = 0°$ or 180°. Therefore, the magnetization of the unstressed magnet should be lined up along the easy axis (z-axis) in the absence of thermal perturbation. If that happens, then no amount of stress can budge the magnetization vector from this orientation since the torque due to stress vanishes when $sin\theta = 0$ [see Equation (2.19)]. Accordingly, $\theta = 0°$ and 180° are called *stagnation points* since the magnetization vector stagnates at these locations. In this section, we show mathematically that thermal torque can overcome stagnation and deflect the magnetization vector from the easy axis ($sin\theta = 0$).

When $sin\theta = 0$ and no stress is applied on the nanomagnet, Equations (2.39) and (2.40)

yield

$$\theta'(t) = \frac{|\gamma|}{M_V} P_\phi(t), \tag{2.43}$$

$$\alpha\theta'(t) = \frac{|\gamma|}{M_V} P_\theta(t). \tag{2.44}$$

Substituting for $P_\theta(t)$ and $P_\phi(t)$ from Equations (2.34) and (2.35), and using $\theta = 180°$, we get

$$\alpha h_x(t) sin\phi(t) - \alpha h_y(t) cos\phi(t) = h_x(t) cos\phi(t) + h_y(t) sin\phi(t) \tag{2.45}$$

which gives the expression for $\phi(t)$ as

$$\phi(t) = tan^{-1}\left(\frac{\alpha h_y(t) + h_x(t)}{\alpha h_x(t) - h_y(t)}\right). \tag{2.46}$$

If we substitute this value of $\phi(t)$ in Equation (2.43) or in Equation (2.44), we get

$$\theta'(t) = -|\gamma| \frac{h_x^2(t) + h_y^2(t)}{\sqrt{(\alpha h_x(t) - h_y(t))^2 + (\alpha h_y(t) + h_x(t))^2}}. \tag{2.47}$$

We can see clearly from the above equation that thermal torque can deflect the magnetization axis when it is *exactly* along the easy axis since the time rate of change of $\theta(t)$ is non-zero. Note that the initial deflection from the easy axis due to the thermal torque does not depend on the component of the random thermal field along the z-axis $h_z(t)$, which is a consequence of having $\pm z$-axis as the easy axes of the nanomagnet. However, once the magnetization direction is even slightly deflected from the easy axis, all three components of the random thermal field along the x-, y-, and z-direction would come into play and affect the deflection.

Fig. 2.14 shows the effect of barrier height on the initial distribution of polar angle θ. The plot is meant for the in-plane ($\phi = \pm 90°$) barrier height as that is where the barrier separating the two stable states is minimum. Note that a higher barrier confines the magnetization more in θ-space, hence, that would lead to less spread in distribution of $\theta_{initial}$. If the barrier height is small, magnetization can switch without any external input. This barrier height should be high enough to retain an information reliably over a long period of time. The switching

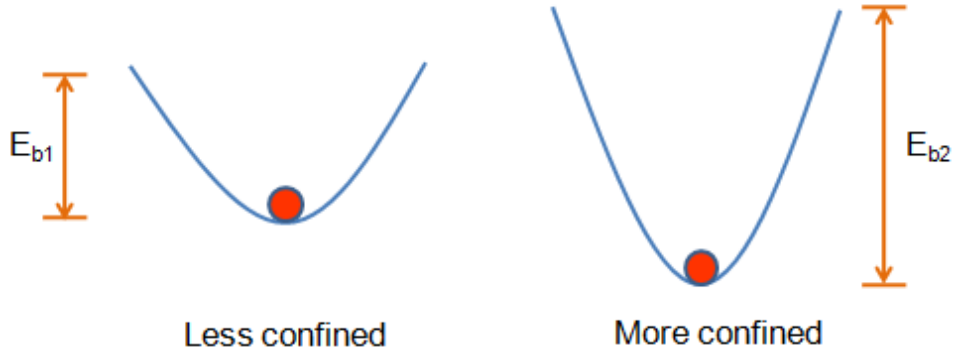

Figure 2.14: Effect of barrier height on initial distribution of polar angle θ. The in-plane ($\phi = \pm 90°$) barrier is meant here. A higher barrier height corresponds to less spread in the initial distribution of θ.

probability over the barrier E_b is $e^{-\frac{E_b}{kT}}$, according to Boltzmann distribution. Also, it needs mention here that the magnitude of thermal torque is dependent on damping parameter α too [see Equation (2.30)], so a high damping parameter will create a higher spread in the distribution of $\theta_{initial}$.

2.4 Magnetization dynamics with an out-of-plane bias field

The thermal distributions of θ and ϕ in the unstressed magnet are found by solving the Equations (2.41) and (2.42) while setting $B_{stress} = 0$. This will yield the distribution of the magnetization vector's initial orientation when stress is turned on. The θ-distribution is Boltzmann peaked at $\theta = 0°$ or $180°$, while the ϕ-distribution is Gaussian peaked at $\phi = \pm 90°$, because these are the minimum energy positions in the magnet's potential landscape (see Fig. 3.41). Since the most probable value of θ is either $0°$ or $180°$, where stress is ineffective (*stagnation point*), there would be a long tail in the switching delay distribution. They are due to the fact that when magnetization starts out from $\theta = 0°, 180°$, we have to wait a while before thermal kick sets the switching in motion as the torque on the magnetization derived from the gradient of magnet's potential landscape is proportional to $sin\theta$, which is small for $\theta \simeq 0°, 180°$ [see Equation (2.19)]. Thus, switching trajectories initiating from a stagnation point are very slow [195, 196].

In order to eliminate a long tail in the switching delay distribution and thus decrease

the mean switching delay, one can apply a small static bias field that will shift the peak of $\theta_{initial}$ distribution away from the easy axis, so that the most probable starting orientation will no longer be a stagnation point. This field is applied along the out-of-plane hard axis ($+x$-direction) so that the potential energy due to the applied magnetic field becomes $E_{mag}(t) = -M_V H\, sin\theta(t)\, cos\phi(t)$, where H is the magnitude of magnetic field. The torque generated due to this field is $\mathbf{T_M}(t) = -\mathbf{n_m}(t) \times \nabla E_{mag}(\theta(t), \phi(t))$. The presence of this field will modify Equations (2.41) and (2.42) to

$$\left(1+\alpha^2\right)\frac{d\theta(t)}{dt} = \frac{|\gamma|}{M_V}[B_{\phi e}(t)sin\theta(t) - 2\alpha B(t)sin\theta(t)cos\theta(t) + \alpha M_V H\, cos\theta(t)\, cos\phi(t) - M_V H\, sin\phi(t) + (\alpha P_\theta(t) + P_\phi(t))], \quad (2.48)$$

$$\left(1+\alpha^2\right)\frac{d\phi(t)}{dt} = \frac{|\gamma|}{M_V}[\alpha B_{\phi e}(t) + 2B(t)cos\theta(t) - [sin\theta(t)]^{-1}\left(M_V H\, cos\theta(t)\, cos\phi(t) + \alpha M_V H\, sin\phi(t)\right) - [sin\theta(t)]^{-1}\left(P_\theta(t) - \alpha P_\phi(t)\right)]. \quad (sin\theta \neq 0.) \quad (2.49)$$

The bias field also makes the potential energy profile of the magnet asymmetric in ϕ-space and the energy minimum will be shifted from $\phi_{min} = \pm 90°$ (the plane of the magnet) to

$$\phi_{min} = cos^{-1}\left[\frac{H}{M_s(N_{d-xx} - N_{d-yy})}\right]. \quad (2.50)$$

However, the potential profile will remain symmetric in θ-space, with $\theta = 0°$ and $\theta = 180°$ remaining as the minimum energy locations. With the parameters as in Table 3.2, a bias magnetic field of flux density 40 mT applied perpendicular to the plane of the magnet ($+x$-direction) would make $\phi_{min} \simeq \pm 87°$, i.e. deflect the magnetization vector $\sim 3°$ from the magnet's plane. Application of the bias magnetic field will also reduce the in-plane shape anisotropy energy barrier from 44 kT to 36 kT at room temperature. We assume that a permanent magnet will be employed to produce the bias field and thus will not require any additional energy dissipation for it to be generated.

2.5 Energy dissipation

The energy dissipated E_{total} during switching has two components: (1) the energy dissipated in the switching circuit that applies the stress on the nanomagnet by generating a voltage (we will term it as 'CV^2' energy dissipation, where C denotes the capacitance of the piezoelectric layer and V is the applied voltage), and (2) the energy dissipated E_d internally in the nanomagnet because of Gilbert damping.

There is no net dissipation due to random thermal torque, however, that does not mean that the temperature has no effect on either E_d or the 'CV^2' dissipation. It affects E_d since it raises the critical stress needed to switch with ∼100% probability and it also affects the stress needed to switch with a given probability. Furthermore, it affects 'CV^2' because V must exceed the thermal noise voltage [197] to prevent random switching due to noise. In other words, we must enforce $CV^2 > kT$. For the estimated capacitance of our structure (2.6 fF, assuming a parallel-plate capacitor with lateral dimensions 100 nm × 90 nm, thickness of 24 nm, and dielectric constant of 1000 for PZT), this translates to $V > 1.3$ mV at room-temperature.

2.5.1 Dissipation in external circuitry

If we assume that the voltage generating stress is turned on abruptly, the energy dissipated in the switching circuit during turn-on is $(1/2)CV^2$, where C is the capacitance of the piezoelectric layer plus any line capacitance. Since the piezoelectric layer has a very large relative dielectric constant (1000), its capacitance will dominate over the line capacitance which can be neglected. We maintain the stress until polar angle θ of magnetization reaches 90°. Then if we reduce the voltage to zero abruptly and therefore the energy dissipated during turn-off is also $(1/2)CV^2$. So the total energy dissipated in the switching circuit is CV^2.

However, if the ramp rate is finite, then this energy is reduced and its exact value will depend on the ramp duration or ramp rate. We assume that the voltage applied on the piezoelectric is ramped up linearly to its steady-state value in time T which we call the *rise time*. When the stress is ramped down, we use the same rate, i.e. we reduce the stress from its maximum value to zero in time T. In all cases, the rise time is equal to the fall time.

We also assume that the PZT layer, which acts as a capacitor, is electrically accessed with

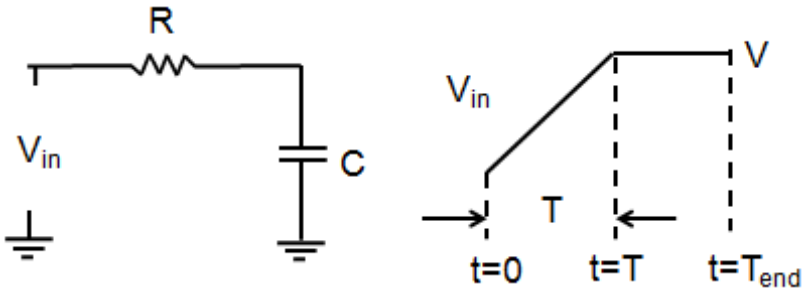

Figure 2.15: The switching circuit and ramp parameters.

a silver wire of resistivity ∼2.6 $\mu\Omega$-cm [198] so that a typical access line of length 10 μm and cross section 50 nm × 50 nm will have a resistance of ∼100 Ω. Based on the dimensions of the PZT layer (∼100 nm lateral dimensions and ∼40 nm thickness), and assuming that the relative dielectric constant of PZT is 1000, the capacitance of the PZT layer will be ∼2 fF. Therefore, the RC time constant associated with charging the capacitor is ∼0.2 ps. For a range of ramp time 1-150 ps, we are in the *adiabatic* limit ($T \gg RC$) and hence the energy dissipation in the external circuit that generates the voltage V across the PZT layer will be less than $(1/2)CV^2$. We assume that the charging circuit is represented by the circuit diagram in Figure 2.15. The energy dissipated $E_{d,rise}$ during the rise of the voltage (charging cycle) for a signal of total time-period T_{end} and ramp-period T can be calculated as below.

$$E_{d,rise} = CV^2 \left(\frac{RC}{T}\right) \left\{ 1 - \frac{RC}{T} + \frac{RC}{T} e^{-T/RC} - \frac{1}{2}\left(\frac{RC}{T}\right)\left(1 - e^{-T/RC}\right)^2 e^{-2(T_{end}-T)/RC} \right\}, \quad (2.51)$$

where C is the capacitance of the PZT layer and V is the steady state voltage that generates the required stress. The last term in the above expression comes from a finite value of T_{end}.

The energy dissipated during the discharging cycle is $E_{d,fall}$, which can be calculated from an expression similar to the one above, except that the value of T_{end} may be different. For the sake of brevity, we will term the total energy dissipated in the charging circuit $E_{d,rise} + E_{d,fall}$ as the 'CV^2' energy dissipation.

2.5.2 Internal energy dissipation

Because of Gilbert damping in the magnet, an additional energy E_d is dissipated when the magnetization switches. This energy is given by the expression

$$\int_0^{\tau} P_d(t)dt, \tag{2.52}$$

where τ is the switching delay and $P_d(t)$, the dissipated power, which through some vector algebra and using Equation (2.6) is given by [199, 79]

$$\begin{aligned} P_d(t) &= \mathbf{H}(t).\frac{d\mathbf{M}(t)}{dt} \\ &= \frac{\alpha\left|\gamma\right|}{(1+\alpha^2)M_V}\left|\mathbf{M}(t)\times\mathbf{H}(t)\right|^2 \\ &= \frac{\alpha\left|\gamma\right|}{(1+\alpha^2)M_V}\left|\mathbf{T_E}(t)+\mathbf{T_M}(t)\right|^2. \end{aligned} \tag{2.53}$$

We have not included the random (with mean zero) thermal torque $\mathbf{T_{TH}}$ in the expression of power dissipation in Equation (2.53). The average power dissipated during switching is simply E_d/τ.

Chapter 3

Simulation Results

In this chapter, we provide the simulation results by numerically solving the coupled-dynamics of polar angle and azimuthal angle of magnetization vector as derived in the previous chapter. We will exemplify the theoretical insights developed in the previous chapter and explain wide-range of magnetization dynamics for different materials, various magnitudes of stresses and ramp rates, considering room-temperature thermal fluctuations, and an out-of-plane bias field.

3.1 Instantaneous ramp

In this section, we consider first the simplified condition of *instantaneous* ramp [168][1] so that we can focus on some key explanations rather than going into other complexities like ramp rate effects, thermal fluctuations etc., which we will go through step-by-step in the remaining sections. We numerically solve the coupled dynamics of polar angle θ and azimuthal angle ϕ of magnetization vector following the expressions as in Equations (2.25) and (2.26) derived in Chapter 2. We will assume that magnetization starts for $\theta = 179°$ to avoid the stagnation point exactly at $\theta = 180°$. Stress is ramped up instantaneously at beginning and when magnetization reaches $\theta = 90°$, stress is withdrawn instantaneously. The switching is deemed to have completed when magnetization reaches at $\theta = 1°$. The initial orientation of azimuthal angle ϕ

[1]Note that the LLG equation (Equation 4) in Ref. [168] should have used negative values for gyromagnetic ratio γ and consequently for the damping constant α during simulations, since for electrons gyromagnetic ratio is negative. This will change the direction of ϕ-rotation of magnetization. The θ-curves and the calculated metrics, e.g., switching delay and energy dissipation would remain unchanged. A very similar mistake is there in Ref. [95].

	Terfenol-D	Nickel	Cobalt
Major axis (a)	101.75 nm	105 nm	101.75 nm
Minor axis (b)	98.25 nm	95 nm	98.25 nm
Thickness (t)	10 nm	10 nm	10 nm
Young's modulus (Y)	8×10^{10} Pa	2.14×10^{11} Pa	2.09×10^{11} Pa
Magnetostrictive coefficient ($(3/2)\lambda_s$)	$+90\times10^{-5}$	-3×10^{-5}	-3×10^{-5}
Saturation magnetization (M_s)	8×10^5 A/m	4.84×10^5 A/m	8×10^5 A/m
Gilbert's damping constant (α)	0.1	0.045	0.01

Table 3.1: Material parameters for different materials used as magnetostrictive layers and dimensions of the nanomagnets.

is considered to be on magnet's plane, i.e., $\phi_{init} = 90°$. Choice of the other in-plane orientation of ϕ, i.e., $\phi_{init} = -90°$ would be analogous.

We consider a multiferroic nanomagnet composed of a PZT layer (lead-zirconate-titanate) and a magnetostrictive layer which is made of either polycrystalline Terfenol-D, or polycrystalline nickel, or polycrystalline cobalt. Because it is polycrystalline, the magnetocrystalline layer does not have significant magnetocrystalline anisotropy. The material parameters and dimensions for the magnetostrictive layer are given in Table 3.1 [200, 201, 202, 203, 204]. They ensure that the shape anisotropy energy barrier is ∼32 kT at room temperature for all the three materials, so the static error probability is e^{-32}. The PZT layer is assumed to be four times thicker than the magnetostrictive layer so that any strain generated in it is transferred almost completely to the magnetostrictive layer. We will assume that the maximum strain that can be generated in the PZT layer is 500 ppm [205], which would require a voltage of 111 mV because d_{31}=1.8e-10 m/V for PZT [206]. The corresponding stress is the product of the generated strain (500×10^{-6}) and the Young's modulus of the magnetostrictive layer. Based on available data for Young's modulus, the maximum allowable stresses for Terfenol-D, nickel, and cobalt are 40 MPa, 107 MPa, and 104.5 MPa, respectively.

Fig. 3.1 shows the dynamics of polar angle θ and azimuthal angle ϕ of the magnetization vector in the Terfenol-D/PZT multiferroic nanomagnet for 10 MPa stress and assuming instantaneous ramp. First, we will explain the ϕ-dynamics as in the Fig. 3.1(b). The initial orientation of ϕ is 90°. As the stress of 10 MPa is turned on abruptly, magnetization gets deflected from its plane. Note that magnetization gets deflected in the "good" quadrant $(90°, 180°)$ as stress rotates the magnetization out-of-plane in the anti-clockwise direction. As magnetization

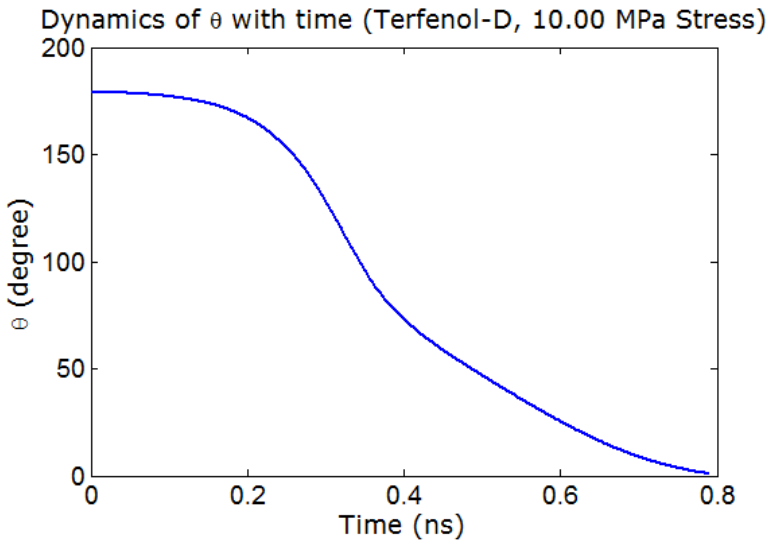

(a)

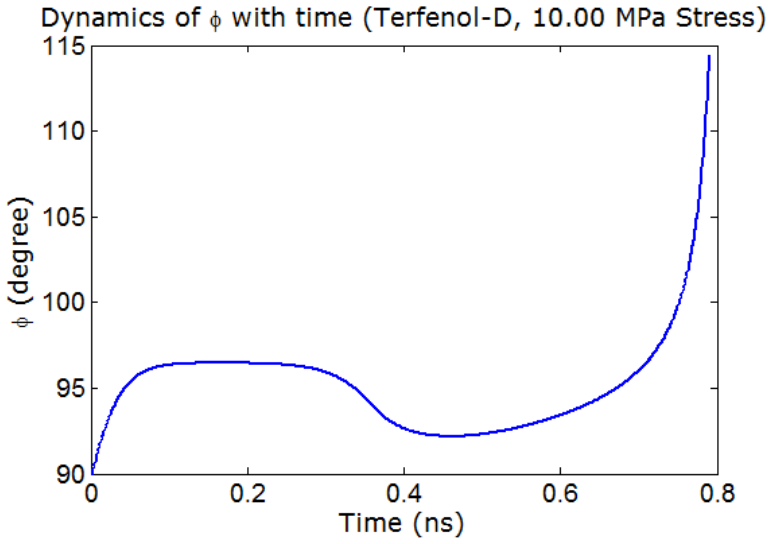

(b)

Figure 3.1: Magnetization dynamics in the Terfenol-D/PZT multiferroic nanomagnet for stress 10 MPa assuming instantaneous ramp: (a) polar angle θ versus time, and (b) azimuthal angle ϕ versus time. The switching delay is 789 ps.

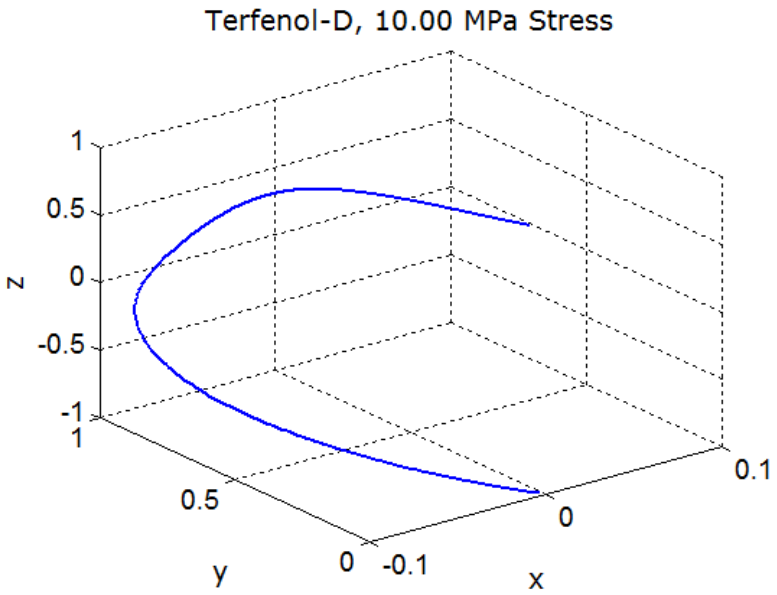

Figure 3.2: Trajectory traced out by the tip of the magnetization vector in the Terfenol-D/PZT multiferroic nanomagnet while switching occurs for stress 10 MPa assuming instantaneous ramp.

gets deflected out-of-plane, the shape-anisotropy torque due to explicit dependence of shape-anisotropy energy on the azimuthal angle ϕ comes into play as explained in Chapter 2 and the corresponding motion tries to keep the magnetization in-plane. Due to this counteraction, magnetization gets stabilized out-of-plane with about 6° of deflection. In the mean time, as shown in the Fig. 3.1(a), the polar-angle θ goes toward 90° in a directed way as explained in the Chapter 2. It happens because the additional motion of magnetization due to its out-of-plane excursion happens to be in the correct direction for switching to take place. In fact, this additional motion helps reducing the switching delay by a couple of orders in magnitude. As magnetization reaches $\theta = 90°$ and stress is withdrawn abruptly, magnetization still resides out-of-plane and thus the polar angle θ traverses toward $\theta = 1°$ due to the same reason as described in Chapter 2.

The reasoning why magnetization moves so much out-of-plane at the end of switching as can be seen in the Fig. 3.1(b) needs mention here. Note that in the ϕ-dynamics [Equation (2.26)], the second term is proportional to $cos\theta$; so when magnetization traverses from $\theta = 90°$ towards $\theta = 1°$, this term gets stronger ad stronger. Note that when stress is withdrawn, this second term is positive and hence it rotates azimuthal angle ϕ of magnetization in the anti-clockwise direction. This increasing second term eventually surpasses the first term, which is a negative

quantity for $\phi \in (90°, 180°)$. Hence, the azimuthal angle ϕ of magnetization moves anti-clockwise significantly.

Fig. 3.2 shows an illustrative dynamics of the tip of magnetization vector in three-dimensional space with 10 MPa stress and assuming instantaneous ramp. It is apparent from the plot that magnetization has deflected out-of-plane rather than being in-plane during switching. This shows that assuming magnetization to be on magnet's plane will be not only quantitatively inaccurate but also qualitatively inaccurate.

Fig. 3.3 shows the dynamics of polar angle θ and azimuthal angle ϕ of the magnetization vector in the Terfenol-D/PZT multiferroic nanomagnet for 1.92 MPa stress and assuming instantaneous ramp. We see that unlike the previous case with 10 MPa stress, the azimuthal angle ϕ of magnetization has not been deflected much from the magnet's plane. However, there is a slight entrance in the quadrant $(90°, 180°)$, which aids magnetization moving in its desired direction. But ϕ never reaches exactly 90° when $\theta = 90°$. This avoids a possible stagnation point at the hard axis. Since the out-of-plane excursion of magnetization vector is small, the motion of magnetization is sluggish this time and magnetization stays near to $\theta = 90°$ for a long time. Once magnetization reaches $\theta = 90°$, and stress is withdrawn, the azimuthal angle ϕ of magnetization can traverse deep into the quadrant $(90°, 180°)$ due the same reason explained for the case 10 MPa stress. Then, magnetization's motion gets swift due to the significant additional motion generated by the out-of-plane excursion of magnetization and thus magnetization completes its switching fast. The total switching delay in this case is ∼100 ns, out of which magnetization lingers around the hard axis for nearly ∼80 ns.

Fig. 3.4 shows the dynamics of polar angle θ and azimuthal angle ϕ of the magnetization vector in the Terfenol-D/PZT multiferroic nanomagnet for 30 MPa stress and assuming instantaneous ramp. We see that unlike the previous case with 1.92 MPa stress, the azimuthal angle ϕ of magnetization has got deflected a lot (of about 10°) from the magnet's plane. And, once again, note that, magnetization has deflected in the "good" quadrant $(90°, 180°)$, which facilitated magnetization to move in its desired direction much faster. Once magnetization reaches $\theta = 90°$, and stress is withdrawn, magnetization approaches towards $\theta = 1°$. As explained beforehand for the case 10 MPa stress, the azimuthal angle ϕ of magnetization traverses deeper in the quadrant $(90°, 180°)$, which help magnetization rotates fast towards $\theta = 1°$. However,

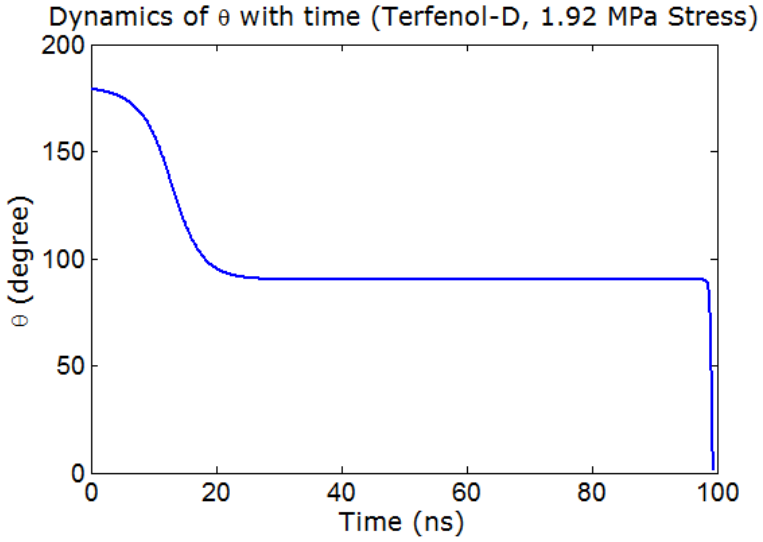

(a)

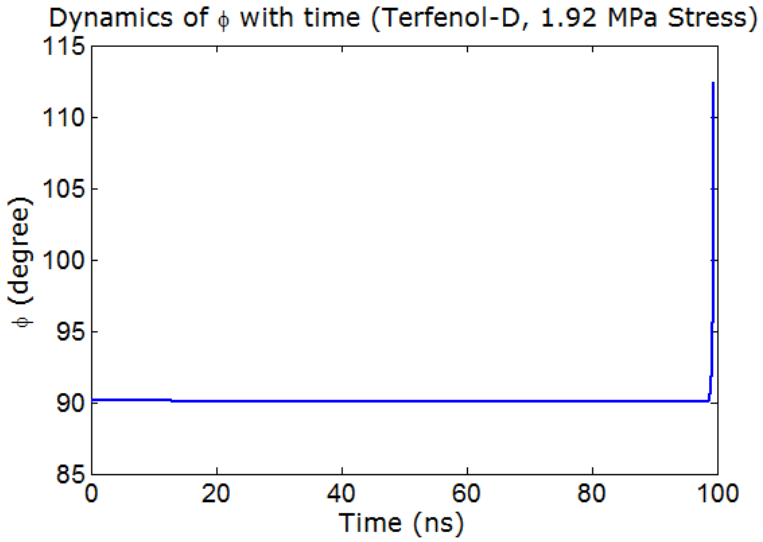

(b)

Figure 3.3: Magnetization dynamics in the Terfenol-D/PZT multiferroic nanomagnet for stress 1.92 MPa assuming instantaneous ramp.: (a) polar angle θ versus time, and (b) azimuthal angle ϕ versus time. The switching delay is about 100 ns.

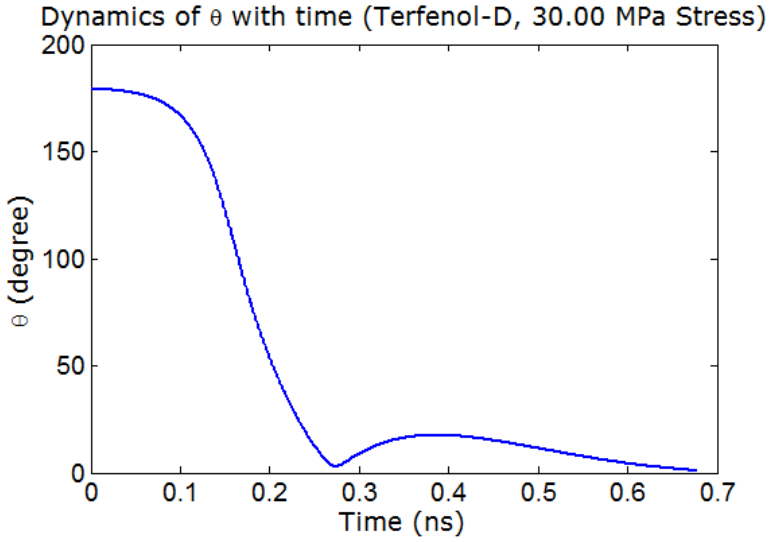

(a)

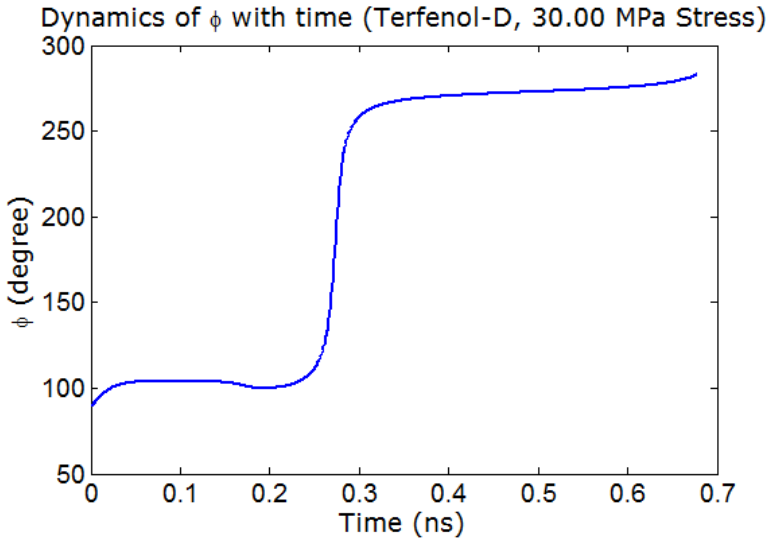

(b)

Figure 3.4: Magnetization dynamics in the Terfenol-D/PZT multiferroic nanomagnet for stress 30 MPa assuming instantaneous ramp.: (a) polar angle θ versus time, and (b) azimuthal angle ϕ versus time. The switching delay is 0.68 ns.

this time with much higher stress of 30 MPa, an additional dynamics comes into play that needs mention here. The ϕ-rotation is so fast this case that ϕ enters the "bad" quadrant $(180°, 270°)$ traversing through the "good" quadrant $(90°, 180°)$, which impedes the magnetization's motion. The consequence of this is detrimental to magnetization's dynamics as magnetization backtracks in θ-space back towards $\theta = 179°$. However, it cannot backtrack indefinitely since the azimuthal angle ϕ of magnetization comes to another "good" quadrant $(270°, 360°)$ and thus magnetization again traverses towards it desired direction and this time it completes the switching. Note that once θ reaches close to 0° (i.e., 1°), the value of ϕ becomes irrelevant since it makes the combination $z \simeq 1$, $x \simeq y \simeq 0$, in anyway. The temporary backtracking of magnetization as described above has left one ripple in magnetization dynamics [see Fig. 3.4(a)], which happens because magnetization traverses from one "good" quadrant to another "good" quadrant through one "bad" quadrant. This kind of scenario depicts that a very high stress may not be helpful in reducing the switching delay much.

Fig. 3.5 shows the trajectories traced out by the magnetization vector in the Terfenol-D/PZT multiferroic nanomagnet for stresses 1.92 MPa and 30 MPa, assuming instantaneous ramp. We can notice that 1.92 MPa stress has moved magnetization out-of-plane just a little [see Fig. 3.5(a)], while 30 MPa stress has rotates the magnetization out-of-plane quite a bit [see Fig. 3.5(a)]. Note the sign of ripple at the end of magnetization dynamics in the Fig. 3.5(b) for 30 MPa stress (as we have seen earlier in Fig. 3.4 in both *theta*- and ϕ-dynamics).

Fig. 3.6 shows the *in-plane* potential profiles of a stressed and unstressed Terfenol-D/PZT multiferroic nanomagnet for stresses 10 MPa and 1.92 MPa. Note that for both the stresses, the potential energy profile has got inverted, but with a higher stress of 10 MPa, the energy profile has got inverted much more than that for the lower stress of 1.92 MPa. Since the torque on the magnetization vector is derived from the gradient of the potential landscape, obviously, magnetization's motion will be faster with stress 10 MPa. Also, since the energy barrier height is smaller with lower stress levels, thermal fluctuations have higher possibility to interfere during switching and cause switching failures. We will see such analysis due to thermal fluctuations in a later section.

Fig. 3.7 shows the energy dissipated in the switching circuit (CV^2) and the total energy dissipated (E_{total}) as functions of delay for three different materials (Terfenol-D, nickel, and

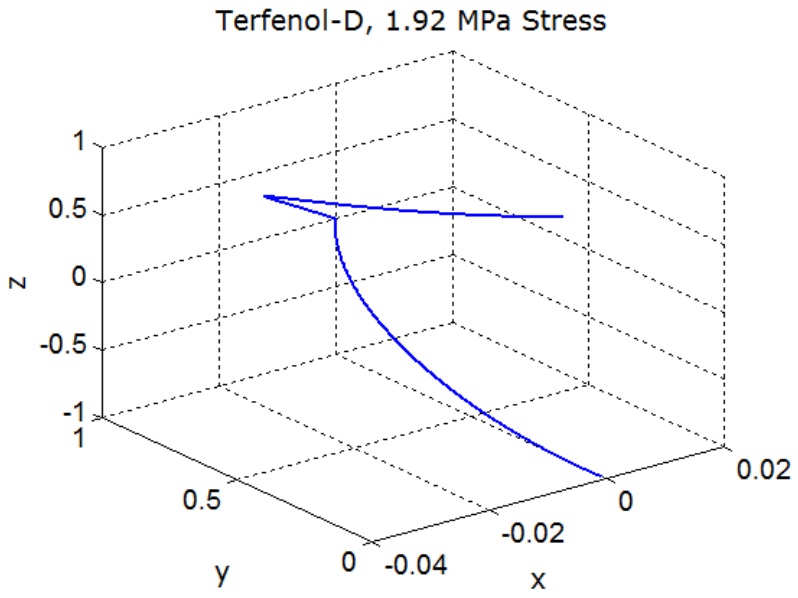

(a)

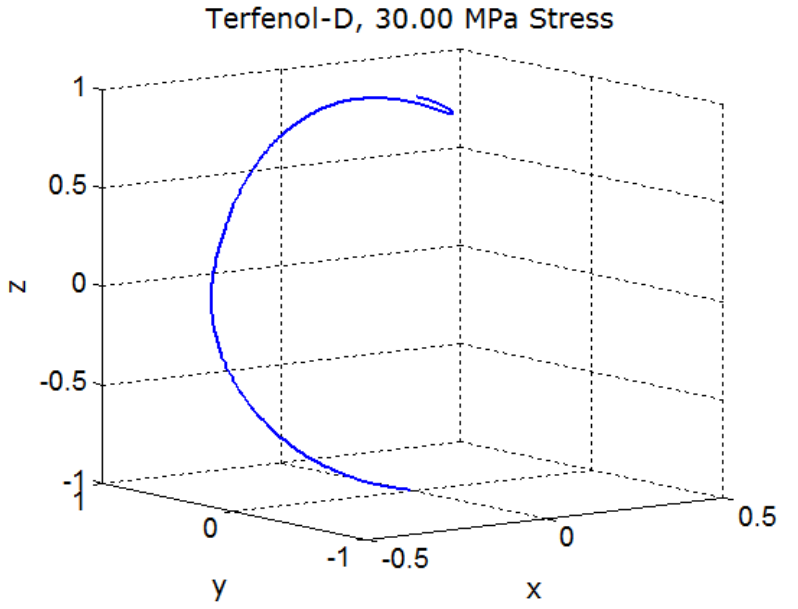

(b)

Figure 3.5: Trajectories traced out by the tip of the magnetization vector in the Terfenol-D/PZT multiferroic nanomagnet while switching occurs assuming instantaneous ramp: (a) 1.92 MPs stress, and (b) 30 MPa stress.

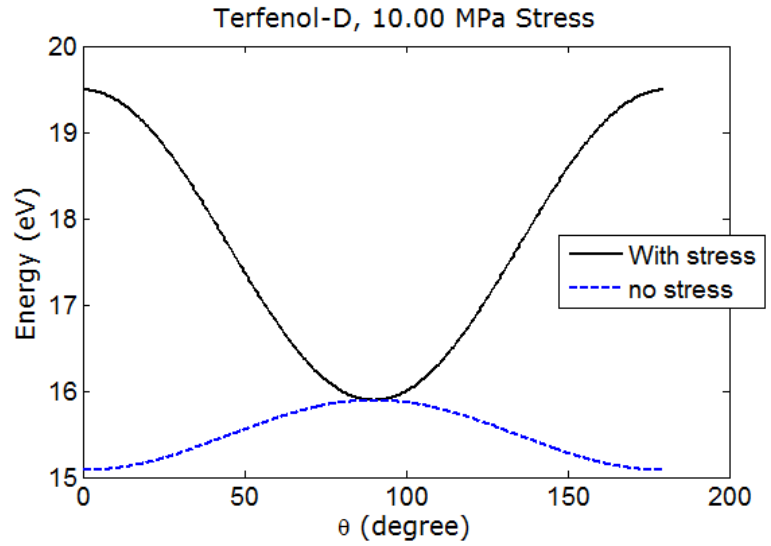

(a)

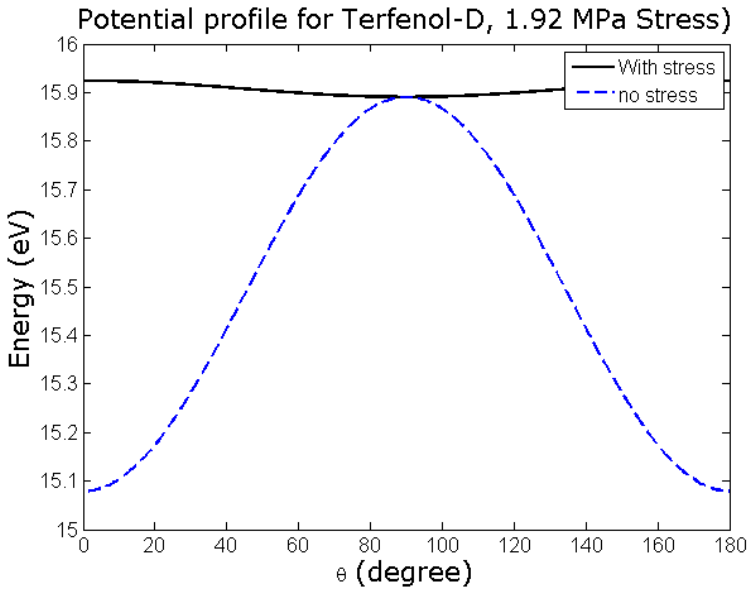

(b)

Figure 3.6: Steady state energy profiles of a stressed and unstressed Terfenol-D/PZT multiferroic nanomagnet.: (a) 10 MPs stress, and (b) 1.92 MPa stress. Magnetization is assumed to be in-plane, i.e., $\phi = \pm 90°$. Without any applied stress, the potential profile depicts the shape anisotropy energy barrier which is 0.8 eV or $\sim$32 kT.

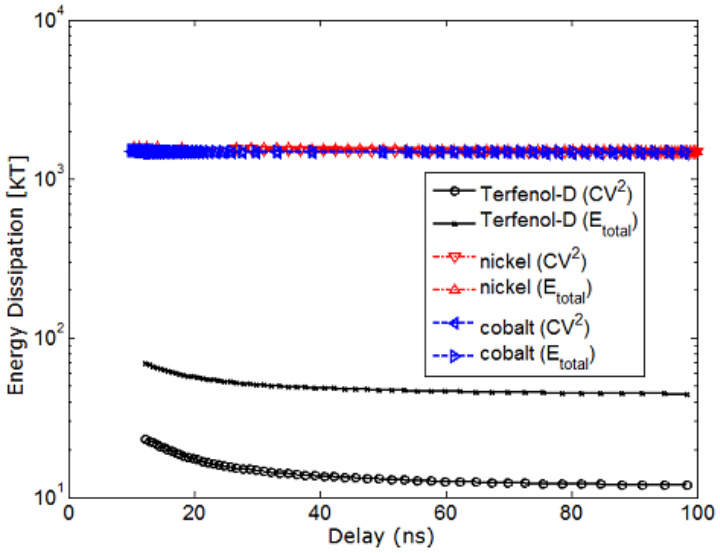

Figure 3.7: Energy dissipated in the switching circuit (CV^2) and the total energy dissipated (E_{total}) as functions of delay for three different materials (Terfenol-D, nickel, and cobalt) used as the magnetostrictive layer in the multiferroic nanomagnet.

cobalt) used as the magnetostrictive layer in the multiferroic nanomagnet. Once we have found the switching delay τ for a given stress σ by solving Equations (2.25) and (2.26), we can invert the relationship to find σ versus τ and hence the energy dissipated versus τ. For Terfenol-D, the stress required to switch in 100 ns is 1.92 MPa and that required to switch in 10 ns is 2.7 MPa. Note that for a stress of 1.92 MPa, the stress anisotropy energy B_{stress} is 32.7 kT while for 2.7 MPa, it is 46.2 kT. As expected, they are larger than the shape anisotropy barrier of $\sim$32 kT which had to be overcome by stress to switch. A larger excess energy is needed to switch faster. The energy dissipated and lost as heat in the switching circuit (CV^2) is only 12 kT for a delay of 100 ns and 23.7 kT for a delay of 10 ns. The total energy dissipated is 45 kT for a delay of 100 ns and 70 kT for a delay of 10 ns.

Fig. 3.8 shows the voltage required to switch the magnetization versus switching delay for three different materials (Terfenol-D, nickel, and cobalt) used as the magnetostrictive layer in the multiferroic nanomagnet. Terfenol-D requires the smallest voltage since it has the highest magnetostrictive coefficient. Note that the stress-anisotropy energy is proportional to stress (i.e. voltage) and magnetostriction coefficient. This tiny voltage requirement makes this mode of switching magnetizations extremely energy-efficient.

Fig. 3.9 plots the energy dissipated in the switching circuit (CV^2) and the total energy dissipated (E_{total}) versus switching delay for Terfenol-D/PZT multiferroic. This plot extends

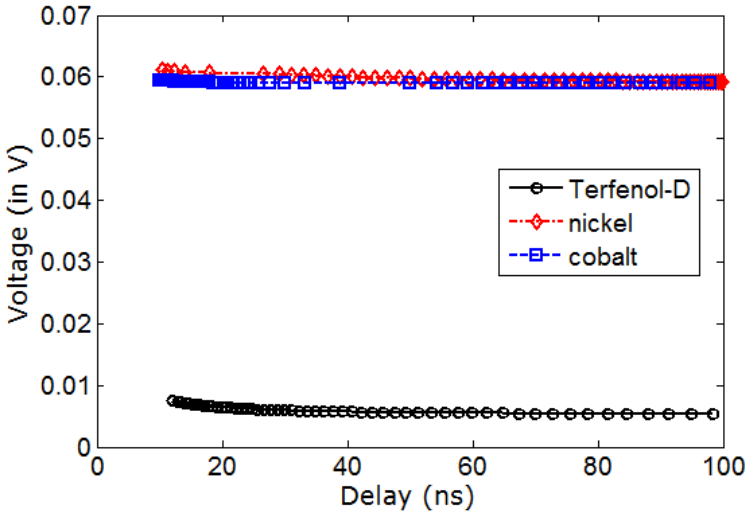

Figure 3.8: Voltage required to switch the magnetization versus switching delay for three different materials (Terfenol-D, nickel, and cobalt) used as the magnetostrictive layer in the multiferroic nanomagnet.

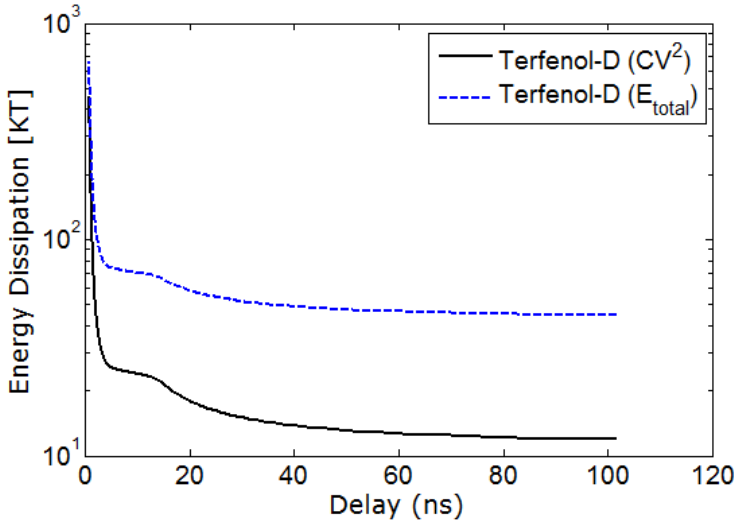

Figure 3.9: Energy dissipated in the switching circuit (CV^2) and the total energy dissipated (E_{total}) versus switching delay for Terfenol-D/PZT multiferroic.

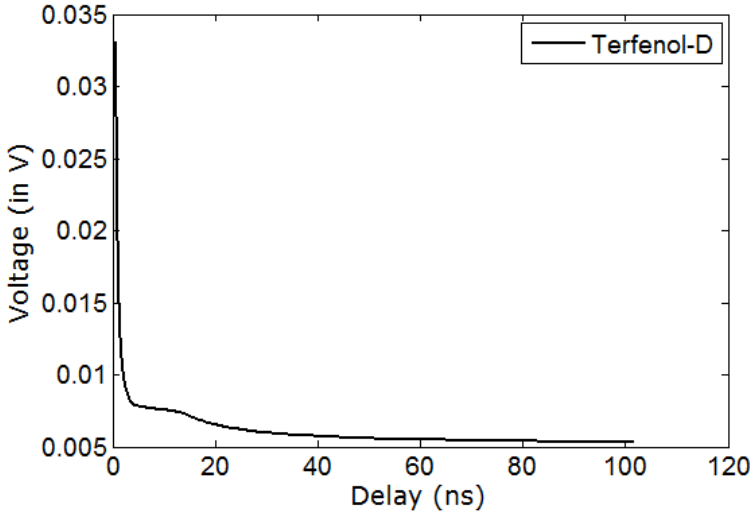

Figure 3.10: Voltage required to switch a Terfenol-D/PZT multiferroic versus switching delay extended to sub-nanosecond switching regime.

the data in the Fig. 3.7 to sub-nanosecond delay range for the case of Terfenol-D as the magnetostrictive layer. Switching delay as low as ∼0.7 ns can be achieved while dissipating ∼650 kT with 12 MPa stress.

Fig. 3.10 plots the voltage required to switch a Terfenol-D/PZT multiferroic versus switching delay. This plot extends the data in the Fig. 3.8 to sub-nanosecond delay range for the case of Terfenol-D as the magnetostrictive layer. The voltage required to generate 12 MPa stress on the magnetostrictive layer is ∼33 mV, which results in a switching delay of ∼0.7 ns. This tiny voltage requirement makes this mode of switching magnetizations extremely energy-efficient while achieving high-speed of operation too.

In this section, we have considered *instantaneous* ramp to explain some theoretical insights developed in Chapter 2 with simulation results by solving the LLG dynamics numerically. However, *instantaneous* ramp is not practical to assume and consideration of finite ramp can have paramount effect on the device characteristics, which we would explore in the next section.

3.2 Finite ramp rate

In this section, we are concerned with the following issue. The applied voltage cannot generate strain in the magnetostrictive layer instantaneously. If we ramp up the voltage gradually with a rise time longer than the response time of strain, then strain may be able to follow the

voltage quasi-statically. In that case, by controlling the ramp rate of the voltage, we can control the rise time of the strain. This may have significant effects on both the switching delay and the energy dissipated in the switching process. The purpose of this section is to investigate this possibility [169][2].

We will consider the same materials and material parameters used in the previous section as in the Table 3.1. In all our simulations, the initial orientation of the magnetization vector is: $\theta = 179°$ and $\phi = 90°$. Stress is applied as a linear ramp and we solve Equations (2.25) and (2.26) at each time step. Once θ becomes 90°, stress is reversed and we follow the magnetization vector in time until θ becomes 1°. At that point, switching is deemed to have occurred.

Note that the reversal of stress rather than just withdrawing it makes the potential landscape more steep in θ-space. But, it does not necessarily mean that the switching will be completed faster since reversal of stress can cause magnetization to traverse into "bad" quadrants in ϕ-space causing magnetization to precess and switching delay may be increased. Such increase in switching delay may happen particularly for higher stress levels as described earlier.

We assume that the voltage generating the stress in PZT is applied from a voltage source with the PZT layer acting as a capacitance. The access resistance to the layer (through metallic wires) is around 100 ohms, and the capacitance of the PZT layer is ∼2 fF. Hence, the switching circuit is a simple series resistance-capacitance (RC) circuit with a time constant of around 0.2 ps, which makes the assumed ramp durations of 1-150 ps are reasonable. Since ferroelectrics can be switched in ∼50 ps and possibly there is no obstacle in getting into less time [150], we assume that with these ramp rates, the stress follows the voltage quasi-statically.

We analyze the magnetization dynamics of the magnetostrictive layer as a function of both the magnitude and the rise time of the stress for three different materials (Terfenol-D, nickel, cobalt). The rise time is always equal to the fall time in our simulations. The three materials that we selected were chosen because of their different material parameters such as Gilbert damping constant, saturation magnetization, and magnetostrictive coefficient. A wide range of ramp time (1-150 ps) has been used in the simulation so that we can exhaustively probe the

[2]Note that the LLG equation (Equation 14) in Ref. [169] should have used negative values for gyromagnetic ratio γ and consequently for the damping constant α during simulations, since for electrons gyromagnetic ratio is negative. Also, Equations 9 and 10 should *not* have used the extra terms $\delta\sigma/\delta\theta$ and $\delta\sigma/\delta\phi$, since stress is assumed to be independent of θ and ϕ, although they are related via time t, which just acts as a parameter. However, these modifications do not affect the significance of the study on ramp rate effects presented in Ref. [169].

effect of rise time on total switching delay and energy dissipation. The energy dissipation is calculated following the prescription in Section 2.5. The simulation results are presented in the ensuing subsections.

3.2.1 Terfenol-D

Terfenol-D has a positive magnetostrictive coefficient (see Table 3.1). Therefore, we will need a *compressive* stress to rotate the magnetization vector away from its initial alignment close to easy axis ($\theta = 179°$) towards $\theta = 90°$. Note that we need to use the correct voltage polarity to ensure that a compressive stress is generated on the Terfenol-D layer. The maximum stress that can be generated on the Terfenol-D layer with the maximum allowed 500 ppm strain in the PZT layer is 40 MPa, and the minimum stress that is needed to switch the nanomagnet is found by equating the stress anisotropy energy to the shape anisotropy energy barrier. This stress is 1.91 MPa.

Ramp rate and switching delay

Equations (2.25) and (2.26), derived in Chapter 2, are solved numerically to find the values of $\theta(t)$ and $\phi(t)$ at any given instant t. This yields the magnetization dynamics under various stresses and ramp rates.

Fast ramp: The stress on the Terfenol-D layer is ramped up linearly in time from 0 to the maximum possible value of 40 MPa in 1 ps. The corresponding magnetization dynamics is shown in Fig. 3.11. We notice that the polar angle θ continuously evolves from its initial value of 179° towards its final value of 1° for the first 200 ps. However, since stress rotates magnetization out-of-plane, $\phi(t)$ continues to deviate from its initial value of 90° moving deep into the "good" quadrant $(90°, 180°)$ and at around 220 ps, the magnetization vector enters a "bad" quadrant $(180°, 270°)$ for ϕ, which hinders the motion of magnetization as explained in Chapter 2. This makes the magnetization vector execute precessional motion in space while its projection on the magnet's plane changes course and rotates in the direction opposite to the desired direction so that $\theta(t)$ begins to increase with time instead of decreasing. Eventually, magnetization vector enters into another "good" quadrant $(270°, 360°)$ for ϕ, which happens

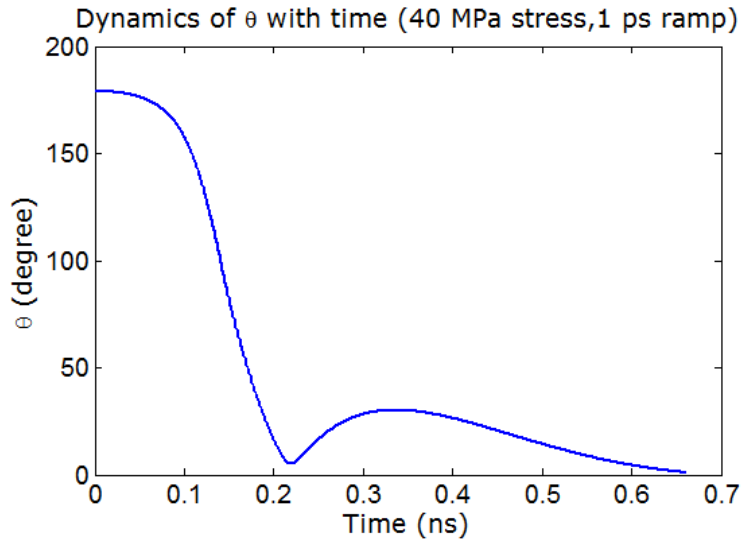

(a)

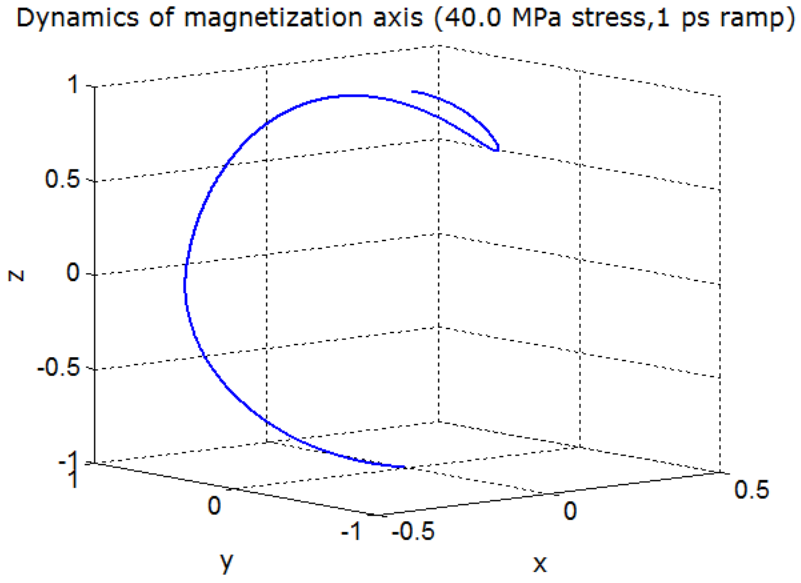

(b)

Figure 3.11: Magnetization dynamics in the Terfenol-D/PZT multiferroic nanomagnet. The stress is ramped up from 0 to 40 MPa in 1 ps: (a) polar angle θ versus time, and (b) the trajectory traced out by the tip of the magnetization vector in three-dimensional space while switching occurs, i.e. during the time θ changes from 179° to 1°. Note that the magnet's plane is $x = 0$.

around 330 ps, and thus it rotates towards its final destination, ultimately reaching $\theta = 1°$. Because of the interplay between the θ- and ϕ-dynamics, which causes the magnetization vector to precess rather always residing on magnet's plane, the complete switching takes around 650 ps, rather than about 220 ps.

Slow ramp: Fig. 3.12 shows the magnetization dynamics for a slow ramp that takes 50 ps to rise linearly from 0 to 40 MPa. In this case, as the stress is ramped up, the potential landscape of the magnet starts to get inverted and as soon as magnetization's minimum energy position is changed to $\theta = 90°$, the magnetization vector starts rotating from its initial orientation $\theta = 179°$. The azimuthal angle ϕ also rotates into the "good" quadrant $(90°, 180°)$, which aids the rotation of magnetization towards its destination $\theta = 1°$ as explained in Chapter 2. Eventually, the magnetization vector rotates towards its final destination of $\theta = 1°$ without ever changing course and rotating in the opposite direction, unlike the previous case. The magnetization vector clearly does not precess as much as in the previous case with fast ramp (see the trajectory plots) and it resides inside the "good" quadrant $(90°, 180°)$ for ϕ so the magnetization did not backtrack as in the previous case with fast ramp. The switching thus is actually *faster* now and takes about 400 ps compared to 650 ps for the previous case. Thus, a slower ramp can be beneficial when high stresses are applied. It eliminates the ripple and ringing in the switching characteristic seen in the previous case by limiting the out-of-plane excursion of the magnetization vector and saves precious time.

Fig. 3.13 shows the switching delay as a function of the ramp's rise (or fall) time with the magnitude of stress as a parameter. We see that for stresses of 5 MPa and 10 MPa, the switching delay increases linearly with the ramp time, but for higher stresses of 30 MPa and 40 MPa, the switching delay shows clear non-monotonic behavior. Normally, it is expected that the switching delay increases continuously with the ramp's rise (and fall) time, but the out-of-plane dynamics and precession of the magnetization vector can hamper this trend and cause the non-monotonic behavior. We have seen that with 40 MPa stress and ramp rise (and fal) time of 50 ps, there occurs no ripple in magnetization dynamics (see Fig. 3.12). This is because of the fact that magnetization does not venture into any "bad" quadrant for ϕ. However, magnetization traverses into a "bad" quadrant for ϕ for both lower and higher ramp

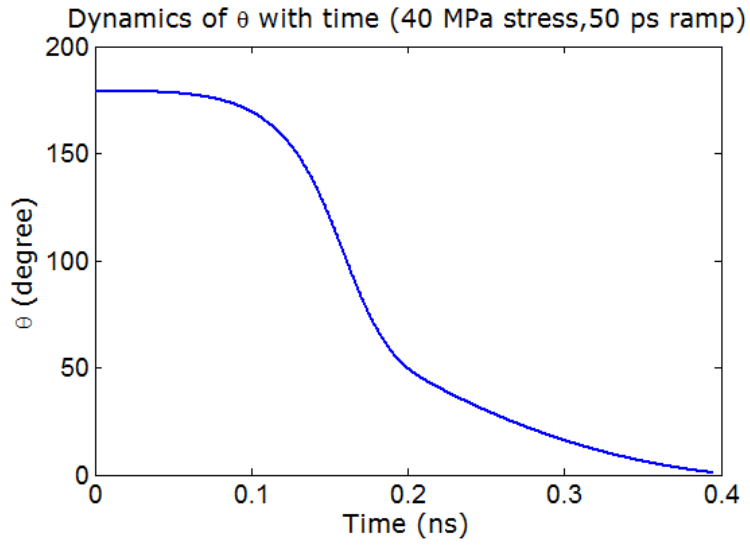

(a)

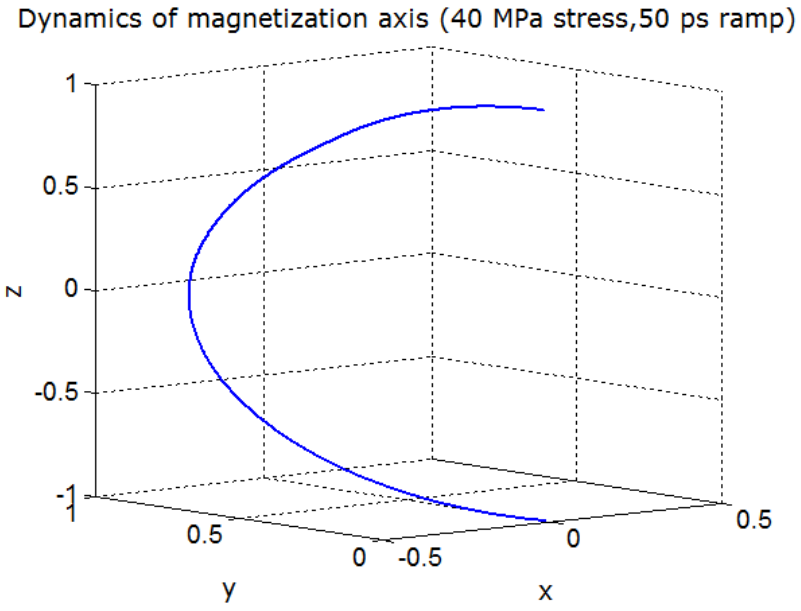

(b)

Figure 3.12: Magnetization dynamics in the Terfenol-D/PZT multiferroic nanomagnet. The stress is ramped up from 0 to 40 MPa in 50 ps: (a) polar angle θ versus time, and (b) the trajectory traced out by the tip of the magnetization vector while switching occurs.

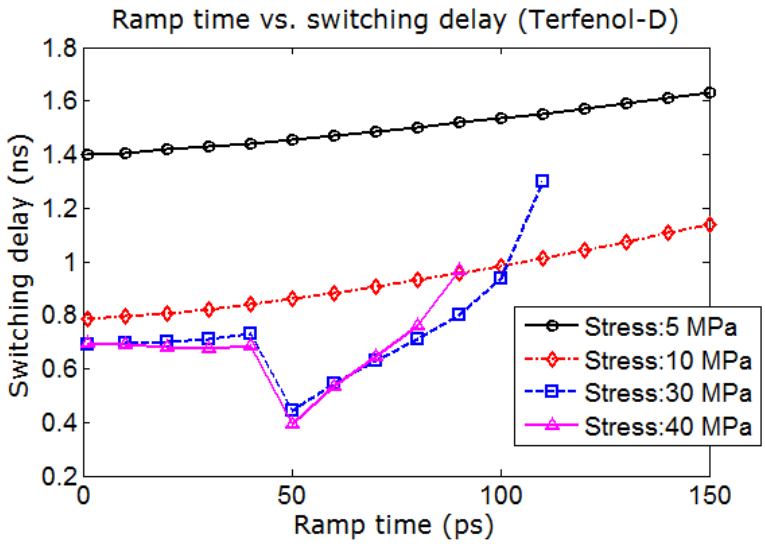

Figure 3.13: Switching delay in flipping the magnetization of the Terfenol-D/PZT nanomagnet as a function of the rise (or fall) time of the ramp, with the magnitude of stress as a parameter.

duration than 50 ps, which causes the non-monotonicity in the curves for 30 MPa and 40 MPa stresses in Fig. 3.13. Switching fails to happen for higher ramp durations with 30 MPa and 40 MPa stress, so the corresponding data points could not be shown.

Figs. 3.14 and 3.15 show the magnetization dynamics with 40 MPa stress and for ramp rise (and fall) times of 40 ps and 70 ps, respectively. For both of the cases, magnetization ventures into a "bad" quadrant for ϕ. For the case of 40 ps ramp duration, magnetization traverses through the "bad" quadrant $(180°, 270°)$, while for the case of 70 ps ramp duration, magnetization slips into the "bad" quadrant $(0°, 90°)$. The former case happens when magnetization is close to its destination and is due to high stress, while the latter case occurs due to long ramp duration during the ramp-down phase. Accordingly, while a higher ramp duration can eliminate ripples from magnetization dynamics and decrease the switching delay, much higher ramp duration on the other hand is detrimental to switching. This may even cause switching to fail, e.g., switching fails with 40 MPa stress for 100 ps to 150 ps ramp durations. Fig. 3.16 shows the magnetization dynamics with 40 MPa stress and for ramp rise (and fall) time 150 ps. Magnetization has backtracked even after it has crossed $\theta = 90°$ towards $\theta = 1°$. This is caused because magnetization has ventured into the "bad" quadrant $(0°, 90°)$ and stayed there for a long time during the long ramp-down phase.

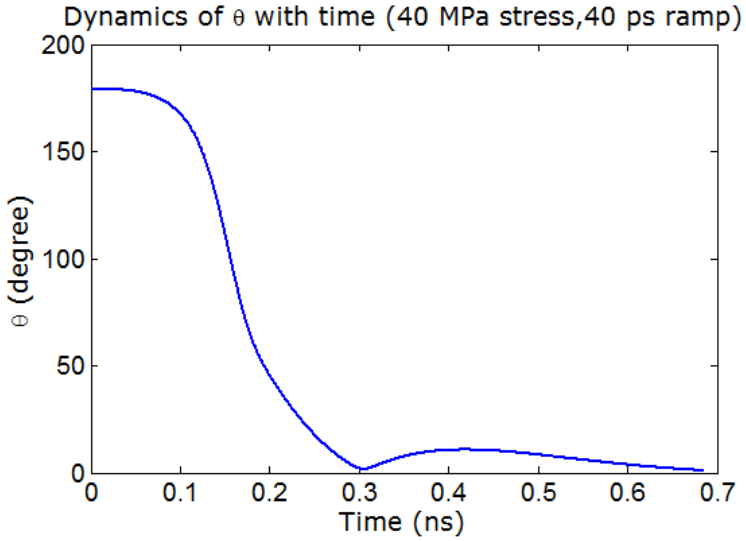

(a)

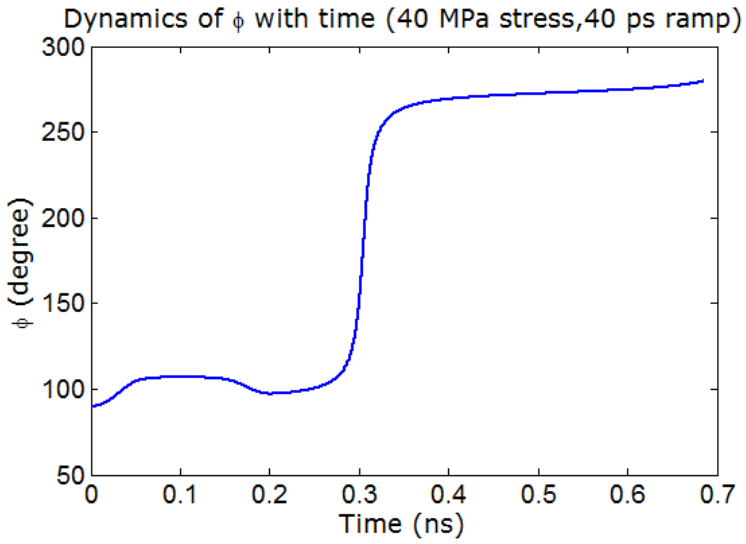

(b)

Figure 3.14: Magnetization dynamics in the Terfenol-D/PZT multiferroic nanomagnet. The stress is ramped up from 0 to 40 MPa in 40 ps: (a) polar angle θ versus time, and (b) azimuthal angle ϕ versus time. There is a ripple in the magnetization dynamics which causes because magnetization enters the "bad" quadrant $(180°, 270°)$ for ϕ. The switching delay is 686 ps.

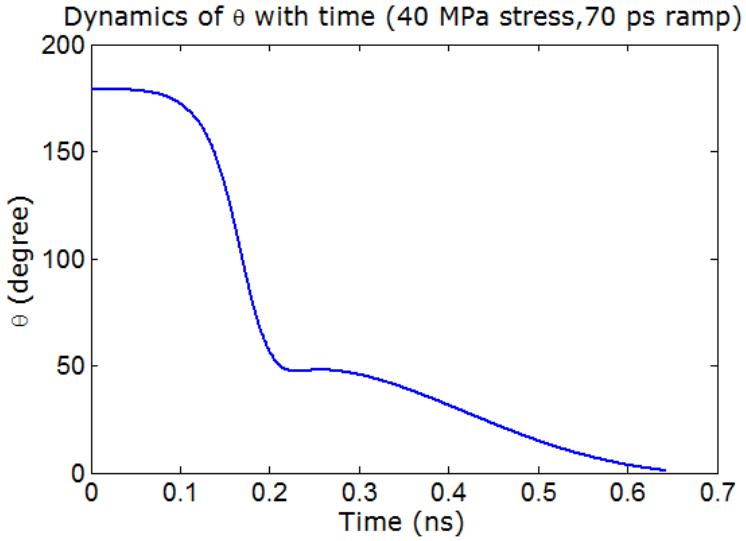

(a)

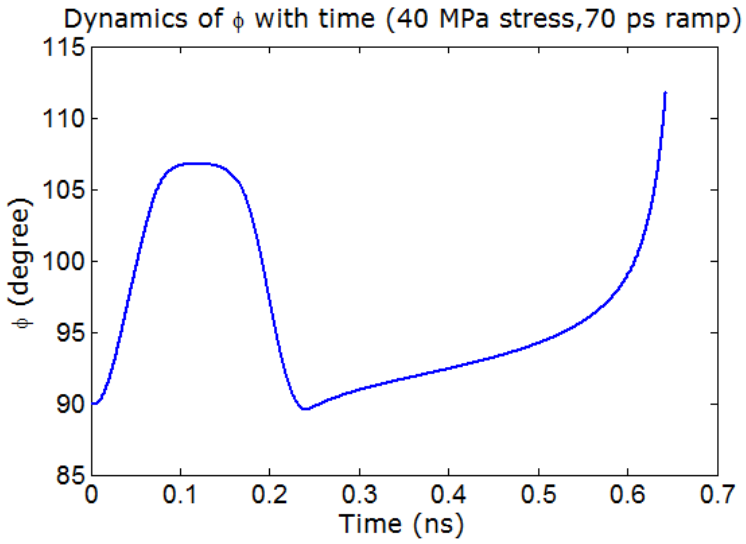

(b)

Figure 3.15: Magnetization dynamics in the Terfenol-D/PZT multiferroic nanomagnet. The stress is ramped up from 0 to 40 MPa in 70 ps: (a) polar angle θ versus time, and (b) azimuthal angle ϕ versus time. There is a ripple in the magnetization dynamics which causes because magnetization enters the "bad" quadrant $(0°, 90°)$ for ϕ. The switching delay is 643 ps.

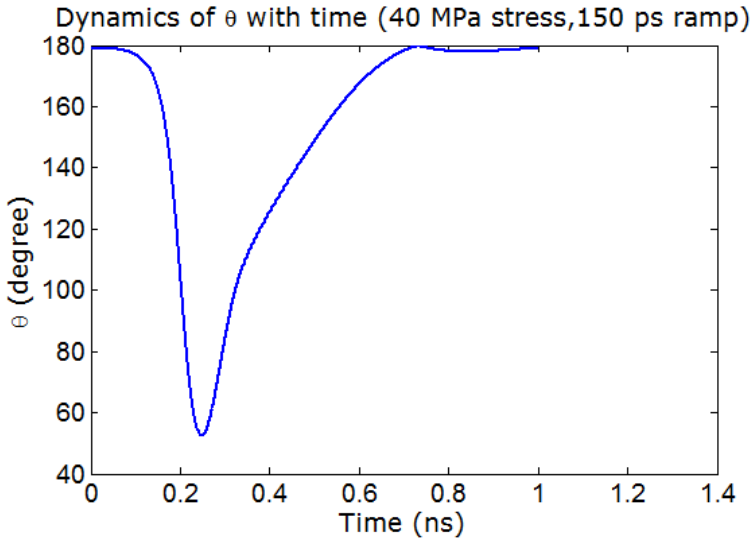

(a)

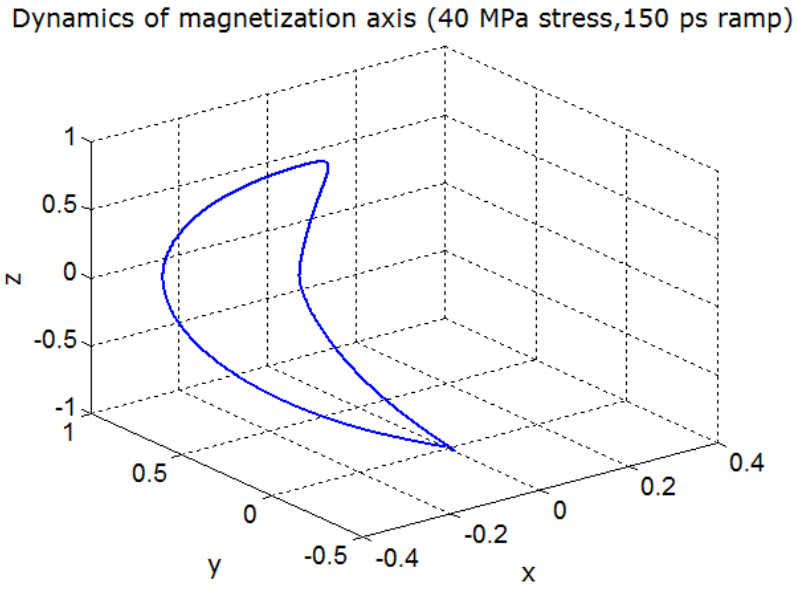

(b)

Figure 3.16: Magnetization dynamics in the Terfenol-D/PZT multiferroic nanomagnet. The stress is ramped up from 0 to 40 MPa in 150 ps: (a) polar angle θ versus time, and (b) the trajectory traced out by the tip of the magnetization vector while switching occurs.

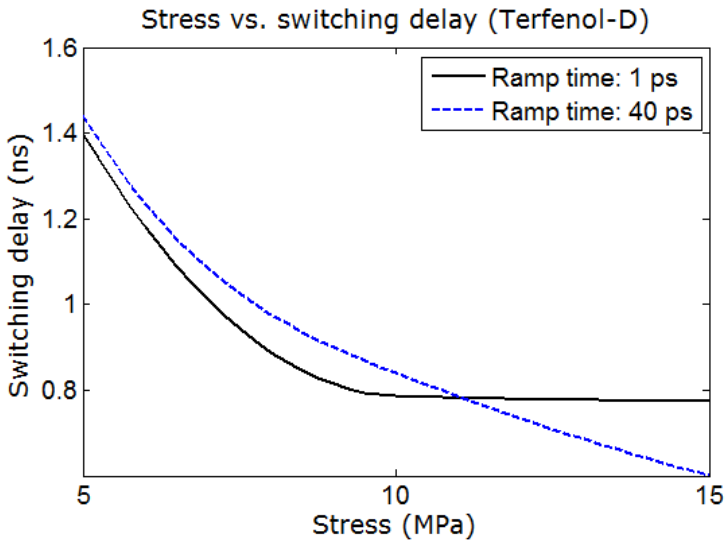

Figure 3.17: Switching delay versus stress for the Terfenol-D/PZT multiferroic nanomagnet for two different ramp rise (and fall) times of 1 ps and 150 ps.

Switching delay and energy dissipation

Fig. 3.17 shows the dependence of the switching delay on stress in the Terfenol-D/PZT nanomagnet, with the ramp's rise (or fall) time as a parameter. The two rise (and fall) times considered are 1 ps and 40 ps. There is a cross over at around 11 MPa stress. At low stress levels below 11 MPa, not much ripple is generated by a fast ramp so that the switching delay is shorter for the faster ramp. At high stress levels exceeding 11 MPa, a fast ramp generates enough ripple that the switching delay becomes longer for the faster ramp. This is the reason for the cross over.

Fig. 3.18 shows the energy dissipated in flipping the magnetization of the Terfenol-D/PZT multiferroic nanomagnet as a function of switching delay for a fixed rise (and fall) time of 150 ps. The switching delay is varied by varying the stress on the nanomagnet between 2.5 and 10 MPa. The energy dissipated internally in the nanomagnet (E_d) and the energy dissipated in the switching circuit ('CV^2') are shown separately. They both tend to saturate at larger delays.

For longer switching delays, the stress needed to flip the magnetization is less and hence the voltage V needed to generate the stress is smaller. This leads to a smaller 'CV^2' dissipation in the switching circuit. At the same time, the energy E_d dissipated internally in the nanomagnet is smaller when we switch slowly. In this range of switching delay, the energy dissipated in the external circuit is much smaller than the energy dissipated internally in the nanomagnet

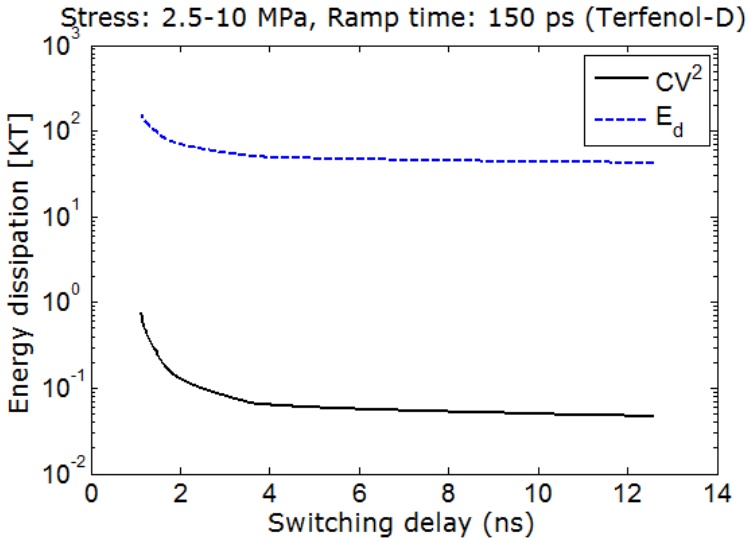

Figure 3.18: Energy dissipated in flipping the magnetization of the Terfenol-D/PZT multiferroic nanomagnet as a function of switching delay for a ramp rise (and fall) time of 150 ps. This range of switching delay corresponds to a stress range of 2.5 MPa to 10 MPa. The energy dissipated in the nanomagnet due to Gilbert damping (E_d) and the energy dissipated in the external switching circuit ('CV^2') are shown separately.

since the switching is *adiabatic* (the rise (and fall) time is much longer than the RC time constant of the switching circuit). The ratios of the two energies however decreases with decreasing switching delay. Below a switching delay of 4 ns, the energy dissipated internally in the nanomagnet and energy dissipated in the switching circuit both increase super-exponentially with decreasing switching delay. At 1 ns switching delay, the total energy dissipated in switching is only about 200 kT, which makes this switching methodology *extremely energy-efficient*. For this switching delay, the energy dissipated to switch a state-of-the-art transistor would have been at least two orders of magnitude larger [207], and the energy dissipated to switch the same nanomagnet with spin transfer torque will be also at least two orders of magnitude larger [136].

Fig. 3.19 plots the energy dissipation as a function of switching delay for a fixed stress of 40 MPa. Here, the switching delay is varied by varying the ramp's rise (and fall) time between 10 and 40 ps. Note the decrease of switching delay with increasing ramp duration for 40 MPa stress in Fig. 3.13. Both E_d and the 'CV^2' dissipations fall off with decreasing switching delay, which depicts the *unusual* trade-off between switching delay and energy. This is apparently a consequence of out-of-plane excursion of magnetization that makes both the switching delay and energy dissipation decrease with increasing ramp duration. This figure shows that we can switch magnetization in ∼0.7 ns by dissipating about 700 kT of energy. Switching delay can

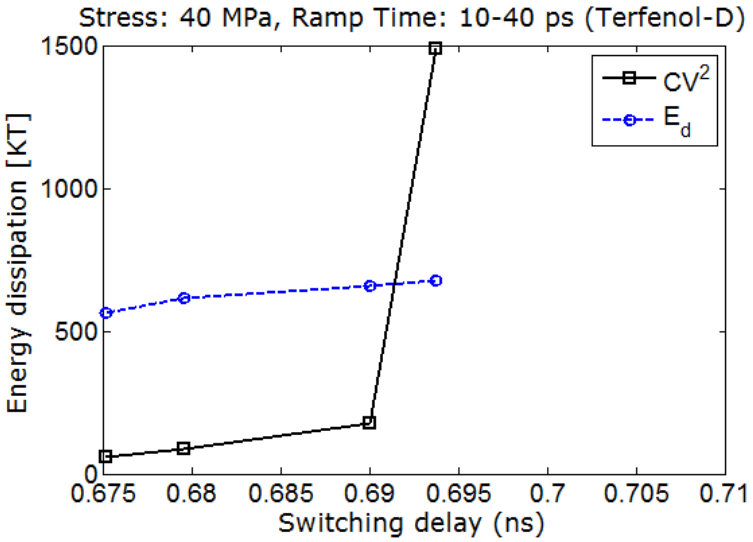

Figure 3.19: For a fixed stress of 40 MPa, energy dissipated in flipping the magnetization of the Terfenol-D/PZT nanomagnet as a function of switching delay when the latter is varied by varying the ramp's rise (and fall) time from 10-40 ps.

be decreased if we consider a bit higher ramp duration that can remove the ripples completely from magnetization dynamics (see Fig. 3.13).

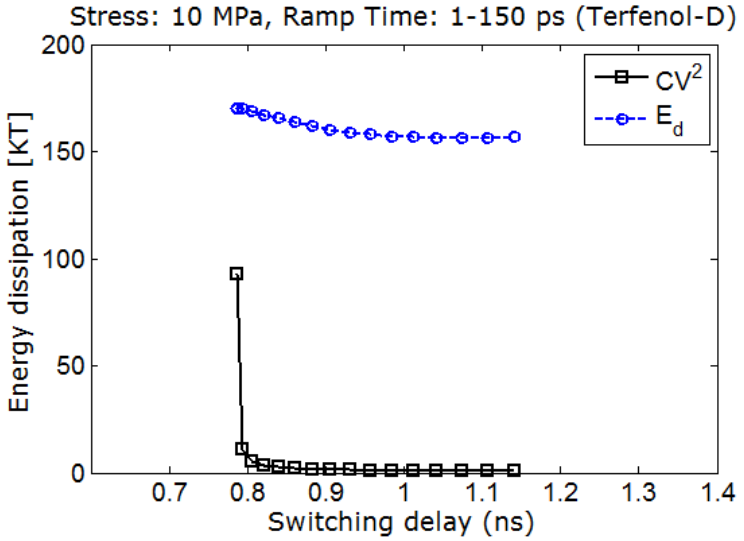

Figure 3.20: For a fixed stress of 10 MPa, energy dissipated in flipping the magnetization of the Terfenol-D/PZT nanomagnet as a function of switching delay when the latter is varied by varying the ramp's rise (and fall) time from 1-150 ps.

A similar plot but with *usual* switching delay-energy trade-off for a lower fixed stress of 10 MPa is shown in Fig. 3.20. Here, the switching delay is varied by varying the rise (and fall) time between 1 ps and 150 ps since there is no issue of non-monotonic behavior at such low stress values (see Fig. 3.13). We see that the energy dissipated internally in the nanomagnet (E_d) decreases with increasing switching delay which shows the correct trade-off between switch-

ing delay and energy. In this case, the average power dissipation goes down with increasing switching delay (and decreasing energy dissipation) since energy dissipation is the product of the average power and the switching delay. The 'CV^2' energy dissipation in the external circuit also does goes down with increasing delay since switching becomes more adiabatic (higher ramp duration) as the delay becomes longer. This figure shows that we can switch magnetization in ∼1 ns by dissipating roughly 200 kT of energy.

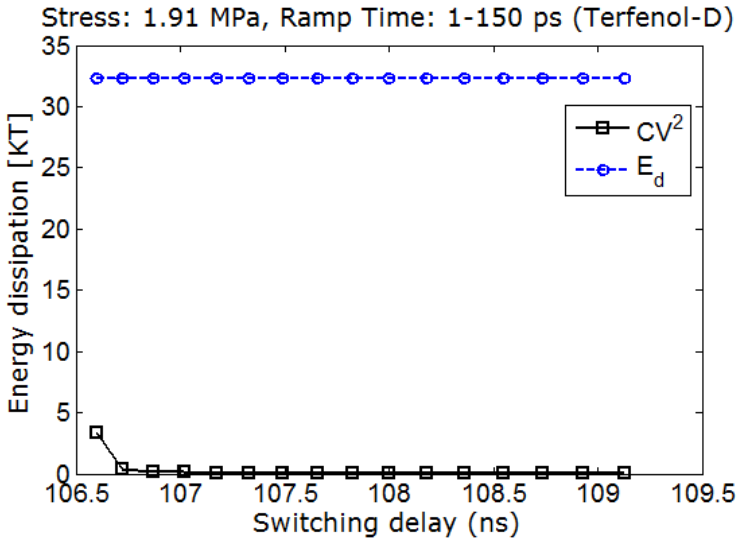

Figure 3.21: For a fixed stress of 1.91 MPa, energy dissipated in flipping the magnetization of the Terfenol-D/PZT nanomagnet as a function of switching delay when the latter is varied by varying the ramp's rise (and fall) time from 1-150 ps.

Fig. 3.21 shows the energy dissipation as a function of switching delay for a fixed stress of 1.91 MPa. Once again, the delay is varied by varying the ramp's rise (and fall) time between 1 and 150 ps. In this case, E_d is nearly independent of the switching delay, meaning that the average power dissipation in the nanomagnet varies inversely with the switching delay. The 'CV^2' dissipation in the external circuit still goes down with increasing delay as expected because switching becomes increasingly 'adiabatic'. This figure shows that we can switch in 110 ns by dissipating only ∼35 kT of energy at room temperature. The corresponding average power dissipation in this case is roughly 35 kT/110 ns = 1.33 pW per nanomagnet per bit flip. If we have an array of magnets with areal density 10^{10} cm^{-2} (10 Gbits/cm^2) and 10% of them are being flipped at any given time (10% activity level), then the power dissipated is 1.3 mW/cm^2. The energy needed to run at such low power levels can be harvested from the local surroundings using existing energy harvesting devices [182, 208, 209, 210] without requiring a

battery or external energy source! This opens up the possibility of unique applications such as medically implanted devices (e.g. processors implanted in a patient's brain which warn of impending epileptic seizures) that run by harvesting energy from a patient's body movements without requiring a battery, buoy mounted processors in the open sea that harvest energy from swaying motion induced by sea waves, or distributed sensor-processor networks for structural health monitoring of bridges and buildings that harvest energy from vibrations of the structure due to wind or passing traffic. These applications are made possible by the extreme energy efficiency of strain-induced switching.

3.2.2 Nickel

Nickel has a negative magnetostrictive coefficient (see Table 3.1) so that a nickel/PZT multiferroic nanomagnet will require a *tensile* stress to initiate rotation away from the easy axis. Note that the torque generated due to the stress would be of same sign as that in the case of Terfenol-D since it depends on the *product* of the magnetostrictive coefficient (λ_s) and stress (σ). For the dimensions of the nanomagnet chosen, the minimum stress that we will need in a nickel/PZT multiferroic to switch is 57 MPa, while the maximum stress that can be generated by the 500 ppm strain in the PZT layer is 107 MPa.

Note that nickel's magnetostriction coefficient is 30 times lower than that of Terfenol-D (see Table 3.1), however, the maximum stress that can be generated on the nickel layer is around 3 times more than that of Terfenol-D. Since the generated stress anisotropy is the product of magnetostriction coefficient and stress, using nickel, the potential barrier would be inverted quite less ($\sim$10 times) than that of using Terfenol-D. This is why using nickel as magnetostrictive layer would give us higher switching delay and lead us to higher vulnerability to thermal fluctuations.

Ramp rate and switching delay

Just as in the case of Terfenol-D, Equations (2.25) and (2.26) are solved numerically to find the values of $\theta(t)$ and $\phi(t)$ at any given instant t for the nickel/PZT nanomagnet. This yields the magnetization dynamics under various stresses and ramp rates.

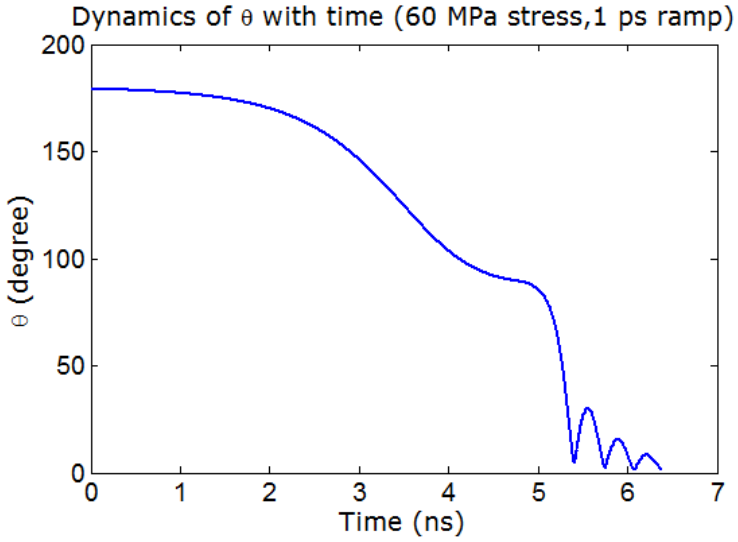

(a)

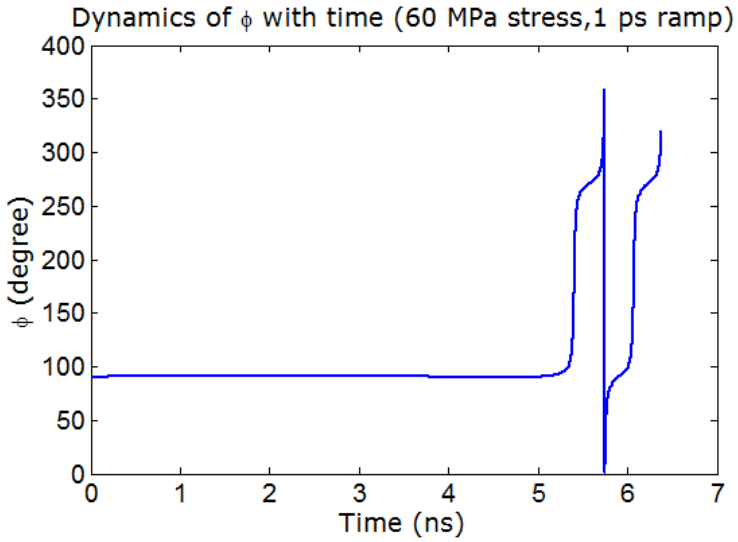

(b)

Figure 3.22: Magnetization dynamics in the nickel/PZT multiferroic nanomagnet. The stress is ramped up from 0 to 60 MPa in 1 ps: (a) polar angle θ versus time, and (b) azimuthal angle ϕ over time while switching occurs, i.e. during the time θ changes from 179° to 1°.

Fast ramp: Fig. 3.22 shows the magnetization dynamics of a nickel/PZT multiferroic nanomagnet when the stress is ramped up linearly in time from 0 to 60 MPa in 1 ps. The in-plane and out-of-plane dynamics of the magnetization vector are qualitatively similar to the case of Terfenol-D, except now we see a more ripples since there is more out-of-plane excursion and precession as can be seen in Fig. 3.22. Nickel shows more ripples and more precession because it has a smaller Gilbert damping constant than Terfenol-D. Consequently, the precessional motion is less damped. The switching delay is about 6.39 ns.

Slow ramp: Figs. 3.23 and 3.24 show the magnetization dynamics of a nickel/PZT multiferroic nanomagnet when the stress is ramped up linearly in time from 0 to 60 MPa in 100 ps and 150 ps, respectively. Comparing Fig. 3.23 with the case of fast ramp one (Fig. 3.22), we notice that it takes more time for magnetization to switch with higher ramp duration of 100 ps. The sluggish ramp-up and ramp-down phases have increased the switching delay to 9.38 ns for the case of 100 ps ramp duration. Note that there exists same number of ripples at the end of magnetization dynamics for both cases of 1 ps and 100 ps ramp durations. Thus there are not much qualitative differences between the Figs. 3.22 and 3.23.

However, for a slower ramp of duration 150 ps, there occurs a qualitative difference in magnetization dynamics as shown in the Fig. 3.24. During the ramp-up phase, the azimuthal angle ϕ has rotated clockwise in the quadrant $(0°, 90°)$ and then in the quadrant $(270°, 360°)$. As we have explained that out-of-plane excursion of magnetization in the "good" quadrant $(270°, 360°)$ facilitates magnetization rotating towards its destination, magnetization has now, in fact, switched faster (in 7.26 ns) than that of the case of lower ramp duration of 100 ps. This is certainly a qualitative difference. Note that there exists same number of ripples at the end of magnetization dynamics for both cases of 100 ps and 150 ps ramp durations.

Fig. 3.25 shows the trajectory traced out by the magnetization vector in three-dimensional space with stress 60 MPa and ramp durations of 1 ps and 150 ps. We have already mentioned that for the case of 1 ps ramp duration, magnetization resides in the quadrant $(90°, 180°)$, while it strays into the quadrants $(0°, 90°)$ and $(270°, 360°)$ for the case of 150 ps ramp duration. This is what we see in the Fig. 3.25 that when magnetization starts from around $z = -1$, magnetization's x-value is negative for the case of 1 ps ramp duration, while that is positive for

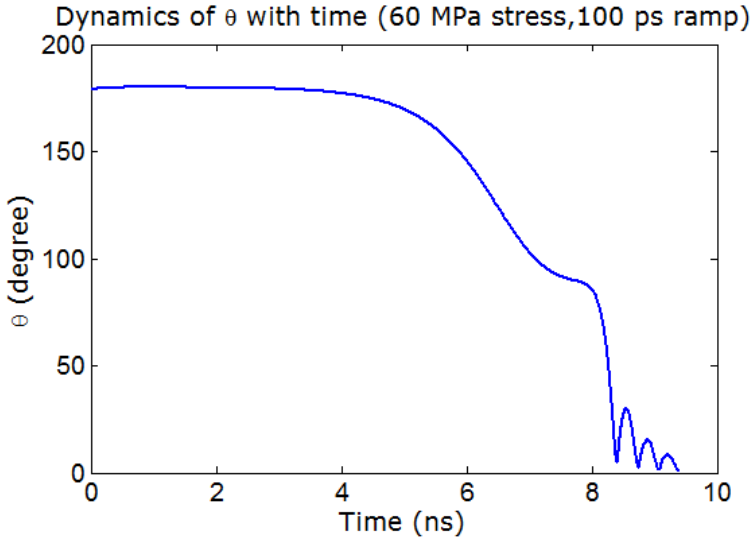

(a)

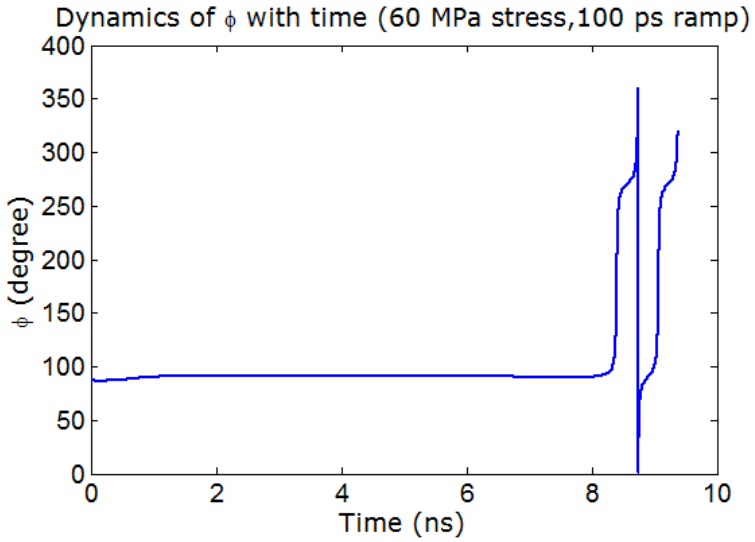

(b)

Figure 3.23: Magnetization dynamics in the nickel/PZT multiferroic nanomagnet. The stress is ramped up from 0 to 60 MPa in 100 ps: (a) polar angle θ versus time, and (b) azimuthal angle ϕ over time while switching occurs, i.e. during the time θ changes from 179° to 1°.

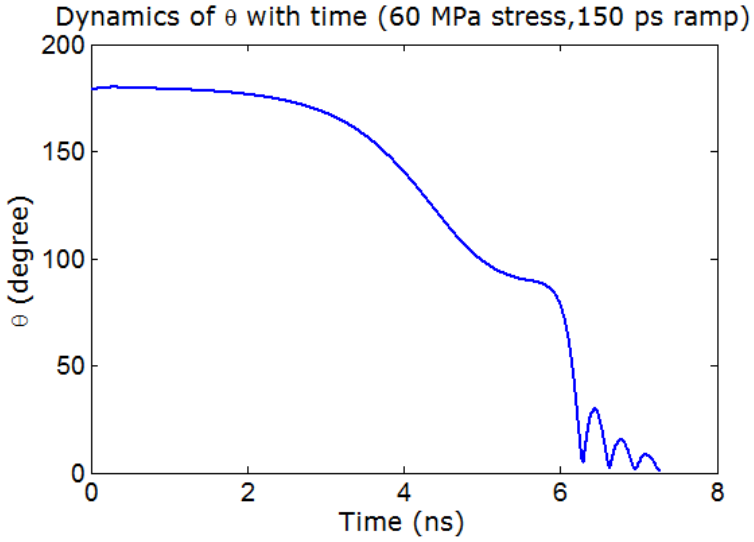

(a)

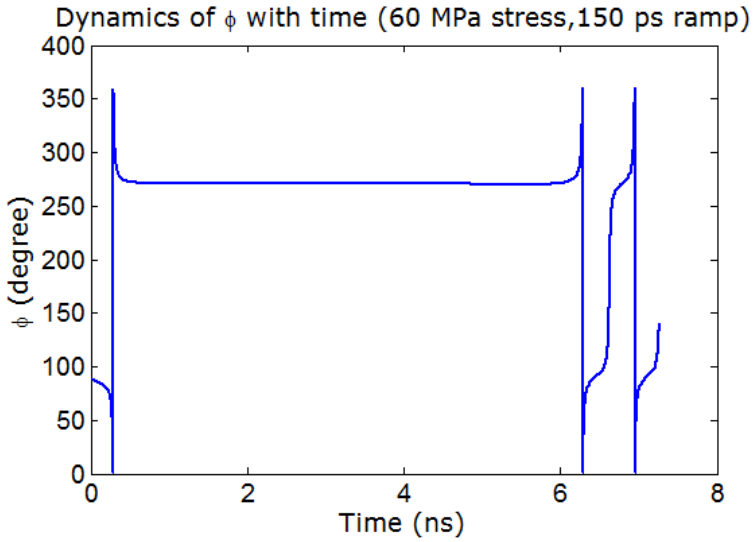

(b)

Figure 3.24: Magnetization dynamics in the nickel/PZT multiferroic nanomagnet. The stress is ramped up from 0 to 60 MPa in 150 ps: (a) polar angle θ versus time, and (b) azimuthal angle ϕ over time while switching occurs, i.e. during the time θ changes from 179° to 1°.

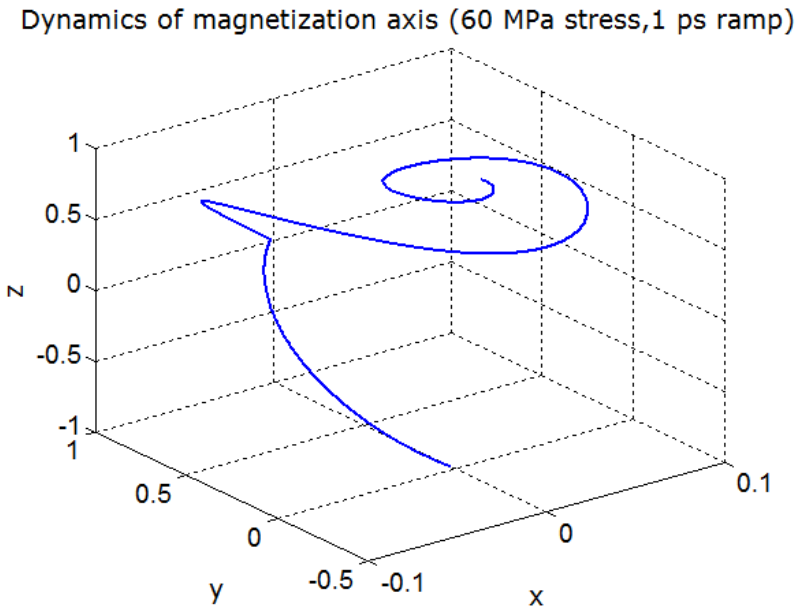

(a)

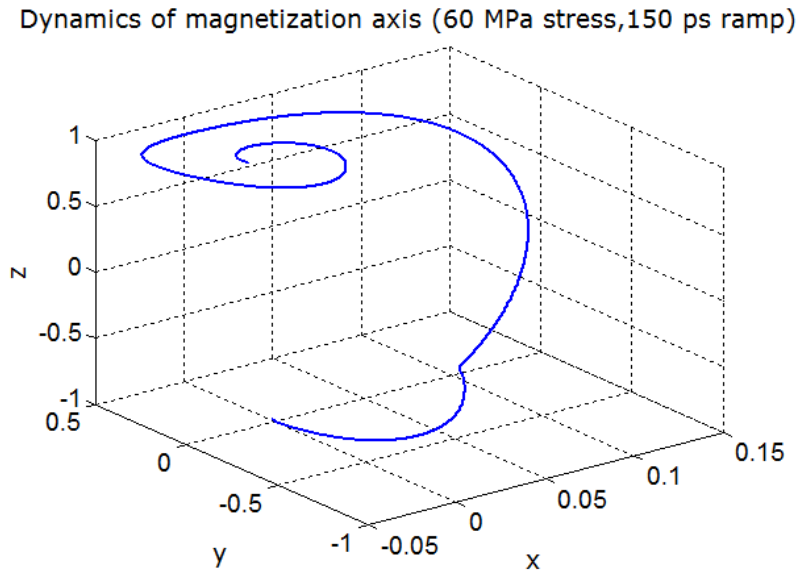

(b)

Figure 3.25: Trajectories traced out by the tip of the magnetization vector in the nickel/PZT multiferroic nanomagnet with 60 MPa stress while switching occurs: (a) 1 ps ramp duration, and (b) 150 ps ramp duration.

150 ps ramp duration before it goes into spiral precessional motion at the end of the dynamics.

Fig. 3.26 shows the magnetization dynamics of a nickel/PZT multiferroic nanomagnet when the stress is ramped up linearly in time from 0 to 107 MPa in 150 ps. Note that for this case the azimuthal angle ϕ has not rotated clockwise in the quadrant $(0°, 90°)$ as for the case with 60 MPa stress. This happens because a higher stress of 107 MPa has been able to keep the magnetization out-of-plane in the "good" quadrant $(90°, 180°)$ rotating the azimuthal angle ϕ in *anti-clockwise* direction. So the magnetization dynamics becomes qualitatively similar to the case with 60 MPa stress and for 1 ps and 100 ps ramp durations (see Figs. 3.22 and 3.23). The switching delay for this case is about 2.16 ns. The application of higher stress has made the switching faster in this case.

Note that for all the cases, θ comes very close to 1°, but the magnetization vector enters into "bad" and "good" quadrants alternatingly and vacillate before reaching the final destination. This causes the ringing which prolongs the switching duration and increases the delay.

Fig. 3.27 shows switching delay as a function of the ramp's rise (and fall) time for various stresses. At higher stress levels (80 - 107 MPa), the switching delay *increases* with increasing rise (and fall) time, which is an intuitive result, but contrary to the case of Terfenol-D. However, for lower stress levels of 60 MPa, we observe a non-monotonic behavior in switching delay, which is already explained through Figs. 3.22, 3.23, and 3.24. Similar non-monotonic behavior is expected to occur with higher stresses too if we extend the ramp rise (and fall) time to higher ramp duration than 150 ps. Such symptom is clearly observed from the curve with 70 MPa stress. However, a very high ramp fall time would cause switching failure as has been described earlier.

The strong dependence of switching delay on stress at low stress levels is illustrated in Fig. 3.28 which plots switching delay as a function of stress for two different rise (and fall) times of 1 ps and 150 ps. Notice that switching delay increases rapidly with decreasing stress in the interval [60 MPa, 70 MPa] but much less rapidly at higher stress levels exceeding 80 MPa. This is purely a consequence of the complex out-of-plane dynamics of the magnetization vector. This shows that any analysis which ignores the out-of-plane dynamics, and tacitly assumes that the motion of the magnetization vector will be always constrained to the plane of the nanomagnet since $N_{d-xx} \gg N_{d-yy}, N_{d-zz}$, will not only be quantitatively wrong, but

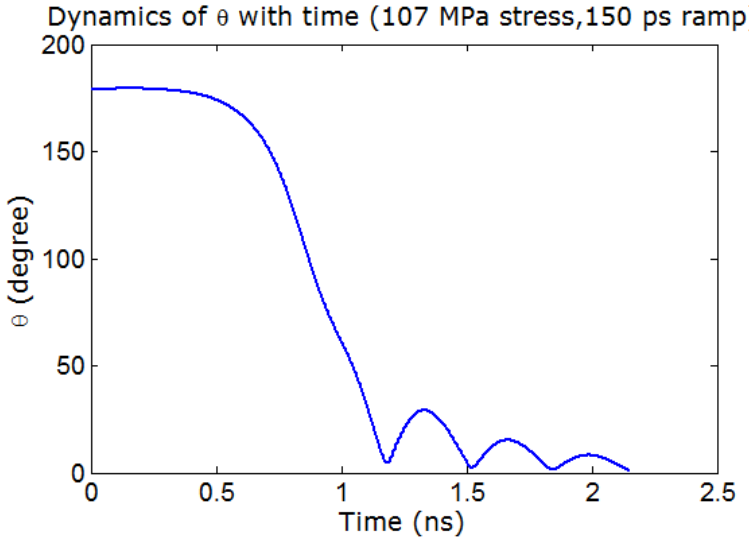

(a)

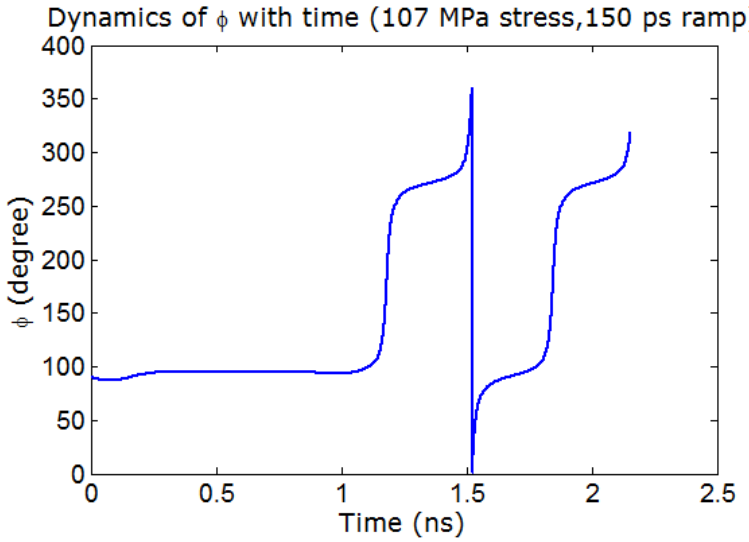

(b)

Figure 3.26: Magnetization dynamics in the nickel/PZT multiferroic nanomagnet. The stress is ramped up from 0 to 107 MPa in 150 ps: (a) polar angle θ versus time, and (b) azimuthal angle ϕ over time while switching occurs, i.e. during the time θ changes from 179° to 1°.

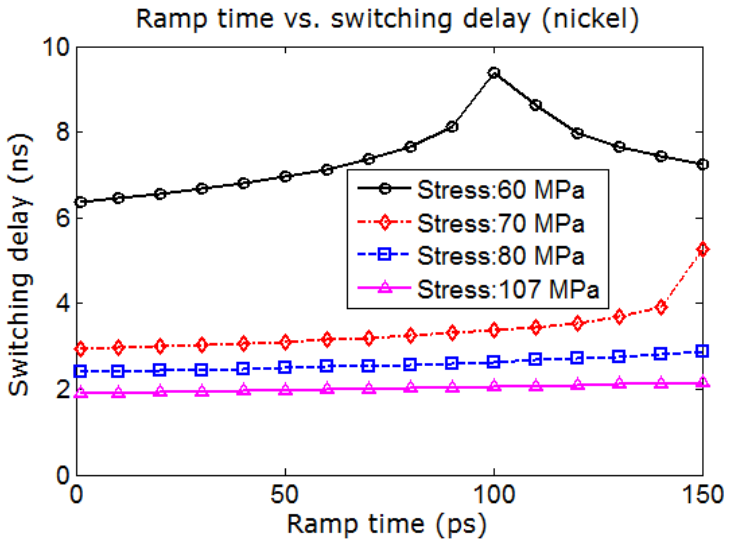

Figure 3.27: Switching delay in flipping the magnetization of the nickel/PZT nanomagnet as a function of the rise (or fall) time of the ramp, with the magnitude of stress as a parameter.

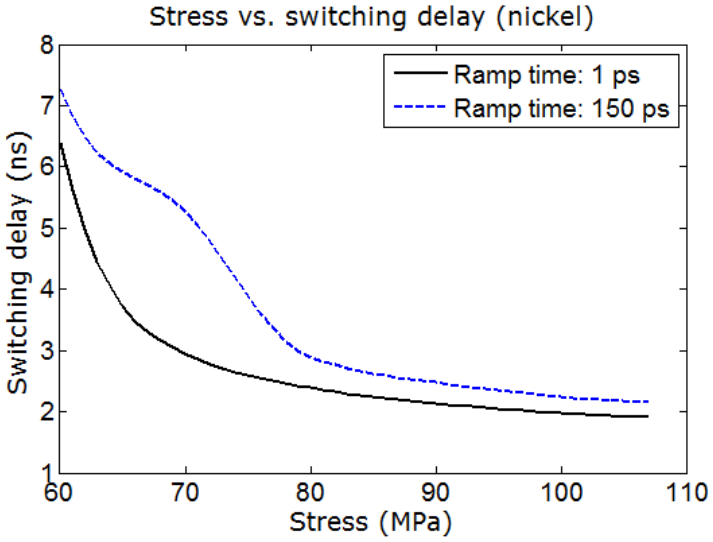

Figure 3.28: Switching delay versus stress for the nickel/PZT multiferroic nanomagnet for two different ramp rise (and fall) times of 1 ps and 150 ps.

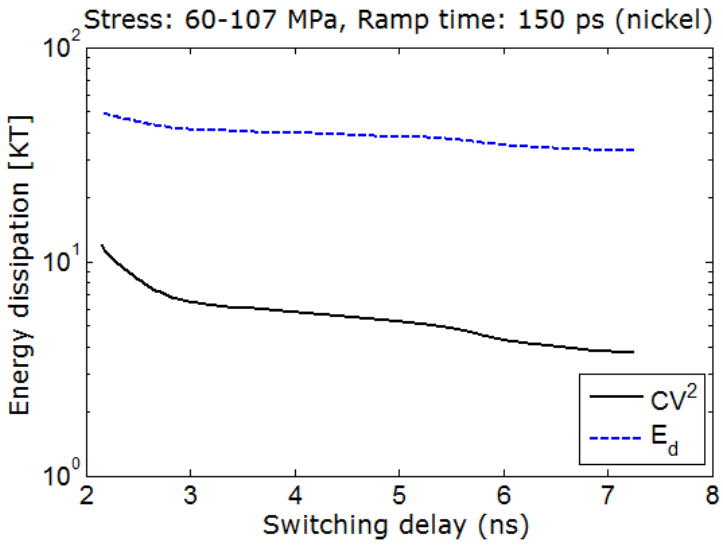

Figure 3.29: Energy dissipated in flipping the magnetization of the nickel/PZT multiferroic nanomagnet as a function of switching delay for a ramp rise (and fall) time of 150 ps. This range of switching delay corresponds to a stress range of 60 MPa to 107 MPa. The energy dissipated in the nanomagnet due to Gilbert damping and the energy dissipated in the external switching circuit ('CV^2') are shown separately.

qualitatively wrong as well. Basically, a sufficiently high stress can keep the magnetization in "good" quadrant and it generates a helpful motion that facilitates magnetization's motion in its desired direction. The extent of out-of-plane excursion determines how fast magnetization would be able to switch.

The curve for ramp rise (and fall) time of 150 ps in Fig. 3.28 is a bit tortuous at lower stress levels. The reasoning behind that can be explained with the help of the dynamics presented in the Fig 3.24. At low stress levels and higher ramp duration, the azimuthal angle ϕ of magnetization rotates clockwise rather than anti-clockwise and dynamics gets different and complex as explained for the case presented in Fig. 3.24. This would not be repeated here and this too is a consequence of the out-of-plane dynamics.

Switching delay and energy dissipation

Fig. 3.29 shows the energy dissipated in flipping the magnetization of the nickel/PZT multiferroic nanomagnet as a function of the switching delay. The latter is varied by varying the applied stress between 60 MPa and 107 MPa with fixed rise (and fall) time of 150 ps for the stress ramp. The energy dissipated internally in the nanomagnet due to Gilbert damping and the 'CV^2' energy dissipated in the external circuit are shown separately. Both dissipation com-

ponents decrease with increasing switching delay, implying that the average power dissipated during switching decreases rapidly with increasing delay. Both tend to saturate as the switching delay becomes longer.

In Fig. 3.29, note that the 'CV^2' energy dissipated in the switching circuit is 1-2 orders of magnitude higher for nickel than for Terfenol-D for the same switching delay. Since the voltage V is proportional to stress, the 'CV^2' energy is quadratically proportional to stress. Since the magnetostrictive coefficient of Terfenol-D is considerably higher than that of nickel, Terfenol-D requires much less stress to generate the same stress anisotropy energy and hence requires much less stress to switch. This results in a significant reduction of 'CV^2' energy dissipation in the case of Terfenol-D.

The total energy dissipation is however dominated by the energy E_d dissipated internally in the nanomagnet due to Gilbert damping. This energy is actually smaller in nickel than in Terfenol-D, because the Gilbert damping constant of nickel is more than twice smaller than that of Terfenol-D. As long as we are switching adiabatically, E_d will be the primary source of dissipation, and in that case, the material with the lower Gilbert damping constant will be superior since it will reduce total dissipation. *The situation may change completely if we are switching abruptly.* In that case, the 'CV^2' energy may very well be the major component of dissipation. If that happens, then the material with the larger magnetostrictive coefficient will be better since it will need less stress to switch and hence less voltage and less 'CV^2' dissipation. In other words, nickel is better than Terfenol-D (from the perspective of energy dissipation) when switching is adiabatic, but the opposite may very well be true when the switching is abrupt.

If speed is the primary concern, then what is important is the product of the magnetostrictive coefficient and the Young's modulus. Since the maximum strain that can be generated in the magnetostrictive layer is fixed and determined by the PZT layer, the maximum stress anisotropy energy that can be generated in the nanomagnet depends on the aforesaid product. The higher the stress anisotropy energy is, the faster will be the switching. Since the product is higher for Terfenol-D than for nickel, the Terfenol-D/PZT multiferroic switches faster. It can be switched in sub-ns by the maximum strain generated in the PZT layer, but that same strain cannot switch a nickel/PZT multiferroic in less than 1 ns.

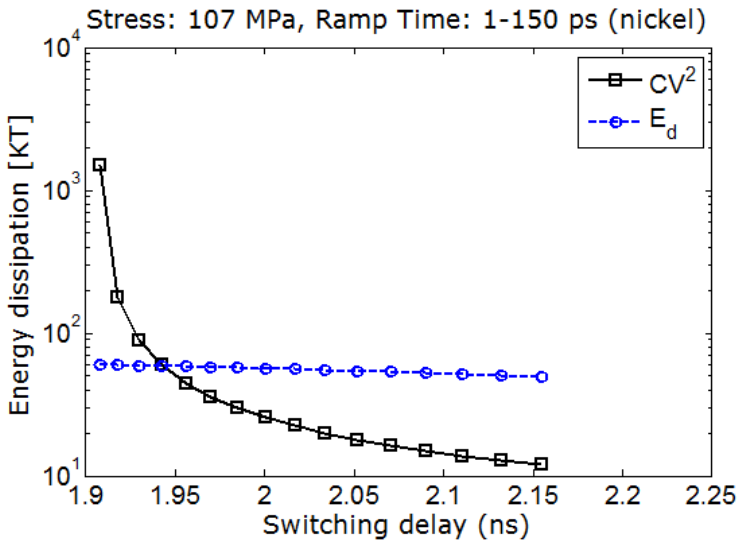

Figure 3.30: For a fixed stress of 107 MPa, energy dissipated in flipping the magnetization of the nickel/PZT nanomagnet as a function of switching delay when the latter is varied by continuously increasing the ramp's rise (and fall) time from 1-150 ps.

Fig. 3.30 shows the energy dissipated as a function of switching delay when the latter is varied by varying the ramp's rise (and fall) time between 1 ps and 150 ps, while holding the stress constant at 107 MPa. The 'CV^2' component decreases with increasing rise (and fall) time because switching becomes increasingly adiabatic. However, the dependence of E_d on switching delay is more-or-less constant, which varies around 10% if viewed in smaller scale. The switching delay is more-or-less constant with 107 MPa stress for varying ramp durations (see Fig. 3.27). This happens because 107 MPa stress is high enough to dissuade any detrimental effect of long ramp duration as high as 150 ps. It means that there is not much difference in the magnetization dynamics for varying ramp durations for high enough stress, which makes the internal energy dissipation E_d during switching constant. This too is a consequence of the out-of-plane dynamics.

3.2.3 Cobalt

Cobalt has a negative magnetostrictive coefficient that is similar to nickel's. Therefore, we will need a *tensile* stress to initiate magnetization rotation away from the easy axis. Its Gilbert damping constant is however smallest among the three materials considered (see Table 3.1) and hence we expect it to be least dissipative internally. For the dimensions of the nanomagnet chosen, the minimum stress that we will need in a cobalt/PZT multiferroic to switch is 57 MPa,

while the maximum stress that can be generated by the 500 ppm strain in the PZT layer is 104.5 MPa.

Note that cobalt's magnetostriction coefficient (same as nickel) is 30 times lower than that of Terfenol-D (see Table 3.1), however, the maximum stress that can be generated on the cobalt layer is around 3 times more than that of Terfenol-D. Since the generated stress anisotropy is the product of magnetostriction coefficient and stress, using cobalt, the potential barrier would be inverted quite less (∼10 times) than that of using Terfenol-D. This is why using cobalt as magnetostrictive layer would give us higher switching delay and lead us to higher vulnerability to thermal fluctuations.

Ramp rate and switching delay

Just as in the case of Terfenol-D and nickel, Equations (2.25) and (2.26) are solved numerically to find the values of $\theta(t)$ and $\phi(t)$ at any given instant t for the cobalt/PZT nanomagnet. This yields the magnetization dynamics under various stresses and ramp rates.

Fast ramp: Fig. 3.31 shows the magnetization dynamics of a cobalt/PZT multiferroic nanomagnet when the stress is ramped up linearly in time from 0 to 57 MPa in 1 ps. The in-plane and out-of-plane dynamics of the magnetization vector are very similar to the case of Terfenol-D and nickel, except now we see a more ripples since there is more out-of-plane precession as can be seen in Fig. 3.31. Cobalt shows even more ripples and more precession than that of nickel because it has a smaller Gilbert damping constant than nickel. Consequently, the precessional motion is less damped. The switching delay is about 6.93 ns.

Slow ramp: Figs. 3.32 and 3.33 show the magnetization dynamics of a cobalt/PZT multiferroic nanomagnet when the stress is ramped up linearly in time from 0 to 57 MPa in 50 ps and 150 ps, respectively. Comparing Fig. 3.32 with the fast ramp one (Fig. 3.31), we notice that it takes more time for magnetization to switch with higher ramp duration of 50 ps. The sluggish ramp-up and ramp-down phases have increased the switching delay to 9.33 ns for the case of 50 ps ramp duration. Note that there exists same number of ripples at the end of magnetization dynamics for both cases of 1 ps and 50 ps ramp durations. Thus there are not much qualitative differences between the Figs. 3.31 and 3.32.

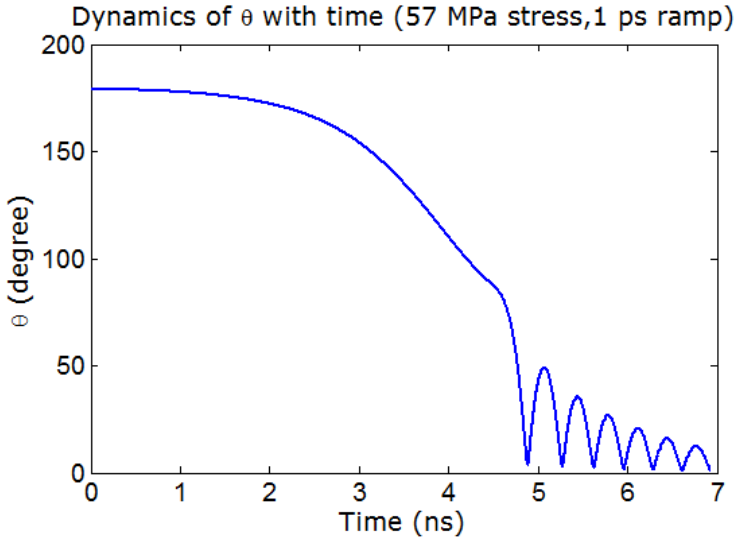

(a)

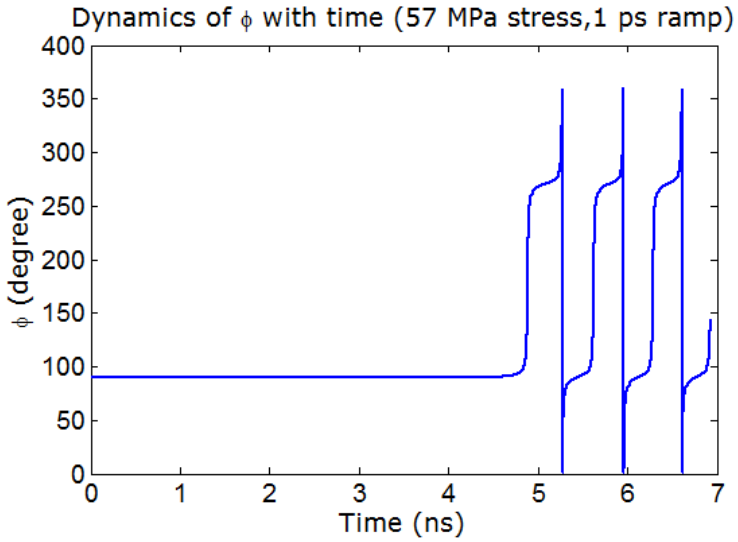

(b)

Figure 3.31: Magnetization dynamics in the cobalt/PZT multiferroic nanomagnet. The stress is ramped up from 0 to 57 MPa in 1 ps: (a) polar angle θ versus time, and (b) azimuthal angle ϕ over time while switching occurs, i.e. during the time θ changes from 179° to 1°.

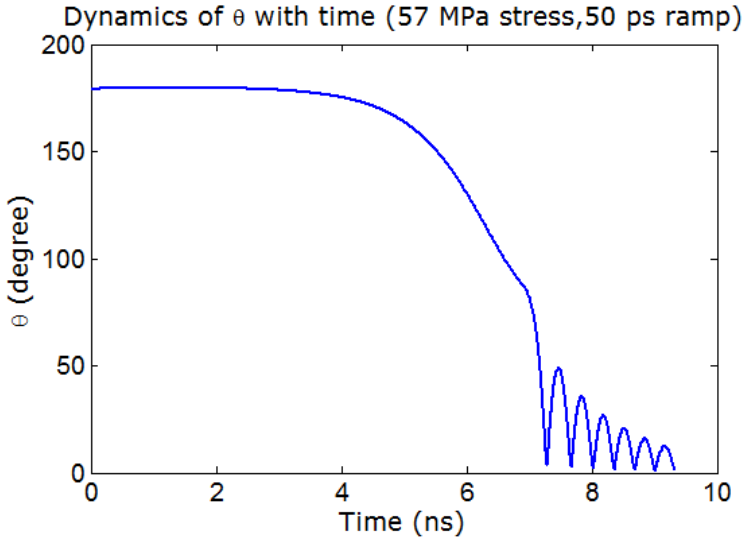

(a)

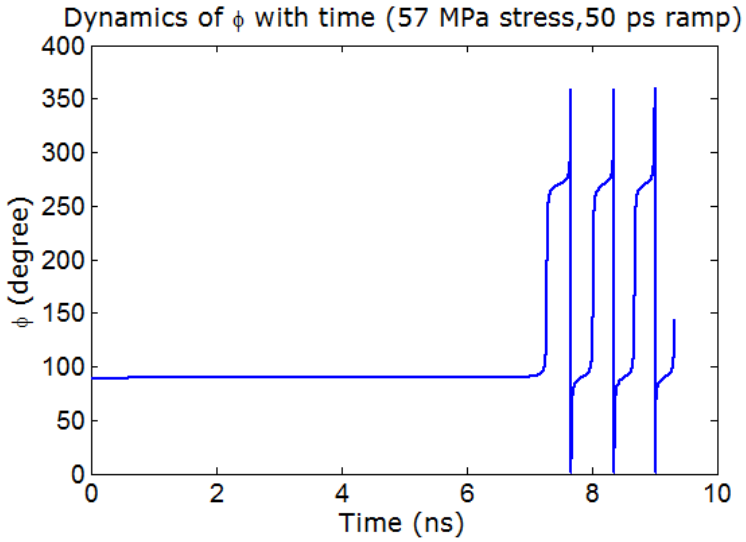

(b)

Figure 3.32: Magnetization dynamics in the cobalt/PZT multiferroic nanomagnet. The stress is ramped up from 0 to 57 MPa in 50 ps: (a) polar angle θ versus time, and (b) azimuthal angle ϕ over time while switching occurs, i.e. during the time θ changes from 179° to 1°.

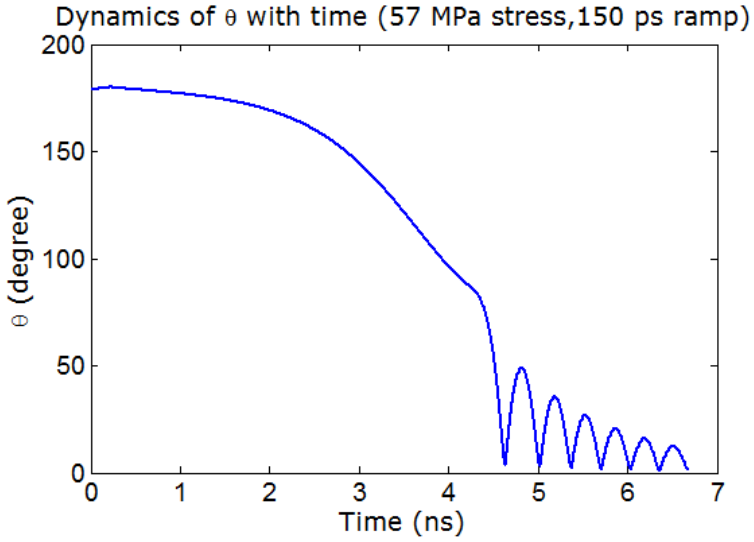

(a)

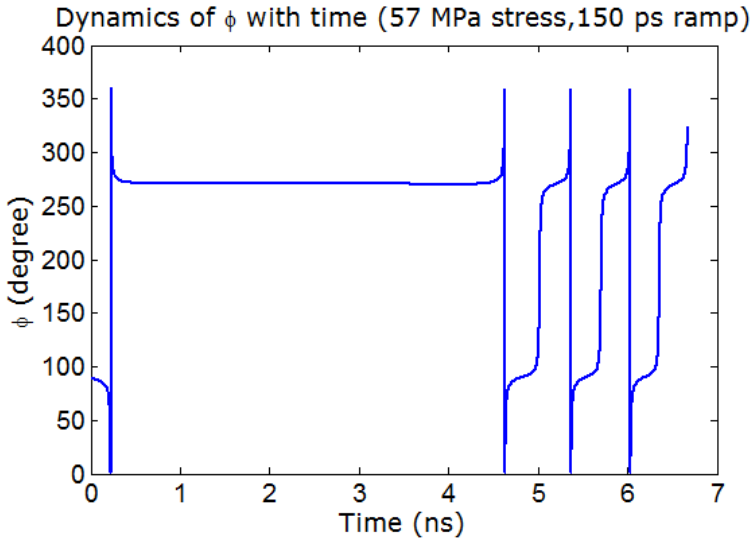

(b)

Figure 3.33: Magnetization dynamics in the cobalt/PZT multiferroic nanomagnet. The stress is ramped up from 0 to 57 MPa in 150 ps: (a) polar angle θ versus time, and (b) azimuthal angle ϕ over time while switching occurs, i.e. during the time θ changes from 179° to 1°.

However, for a slower ramp of duration 150 ps, there occurs a qualitative difference in magnetization dynamics as shown in the Fig. 3.33. During the ramp-up phase, the azimuthal angle ϕ has rotated clockwise in the quadrant $(0°, 90°)$ and then in the quadrant $(270°, 360°)$. As we have explained that out-of-plane excursion of magnetization in the "good" quadrant $(270°, 360°)$ facilitates magnetization rotating towards its destination, magnetization has now, in fact, switched faster (in 6.67 ns) than that of the case of lower ramp duration of 50 ps. This is qualitative difference outright. Note that there exists same number of ripples at the end of magnetization dynamics for both cases of 50 ps and 150 ps ramp durations.

Fig. 3.34 shows the trajectory traced out by the magnetization vector in three-dimensional space with stress 57 MPa and ramp durations of 1 ps and 150 ps. We have already mentioned that for the case of 1 ps ramp duration, magnetization resides in the quadrant $(90°, 180°)$, while it strays into the quadrants $(0°, 90°)$ and $(270°, 360°)$ for the case of 150 ps ramp duration. This is what we see in the Fig. 3.34 that when magnetization starts from around $z = -1$, magnetization's x-value is negative for the case of 1 ps ramp duration, while that is positive for 150 ps ramp duration before it goes into spiral precessional motion at the end of the dynamics.

Fig. 3.35 shows the magnetization dynamics of a cobalt/PZT multiferroic nanomagnet when the stress is ramped up linearly in time from 0 to 104.5 MPa in 150 ps. Note that for this case the azimuthal angle ϕ has not rotated clockwise in the quadrant $(0°, 90°)$ as for the case with 57 MPa stress. This happens because of the reason that a higher stress of 104.5 MPa has been able to keep the magnetization out-of-plane in the "good" quadrant $(90°, 180°)$ rotating the azimuthal angle ϕ in *anti-clockwise* direction. So the magnetization dynamics becomes qualitatively similar to the case with 57 MPa stress and for 1 ps and 50 ps ramp durations (see Figs. 3.31 and 3.32). The switching delay for this case is about 3.1 ns. The application of higher stress has made the switching faster in this case.

Note that for all the cases, θ come very close to 1°, but the magnetization vector enters into "bad" and "good" quadrants alternatingly and vacillate before reaching the final destination. This causes the ringing which prolongs the switching duration and increases the delay. This is very similar to the dynamics for the cases of nickel/PZT nanomagnet. However, the number of ripples has got increased quite for the case of cobalt since cobalt has much lower Gilbert damping constant than that of nickel.

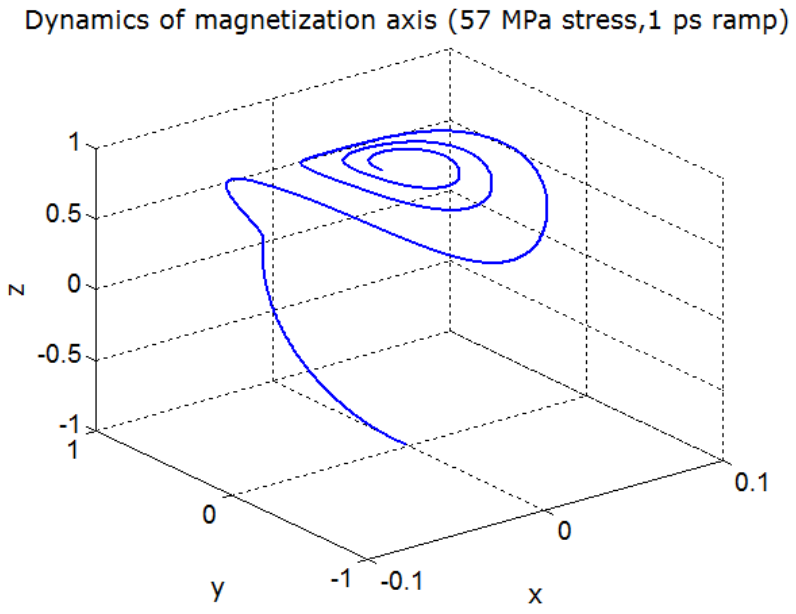

(a)

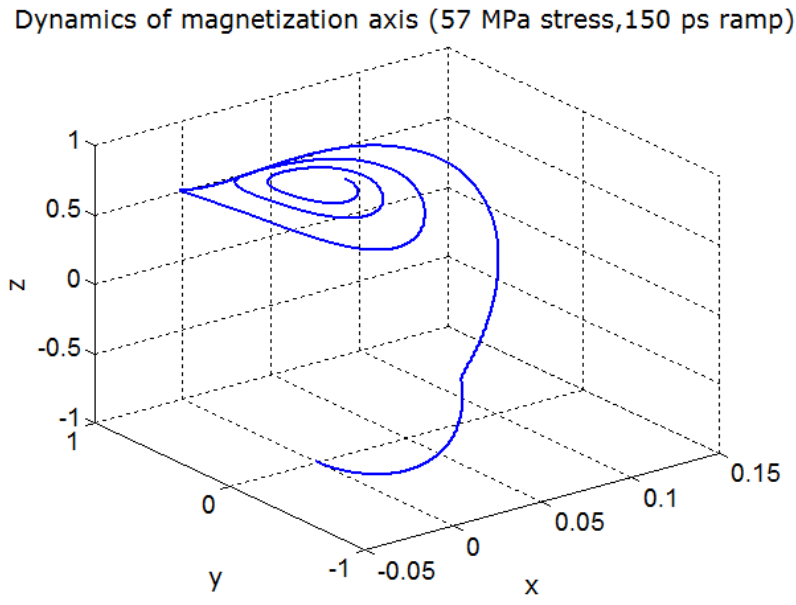

(b)

Figure 3.34: Trajectories traced out by the tip of the magnetization vector in the cobalt/PZT multiferroic nanomagnet with 60 MPa stress while switching occurs: (a) 1 ps ramp duration, and (b) 150 ps ramp duration.

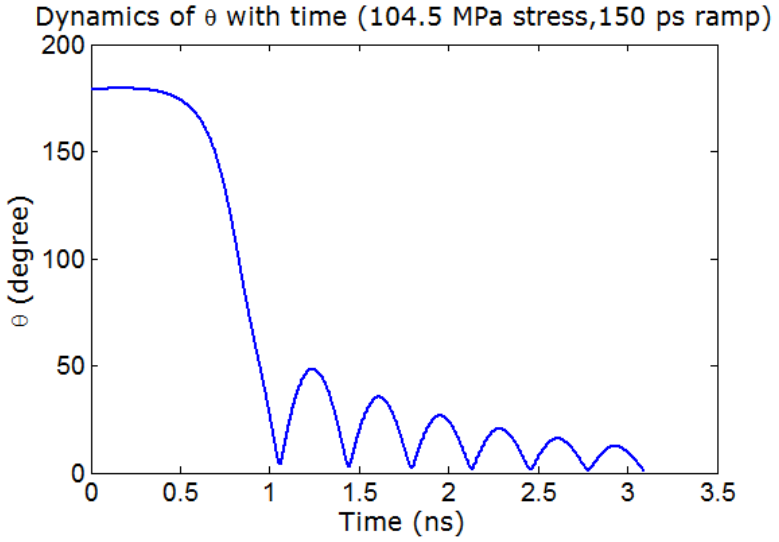

(a)

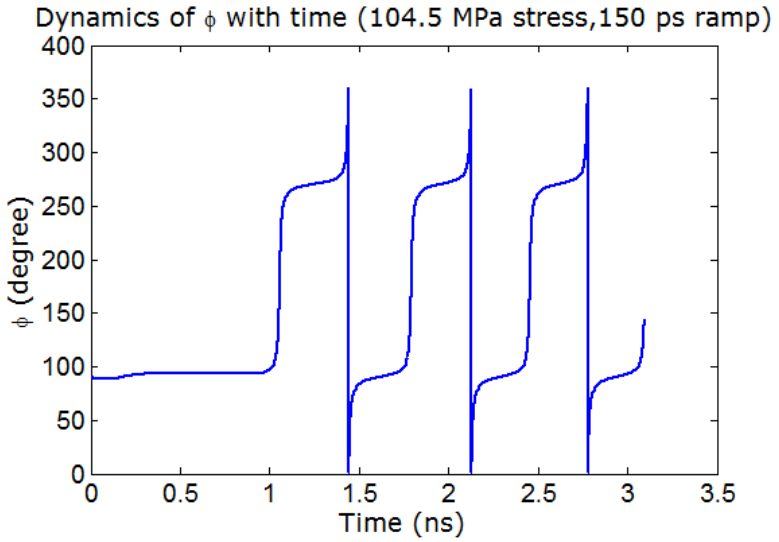

(b)

Figure 3.35: Magnetization dynamics in the cobalt/PZT multiferroic nanomagnet. The stress is ramped up from 0 to 104.5 MPa in 150 ps: (a) polar angle θ versus time, and (b) azimuthal angle ϕ over time while switching occurs, i.e. during the time θ changes from 179° to 1°.

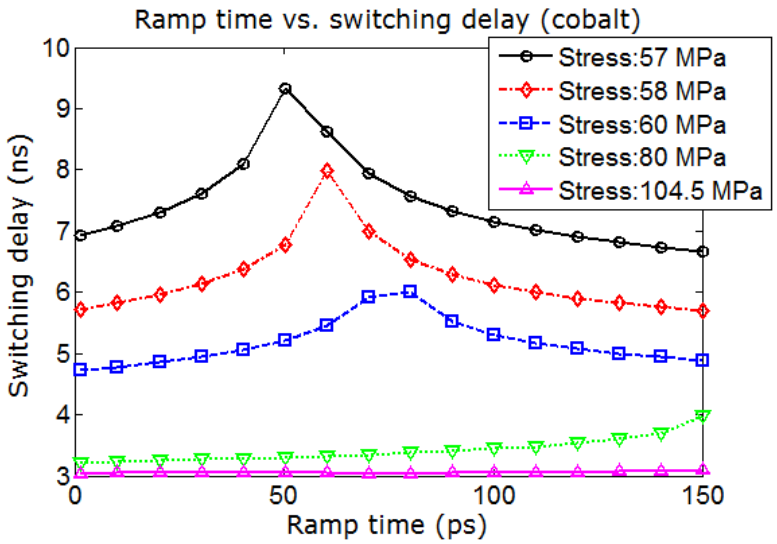

Figure 3.36: Switching delay in flipping the magnetization of the cobalt/PZT nanomagnet as a function of the rise (or fall) time of the ramp, with the magnitude of stress as a parameter.

Fig. 3.36 shows switching delay as a function of the ramp's rise (and fall) time for various stresses. At higher stress levels (80 - 104.5 MPa), the switching delay *increases* with increasing rise (and fall) time, which is an intuitive result and qualitatively similar to nickel. However, for the lower stress levels, we observe a non-monotonic behavior in switching delay, which is already explained through Figs. 3.31, 3.32, and 3.33. Similar non-monotonic behavior is expected to occur with higher stresses too if we extend the ramp rise (and fall) time to higher ramp duration than 150 ps. Such symptom is clearly observed from the curve with 80 MPa stress. However, a very high ramp fall time would cause switching failure as has been described earlier. This plot shows a clear analogy for the case of nickel/PZT nanomagnet (see Fig. 3.27).

The strong dependence of switching delay on stress at low stress levels is illustrated in Fig. 3.37 which plots switching delay as a function of stress for two different rise (and fall) times of 1 ps and 150 ps. Notice that switching delay increases rapidly with decreasing stress in the interval [57 MPa, 70 MPa] but much less rapidly at higher stress levels exceeding 80 MPa. This is purely a consequence of the complex out-of-plane dynamics of the magnetization vector. This has been explained for the case of nickel/PZT nanomagnet and thus would not be repeated here.

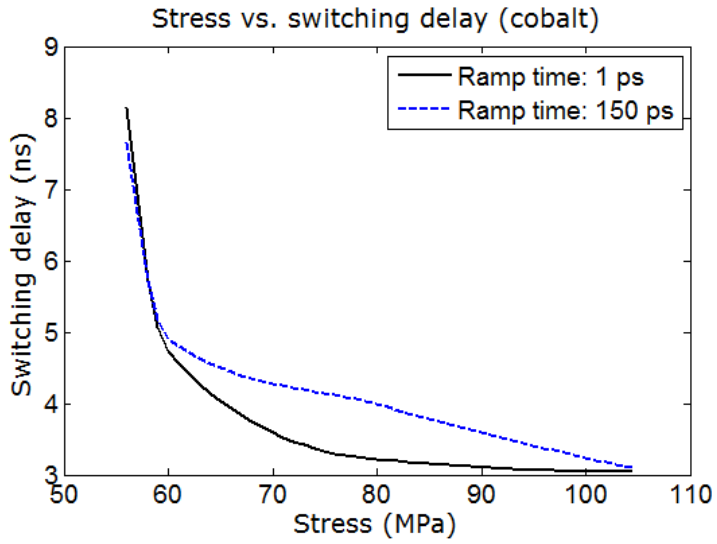

Figure 3.37: Switching delay versus stress for the cobalt/PZT multiferroic nanomagnet for two different ramp rise (and fall) times of 1 ps and 150 ps.

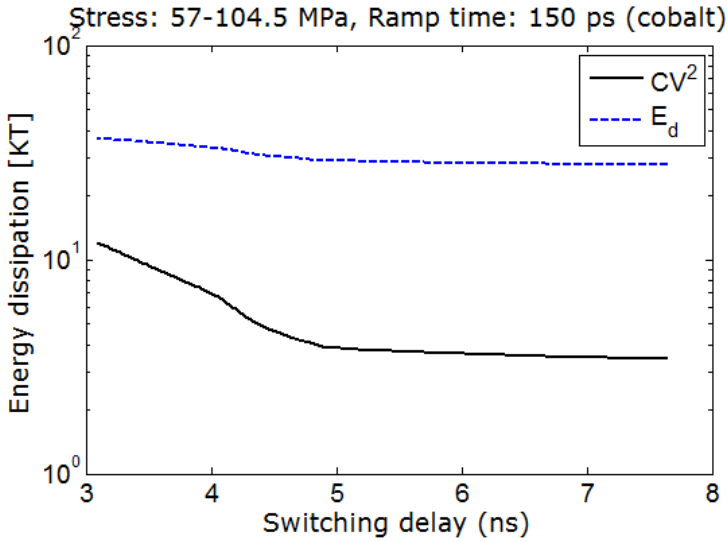

Figure 3.38: Energy dissipated in flipping the magnetization of the cobalt/PZT multiferroic nanomagnet as a function of switching delay for a ramp rise (and fall) time of 150 ps. This range of switching delay corresponds to a stress range of 57 MPa to 104.5 MPa. The energy dissipated in the nanomagnet due to Gilbert damping (E_d) and the energy dissipated in the external switching circuit ('CV^2') are shown separately.

Switching delay and energy dissipation

Fig. 3.38 shows the energy dissipated in flipping the magnetization of the cobalt/PZT multiferroic nanomagnet as a function of the switching delay. The latter is varied by varying the applied stress between 57 MPa and 104.5 MPa with fixed rise (and fall) time of 150 ps for the stress ramp. The energy dissipated internally in the nanomagnet due to Gilbert damping and the 'CV^2' energy dissipated in the external circuit are shown separately. Both dissipation components decrease with increasing switching delay, implying that the average power dissipated during switching decreases rapidly with increasing delay. Both tend to saturate as the switching delay becomes longer.

In Fig. 3.38, note that the 'CV^2' energy dissipated in the switching circuit for cobalt is 1-2 orders of magnitude higher than for Terfenol-D and similar to nickel for the same switching delay. For both the cases of nickel and cobalt, stress levels are very similar; also their magnetostrictive coefficients are same. The reasoning behind the energy dissipated in the switching circuitry has been described earlier for the case of nickel and thus would not be repeated here.

The total energy dissipation is however dominated by the energy E_d dissipated internally in the nanomagnet due to Gilbert damping. This energy turns out to be similar as for the case of nickel even if cobalt's damping constant is 5 times less than that of nickel. It's true that energy dissipation is proportional to the damping constant but due to low damping constant magnetization in cobalt/PZT nanomagnet experiences an increasing number of spiral precessional motions at the end of the dynamics, which on the other hand increase the energy dissipation during switching.

Fig. 3.39 shows the energy dissipated as a function of switching delay when the latter is varied by varying the ramp's rise (and fall) time between 100 ps and 150 ps, while holding the stress constant at 104.5 MPa. The 'CV^2' component decreases with increasing rise (and fall) time because switching becomes increasingly adiabatic. The internal energy dissipation E_d on switching delay varies by 10% and the same reasoning, which is a consequence of out-of-plane dynamics and described for the case of nickel applies here.

We have analyzed the switching dynamics in a multiferroic nanomagnet consisting of a PZT layer and a magnetostrictive layer subjected to time-varying stress. The stress is ramped up

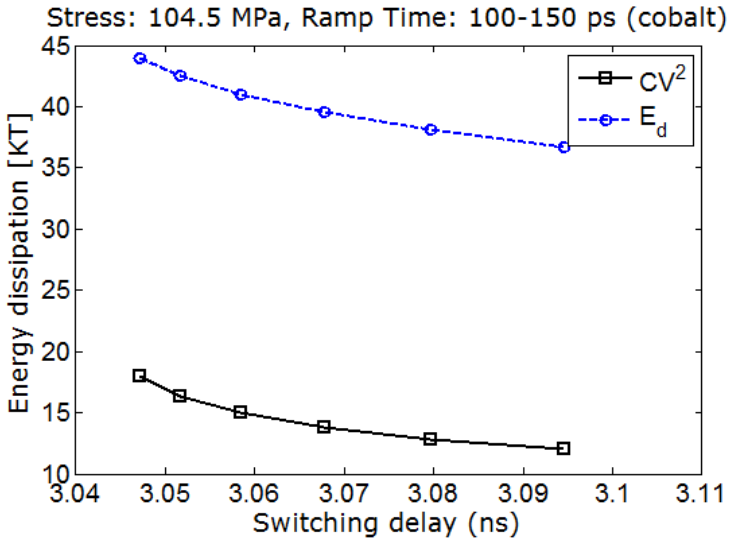

Figure 3.39: For a fixed stress of 104.5 MPa, energy dissipated in flipping the magnetization of the cobalt/PZT nanomagnet as a function of switching delay when the latter is varied by continuously increasing the ramp's rise (and fall) time from 100-150 ps.

linearly in time with different rates or rise (and fall) times. Three different materials (Terfenol-D, nickel, cobalt) were considered for the magnetostrictive layer. They show different behavior because of different material parameters (Young's modulus, magnetostrictive coefficient and Gilbert damping).

For the type of magnets chosen (materials and dimensions), the minimum switching delay that we have found is 0.4 ns obtained with Terfenol-D using a rise (and fall) time of 50 ps for a stress of 40 MPa. The corresponding 'CV^2' energy dissipation in the switching circuit is 36 kT and the energy dissipated internally in the nanomagnet due to Gilbert damping is E_d = 485 kT. However, sub-nanosecond switching delay can be still achieved by expending about 150 kT energy using lower stress of 10 MPa. With nickel, 107 MPa stress and 150 ps ramp duration produce 2.2 ns switching delay, 'CV^2' energy dissipation of 12 kT, and dissipation due to Gilbert damping E_d = 50 kT. For nickel, 104.5 MPa stress and 150 ps ramp duration produce 3.1 ns switching delay, 'CV^2' energy dissipation of 12 kT, and dissipation due to Gilbert damping E_d = 36 kT.

For nickel and cobalt, sub-nanosecond switching delay is unattainable because of the low stress anisotropy energy produced due to low magnetostriction coefficient. Also, low stress anisotropy energy will cause vulnerability to thermal fluctuations during switching. Therefore, we will not consider nickel and cobalt as magnetostrictive layers in the forthcoming section.

3.3 Thermal fluctuations

In this section, we will consider room-temperature thermal fluctuations and analyze the magnetization dynamics by numerically solving the coupled θ- and ϕ-dynamics as derived in Equations (2.41) and (2.42) [170]. These equations are derived by adding a random thermal torque to the original LLG dynamics as in Equations (2.25) and (2.26). Accordingly, the basic dynamics that we have presented in the previous two sections remain unchanged. We will analyze the magnetization dynamics with only Terfenol-D as magnetostrictive layer in the presence of room-temperature thermal fluctuations since for the other two materials (nickel and cobalt), the magnetostriction coefficient is low and thus the stress anisotropy energy is low too making the device unreliable with high error probability for room-temperature operation.

	Terfenol-D
Major axis (a)	100 nm
Minor axis (b)	90 nm
Thickness (t)	6 nm
Young's modulus (Y)	8×10^{10} Pa
Magnetostrictive coefficient ($(3/2)\lambda_s$)	$+90\times10^{-5}$
Saturation magnetization (M_s)	8×10^{5} A/m
Gilbert's damping constant (α)	0.1

Table 3.2: Material parameters for Terfenol-D used as magnetostrictive layer and dimensions of the nanomagnet for the study of magnetization dynamics in the presence of thermal fluctuations.

The material parameters and dimensions that characterize the Terfenol-D magnetostrictive layer are given in Table 3.2 [200, 201, 202, 204]. For the piezoelectric layer, we use lead-zirconate-titanate (PZT). The PZT layer is assumed to be four times thicker than the magnetostrictive layer so that any strain generated in it is transferred almost completely to the magnetostrictive layer. We will assume that the maximum strain that can be generated in the PZT layer is 500 ppm [205], which would require a voltage of 67 mV because d_{31}=1.8e-10 m/V for PZT [206]. The corresponding stress is the product of the generated strain (500×10^{-6}) and the Young's modulus of the magnetostrictive layer. So the maximum stress that can be generated on the Terfenol-D layer is 40 MPa.

The first and foremost effect while considering thermal fluctuations is that it creates a distribution of initial orientation of magnetization at the very beginning of switching, which we must take into account. Magnetization just fluctuates around its initial stable orientation due to

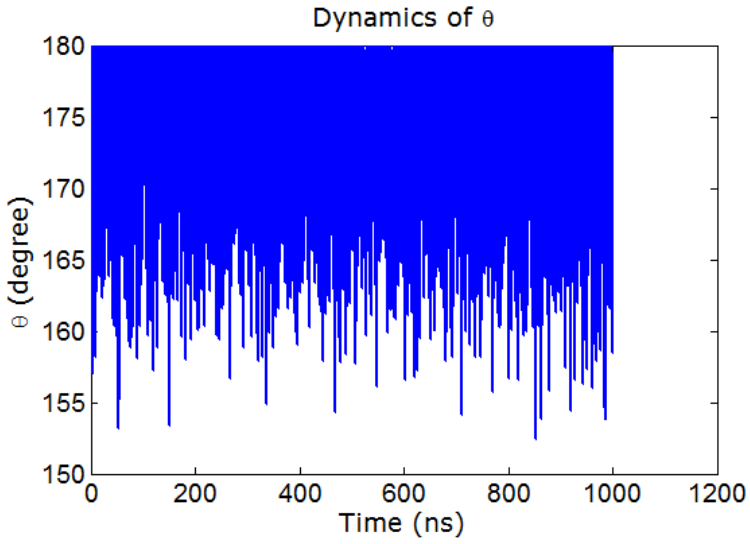

Figure 3.40: Magnetization fluctuates around its stable orientation $\theta = 180°$ due to room-temperature (300 K) thermal agitations for the Terfenol-D/PZT multiferroic nanomagnet, when no stress is applied.

thermal kicks. Fig. 3.40 shows that magnetization is fluctuating around $\theta = 180°$ due to room-temperature (300 K) thermal agitations. No stress is applied and thus the minimum energy positions in the potential landscape of the nanomagnet are still $\theta = 0°$ and 180°. But, thermal fluctuations at finite temperature would create a distribution of $\theta_{initial}$, while the most probable orientation of magnetization would be still $\theta = 180°$ according to the Boltzmann distribution. The simulation period for this result is chosen to be 1000 ns, which is long enough as simulating for longer period of times did not change the mean of the corresponding distribution.

Fig. 3.41 shows the initial distributions of polar angle $\theta_{initial}$ and $\phi_{initial}$ for the magnetization vector in the Terfenol-D/PZT multiferroic nanomagnet in the presence of room-temperature (300 K) thermal fluctuations. The nanomagnet is unstressed and while the most likely value of magnetization is still at $\theta = 180°$ (since that is a minimum energy position in the potential landscape), room-temperature thermal agitations have caused magnetization sometimes to climb up the potential hill around and a spread of 25° have occurred. The mean of the distribution is ∼175°. Simulation for a longer time period could have well caused more spread in the distribution, however, the mean value would be more-or-less unchanged since any extension in the tail of the distribution is of small probability. However, it needs mention here that the tail of this distribution has immense importance since that will determine the successful hold time of a bit of information.

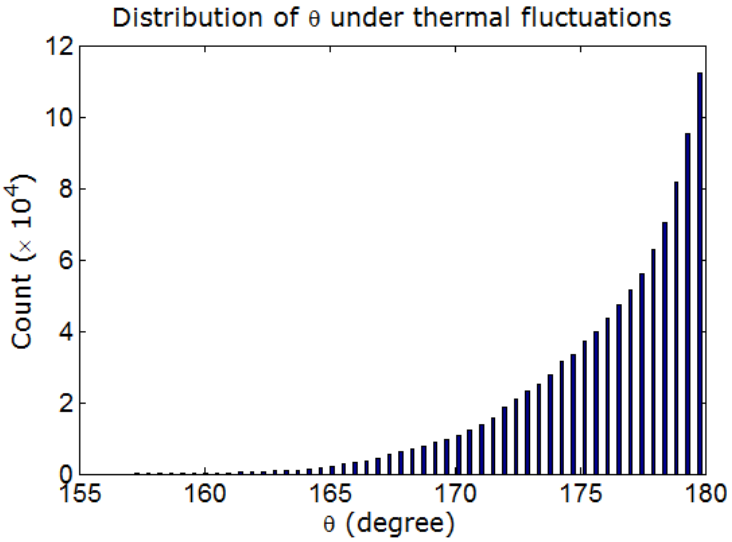

(a)

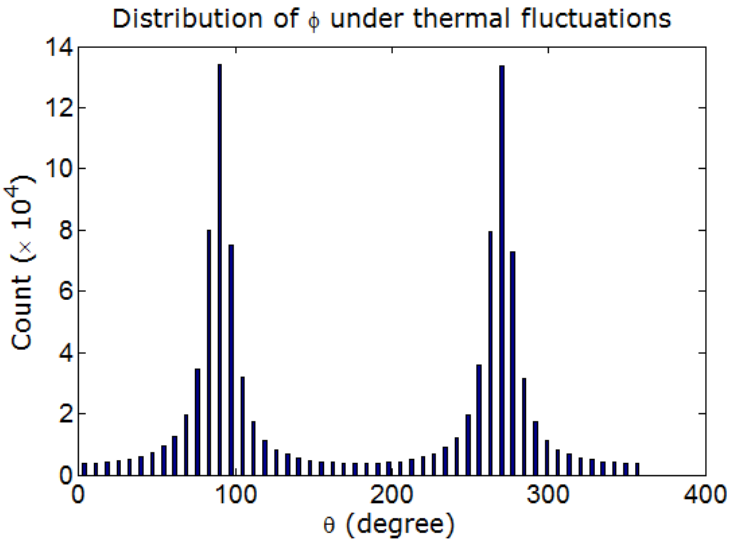

(b)

Figure 3.41: Distributions of polar angle $\theta_{initial}$ and azimuthal angle $\phi_{initial}$ due to thermal fluctuations at room temperature (300 K) for the Terfenol-D/PZT multiferroic nanomagnet. (a) Distribution of the polar angle $\theta_{initial}$. The mean of the distribution is ∼175°, while the most likely value is 180°. This is a nearly exponential distribution (Boltzmann-like). (b) Distribution of the azimuthal angle $\phi_{initial}$. These are two Gaussian distributions with peaks centered at 90° and 270° (or -90°), which means that the most likely location of the magnetization vector is in the plane of the nanomagnet.

The intial distribution of azimuthal angle, $\phi_{initial}$ as shown in the Fig. 3.41(b) shows two peaks centered at 90° and 270°, (or -90°). The positions of these peaks correspond to magnet's plane. The reasoning is obvious that these are the minimum energy positions in the potential landscape of the nanomagnet. However, room-temperature thermal agitations have caused magnetization sometimes to climb up the potential hill around and thus the initial orientation of the azimuthal angle of magnetization can be any value inside its whole range $(0°, 360°)$. Because of this reason, we must analyze magnetization's dynamics for any value in the ϕ-space.

Fig. 3.42 shows the magnetization dynamics for the Terfenol-D/PZT multiferroic nanomagnet with a fixed $\theta_{initial} = 175°$ and for the two in-plane values of azimuthal angle $\phi_{initial} = \pm 90°$. The initial deflection of θ is the mean value of the $\theta_{initial}$ distribution, however, thermal fluctuations are not considered *during switching* of the magnetization. The magnitude of stress is 10 MPa and the ramp duration is 60 ps. Since stress rotates the magnetization in $+\hat{\mathbf{e}}_\phi$-direction and stress can beat the in-plane shape-anisotropy energy barrier, ϕ increases with time and gets stabilized in the "good" quadrant $(90°, 180°)$ for $\phi_{initial} = +90°$ or in the other "good" quadrant $(270°, 360°)$ for $\phi_{initial} = 270°$ (note the flat regions of the ϕ-plots). The reasoning behind the same has been explained in Chapter 2 and in the previous sections. So both the motions (damped motion due to applied stress and the motion due to out-of-plane excursion depicted as $-2\alpha B(\phi) sin\theta cos\theta\, \hat{\mathbf{e}}_\theta$ and $-|B_{\phi e}(\phi)| sin\theta\, \hat{\mathbf{e}}_\theta$, respectively in the Fig. 2.8) of magnetization are in the $-\hat{\mathbf{e}}_\theta$ direction decreasing θ with time and the magnetization rotates in the correct direction towards $\theta = 90°$. When θ reaches 90°, the torque due to stress and shape anisotropy vanishes. At this point, we start to reverse the stress and the damped motion due to stress and shape anisotropy eventually becomes again in the $-\hat{\mathbf{e}}_\theta$ direction. That continues to rotate the magnetization in the right direction towards $\theta = 0°$, ending in successful switching. Slightly past 0.4 ns, continuing ϕ-rotation because of precessional motion due to stress and shape anisotropy pushes ϕ into a "bad" quadrant, but eventually it escapes into the other "good" quadrant. This brief excursion into the "bad" quadrant causes the ripple in $\theta(t)$ versus t. Note that the θ-motions in the two Figs. 3.42(a) and 3.42(b) are very similar and thus the switching delays are also same. This clearly depicts that the in-plane azimuthal angles ($\phi_{initial} = \pm 90°$) are contemporary in dictating the magnetization dynamics in θ-space.

Fig. 3.43 shows the magnetization dynamics for the Terfenol-D/PZT multiferroic nano-

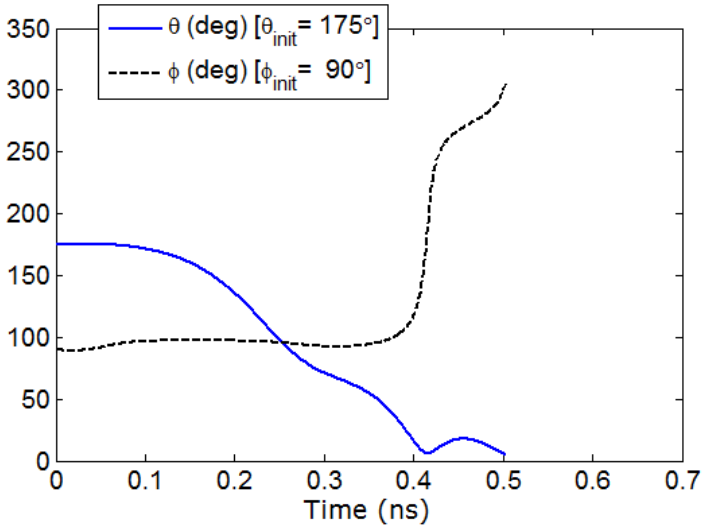

(a)

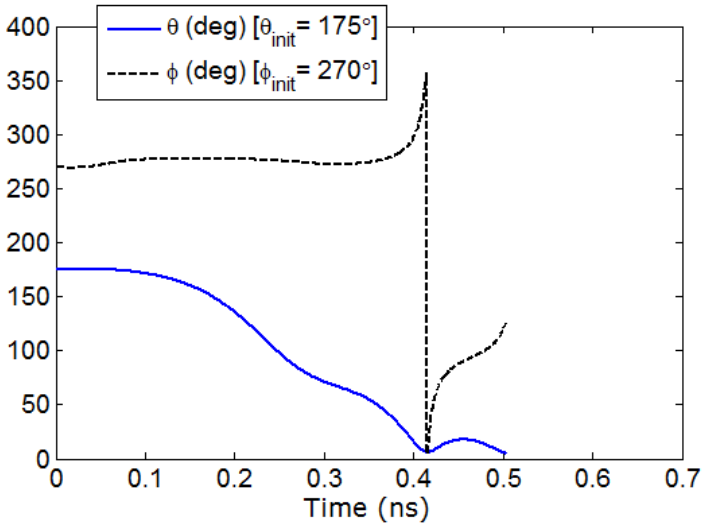

(b)

Figure 3.42: Temporal evolution of polar angle $\theta(t)$ and azimuthal angle $\phi(t)$ for a fixed $\theta_{initial} = 175°$ and two different values of $\phi_{initial} = \{90°, 270°\}$. The applied stress is 15 MPa and the ramp duration is 60 ps. Thermal fluctuations have been ignored during switching. (a) Temporal evolution when $\theta_{initial} = 175°$, $\phi_{initial} = 90°$. (b) Temporal evolution when $\theta_{initial} = 175°$, $\phi_{initial} = 270°$. Note that when θ reaches 90° or even earlier, ϕ always resides in the "good" quadrant $[(90°, 180°)$ or $(270°, 360°)]$, which makes the switching successful.

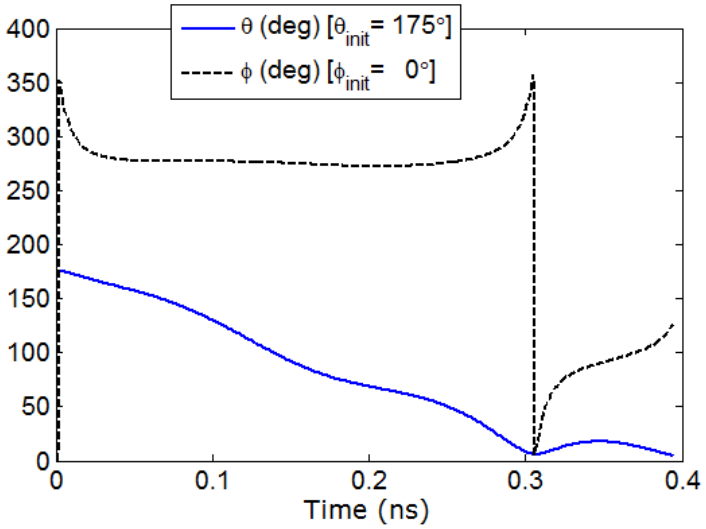

(a)

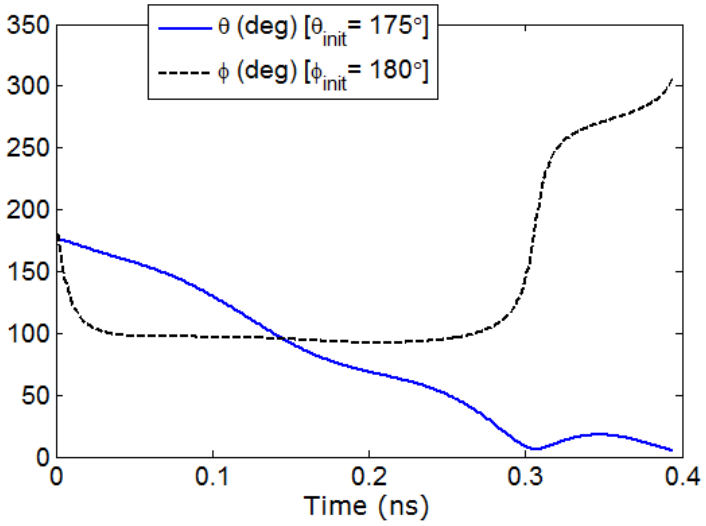

(b)

Figure 3.43: Temporal evolution of polar angle $\theta(t)$ and azimuthal angle $\phi(t)$ for a fixed $\theta_{initial} = 175°$ and four different values of $\phi_{initial} = \{0°, 180°\}$. The applied stress is 15 MPa and the ramp duration is 60 ps. Thermal fluctuations have been ignored during switching. (a) Temporal evolution when $\theta_{initial} = 175°$, $\phi_{initial} = 0°$. (b) Temporal evolution when $\theta_{initial} = 175°$, $\phi_{initial} = 180°$. Note that when θ reaches 90° or even earlier, ϕ always resides in the "good" quadrant $[(90°, 180°)$ or $(270°, 360°)]$, which makes the switching successful.

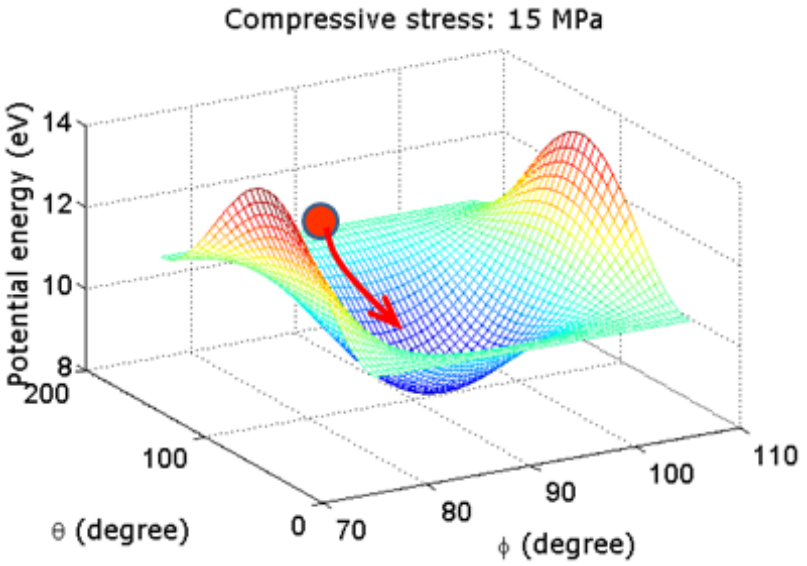

(a)

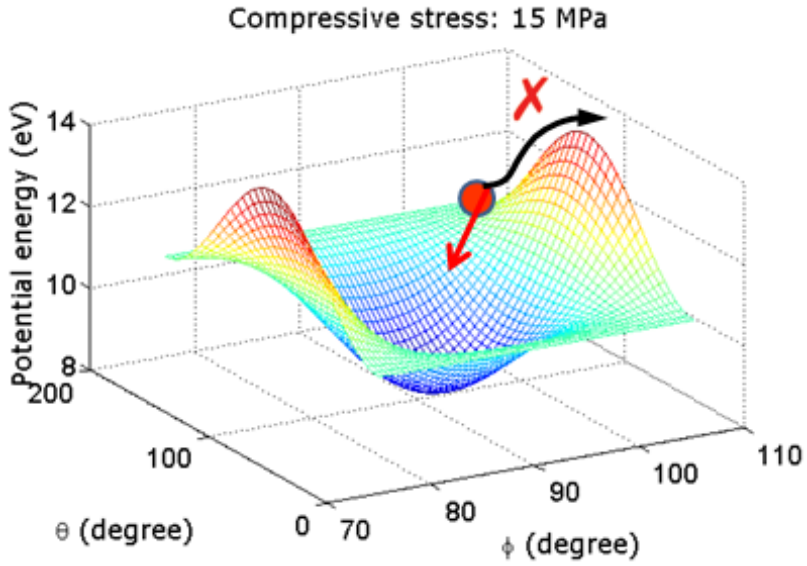

(b)

Figure 3.44: Illustration of magnetization's motion when magnetization is out-of-plane and the high shape-anisotropy energy barrier therein cannot be overcome by stress anisotropy. (a) Magnetization is in-plane of the magnet, where the potential landscape is inverted by the stress anisotropy and thus magnetization does not face a potential hill while starting to switch. (b) Magnetization is out-of-plane of the magnet, where the potential landscape cannot be inverted by the stress anisotropy and thus magnetization does face a potential hill at start. However, due to ϕ-motion of magnetization, it eventually surpasses the potential hill and comes near to magnet's plane, where from it can start switching in θ-space.

magnet with a fixed $\theta_{initial} = 175°$ and for the two *out-of-plane* values of azimuthal angle $\phi_{initial} = 0°$ and 180°. The intial deflection of θ is the mean value of the $\theta_{initial}$ distribution, however, thermal fluctuations are not considered *during switching* of the magnetization. Since the magnetization vector is initially lifted far out of the magnet's plane ($\phi_{initial} = 0°, 180°$), where the huge out-of-plane shape anisotropy energy barrier cannot be overcome by the stress anisotropy. This is depicted in Fig. 3.44. Thus, $B(\phi)$ becomes positive (as $|B_{stress}| < |B_0(\phi)|$) and magnetization precesses in the clockwise direction ($-\hat{\mathbf{e}}_\phi$) rather than in the anticlockwise direction ($+\hat{\mathbf{e}}_\phi$). Therefore ϕ decreases with time, which immediately takes magnetization inside a "good" quadrant and eventually $|B_{stress}|$ becomes greater than $|B_0(\phi)|$. Then ϕ assumes a stable value in a "good" quadrant (note the flat regions of the ϕ-plots). Afterwards, switching occurs similarly as for the cases described in the Fig. 3.42. Note that the θ-motions in the two Figs. 3.43(a) and 3.43(b) are very similar and thus the switching delays are also same. This clearly depicts that the out-of-plane azimuthal angles ($\phi_{initial} = \{0°, 180°\}$) are contemporary in dictating the magnetization dynamics in θ-space.

An interesting point would be to compare the switching delays in the Figs. 3.42 and 3.43. Note that the switching delay decreases by 0.1 ns when magnetization starts from out-of-plane than from in-plane. This is a very consequence of the reasoning that out-of-plane excursion of magnetization in the "good" quadrants aids magnetization moving faster in θ-space. When magnetization starts out-of-plane, magnetization spends more time deep inside a "good" quadrant; hence, switching gets faster than that of the case when magnetization starts in-plane of the magnet.

Fig. 3.45 shows the statistical distributions of different quantities when 15 MPa stress is applied with 60 ps ramp duration on the magnet at room temperature (300 K) for the magnetization in Terfenol-D/PZT multiferroic nanomagnet. The wide distribution in Fig. 3.45(a) is caused by: (1) the initial angle distributions in Fig. 3.41 and (2) thermal fluctuations *during the transition* from some $\theta = \theta_{initial}$ to 90°. We do need to tackle such distribution by keeping the magnetization out-of-plane far enough, otherwise, we can use a sensing circuitry to detect when θ reaches around 90°, so that we can ramp down the stress thereafter. The sensing circuitry can be implemented with a spin-valve measurement of the magnetization. Such sensing circuitry is not uncommon in electronic circuits [211]. Some tolerance is nonetheless required

since the sensing circuitry cannot be perfect. Our simulation shows that the internal dynamics works correctly as long as the stress is ramped down when θ is in the interval [85°, 110°], i.e. it does not have to be exactly 90°. If magnetization reaches at $\theta = 90°$ (even past it) and stress is not withdrawn soon enough, then magnetization can end up at $\phi = \pm 90°$ (potential energy minima), upon which the success probability would be 50% since thermal fluctuations can put it in either direction of the potential landscape. Thus, we take advantage of such non-equilibrium scenario for which a sufficiently high magnitude of stress and a sufficiently fast ramp rate are necessary. In Fig. 3.45(b), note that ϕ always resides in the "good" quadrant [$(90°, 180°)$ or $(270°, 360°)$] when θ reaches 90°. A sufficiently high stress and a sufficiently fast ramp rate are required to ensure that ϕ is in the "good" quadrants, which is conducive to successful switching.

As the magnetization leaves from $\theta = 90°$ towards $\theta \simeq 0°$ and stress is ramped down, the torque due to stress tries to rotate the azimuthal angle ϕ of magnetization *clockwise* rather than anticlockwise (mathematically note that $cos\,\theta$ is positive for $90° \geq \theta \geq 0°$ and $B(\phi)$ is still negative when stress has not been brought down significantly, i.e., still $|B_{stress}| > |B_0(\phi)|$). For a *slow ramp-rate* this rotation may be considerable and magnetization can stray into "bad" quadrants. Moreover, thermal fluctuations can aggravate the scenario. Switching may impede and magnetization vector can backtrack towards where it started ($\theta \simeq 180°$) causing a switching failure. In this way, switching failure may happen even after the magnetization has crossed the hard axis ($\theta = 90°$) towards its destination ($\theta \simeq 0°$). This is why it does need a fast enough ramp rate during the ramp-down phase of stress. Note that when the potential landscape gets inverted from its unperturbed position (between the instants of time t_0 and t_1 in Fig. 2.9), the effect of thermal fluctuations does not matter since it can only delay the magnetization to come at $\theta = 90°$.

Straying into a "bad" quadrant for azimuthal angle ϕ during the ramp-down phase does not necessarily mean that the magnetization would fail to switch. Particularly if magnetization is close to its destination $\theta \simeq 0°$, the shape anisotropy torque alongwith the *negative* stress anisotropy torque (since stress is *reversed*) would have enough control to bring the magnetization back to the other "good" quadrant for ϕ and complete the switching. Thus, there may be ripples appearing in the magnetization dynamics at the end of switching, which is because of the transition of azimuthal angle ϕ between two "good" quadrants through one "bad" quadrant.

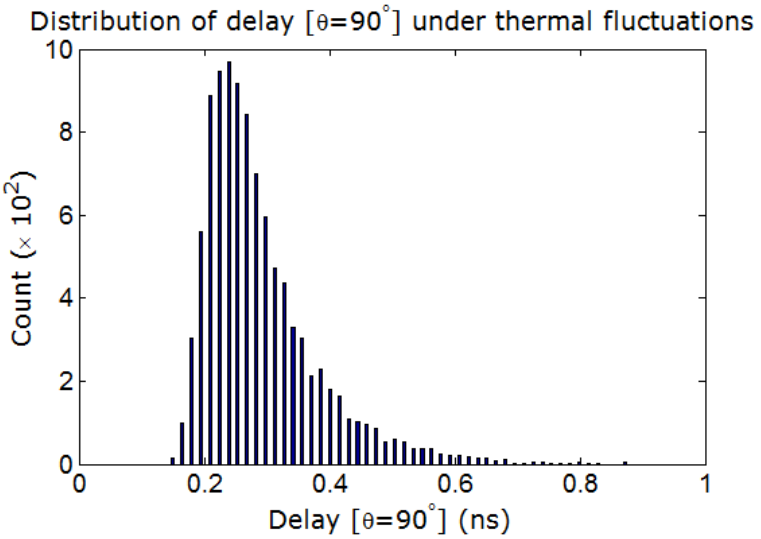

(a)

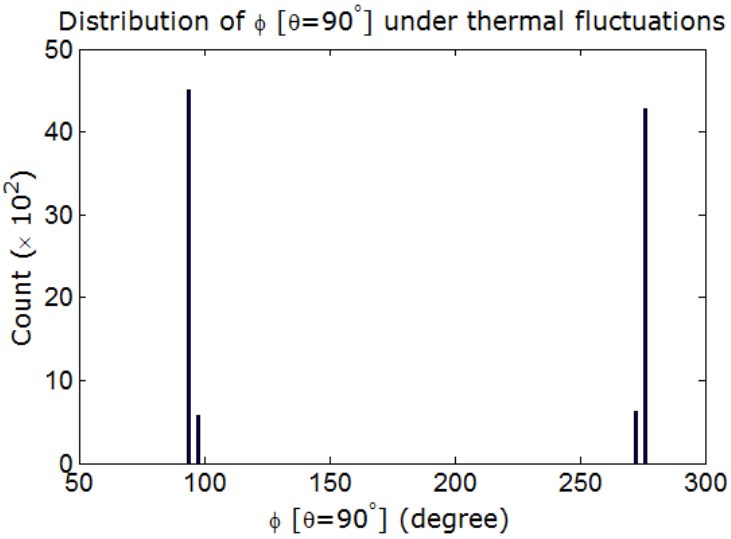

(b)

Figure 3.45: Statistical distributions of different quantities when 15 MPa stress is applied with 60 ps ramp duration on the magnet at room temperature (300 K). (a) Distribution of time taken for θ to reach 90° starting from ($\theta_{initial}$,$\phi_{initial}$) where the latter are picked from the distributions in the presence of thermal fluctuations (see Fig. 3.41). (b) Distribution of azimuthal angle ϕ when θ reaches 90°. Note that ϕ always resides in the "good" quadrant [(90°, 180°) or (270°, 360°)] and has a fairly narrow distribution.

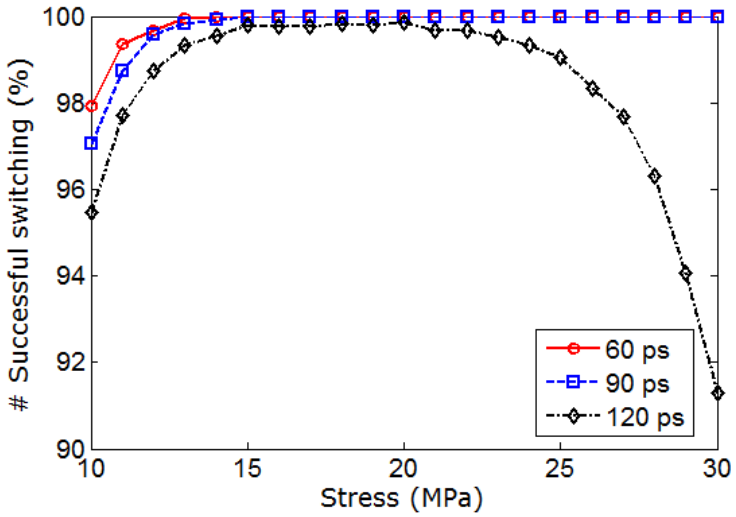

Figure 3.46: Percentage of successful switching events at room temperature (300 K) in a Terfenol-D/PZT multiferroic when subjected to stress between 10 MPa and 30 MPa for ramp durations of 60 ps, 90 ps, and 120 ps. The critical stress at which switching becomes ∼100% successful increases with ramp duration. However, at high ramp duration (e.g., 120 ps), we may not achieve ∼100% switching probability for any values of stress and stress-dependence of the success probability becomes non-monotonic.

Therefore, we require the following two criteria for successful switching without creating any asymmetry in the potential landscape even in the presence of thermal fluctuations: (1) a high enough stress that keeps the magnetization more out-of-plane inside the "good" quadrants; and (2) a fast enough ramp rate that reduces the possibility of backtracking of magnetization while it is crossing (or even after crossing) the hard axis ($\theta = 90°$) towards its destination. A high stress and a fast ramp rate also increase the switching speed and surpass the detrimental effects of thermal fluctuations.

Fig. 3.46 shows the switching probability for different values of stress (10-30 MPa) and ramp durations (60 ps, 90 ps, 120 ps) at room temperature (300 K). A moderately large number (10,000) of simulations were performed for each value of stress and ramp duration to generate these results. Initial angle distributions at 300 K for both θ and ϕ are taken into account during simulations. The minimum stress needed to switch the magnetization at 0 K is ∼5 MPa, but the minimum stress needed to ensure switching at 300 K is ∼14 MPa for 60 ps ramp duration and ∼17 MPa for 90 ps ramp duration. For 120 ps ramp duration, ∼100% success probability is unattainable for any values of stress since thermal agitations have higher latitude to divert the magnetization in wrong direction while stress is ramped down; at higher stresses

accompanied by a high ramp duration, there occurs higher out-of-plane excursion pushing the magnetization in "bad" quadrants, which further aggravates the error probability. The plots of switching delays and energy dissipations for different stress levels and ramp durations would be provided in the next section (Section 3.4) after the application of a bias field as described in Chapter 2.

We will describe some illustrative dynamics of magnetization in the presence of thermal fluctuations from a wide-range of possible dynamics for the Terfenol-D/PZT multiferroic nanomagnet. Fig. 3.47 shows the magnetization dynamics for the Terfenol-D/PZT multiferroic nanomagnet in the presence of thermal fluctuations when magnetization start nearly from magnetization's plane. Note that for the case in Fig. 3.47(a), magnetization starts in the "bad" quadrant $(0°, 90°)$, however, stress is able to shift the magnetization in the nearby "good" quadrant $(90°, 180°)$ and thus the out-of-plane excursion of magnetization aids switching in the correct direction. On the other hand, note that for the case in Fig. 3.47(b), magnetization starts in the "good" quadrant $(270°, 360°)$ itself and it stays in that quadrant when θ reaches $90°$. The switching occurs in a similar way as in the previous case. In both the plots, note that at the end of magnetization dynamics after switching is completed, the azimuthal angle ϕ is traversing through its range $(0°, 360°)$ repeated times, which simply happens because magnetization is moving around the north pole in a small cone ($\theta \simeq 0°$) due to thermal fluctuations. Similar signatures would be also visible in the several curves that include thermal fluctuations.

Fig. 3.48 shows the magnetization dynamics for the Terfenol-D/PZT multiferroic nanomagnet in the presence of thermal fluctuations when magnetization starts out-of-plane of the magnet. Note that for both cases ($\phi_{initial} \simeq 0°$ and $\phi_{initial} \simeq 180°$), magnetization rotates *clockwise* in the out-of-plane direction as stress anisotropy cannot overcome the high out-of-plane shape-anisotropy energy barrier. Accordingly, magnetization comes inside the "good" quadrant $(90°, 180°)$ or $(270°, 360°)$ and switching is accelerated. Magnetization becomes stable in the "good" quadrants and switching occurs successfully.

Fig. 3.49 shows the magnetization dynamics for the Terfenol-D/PZT multiferroic nanomagnet in the presence of thermal fluctuations when magnetization starts from $\phi_{initial} \simeq 270°$ but traverses towards $\phi \simeq 90°$. Note from the θ-dynamics curve that magnetization has initially backtracked towards $\theta \simeq 180°$ while stress was ramped up and also when magnetization sit-

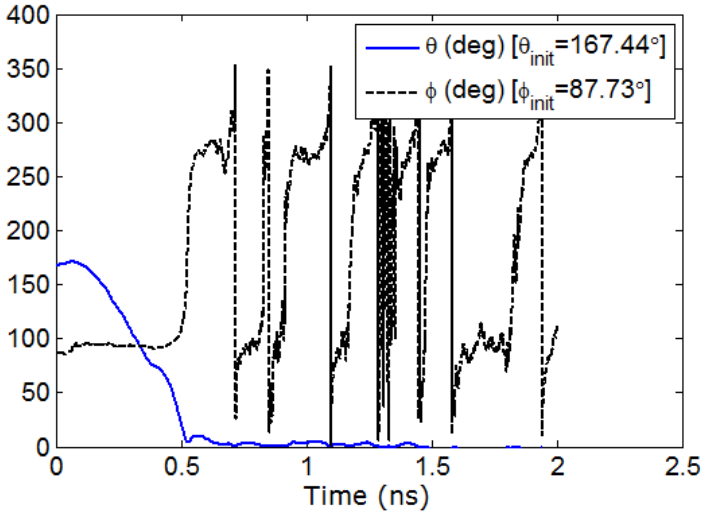

(a)

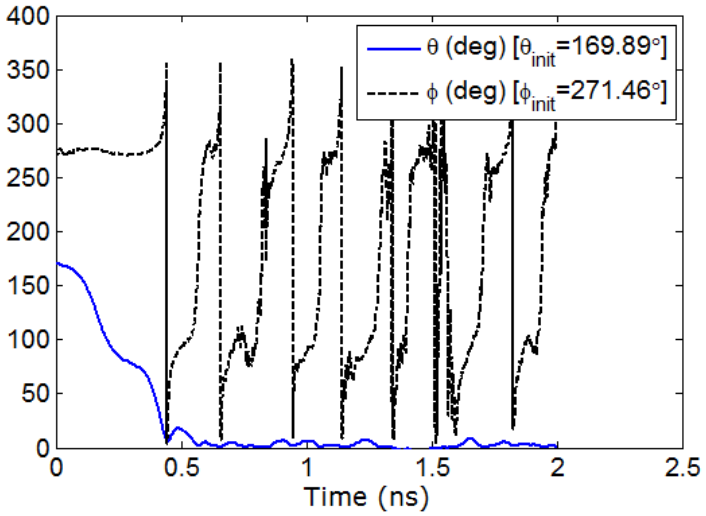

(b)

Figure 3.47: Temporal evolution of polar angle $\theta(t)$ and azimuthal angle $\phi(t)$ of magnetization in the presence of thermal fluctuations for the Terfenol-D/PZT multiferroic nanomagnet when magnetization starts nearly from magnet's plane. The applied stress is 10 MPa and the ramp duration is 60 ps. Thermal fluctuations are considered both at the very beginning of the switching and also during the switching. (a) Temporal evolution when $\phi_{initial} \simeq 90°$. (b) Temporal evolution when $\phi_{initial} \simeq 270°$. Note that when θ reaches 90°, ϕ always resides in the "good" quadrant $[(90°, 180°)$ or $(270°, 360°)]$, which makes the switching successful.

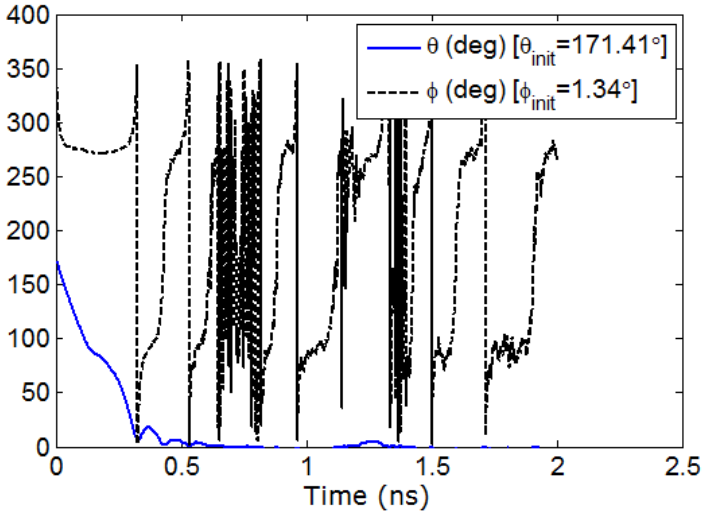

(a)

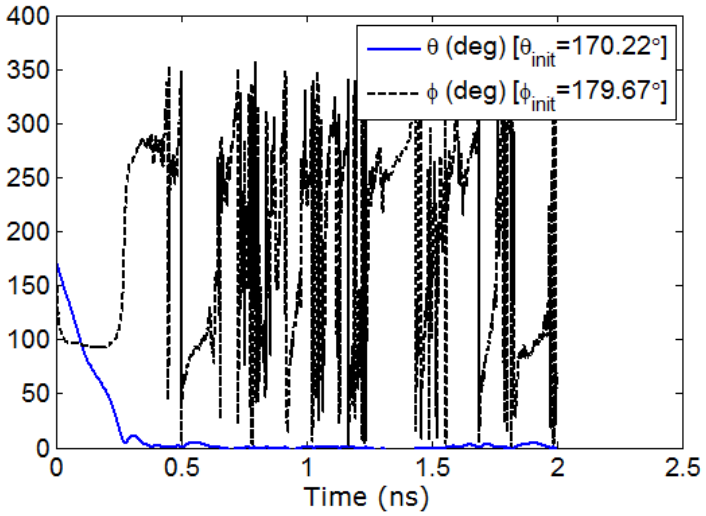

(b)

Figure 3.48: Temporal evolution of polar angle $\theta(t)$ and azimuthal angle $\phi(t)$ of magnetization in the presence of thermal fluctuations for the Terfenol-D/PZT multiferroic nanomagnet when magnetization starts out-of-plane of the magnet. The applied stress is 10 MPa and the ramp duration is 60 ps. Thermal fluctuations are considered both at the very beginning of the switching and also during the switching. (a) Temporal evolution when $\phi_{initial} \simeq 0°$. (b) Temporal evolution when $\phi_{initial} \simeq 180°$. Note that when θ reaches 90°, ϕ always resides in the "good" quadrant $[(90°, 180°)$ or $(270°, 360°)]$, which makes the switching successful.

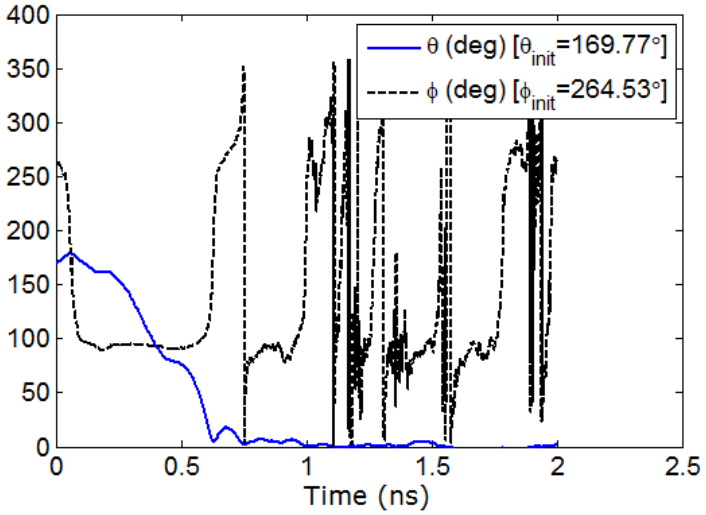

Figure 3.49: Temporal evolution of polar angle $\theta(t)$ and azimuthal angle $\phi(t)$ of magnetization in the presence of thermal fluctuations for the Terfenol-D/PZT multiferroic nanomagnet when magnetization starts from $\phi_{initial} \simeq 270°$ but traverses towards $\phi \simeq 90°$. The applied stress is 10 MPa and the ramp duration is 60 ps. Thermal fluctuations are considered both at the very beginning of the switching and also during the switching. Note that when θ reaches 90°, ϕ always resides in the "good" quadrant $(90°, 180°)$, which makes the switching successful.

uated in the "bad" quadrant $(180°, 270°)$. Eventually, magnetization comes into the "good" quadrant $(90°, 180°)$ to aid switching and magnetization switches successfully onwards.

Fig. 3.50 shows the magnetization dynamics for the Terfenol-D/PZT multiferroic nanomagnet in the presence of thermal fluctuations when magnetization starts in a "good" quadrant but delayed long due to thermal fluctuations. Note that when θ reaches 90°, ϕ resides in the "good" quadrant $(270°, 360°)$ but *very near* at magnet's plane, which makes the switching past $\theta = 90°$ lengthy, albeit successful.

Fig. 3.51 shows the magnetization dynamics for the Terfenol-D/PZT multiferroic nanomagnet in the presence of thermal fluctuations when magnetization start nearly from magnetization's plane for long ramp duration of 120 ps. Note that for both of the cases magnetization has gone past $\theta = 90°$ towards $\theta \simeq 0°$ before backtracking temporarily towards $\theta = 90°$. This happens more due to long ramp duration (rather than due to thermal fluctuations) when magnetization rotates clockwise in out-of-plane direction and pushed into "bad" quadrants temporarily. After stress is brought down significantly during the long ramp duration magnetization is again pushed into a "good" quadrant and switching completes successfully. Thermal fluctuations can however aggravate the scenario and switching may fail, which we will exemplify

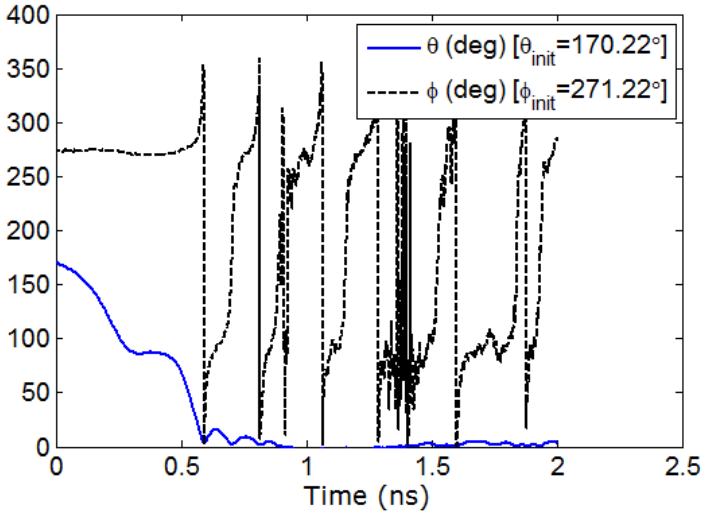

Figure 3.50: Temporal evolution of polar angle $\theta(t)$ and azimuthal angle $\phi(t)$ of magnetization in the presence of thermal fluctuations for the Terfenol-D/PZT multiferroic nanomagnet when magnetization starts in a "good" quadrant $(270°, 360°)$ and around magnet's plane ($\phi_{initial} \simeq 270°$) but still it takes a long time to switch past $\theta = 90°$ due to thermal agitations. The applied stress is 10 MPa and the ramp duration is 60 ps.

later on.

Fig. 3.52 shows the magnetization dynamics for the Terfenol-D/PZT multiferroic nanomagnet in the presence of thermal fluctuations when magnetization starts in a "good" quadrant but delayed long due to long ramp duration and thermal fluctuations. Note that when θ reaches 90°, ϕ resides in the "good" quadrant $(90°, 180°)$ but *very near* at magnet's plane, which makes the switching past $\theta = 90°$ lengthy, albeit successful.

Fig. 3.53 shows the magnetization dynamics for the Terfenol-D/PZT multiferroic nanomagnet in the presence of thermal fluctuations when switching fails as magnetization slips into "bad" quadrants while crossing the hard axis ($\theta = 90°$). The applied stress is 10 MPa and the ramp duration is 60 ps. Since the ramp duration is short enough, these switching failures are caused by thermal fluctuations apparently. When the polar angle θ reaches 90°, the azimuthal angle ϕ has ventured into the "bad" quadrant (0°,90°) or (180°,270°). Thus, switching eventually fails. This is why we do require a high enough stress to keep the magnetization out-of-plane far enough in the "good" quadrants, which is conducive to success.

Fig. 3.54 shows the magnetization dynamics for the Terfenol-D/PZT multiferroic nanomagnet in the presence of thermal fluctuations when switching fails as magnetization slips into "bad" quadrants while crossing the hard axis ($\theta = 90°$) for 30 MPa applied stress and 120 ps

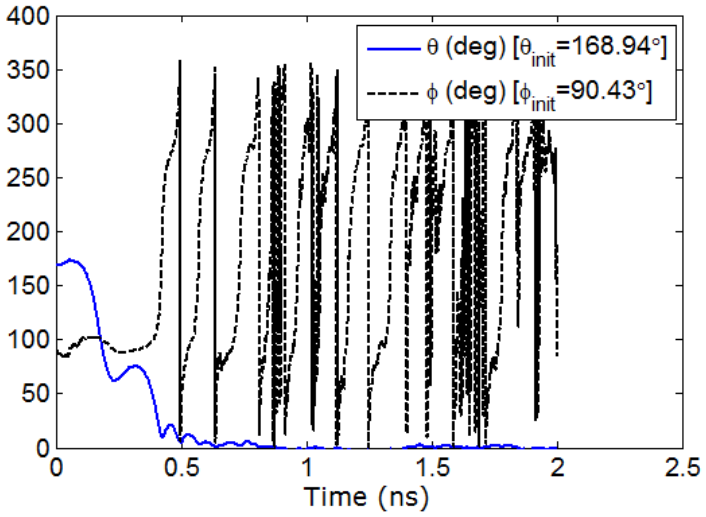

(a)

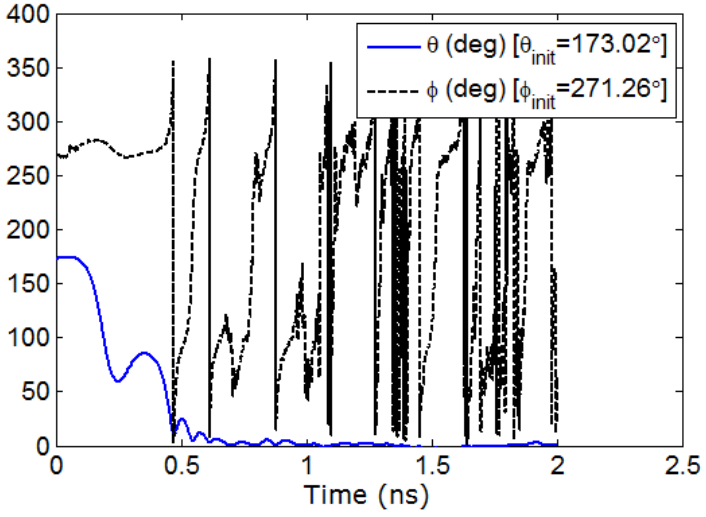

(b)

Figure 3.51: Temporal evolution of polar angle $\theta(t)$ and azimuthal angle $\phi(t)$ of magnetization in the presence of thermal fluctuations for the Terfenol-D/PZT multiferroic nanomagnet when magnetization starts nearly from magnet's plane for long ramp duration. The applied stress is 30 MPa and the ramp duration is 120 ps. Thermal fluctuations are considered both at the very beginning of the switching and also during the switching. (a) Temporal evolution when $\phi_{initial} \simeq 90°$. (b) Temporal evolution when $\phi_{initial} \simeq 270°$. Note that when θ reaches 90°, ϕ always resides in the "good" quadrant $[(90°, 180°)$ or $(270°, 360°)]$, which makes the switching successful.

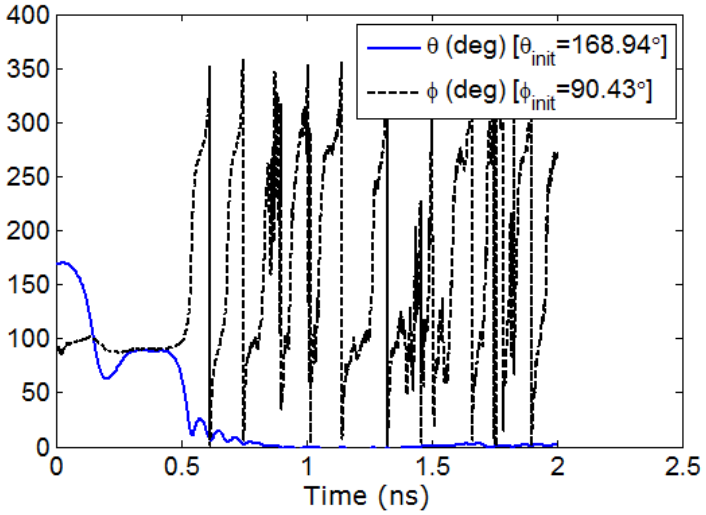

Figure 3.52: Temporal evolution of polar angle $\theta(t)$ and azimuthal angle $\phi(t)$ of magnetization in the presence of thermal fluctuations for the Terfenol-D/PZT multiferroic nanomagnet when magnetization starts in a "good" quadrant $(90°, 180°)$ and around magnet's plane ($\phi_{initial} \simeq 270°$) but still it takes a long time to switch past $\theta = 90°$ due to long time duration and thermal agitations. The applied stress is 30 MPa and the ramp duration is 120 ps.

ramp duration. This happens more due to long ramp duration (rather than due to thermal fluctuations) when magnetization rotates clockwise in out-of-plane direction and pushed into "bad" quadrants. Therefore magnetization backtracks. A high stress makes such situation worse during the long ramp-down phase. Thermal fluctuations have also ample opportunity to scuttle the switching by bringing ϕ into the "bad" quadrants during long ramp-down phase. When the polar angle θ reaches 90°, the azimuthal angle ϕ has ventured into a "bad" quadrant (0°,90°) or (180°,270°). Thus, switching eventually fails.

Fig. 3.55 shows the magnetization dynamics for the Terfenol-D/PZT multiferroic nanomagnet in the presence of thermal fluctuations when magnetization comes into a "good" quadrant even after starting from a "bad" quadrant, but eventually fails to switch successfully. The azimuthal angle of magnetization traverses from the "bad" quadrant $(180°, 270°)$ to the "good" quadrant $(90°, 180°)$ because the 10 MPa or even a 30 MPa stress is not sufficient to invert the out-of-plane ($\sim 9°$ deflection from in-plane, see the $\phi_{initial}$ values) energy barrier. However when magnetization comes close to 90°, it is mainly the thermal fluctuations for the case of 60 ps ramp duration that causes magnetization to slip into the other 'bad" quadrant $(0°, 90°)$ when θ reaches 90° [see Fig. 3.55(a)]. In Fig. 3.55(b), for the case of 120 ps ramp duration, switching of magnetization fails because long ramp duration is detrimental to switching failure

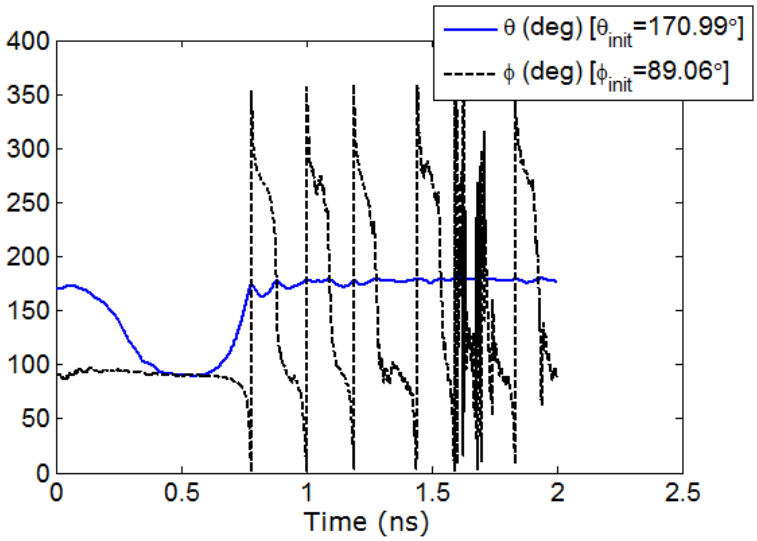

(a)

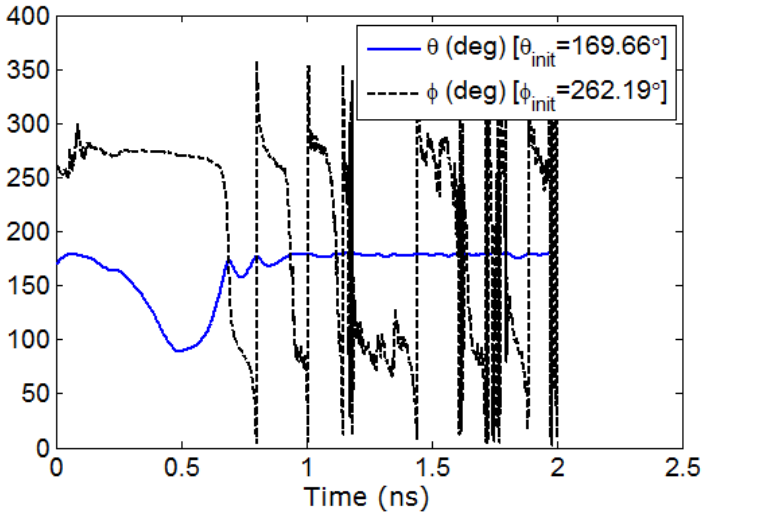

(b)

Figure 3.53: Temporal evolution of the polar angle $\theta(t)$ and azimuthal angle $\phi(t)$ when magnetization fails to switch due to traversing into "bad" quadrants for long ramp duration while crossing the hard axis ($\theta = 90°$) and backtracks to the initial state. The applied stress is 10 MPa and the ramp duration is 60 ps. (a) Temporal evolution when $\phi_{initial} \simeq 90°$. (b) Temporal evolution when $\phi_{initial} \simeq 270°$. Note that when θ reaches 90°, ϕ slips into "bad" quadrants $[(0°, 90°)$ or $(180°, 270°)]$, which causes the switching failures.

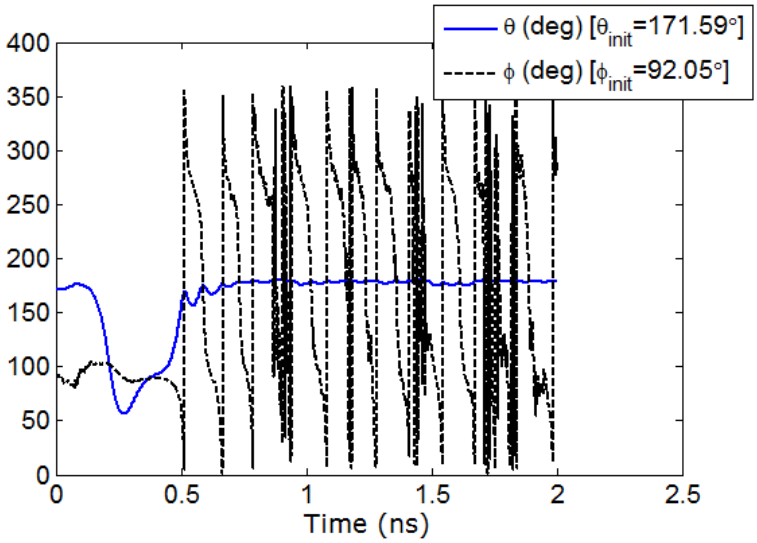

(a)

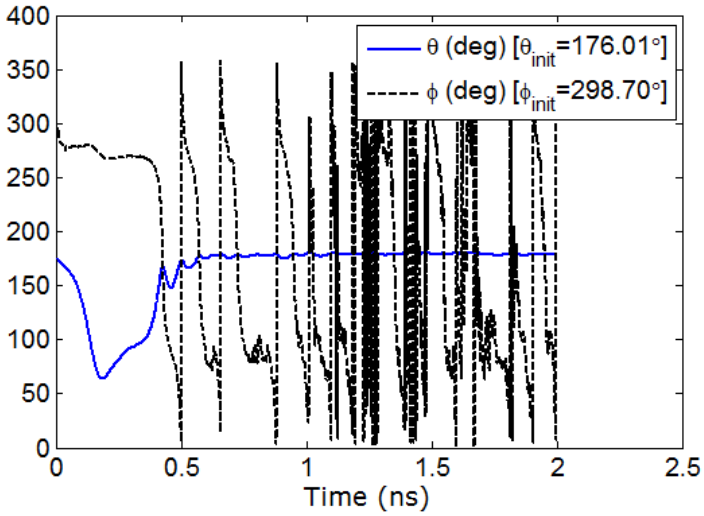

(b)

Figure 3.54: Temporal evolution of the polar angle $\theta(t)$ and azimuthal angle $\phi(t)$ when magnetization fails to switch due to traversing into "bad" quadrants while crossing the hard axis ($\theta = 90°$) and backtracks to the initial state. The applied stress is 30 MPa and the ramp duration is 120 ps. (a) Temporal evolution when $\phi_{initial} \simeq 90°$. (b) Temporal evolution when $\phi_{initial} \simeq 270°$. Note that when θ reaches 90°, ϕ slips into a "bad" quadrant [$(0°, 90°)$ or $(180°, 270°)$], which causes the switching failures.

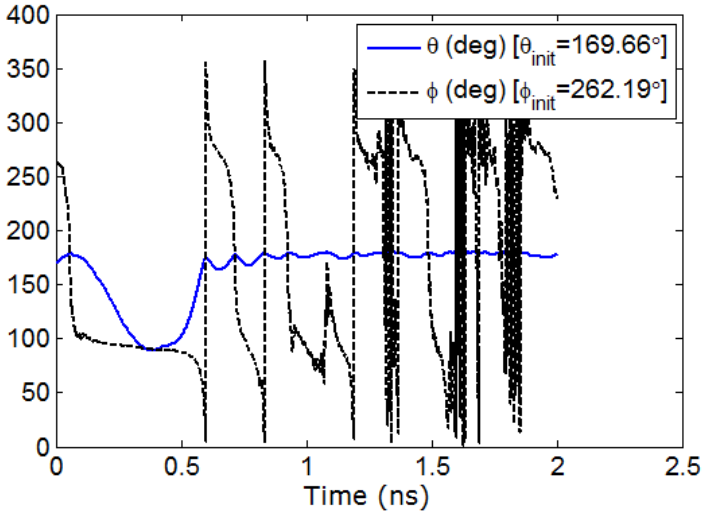

(a)

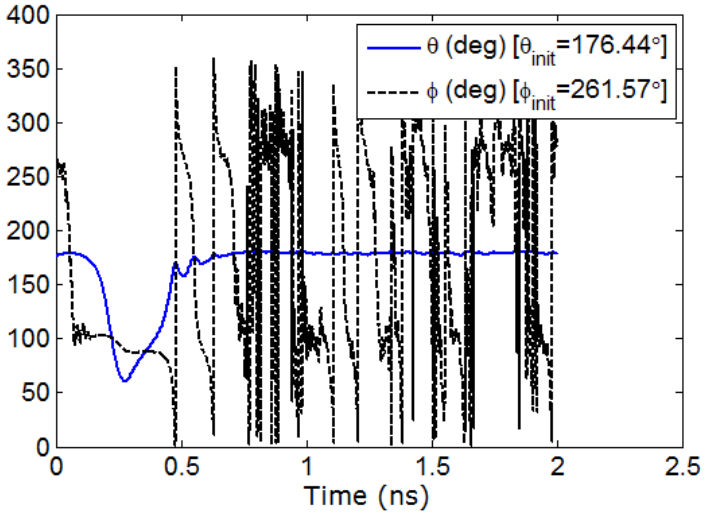

(b)

Figure 3.55: Temporal evolution of the polar angle $\theta(t)$ and azimuthal angle $\phi(t)$ when magnetization comes into a "good" quadrant even after starting from a "bad" quadrant, but incidentally fails to switch successfully. (a) The applied stress is 10 MPa and the ramp duration is 60 ps. (b) The applied stress is 30 MPa and the ramp duration is 120 ps. Note that when θ reaches 90°, ϕ slips into "bad" quadrants [$(0°, 90°)$ or $(180°, 270°)$], which causes the switching failures.

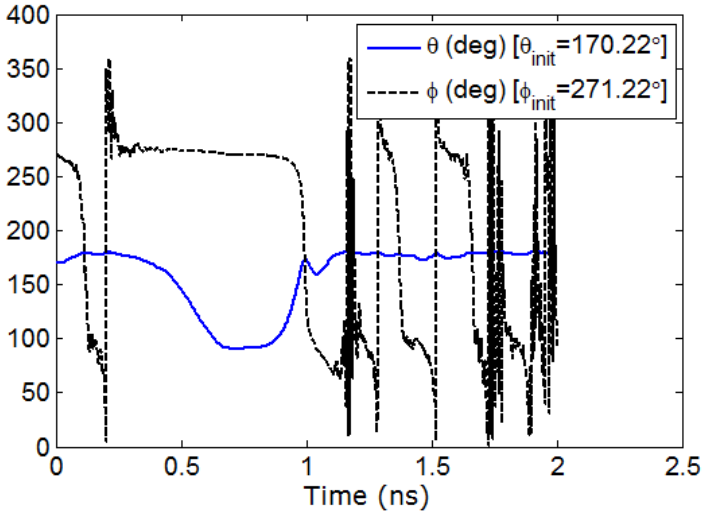

Figure 3.56: Temporal evolution of polar angle $\theta(t)$ and azimuthal angle $\phi(t)$ of magnetization in the presence of thermal fluctuations for the Terfenol-D/PZT multiferroic nanomagnet when magnetization starts in a "good" quadrant but performs a complete rotation in ϕ-space before getting stabilized in the same "good quadrant, however, incidentally switching fails to happen. The applied stress is 10 MPa and the ramp duration is 60 ps. Note that when θ reaches 90°, ϕ slips into the "bad" quadrant $(180°, 270°)$, which causes the switching failure.

as we have explained earlier and also thermal fluctuations may have aggravated the scenario.

Finally, the Fig. 3.56 shows an unusual dynamics of magnetization. It started very close to magnet's plane ($\phi_{inititial} \simeq 270°$) in the "good" quadrant $(270°, 360°)$, but due to thermal fluctuations, it has started rotating out-of-plane clockwise rather than anticlockwise. Thus, magnetization initially backtracks towards $\theta = 180°$. Eventually, it surpasses the "bad" quadrant $(180°, 270°)$ and comes into the other "good" quadrant $(90°, 180°)$ making magnetization to traverse into the correct direction. After that magnetization rotates into another "bad" quadrant $(0°, 90°)$ and magnetization slightly backtracks. However, after one complete rotation, magnetization becomes stable in the "good" quadrant $(270°, 360°)$. When θ reaches 90°, magnetization counters thermal fluctuations to retain itself in the "good" quadrant for a period of time but eventually slips into the nearby "bad" quadrant and thus switching fails.

We have exemplified that magnetization can experience an wide range of dynamics due to thermal fluctuations accompanied by ramp rate effects. A fast enough ramp and a high enough stress are conducive to success and would increase switching probability in a directed way. In the next section, we will provide simulation results after the application of a bias field to reduce the extent of tail in switching delay distribution as described in Chapter 2.

3.4 Out-of-plane bias field

In this section, we will consider the effect of an out-of-plane bias field on top of considering thermal fluctuations and ramp rate effects while analyzing distribution of magnetization's initial orientation, magnetization dynamics, and switching delay-energy metrics [171]. The magnitude of out-of-plane bias magnetic field is of flux density 40 mT and it is applied in the $+x$-direction. We will consider room-temperature thermal fluctuations and analyze the magnetization dynamics by numerically solving the coupled θ- and ϕ-dynamics as derived in Equations (2.48) and (2.49) in Section 2.4. These equations are derived by adding the effect of out-of-plane bias field to stochastic LLG dynamics as in Equations (2.41) and (2.42).

The same material parameters and dimensions of the magnetostricitve layer as in the Table 3.2 would be used. We will use the PZT as piezoelectric layer with the same parameters used in the previous section and would consider linear stress-voltage relationship as we have assumed in all the previous simulations. The strain-voltage relationship in PZT is actually *superlinear* since d_{31} increases with electric field [212]. Hence, the voltage needed to produce 500 ppm strain in the Terfenol-D layer will be *less* than 66.7 mV. Throughout this paper, we have assumed a linear strain-voltage relationship and assumed the low-field value of d_{31}. This will result in overestimation of the voltage needed to generate a given strain in the Terfenol-D layer and also overestimation of the energy dissipation. Thus, our energy dissipation estimates will be pessimistic rather than optimistic.

We assume that when a compressive stress is applied to initiate switching, the magnetization vector starts out from near the south pole ($\theta \simeq 180^\circ$) with a certain ($\theta_{initial}$,$\phi_{initial}$) picked from the initial angle distributions at the given temperature. Stress is ramped up linearly and kept constant until the magnetization reaches the plane defined by the in-plane and the out-of-plane hard axis (i.e. the x-y plane, $\theta = 90^\circ$). This plane is always reached sooner or later since the energy minimum of the stressed magnet in θ-space is at $\theta = 90^\circ$. As soon as the magnetization reaches the x-y plane, the stress is ramped down at the same rate at which it was ramped up, and reversed in magnitude to aid switching. The magnetization dynamics ensures that θ continues to rotate towards 0° with very high probability. When θ becomes $\leq 5^\circ$, switching is deemed to have completed. A moderately large number (10,000) of simulations, with their

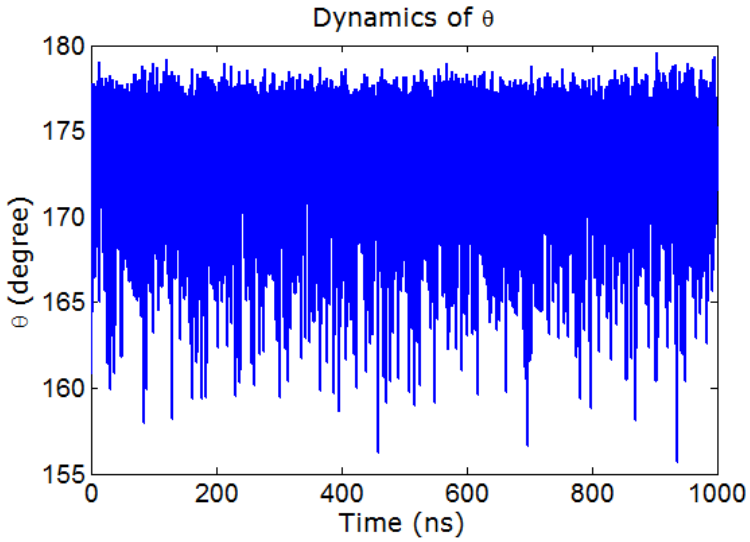

Figure 3.57: Magnetization fluctuates due to room-temperature (300 K) thermal agitations for the Terfenol-D/PZT multiferroic nanomagnet in unstressed condition, when a magnetic field of flux density 40 mT is applied along the out-of-plane hard axis (+x-direction).

corresponding ($\theta_{initial}$,$\phi_{initial}$) picked from the initial angle distributions, are performed for each value of stress and ramp duration to generate the simulation results in this section.

Fig. 3.57 shows that magnetization in the Terfenol-D/PZT multiferroic nanomagnet in unstressed condition is fluctuating due to room-temperature (300 K) thermal agitations, when a magnetic field of flux density 40 mT is applied along the out-of-plane hard axis (+x-direction). Note that magnetization's minimum energy positions in θ-space of its potential landscape are still $\theta = 0°$ and 180°, but in ϕ-space, the minimum energy positions are deflected about 3° [from ±90° to ±87°, see Equation (2.50)]. Thermal fluctuations at room-temperature has created a distribution of $\theta_{initial}$, but the most probable orientation of magnetization has got shifted from $\theta = 180°$. The simulation period for this result is chosen to be 1000 ns, which is long enough as simulating for longer period of times did not change the mean of the corresponding distribution.

Fig. 3.58 shows the distributions of initial angles $\theta_{initial}$ and $\phi_{initial}$ in the presence of thermal fluctuations when a bias magnetic field of flux density 40 mT is applied along the out-of-plane direction (+x-axis). The latter has shifted the peak of $\theta_{initial}$ from the easy axis ($\theta = 180°$) as can be noticed in the Fig 3.58(a). In Fig. 3.58(b), the $\phi_{initial}$ distribution has two peaks and resides mostly within the interval $[-90°, +90°]$ since the bias magnetic field is applied in the +x-direction. Because the magnetization vector starts out from near the south pole ($\theta \simeq 180°$) when stress is turned on, the effective torque on the magnetization $[-|\gamma|/(1+\alpha^2)\,\mathbf{M}\times\mathbf{H}$, where

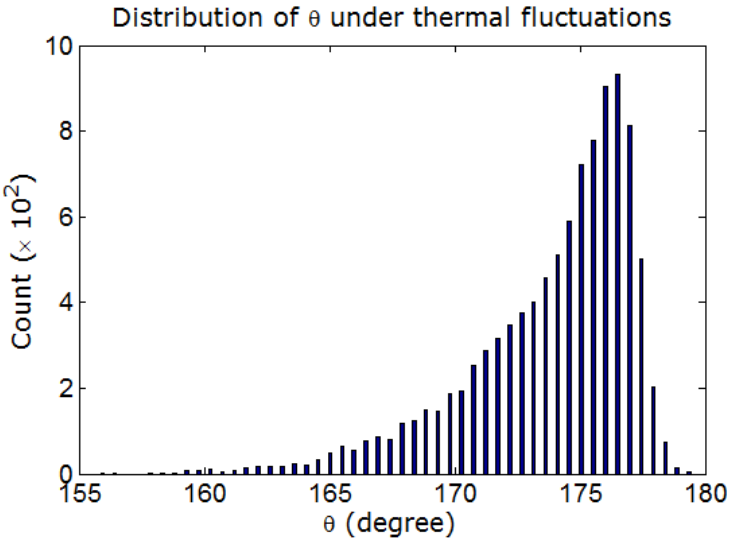

(a)

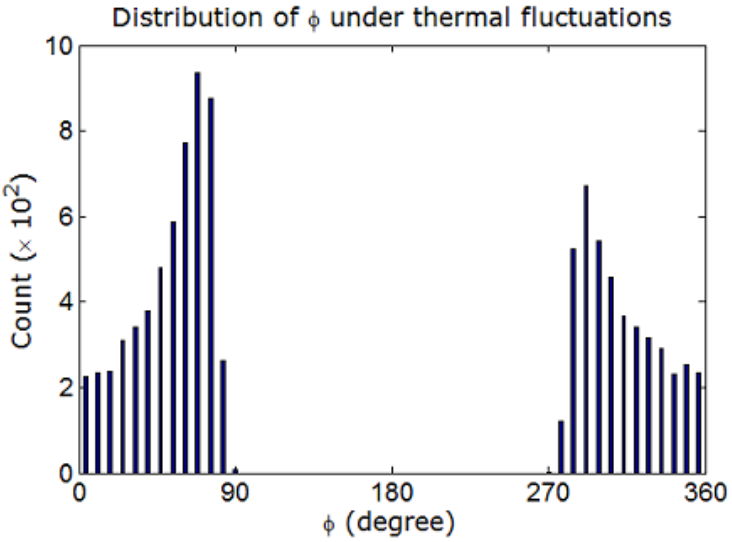

(b)

Figure 3.58: Distributions of polar angle $\theta_{initial}$ and azimuthal angle $\phi_{initial}$ due to thermal fluctuations at room temperature (300 K) when a magnetic field of flux density 40 mT is applied along the out-of-plane hard axis ($+x$-direction). (a) Distribution of polar angle $\theta_{initial}$ at room temperature (300 K). The mean of the distribution is 173.7°, and the most likely value is 175.8°. (b) Distribution of the azimuthal angle $\phi_{initial}$ due to thermal fluctuations at room temperature (300 K). There are two distributions with peaks centered at ∼65° and ∼295°.

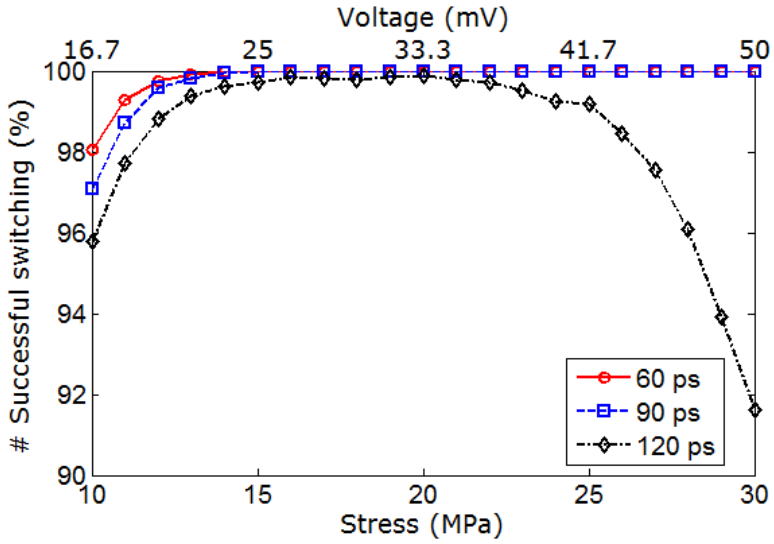

Figure 3.59: Percentage of successful switching events among the simulated switching trajectories (or the switching probability) at room temperature in a Terfenol-D/PZT multiferroic nanomagnet versus (lower axis) stress (10-30 MPa) and (upper axis) voltage applied across the piezoelectric layer, for different ramp durations (60 ps, 90 ps, 120 ps). An out-of-plane ($+x$) bias field of flux density 40 mT is applied. The stress at which switching becomes $\sim$100% successful increases with ramp duration. For large ramp duration (120 ps) or slow ramp rate, $\sim$100% switching probability is unachievable.

M is the magnetization and **H** is the effective field] due to the $+x$-directed magnetic field is such that the magnetization prefers the ϕ-quadrant (0°,90°) slightly over the ϕ-quadrant (270°,360°), which is the reason for the asymmetry in the two distributions of $\phi_{initial}$. Consequently, when the magnetization vector starts out from $\theta \simeq 180°$, the initial azimuthal angle $\phi_{initial}$ is more likely to be in the quadrant (0°,90°) than the quadrant (270°,360°).

Fig. 3.59 shows the switching probability as a function of stress for different ramp durations (60 ps, 90 ps, 120 ps) [169, 150] at room temperature (300 K). The minimum stress needed to switch the magnetization with $\sim$100% probability at 0 K is $\sim$5 MPa, but at 300 K, it increases to $\sim$14 MPa for 60 ps ramp duration and $\sim$17 MPa for 90 ps ramp duration. At low stress levels, the switching probability increases with stress, regardless of the ramp rate. This happens because a higher stress can more effectively counter the detrimental effects of thermal fluctuations when the magnetization vector reaches the x-y plane, and hence increases the success rate of switching. This feature is independent of the ramp rate.

Once the magnetization vector crosses the x-y plane (i.e. in the second half of switching), the stress must be withdrawn as soon as possible. This is because the stress, initially applied to cause switching, forces the energy minimum to remain at $\theta = 90°$, instead of $\theta = 0°$, which will

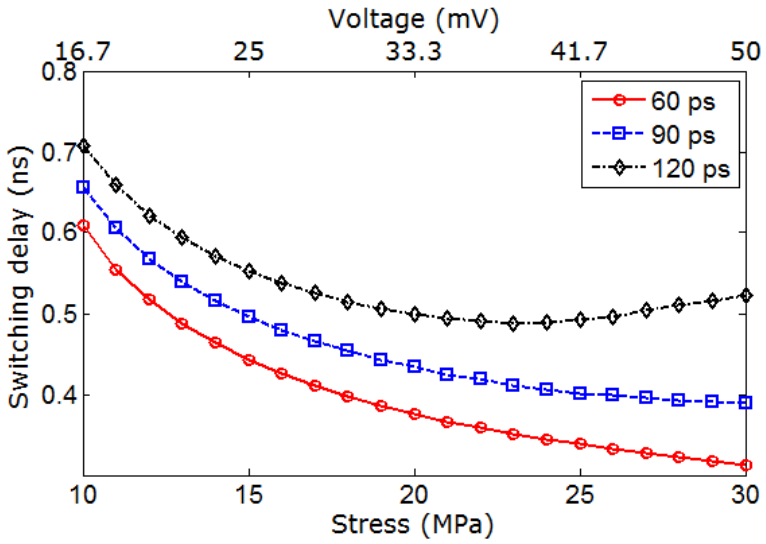

Figure 3.60: The thermal mean of the switching delay (at 300 K) versus (lower axis) stress (10-30 MPa) and (upper axis) voltage applied across the piezoelectric layer, for different ramp durations (60 ps, 90 ps, 120 ps). Switching may fail at low stress levels and also at high stress levels for long ramp durations. Failed attempts are excluded when computing the mean.

make the magnetization linger around $\theta = 90°$ instead of rotating towards the desired location at $\theta \simeq 0°$. This is why stress must be removed or reversed immediately upon crossing the x-y plane so that the energy minimum quickly moves to $\theta = 0°, 180°$, and the magnetization vector rotates towards $\theta = 0°$. If the removal rate is fast, then the success probability remains high since the harmful stress does not stay active long enough to cause significant backtracking of the magnetization vector towards $\theta = 90°$. However, if the ramp rate is too slow, then significant backtracking occurs whereupon the magnetization vector returns to the x-y plane and thermal torques can subsequently kick it to the starting position at $\theta \simeq 180°$, causing switching failure. That is why the switching probability drops with decreasing ramp rate.

The same effect also explains the non-monotonic stress dependence of the switching probability when the ramp rate is slow. During the first half of the switching, when θ is in the quadrant [180°, 90°], a higher stress is helpful since it provides a larger torque to move towards the x-y plane, but during the second half, when θ is in the quadrant [90°, 0°], a higher stress is harmful since it increases the chance of backtracking, particularly when the ramp-down rate is slow. These two counteracting effects are the reason for the non-monotonic dependence of the success probability on stress in the case of the slowest ramp rate.

Fig. 3.60 shows the thermally averaged switching delay versus stress (as well as voltage applied across the piezoelectric layer) for different ramp durations. Only successful switching

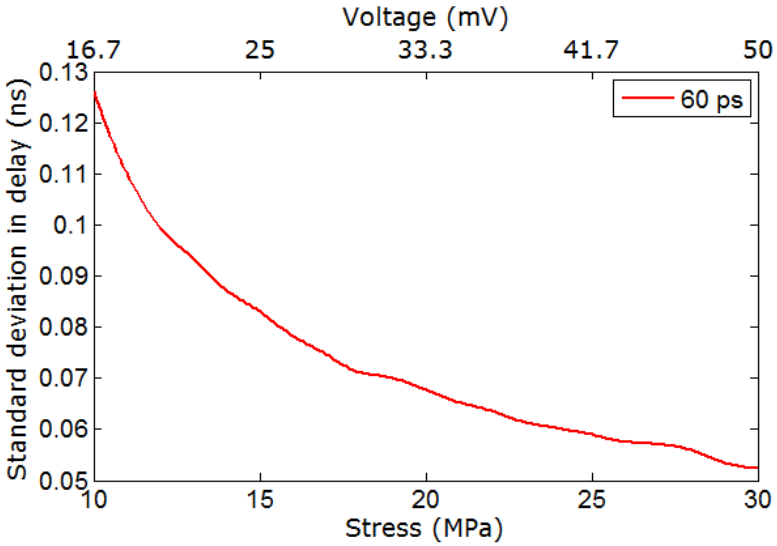

Figure 3.61: The standard deviations in switching delay versus (lower axis) stress (10-30 MPa) and (upper axis) voltage applied across the piezoelectric layer for 60 ps ramp duration at 300 K. We consider only the successful switching events in determining the standard deviations. The standard deviations in switching delay for other ramp durations are of similar magnitudes and show similar trends.

events are counted here since the switching delay will be infinity for an unsuccessful event. For a given stress, decreasing the ramp duration (or increasing the ramp rate) decreases the switching delay because the stress reaches its maximum value quicker and hence switches the magnetization faster. For ramp durations of 60 ps and 90 ps, the switching delay decreases with increasing stress since the torque, which rotates the magnetization, increases when stress increases. However, for 120 ps ramp duration, the dependence is non-monotonic, because of the same reasons that caused the non-monotonicity in Fig. 3.59. Too high a stress is harmful during the second half of the switching since it increases the chances of backtracking. Even if backtracking can be overcome and successful switching ultimately takes place, temporary backtracking still increases the switching delay.

Fig. 3.61 shows the standard deviation in switching delay versus stress (as well as voltage applied across the piezoelectric layer) for 60 ps ramp duration. At higher values of stress, the torque due to stress dominates over the random thermal torque that causes the spread in the switching delay. That makes the distribution more peaked as we increase the stress.

Fig. 3.62 shows the thermal mean of the total energy dissipated to switch the magnetization as a function of stress and voltage across the piezoelectric layer for different ramp durations. The average power dissipation (E_{total}/τ) increases with stress for a given ramp duration and

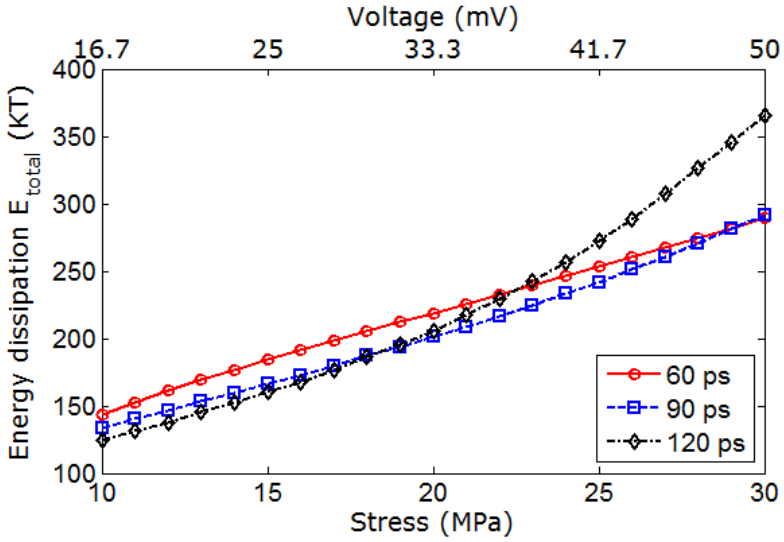

Figure 3.62: Thermal mean of the total energy dissipation versus (lower axis) stress (10-30 MPa) and (upper axis) voltage across the piezoelectric layer for different ramp durations (60 ps, 90 ps, 120 ps). Once again, failed switching attempts are excluded when computing the mean.

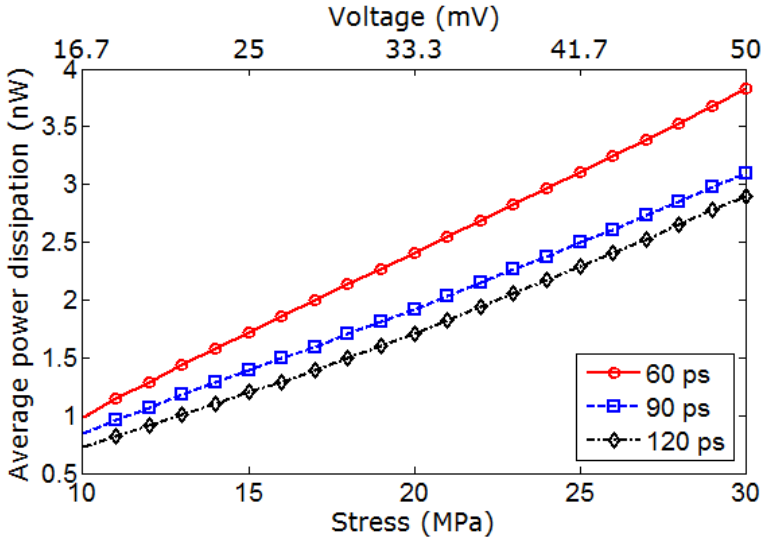

Figure 3.63: Thermal mean of the average power dissipation versus (lower axis) stress (10-30 MPa) and (upper axis) voltage across the piezoelectric layer for different ramp durations (60 ps, 90 ps, 120 ps). Once again, failed switching attempts are excluded when computing the mean.

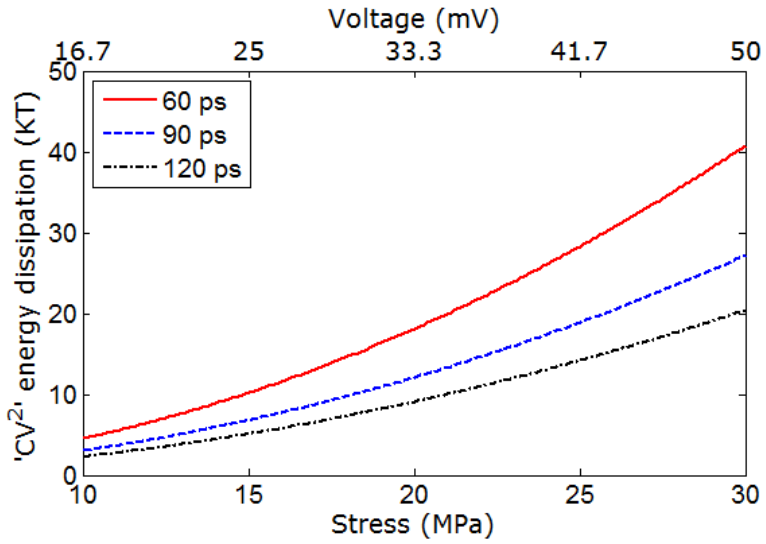

Figure 3.64: The 'CV^2' energy dissipation in the external circuit as a function of (lower axis) stress and (upper axis) voltage applied across the PZT layer for different ramp durations. The dependence on voltage is not exactly quadratic since the voltage is not applied abruptly, but instead ramped up gradually and linearly in time.

decreases with increasing ramp duration for a given stress (see Fig. 3.63). More stress requires more 'CV^2' dissipation and also more internal dissipation because it results in a higher torque. Slower switching decreases the power dissipation since it makes the switching more adiabatic. However, the switching delay curves show the opposite trend (see Fig. 3.60). At a lower ramp rate (higher ramp duration), the average power dissipation E_{total}/τ is always smaller than that of a higher ramp rate, but the switching delay does not decrease as fast as with higher values of stress (in fact switching delay may increase for higher ramp duration), which is why the energy dissipation curves in Fig. 3.62 exhibit the cross-overs.

Fig. 3.64 shows the 'CV^2' energy dissipation in the switching circuitry versus stress and the voltage applied across the PZT layer. Increasing stress requires increasing the voltage V, which is why the 'CV^2' energy dissipation increases rapidly with stress. This dissipation however is a small fraction of the total energy dissipation ($< 15\%$) since a very small voltage is required to switch the magnetization of a multiferroic nanomagnet with stress. The 'CV^2' dissipation decreases when the ramp duration increases because then the switching becomes more 'adiabatic' and hence less dissipative. This component of the energy dissipation would have been several orders of magnitude higher had we switched the magnetization with an external magnetic field [80] or spin-transfer torque [95].

Fig. 3.65 shows the thermal mean of the total energy dissipation versus thermal mean of the

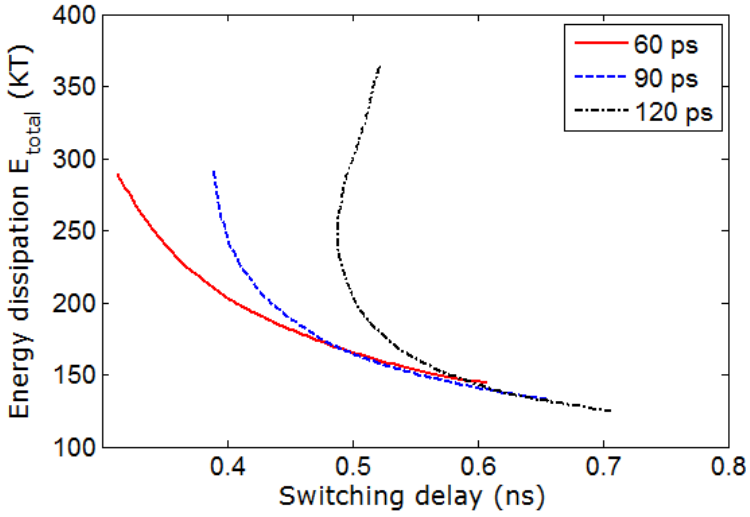

Figure 3.65: Thermal mean of the total energy dissipation versus thermal mean of the switching delay for different stresses (10-30 MPa) with different ramp durations (60 ps, 90 ps, 120 ps) as parameters. Once again, failed switching attempts are excluded when computing the mean.

switching delay for different stresses (10-30 MPa) with different ramp durations (60 ps, 90 ps, 120 ps) as parameters. For ramp durations of 60 ps and 90 ps, energy dissipation decreases with increasing switching delay (and lower stress levels), which shows the correct trade-off between switching delay and energy. However, for the case of 120 ps ramp duration, the switching delay energy shows a non-monotonic behavior, the reason behind which has been already described for Fig. 3.59.

Fig. 3.66 shows the voltage required to switch the magnetization in the Terfenol-D/PZT multiferroic versus thermal mean switching delay for different stresses (10-30 MPa) with different ramp durations (60 ps, 90 ps, 120 ps) as parameters. For ramp durations of 60 ps and 90 ps, the voltage required decreases with increasing switching delay (and lower stress levels), while for the case of 120 ps ramp duration, the switching delay-energy curve shows a non-monotonic behavior, the reason behind which has been already described for Fig. 3.59. This tiny voltage requirement makes this mode of switching magnetizations extremely energy-efficient.

Fig. 3.67 shows the delay and energy distributions in the presence of room-temperature thermal fluctuations for 15 MPa stress and 60 ps ramp duration. The high-delay tail in Fig. 3.67(a) is associated with those switching trajectories that start very close to $\theta = 180^\circ$ which is a stagnation point. In such trajectories, the starting torque is vanishingly small, which makes the switching sluggish at the beginning. During this time, switching also becomes susceptible

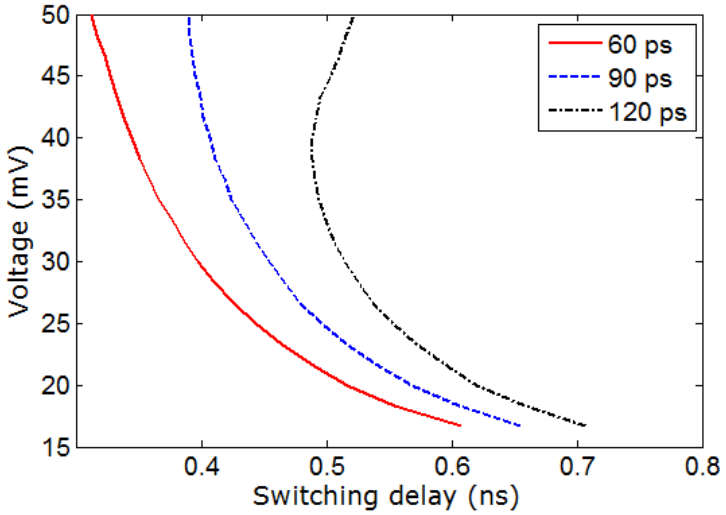

Figure 3.66: Voltage required to switch the magnetization in the Terfenol-D/PZT multiferroic versus thermal mean switching delay for different stresses (10-30 MPa) with different ramp durations (60 ps, 90 ps, 120 ps) as parameters. Once again, failed switching attempts are excluded when computing the mean.

to backtracking because of thermal fluctuations, which increases the delay further. Nonetheless, out of 10,000 simulations of switching trajectories, there was not a single one where the delay exceeded 1 ns, showing that the probability of that happening is less than 0.01%. Since the energy dissipation is the product of the power dissipation and the switching delay, similar behavior is found in Fig. 3.67(b).

Fig. 3.68 shows two illustrative examples of switching dynamics when the applied stress is 10 MPa and the ramp duration is 60 ps. In Fig. 3.68(a), magnetization switches successfully. Thermal fluctuations cause the ripples because of temporary backtracking but θ switches from $\sim$180° to $\sim$0° finally. Note that despite appearances, ϕ is not changing discretely. When it crosses 360°, it re-enters the quadrant $[0°, 90°]$, which is why it appears as if there is a discrete jump in the value of ϕ in Fig. 3.68. On the other hand, Fig. 3.68(b) shows a failed switching dynamic. Here, the magnetization backtracks towards $\theta = 180°$ and settles close to that location, thus failing in its attempt to switch. This happened because of the coupled θ-ϕ dynamics that resulted in a misdirected torque when the magnetization reached the x-y plane. These kinds of dynamics alongwith a wide range of dynamics in the presence of thermal fluctuations have been explained in the previous section and thus would not be repeated here.

We have theoretically investigated stress-induced switching of multiferroic nanomagnets

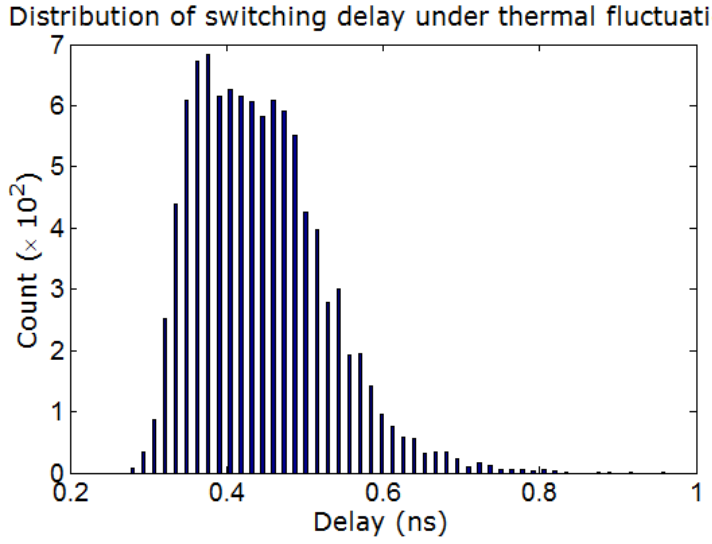

(a)

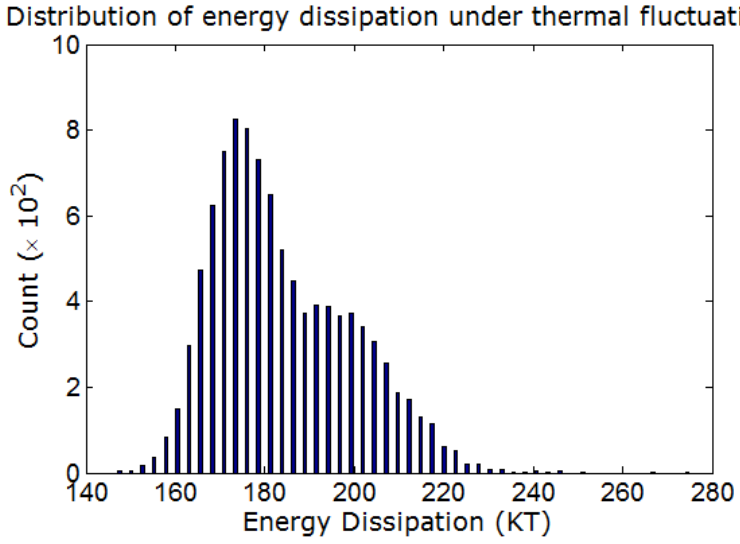

(b)

Figure 3.67: Delay and energy distributions for 15 MPa applied stress and 60 ps ramp duration at room temperature (300 K). (a) Distribution of the switching delay. The mean and standard deviation of the distribution are 0.44 ns and 83 ps, respectively. (b) Distribution of energy dissipation. The mean and standard deviation of the distribution are 184 kT and 15.5 kT at room temperature, respectively.

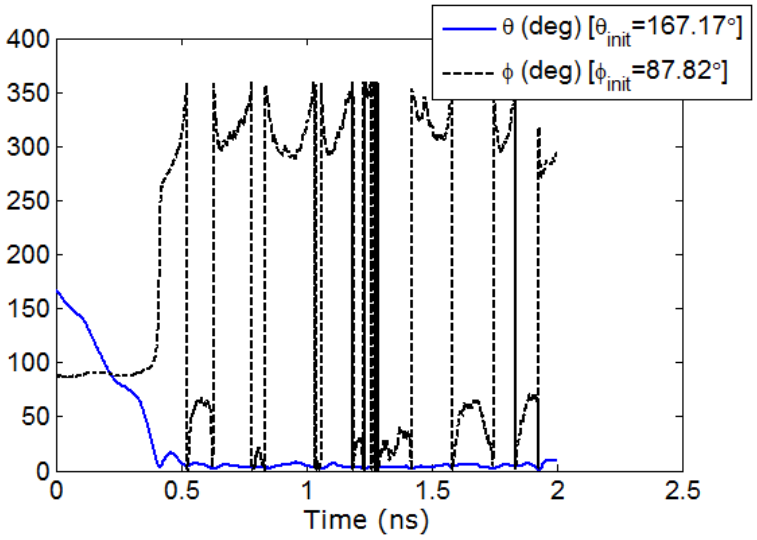

(a)

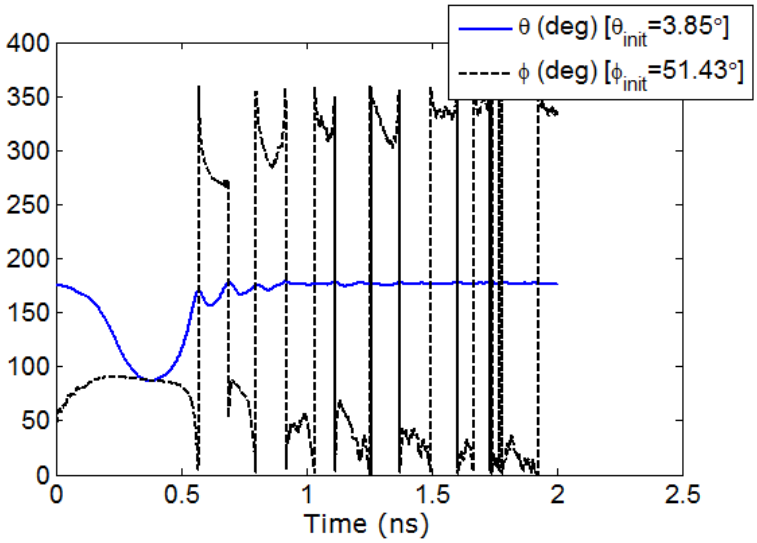

(b)

Figure 3.68: Temporal evolution of the polar angle $\theta(t)$ and azimuthal angle $\phi(t)$ for 10 MPa applied stress and 60 ps ramp duration. Simulations are carried out for room temperature (300 K). (a) Magnetization switches successfully. (b) Magnetization fails to switch and backtracks towards the initial state.

considering ramp rate effects, thermal fluctuations, and out-of-plane bias field to decrease the extent of tail in switching delay distribution. The room-temperature thermal average of the energy dissipation is as small as ∼200 kT while the thermal average of the switching delay is ∼0.5 ns with a standard deviation less than 0.1 ns. This makes strain-switched multiferroic nanomagnets very attractive platforms for implementing non-volatile memory and logic systems because they are minimally dissipative while being adequately fast. Our results also show that a certain critical stress is required to switch with ∼100% probability in the presence of thermal noise. The value of this critical stress increases with decreasing ramp rate until the ramp rate becomes so slow that ∼100% switching probability becomes unachievable. Thus, a faster ramp rate is beneficial. The energy dissipations and switching delays are roughly independent of ramp rate if switching is always performed with the critical stress. All this shows that it is possible to switch multiferroic nanomagnets in less than 1 ns while dissipating energies of ∼200 kT. This range of energy dissipation is far lower than what is encountered in spin transfer torque based switching of nanomagnets with the same switching delay [171].

Chapter 4

Magnetizaton Dynamics in an Array of Multiferroic Devices

In this chapter, based on the same model derived in Chapter 2, we will present the magnetization dynamics in a circuit made of multiple multiferroic devices. An example of signal propagation through a horizontal chain of nanomagnets using so-called Bennett clocking mechanism will be described.

4.1 Dipole Coupling

Dipole coupling between two magnetic moments **M1** and **M2** separated by a distance vector **R** can be expressed by the Equation (4.1) [213].

$$E_{dipole} = \frac{1}{4\pi\mu_0 R^3}\left[(\mathbf{M_1}.\mathbf{M_2}) - \frac{3}{R^2}(\mathbf{M_1}.\mathbf{R})(\mathbf{M_2}.\mathbf{R})\right]. \tag{4.1}$$

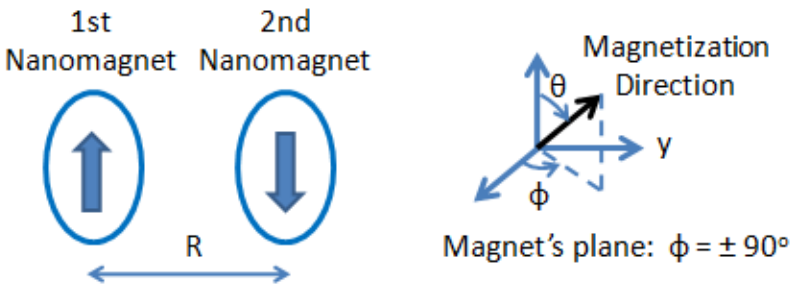

Figure 4.1: Dipole coupling between two magnetic moments.

In standard spherical coordinate system (see Fig. 4.1), the expression of dipole coupling can be translated as

$$E_{dipole} = \frac{\mu_0}{4\pi R^3} M_s^2 \Omega^2 [cos\theta_1 cos\theta_2 + sin\theta_1 sin\theta_2 (cos\phi_1 cos\phi_2 - 2sin\phi_1 sin\phi_2)] \tag{4.2}$$

where $\mathbf{M_1} = \mathbf{M_2} = \mu_0 M_s \Omega$, Ω is the volume of the nanomagnets, M_s is the saturation magnetization, and $\mathbf{R} = R\,\hat{\mathbf{e}}_\mathbf{y}$.

Note that dipole coupling is bi-directional, i.e., $E_{dipole} = E_{dipole,1} = E_{dipole,2}$. Because of the dipole coupling between the magnetizations of the nanomagnets, the potential profiles of both the nanomagnets are tilted and the ground state of the magnetizations are antiferromagnetically coupled as depicted in the Fig. 4.2.

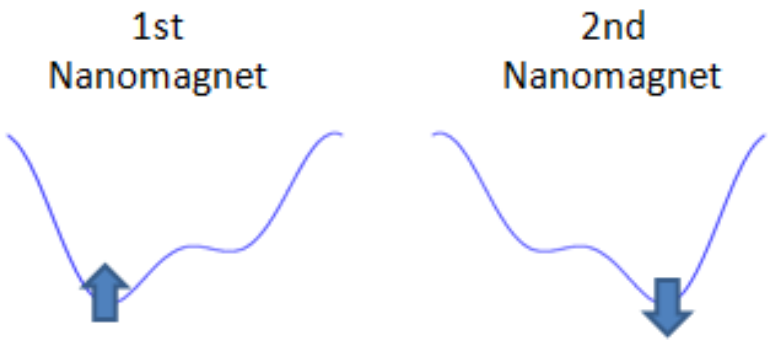

Figure 4.2: Potential profiles of the nanomagnets are tilted to dictate antiferromagnetic coupling between the magnetizations.

Note that if somehow we change the magnetization direction of one nanomagnet, the magnetization of the other nanomagnet would *not* automatically change its direction to assume an antiferromagnetic order. It is because of the reason that there is a barrier separating two magnetization states. It's true that antiferromagnetic order is the ground state, however, during operation of devices, we must remove the barrier and then again restore it to make sure that antiferromagnetic order is maintained. Magnetization may come to antiferromagnetic order after infinitely long time but operation of devices cannot be dependent on that.

4.2 Bennett Clocking

In this section, we will provide a conceptual understanding of Bennett clocking using two-dimensional potential landscapes of the nanomagnets, but in the next section we will consider full three-dimensional potential landscape to derive the magnetization dynamics for Bennett clocking.

In general, we need to propagate a logic bit *unidirectionally* along a chain of nanomagnets. It requires a clock signal to periodically reset the magnetization direction of each nanomagnet. Fig. 4.3 shows the use of a global magnetic field for such a purpose but it does not allow pipelining of data, and magnetization of every nanomagnet must be maintained along hard axis until a bit propagates. It needs an energy minima along hard axis, which can be introduced by biaxial anisotropy [214], but thermal noise would produce a large bit error probability [215].

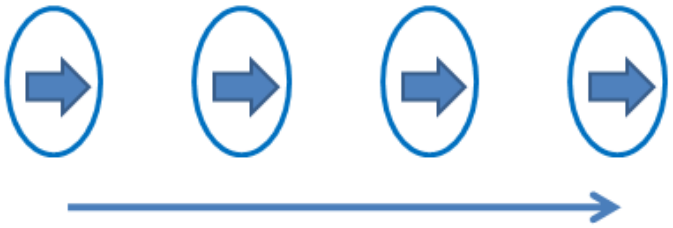

Figure 4.3: Using global magnetic field to propagate a bit of data.

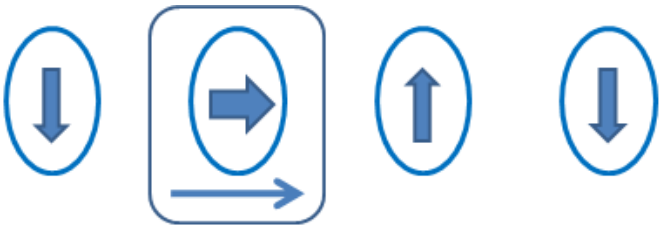

Figure 4.4: Using local magnetic field to propagate a bit of data.

Using a local magnetic field (see Fig. 4.4) eliminates the problems of using global magnetic field, but it is difficult to maintain a magnetic field locally within a dimension of ∼100 nm. Furthermore, generating magnetic field is highly energy consuming. We can use electric-field operated (since electric-field can be maintained locally) multiferroic devices to propagate signals in a chain of nanomagnets [172] using so-called Bennett clocking mechanism, termed in the name of Bennett [3].

Fig. 4.5 depicts the issue behind Bennett clocking in a chain of nanomagnet. First of

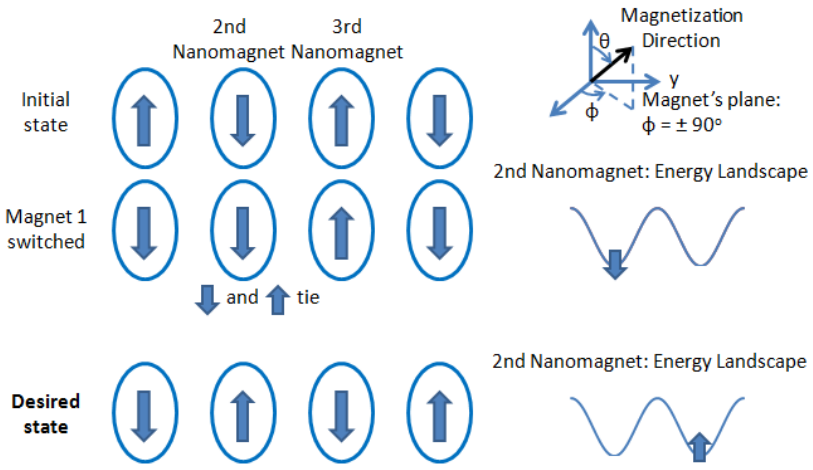

Figure 4.5: The issue behind unidirectionally propagating a bit along a chain of nanomagnets. In the first row, the ground state of an antiferromagnetically coupled chain of four magnets are shown. If the magnetization of the 1st nanomagnet is switched, we wish the desired state of the nanomagnets to be as in the third row, however, 2nd nanomagnet as shown in the second row cannot switch it state because of the combined dipole coupling effect from the 1st and 3rd nanomagnets and therefore gets stuck to its previous value.

all, it should be reemphasized that dipole coupling is bi-directional. So the 2nd nanomagnet experiences dipole coupling effect from both of its neighbors, i.e., 1st and 3rd nanomagnets. Note that we are considering only nearest neighbor interaction, since dipole coupling reduces drastically with distance [see Equation (4.1)]. Thus, if the 1st nanomagnet is switched, the 2nd nanomagnet finds itself in a locked condition as the 1st nanomagnet is telling it to go *up*, while the 3rd nanomagnet is telling it to go *down*. Therefore, it remains on its previous position and thus the change in information on the 1st nanomagnet cannot be propagated through the chain of nanomagnets.

To prevent the lockjam as depicted in the Fig. 4.5 due to the bi-directional nature of dipole coupling, we need to impose the *unidirectionality in time* as shown in the Fig. 4.6 [172]. Both the 2nd and 3rd nanomagnets are stressed to get them aligned to their hard axes (note the third row in Fig. 4.6 and see Figs. 4.7 and 4.8) and then stress is removed/reversed on the 2nd nanomagnet (note the fourth row in Fig. 4.6 and see Fig. 4.9) to relax its magnetization towards the desired state. In this way, subsequently applying stress on the nanomagnets and then releasing/reversing the stress, we can propagate a logic bit *unidirectionally* along a chain of nanomagnets. The slight deflection in the magnetization of the 4th nanomagnet in the third row of Fig. 4.5 is due to dipole coupling, while in the fourth row, the magnetization of 4th nanomagnet is aligned along its hard axis because of applied stress on it. A three-phase clock

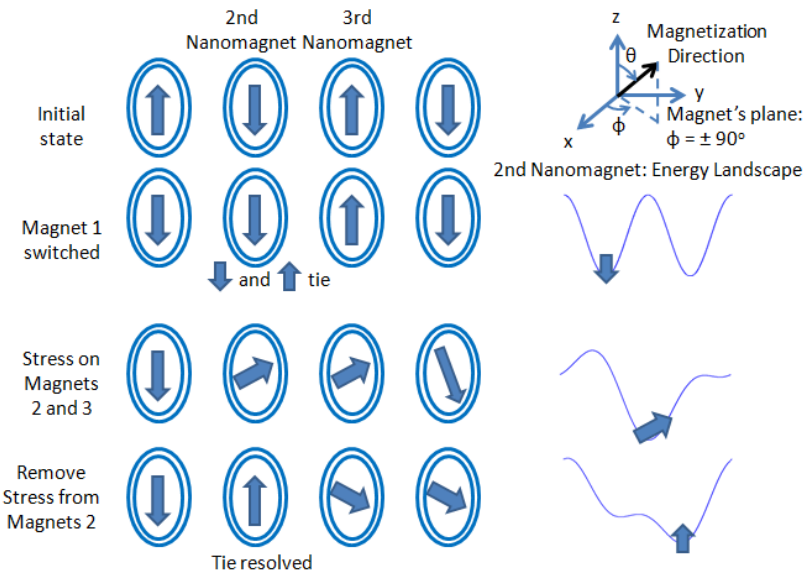

Figure 4.6: Imposing the unidertionality in time to propagate a logic bit through a chain of nanomagnets. The 2nd and 3rd nanomagnets are stressed to align them along their hard axis and then stress is removed/reversed on the 2nd nanomagnet to relax its magnetization along the desired state.

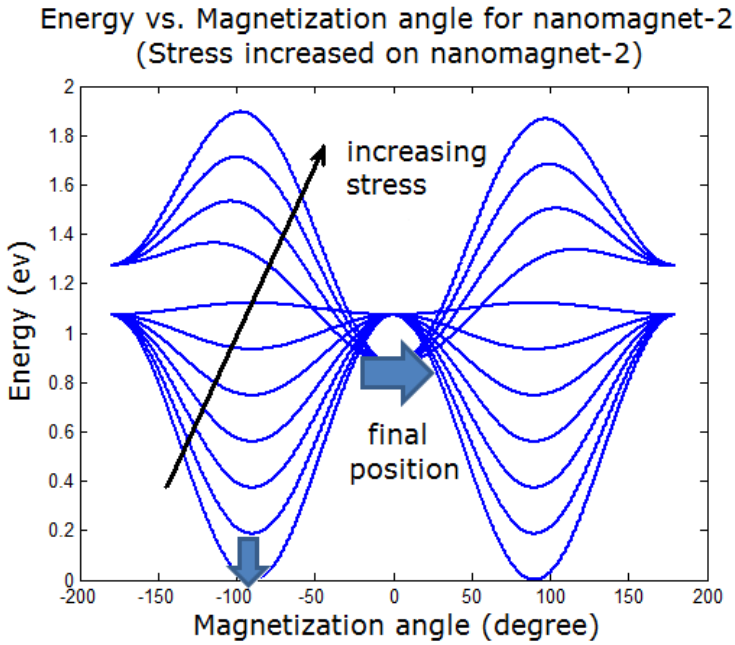

Figure 4.7: Stress is increased on the 2nd nanomagnet to invert its potential landscape and align its magnetization along the hard axis. Note that its potential landscape is symmetric since it experiences an equal and opposite amount of dipole coupling from the neighboring 1st and 3rd nanomagnets. (See the 3rd row of the Fig. 4.6.) Magnetization angle is $90^\circ - \theta$. In-plane potential landscape is considered for illustration, but the full three-dimensional potential landscape will be considered while analyzing magnetization dynamics.

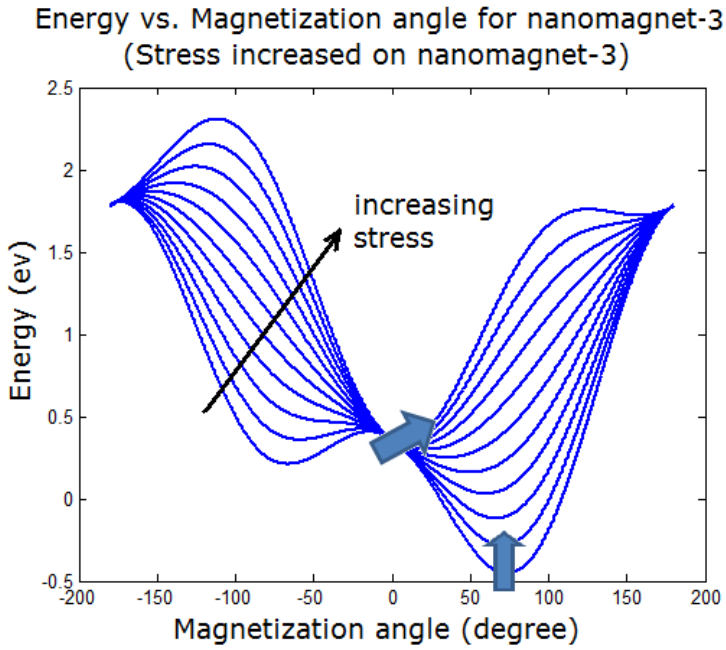

Figure 4.8: Stress is increased on the 3rd nanomagnet to invert its potential landscape and align its magnetization along the hard axis. (See the 3rd row of the Fig. 4.6.) Note that its potential landscape is asymmetric due to different magnitudes of dipole coupling from the neighboring 2nd and 4th nanomagnets. Magnetization angle is $90° - \theta$. In-plane potential landscape is considered for illustration, but the full three-dimensional potential landscape will be considered while analyzing magnetization dynamics.

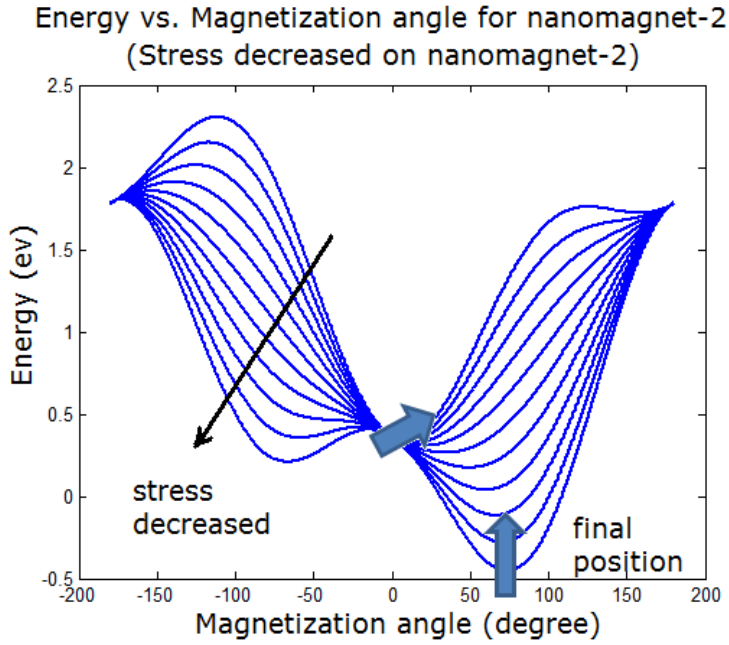

Figure 4.9: Stress is decreased on the 2nd nanomagnet to relax its magnetization along the desired easy axis. (See the 3rd row of the Fig. 4.6.) Note that it potential landscape has got asymmetric because of different magnitudes of dipole coupling from the neighboring 1st and 3rd nanomagnets. This is unlike when the 3rd nanomagnet was not stressed as depicted in the Fig. 4.7, when its potential landscape was symmetric. Magnetization angle is $90° - \theta$. In-plane potential landscape is considered for illustration, but the full three-dimensional potential landscape will be considered while analyzing magnetization dynamics.

would be sufficient to propagate a signal along the chain of nanomagnet. Note that we are explaining with two-dimensional potential landscapes of the nanomagnets (assuming azimuthal angle $\phi = \pm 90°$), but as we have conceived in the Chapters 2 and 3, the out-of-plane excursion of magnetization has immense influence in shaping the magnetization dynamics and reducing the switching delay to a couple of orders in magnitude.

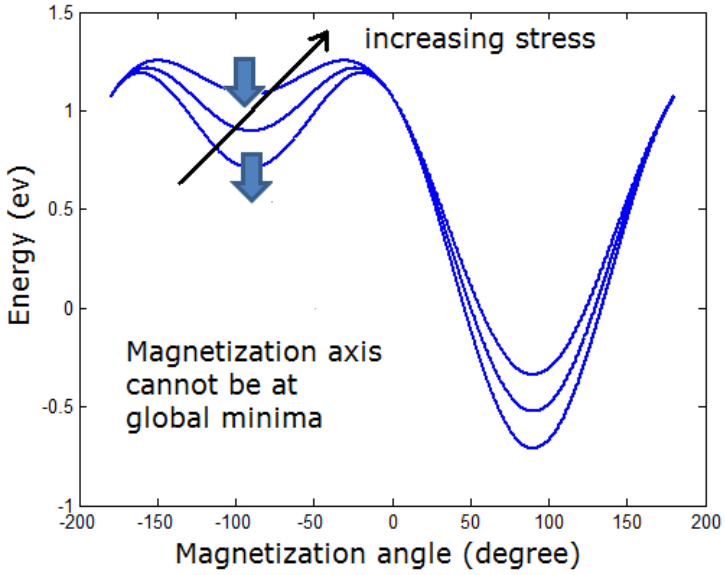

Figure 4.10: Illustration of why magnetization cannot traverse to global minimum when there is a barrier separating the local and global minimum. We must take into account such scenario while performing steady-state calculations.

4.3 Theoretical Formulations

Having conceptually describing the theoretical background on Bennett clocking in the previous section, we will now perform a full three-dimensional analysis for calculating the magnetization dynamics based on Landau-Lifshitz-Gilbert (LLG) equation based on the similar procedure described in Chapter 2 [173]. Here, we have one more component contributing to the total energy apart from the shape anisotropy and stress anisotropy energy, which is the energy due to dipole coupling.

Fig. 4.11 shows a chain of four nanomagnets and we intend to switch the 2nd nanomagnet successfully in its desired direction once the 1st nanomagnet is switched as depicted in the Fig. 4.6. We will use subscripts 1-4 to denote the parameters and metrics for the corresponding nanomagnets. The dipole coupling energy on the 2nd nanomagnet due to 1st and 3rd

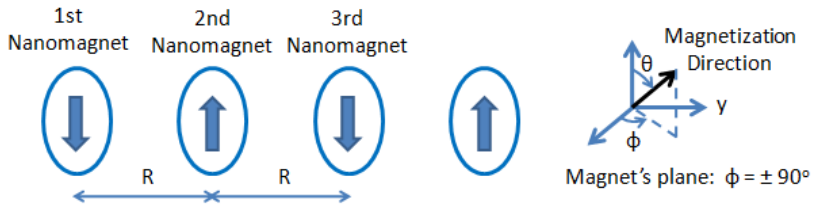

Figure 4.11: A chain of four nanomagnets, the magnetizations of which are considered in full three-dimensional space. The standard spherical coordinate system is used.

nanomagnets can be written following the similar prescription given in the Equation (4.2) as

$$\begin{aligned} E_{dipole,2} = \frac{\mu_0}{4\pi R^3} M_s^2 \Omega^2 [&cos\theta_2 cos\theta_1 + cos\theta_2 cos\theta_3 \\ &+ sin\theta_1 sin\theta_2 (cos\phi_1 cos\phi_2 - 2sin\phi_1 sin\phi_2) \\ &+ sin\theta_3 sin\theta_2 (cos\phi_3 cos\phi_2 - 2sin\phi_3 sin\phi_2)]. \end{aligned} \tag{4.3}$$

The torque acting on the 2nd nanomagnet due to dipole coupling

$$\begin{aligned} \mathbf{T_{dipole,2}}(t) &= -\mathbf{n_m}(t) \times \nabla E_{dipole,2} \\ &= -\hat{\mathbf{e}}_\mathbf{r} \times \left[\frac{\partial E_{dipole,2}}{\partial \theta_2} \hat{\mathbf{e}}_\theta + \frac{1}{sin\theta_2} \frac{\partial E_{dipole,2}}{\partial \phi_2} \hat{\mathbf{e}}_\phi \right] \\ &= -\frac{\partial E_{dipole,2}}{\partial \theta_2} \hat{\mathbf{e}}_\phi + \frac{1}{sin\theta_2} \frac{\partial E_{dipole,2}}{\partial \phi_2} \hat{\mathbf{e}}_\theta \\ &= -T_{dipole,\phi_2} \hat{\mathbf{e}}_\phi + T_{dipole,\theta_2} \hat{\mathbf{e}}_\theta, \end{aligned} \tag{4.4}$$

where

$$\begin{aligned} T_{dipole,\phi_2} &= \frac{\partial E_{dipole,2}}{\partial \theta_2} \\ &= \frac{\mu_0}{4\pi R^3} M_s^2 \Omega^2 [-sin\theta_2 cos\theta_1 - sin\theta_2 cos\theta_3 \\ &\quad + sin\theta_1 cos\theta_2 (cos\phi_1 cos\phi_2 - 2sin\phi_1 sin\phi_2) \\ &\quad + sin\theta_3 cos\theta_2 (cos\phi_3 cos\phi_2 - 2sin\phi_3 sin\phi_2)], \end{aligned} \tag{4.5}$$

and

$$
\begin{aligned}
T_{dipole,\theta_2} &= \frac{1}{sin\theta_2}\frac{\partial E_{dipole,2}}{\partial \phi_2} \\
&= -\frac{\mu_0}{4\pi R^3} M_s^2 \Omega^2 \times \\
&\quad [sin\theta_1(cos\phi_1 sin\phi_2 + 2sin\phi_1 cos\phi_2) \\
&\quad + sin\theta_3(cos\phi_3 sin\phi_2 + 2sin\phi_3 cos\phi_2)]. \qquad (4.6)
\end{aligned}
$$

The torque acting on the 2nd nanomagnet due to shape and stress anisotropy can be derived similarly following the Equation (2.19) in Chapter 2 as

$$
\mathbf{T_{E,2}}(t) = -2B_2(\phi_2(t))sin\theta_2(t)cos\theta_2(t)\,\hat{\mathbf{e}}_\phi - B_{\phi e2}(\phi_2(t))sin\theta_2(t)\,\hat{\mathbf{e}}_\theta, \qquad (4.7)
$$

where

$$
\begin{aligned}
B_2(\phi_2(t)) &= \frac{\mu_0}{2} M_s^2 \Omega \left[N_{d-xx}cos^2\phi_2(t) + N_{d-yy}sin^2\phi_2(t) - N_{d-zz}\right] + (3/2)\,\lambda_s \sigma_2 \Omega, \qquad (4.8) \\
B_{\phi e2}(\phi_2(t)) &= \frac{\mu_0}{2} M_s^2 \Omega (N_{d-xx} - N_{d-yy}) sin(2\phi_2(t)). \qquad (4.9)
\end{aligned}
$$

Adding the contribution due to dipole coupling, we can modify the Equation (2.24) as derived in Chapter 2 as

$$
\theta_2'(t) + \alpha sin\theta_2(t)\,\phi_2'(t) = \frac{|\gamma|}{M_V}[B_{\phi e2}(\phi_2(t))\,sin\theta_2(t) - T_{dipole,\theta_2}] \qquad (4.10a)
$$

$$
sin\theta_2(t)\,\phi_2'(t) - \alpha\theta_2'(t) = \frac{|\gamma|}{M_V}[2B_2(\phi_2(t))sin\theta_2(t)cos\theta_2(t) + T_{dipole,\phi_2}]. \qquad (4.10b)
$$

From Equation (4.10), we get the following coupled dynamics between the polar angle θ_2 and azimuthal angle ϕ_2 for the 2nd nanomagnet.

$$\left(1+\alpha^2\right)\theta_2'(t) = \frac{|\gamma|}{M_V}[B_{0e2}sin\theta_2(t) - 2\alpha B_2 sin\theta_2(t)cos\theta_2(t) - T_{dipole,\theta_2} - \alpha T_{dipole,\phi_2}] \quad (4.11)$$

$$\left(1+\alpha^2\right)\phi_2'(t) = \frac{|\gamma|}{M_V}\frac{1}{sin\theta_2(t)}[\alpha B_{0e2}sin\theta_2(t) + 2B_2 sin\theta_2(t)cos\theta_2(t) + \alpha T_{dipole,\theta_2} + T_{dipole,\phi_2}].$$
$$(sin\theta \neq 0.). \quad (4.12)$$

Note that in a very similar way the equations of dynamics for the other three nanomagnets can be derived. Hence, those equations would not be worked out here, however, in the next section, we will provide simulation results based on those equations.

4.4 Simulation Results

The material parameters and dimensions that characterize the magnetostrictive layer (Terfenol-D) are given in Table 4.1 [200, 201, 202, 204].

	Terfenol-D
Major axis (a)	101.75 nm
Minor axis (b)	98.25 nm
Thickness (t)	10 nm
Young's modulus (Y)	8×10^{10} Pa
Magnetostrictive coefficient ($(3/2)\lambda_s$)	$+90\times10^{-5}$
Saturation magnetization (M_s)	8×10^{5} A/m
Gilbert's damping constant (α)	0.1

Table 4.1: Material parameters for Terfenol-D and dimensions that characterize the magnetostrictive layer used for Bennett clocking.

For the piezoelectric layer, we use lead-zirconate-titanate (PZT). The PZT layer is assumed to be four times thicker than the magnetostrictive layer so that any strain generated in it is transferred almost completely to the magnetostrictive layer. We will assume that the maximum strain that can be generated in the PZT layer is 500 ppm [205], which would require a voltage of 200 mV because d_{31} is assumed to be 1e-10 m/V for PZT [206]. The corresponding stress is the product of the generated strain (500×10^{-6}) and the Young's modulus of the magnetostrictive layer. So the maximum stress that can be generated on the Terfenol-D layer is 40 MPa. The choice of material parameters and dimensions give us the in-plane barrier height 32 kT at

room-temperature (300 K), so the static error probability is e^{-32}.

In all our simulations, the initial orientation of the magnetization vector is: $\theta = 175°$ and $\phi = 90°$. Stress is applied instantaneously and we solve Equations (4.11) and (4.12) for the 2nd nanomagnet (and similar equations for the other three nanomagnets) at each time step. Once θ becomes 90°, stress is *reversed* instantaneously and we follow the magnetization vector in time until θ becomes 5°. At that point, switching is deemed to have occurred.

Fig. 4.12 shows the magnetization dynamics for all the nanomagnets in a chain of four Terfenol-D/PZT multiferroic nanomagnets for Bennett clocking, when a compressive stress of 5.2 MPa is applied on the 2nd and 3rd nanomagnets and then after their magnetizations come to their hard axes, stress is reversed on the 2nd nanomagnet to relax its magnetization towards its desired state. In the Fig. 4.12(b), note that azimuthal angle of magnetization of the 2nd nanomagnet is deflected in the quadrant $(90°, 180°)$ while that for the 3rd nanomagnet is deflected in the quadrant $(0°, 90°)$. Both the quadrants are "good" quadrants for the respective nanomagnets as explained in Chapter 2. Note that the magnetization of 2nd nanomagnet is rotating from $\theta \simeq 180°$ to $\theta \simeq 0°$, so the corresponding "good" quadrants for ϕ_2 are $(90°, 180°)$ and $(270°, 360°)$, while the magnetization of 3rd nanomagnet is rotating from $\theta \simeq 0°$ to $\theta \simeq 180°$, so the corresponding "good" quadrants for ϕ_3 are $(0°, 90°)$ and $(180°, 270°)$. The applied stress has rotated the magnetizations in their corresponding "good" quadrants and switching is aided due to such out-of-plane excursions as explained in Chapter 2. The stress of 5.2 MPa has only shifted the magnetizations out-of-plane by 5° during 90° switching, i.e., when the magnetizations come near to their hard axes. Upon reversing the stress on the 2nd nanomagnet, its magnetization rotates out-of-plane more due to the similar reason as described in the Fig. 3.1(b), but this time at the very end, it has come back to its plane because of the dipole coupling with the 3rd nanomagnet, which tries to align the 2nd nanomagnet's magnetization with its own magnetization. Finally, note that the magnetizations of 1st and 4th nanomagnets remain quite unchanged because no stress is applied on these two nanomagnets, the slight changes in the magnetizations directions occurred because of dipole coupling effect.

Fig. 4.13 shows magnetization dynamics for Bennett clocking with 30 MPa stress, rather than 5.2 MPa stress as we have presented earlier. With high stress, magnetizations have deflected out-of-plane more ($\sim 10°$) than that for the lower stress while reaching hard axis and

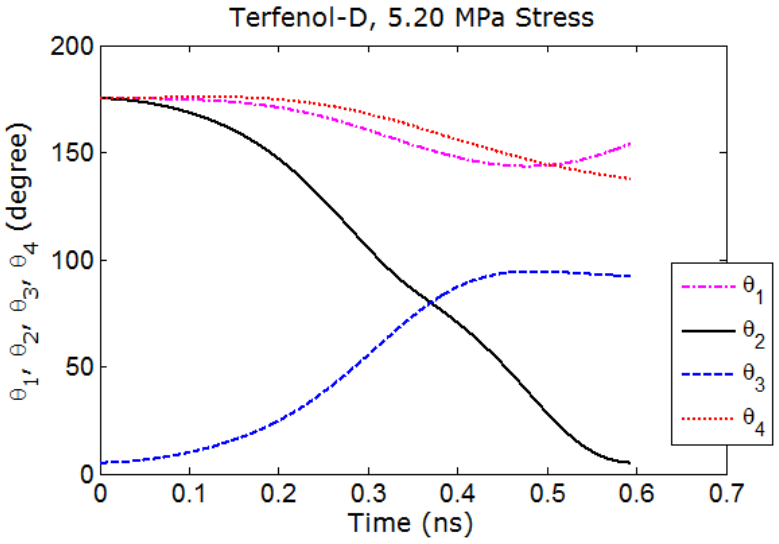

(a)

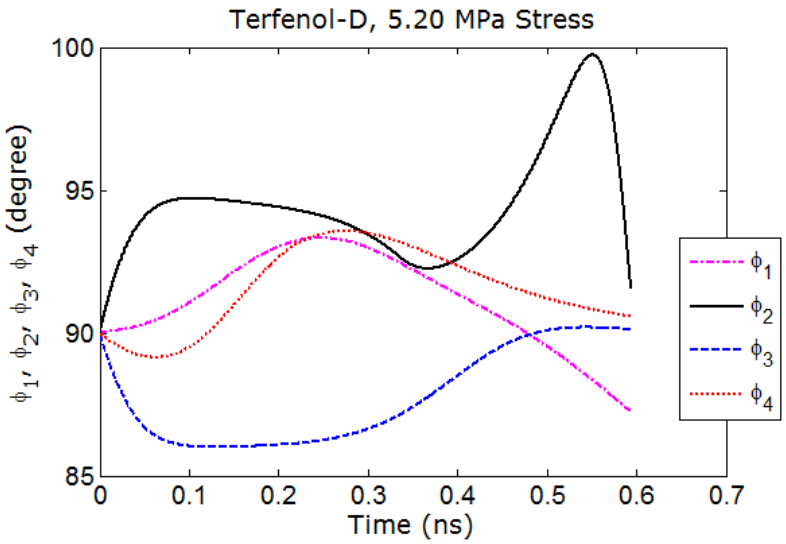

(b)

Figure 4.12: Magnetization dynamics for Bennett clocking in a chain of four Terfenol-D/PZT multiferroic nanomagnets with stress 5.2 MPa and assuming instantaneous ramp: (a) polar angle θ versus time, and (b) azimuthal angle ϕ over time while switching occurs, i.e. during the time θ_2 changes from 175° to 5°.

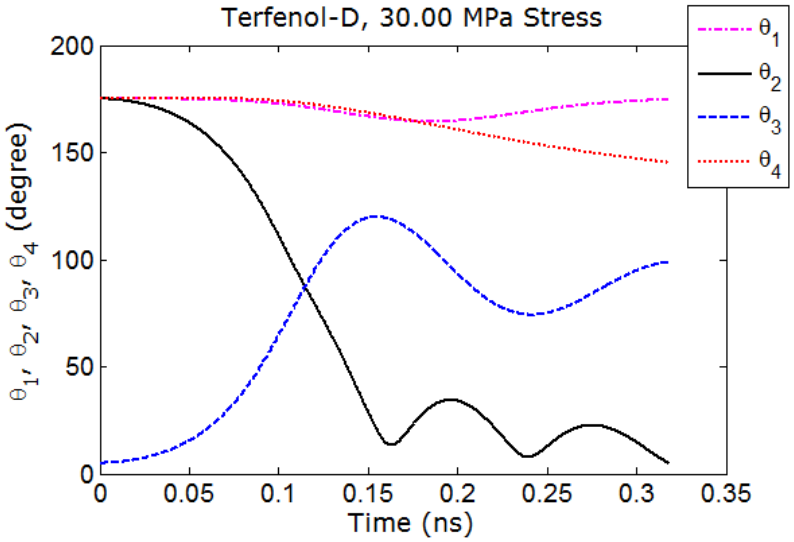

(a)

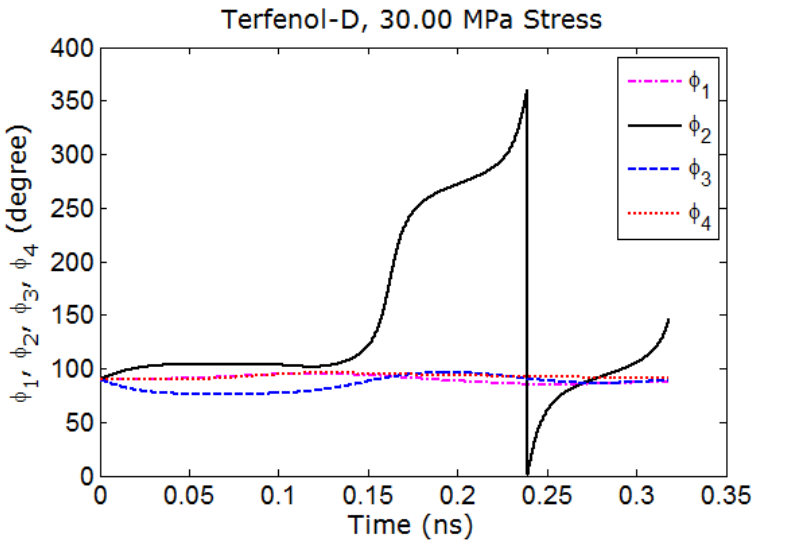

(b)

Figure 4.13: Magnetization dynamics for Bennett clocking in a chain of four Terfenol-D/PZT multiferroic nanomagnets with stress 30 MPa and assuming instantaneous ramp: (a) polar angle θ versus time, and (b) azimuthal angle ϕ over time while switching occurs, i.e. during the time θ_2 changes from 175° to 5°.

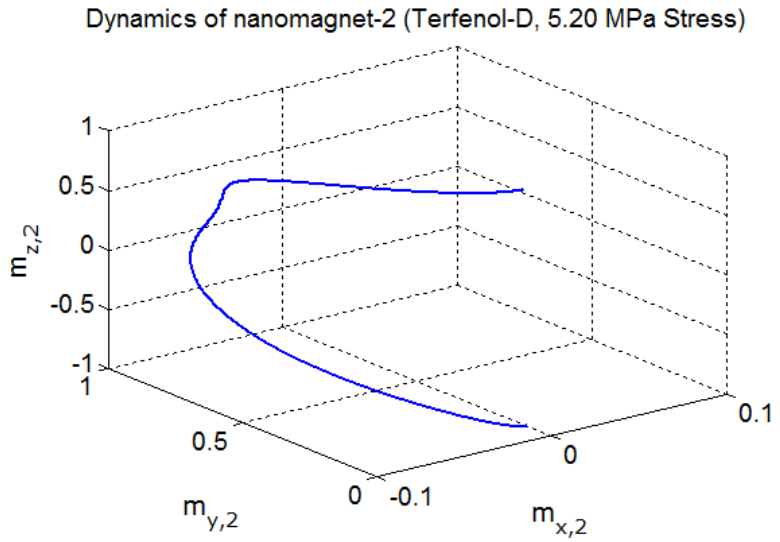

(a)

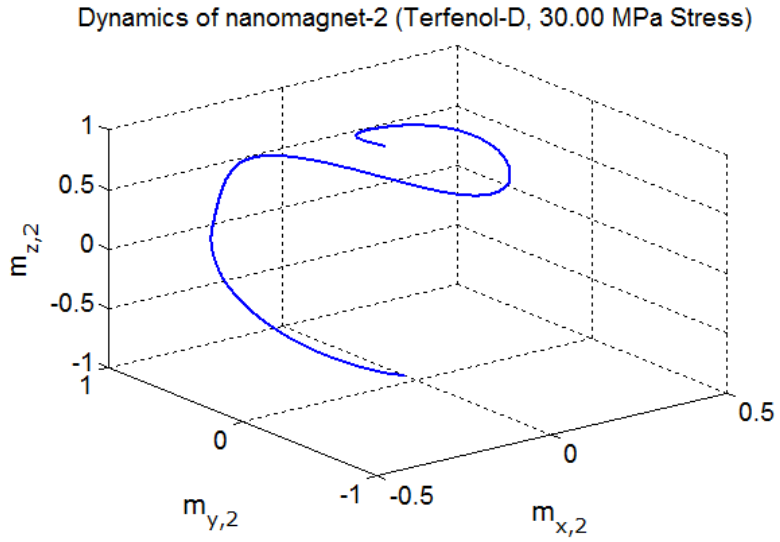

(b)

Figure 4.14: Trajectories traced out by the tip of the magnetization vector for the 2nd nanomagnet in a chain four Terfenol-D/PZT multiferroic nanomagnets for Bennett clocking while switching occurs, i.e. during the time θ_2 changes from 175° to 5°: (a) 5.2 MPs stress, and (b) 30 MPa stress.

the magnetization of 2nd nanomagnet has executed a precessional motion before completing switching. The reason is similar to what we have described earlier that magnetization traverses alternatingly into "good" and "bad" quadrants. Apparently, almost half of the time taken during switching, magnetization experiences such unfruitful motion. Fig. 4.14 shows the trajectory traced out by the tip of the magnetization vector for the 2nd nanomagnet with stresses 5.2 MPa and 30 MPa. Clearly, we see the precession of magnetization at the end of switching for the high stress of 30 MPa.

To reduce such unfruitful motion, one can just use lower stress. Fig. 4.15 shows magnetization dynamics for Bennett clocking with 10 MPa stress, rather than the high stress 30 MPa as we have presented earlier. Note that the switching delay has increased just a bit and magnetization has not executed any precessional motion. The out-of-plane excursion of magnetizations can be explained in a very similar way as we have described earlier. Comparing Figs. 4.15(b) and 4.12(b), we see that for the 2nd nanomagnet, magnetization has not come back to its plane at the end of switching for 10 MPs stress case, which is simply because of the reason that a higher stress of 10 MPa can counter the dipole coupling due to 3rd nanomagnet, unlike the case of 5.2 MPa.

Fig. 4.16 shows the switching delay-energy trade-off of Bennett clocking for a stress range 5.2-30 MPa. A higher stress corresponds to lower switching delay and a higher energy dissipation. Both the "CV^2" energy dissipation and internal dissipation due to Gilbert damping E_d are plotted following the prescription as in the Chapter 2. The "CV^2" energy dissipation can be significantly brought down by decreasing the stress since, stress is proportional to voltage applied, while sacrificing switching delay a bit. Since we have considered instantaneous ramp and stress is reversed during ramp-down phase, the "CV^2" energy dissipation is simply $3CV^2$ for the 2nd nanomagnet. While calculating internal energy dissipation, the sum of the energy dissipations in all the four nanomagnets are considered: dissipations in 1st and 4th nanomagnets are quite negligible since they don't quite switch and dissipation in 2nd nanomagnet is around twice that of in 3rd nanomagnet since 2nd nanomagnet switches a complete 180°, while the 3rd nanomagnet switches only 90°. The instantaneous power dissipation as derived in Chapter 2 is modified to include the torque due to dipole coupling, e.g., for the 2nd nanomagnet, the

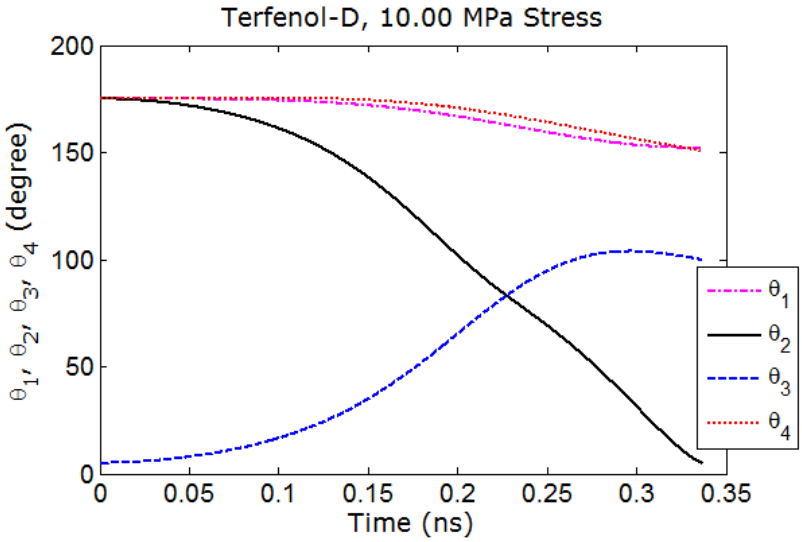

(a)

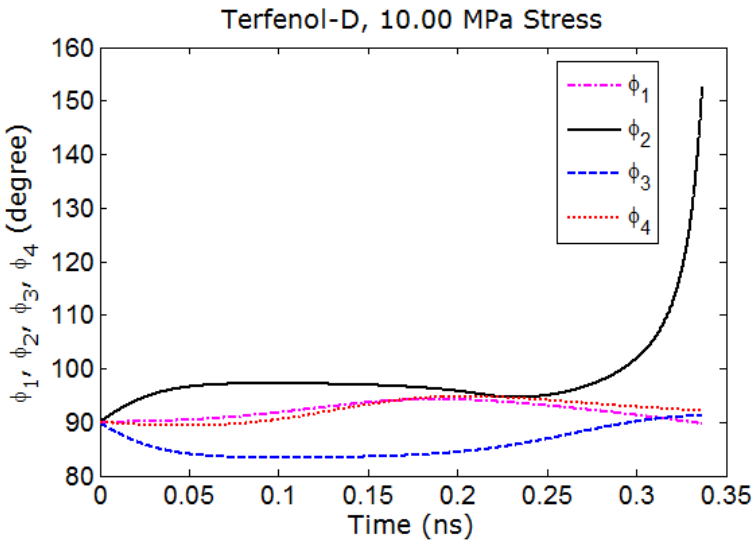

(b)

Figure 4.15: Magnetization dynamics for Bennett clocking in a chain of four Terfenol-D/PZT multiferroic nanomagnets with stress 10 MPa and assuming instantaneous ramp: (a) polar angle θ versus time, and (b) azimuthal angle ϕ over time while switching occurs, i.e. during the time θ_2 changes from 175° to 5°.

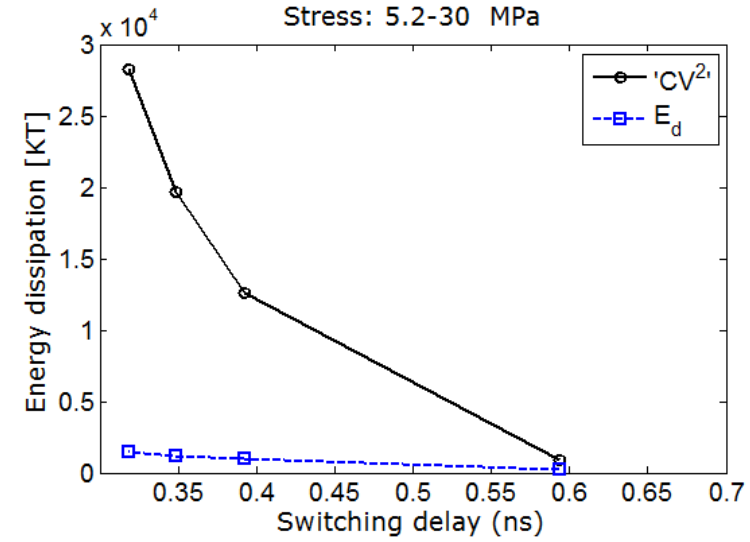

(a)

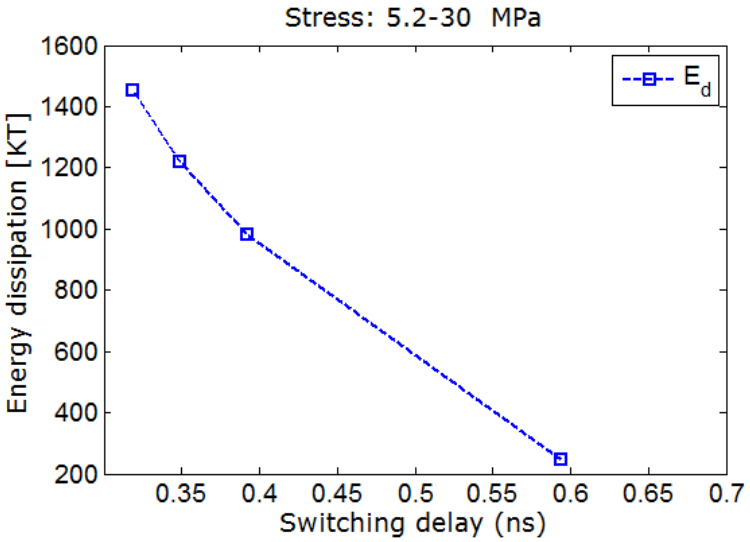

(b)

Figure 4.16: Switching delay-energy for Bennett clocking in a chain of four nanomagnets. (a) Both 'CV^2' energy dissipation and internal energy dissipation E_d, and (b) Only internal energy dissipation E_d.

instantaneous power dissipation can be calculated as

$$P_{d,2}(t) = \frac{\alpha\,|\gamma|}{(1+\alpha^2)M_V}\,|\mathbf{T_{E,2}}(t) + \mathbf{T_{dipole,2}}(t)|^2\,. \tag{4.13}$$

Note that we have not applied any out-of-plane bias field so the term $\mathbf{T_M}(t)$ term as in Equation (2.53) is absent here. The power dissipations are integrated throughout the switching period to get the energy dissipation due to Gilbert damping.

4.5 Discussions

We have studied, based on the same model derived in Chapter 2, the magnetization dynamics of multiferroic nanomagnets in a circuit of multiple nanomagnets, e.g., Bennett clocking in an antiferromagnetically coupled horizontal wire [173]. Also, a similar analysis is possible in the context of a ferromagnetically coupled vertical wire. We have not incorporated ramp rate effect or thermal fluctuations, which one needs to consider and analyze further. Universal logic gates (e.g., NAND and NOR gates) can be also constructed and analyzed using the very same model that includes dipole coupling. Figs. 4.17 depicts such possibilities. In general, magnetizations of an array of nanomagnets can be manipulated to implement computing in MQCA (Magnetic Quantum Cellular Automata) based architecture [216, 174].

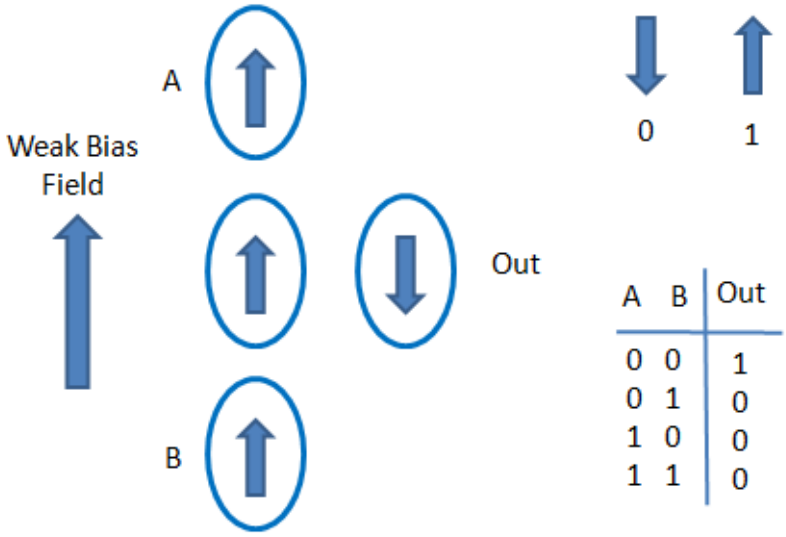

(a)

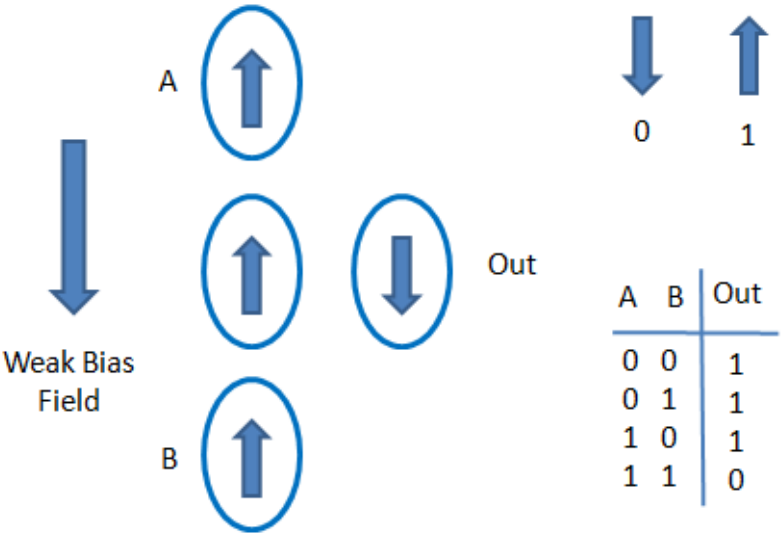

(b)

Figure 4.17: Schematic of universal logic gates employing Magnetic Quantum Cellular Automata (MQCA) based architecture: (a) NOR gate, and (b) NAND gate. Note that a *weak* bias field in the specified direction is required to break the tie when the input bits are different. The bias field must be weak enough so that it does not interfere in the operation when the input bits are 0s for NOR gate and 1s for NAND gate.

Chapter 5

Preliminary Experimental Works

In this chapter, the preliminary experimental results on fabrication of *single-domain* nanomagnets would be presented. This is the foremost step on building multiferroic composites for which a piezoelectric layer needs to be in contact with the single-domain nanomagnets. The procedures to fabricate and view single-domain nanomagnets are described below [217].

5.1 Electron-Beam Lithography

The nanomagnet arrays are fabricated by electron-beam lithography (EBL) [218], magnetic metal deposition, and lift-off. Poly-Methyl-methacrylate (PMMA) of ∼100 nm is spun over a silicon wafer. The patterns are defined using an Hitachi SU70 SEM (Scanning Electron Microscope) and EBL system with NPGS (Nanometer Pattern Generation System) software [219]. Different parameters in the system, e.g., condenser lens setting (using setting 12 instead of 5), extraction voltage (1.5 V), objective aperture (set at 4), anode aperture (set at 4), beam current (60 pA), extraction voltage (1.5 V) are optimized to get a good amount of accuracy and perfection in fabrication using EBL system. The maximum beam voltage that is allowed in our system is 30 kV. A higher beam voltage (∼100 kV) would be required to fabricate very fine structures with 10 nm dimensions. However, 30 kV beam voltage is fine to fabricate nanomagnets of around 100 nm × 60 nm dimensions, as we will see image later in this chapter. Several doses in the EBL system were played around to have an understanding about the working doses. Photoresist development is done by a solution of methyl-isobuthylketone

(MIBK): isopropanol (IPA) = 1:3 for 70 seconds followed by only IPA for 20 seconds. A 10 nm nickel layer and a 10 nm gold cap-layer were e-beam evaporated subsequently. Liftoff is done in dichloromethane [220].

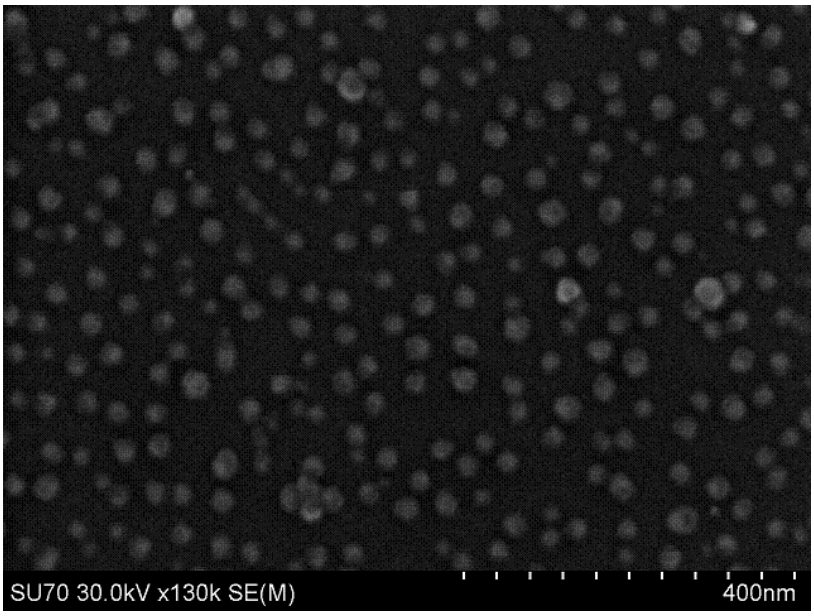

Figure 5.1: Gold standard (15 nm dots on average) viewed in SEM.

Fig. 5.1 shows an SEM image of 15 nm (on average) gold-standard. This is done to verify that the sample is well focused before doing EBL and subsequently EBL was performed on an adjacent sample on the same mount. Note that it also requires some fine settings on the sample itself since SEM settings may get a little changed when moving from gold standard to the sample. For this reason, a couple of scratches were made on the sample at an edge and SEM was focused and adjusted a bit on the sample at the scratches. EBL was done very near to the scratches far end from the edge of the sample.

Fig. 5.2 shows the dots and lines fabricated using EBL. A good enough resolution has been achieved with ∼20 nm dimensions. This gives us an understanding that how good it would be in producing nanomagnets of around 100 nm dimensions. Fig. 5.3 shows the arrays of magnets fabricated using EBL system. A lateral dimension of ∼100 nm × 60 nm of nanomagnets has been well achieved. The sizes are not perfectly elliptical because of noise in the EBL system and also due to not-so-small possible dot sizes. Fig. 5.4 shows magnets fabricated with small distance in between as low as less than 50 nm.

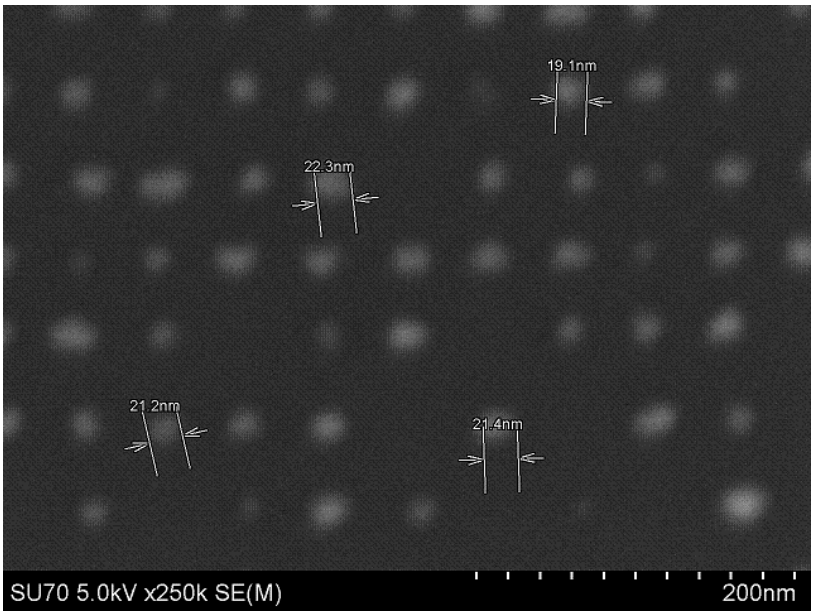

(a)

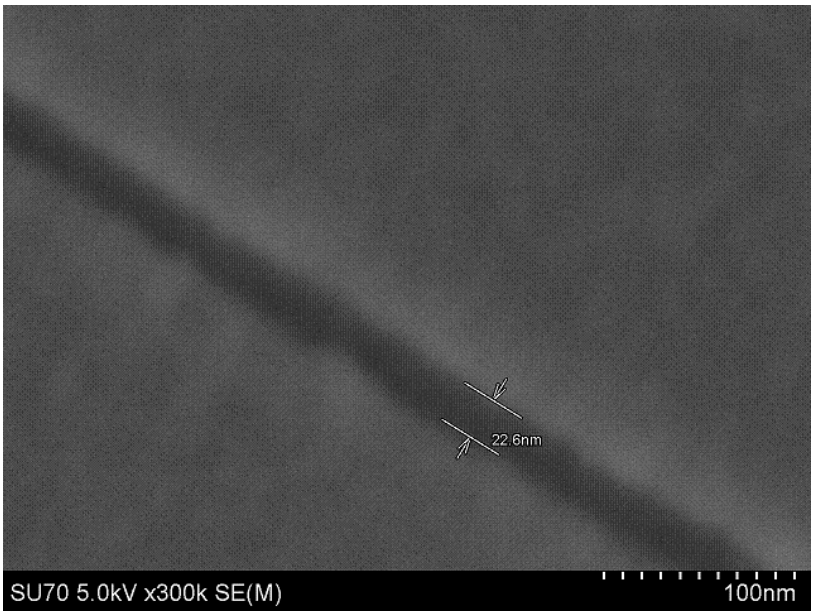

(b)

Figure 5.2: Dots and lines fabricated by electron-beam lithography and viewed in SEM. (a) ∼20 nm (even less-sized) dots, and (b) ∼20 nm line width.

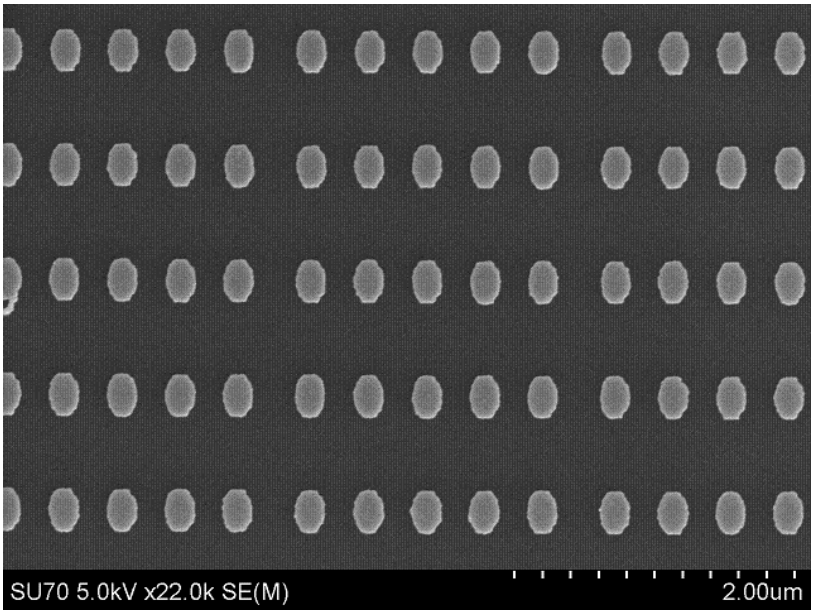

(a)

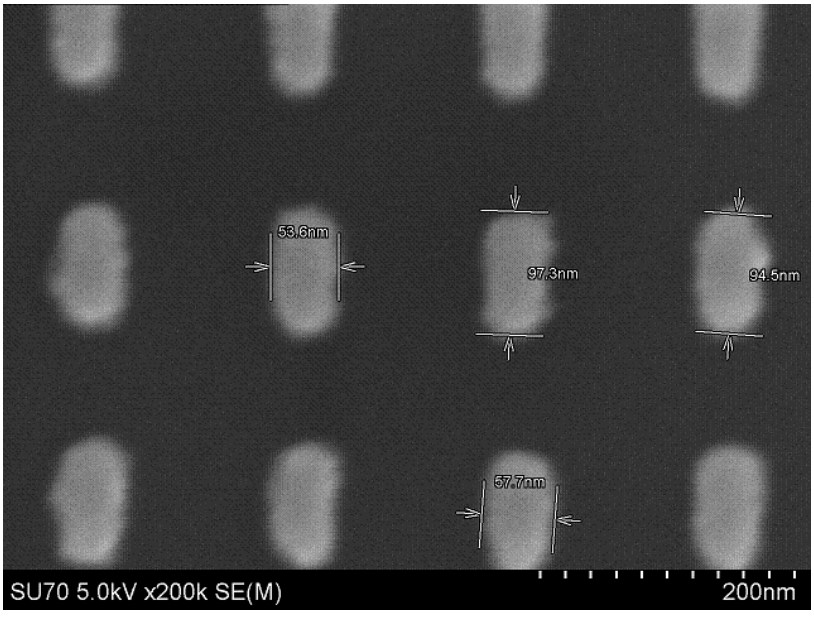

(b)

Figure 5.3: Array of magnets fabricated by electron-beam lithography and viewed in SEM: (a) lateral dimensions ∼300 nm × 200 nm, and (b) lateral dimensions ∼100 nm × 60 nm.

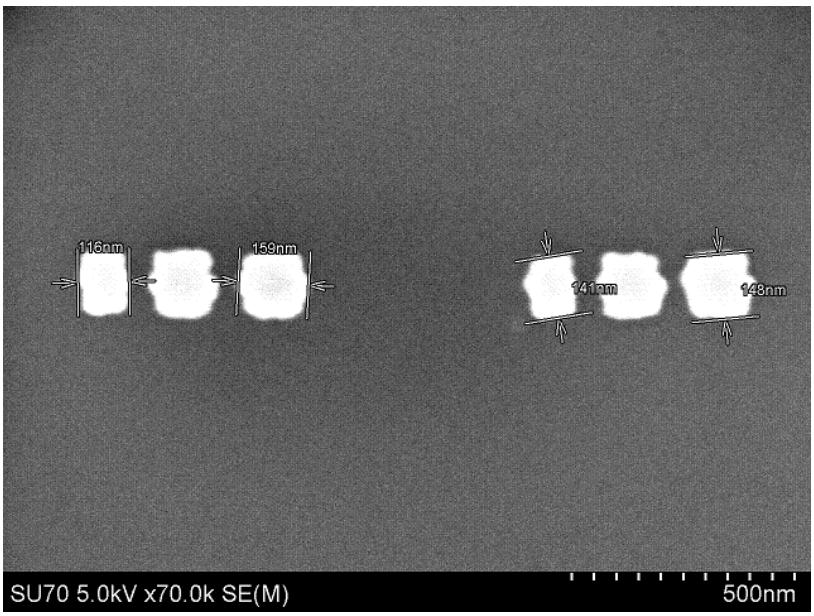

Figure 5.4: Magnets fabricated with small distances in between.

5.2 Magnetic Force Microscopy

Nanomagnets are viewed using tapping mode Magnetic Force Microscopy (MFM) to observe whether they are single-domain or not. An MFM system from VEECO [221] is used and MFM tips from Mikromasch with the following characteristics have been utilized: Ultrasharp Magnetic Si cantilevers, MSC18/FeCoNi/3, Resonant Frequency: 75 KHz, Spring Constant: 3 N/m, Drive amplitude during auto-tune: ∼2.5 V. Fig. 5.5 shows an MFM image of an array of nanomagnets. Some nanomagnets are circled and pointed out to be single-domain as they have one side white and the other side as dark, which is the adopted convention of assuring *single-domain* nanomagnet using MFM.

Such nanomagnets need to be attached to piezoelectric layer to build multiferroic composites and the demonstration of magnetization switching in such devices are deemed as future works [217].

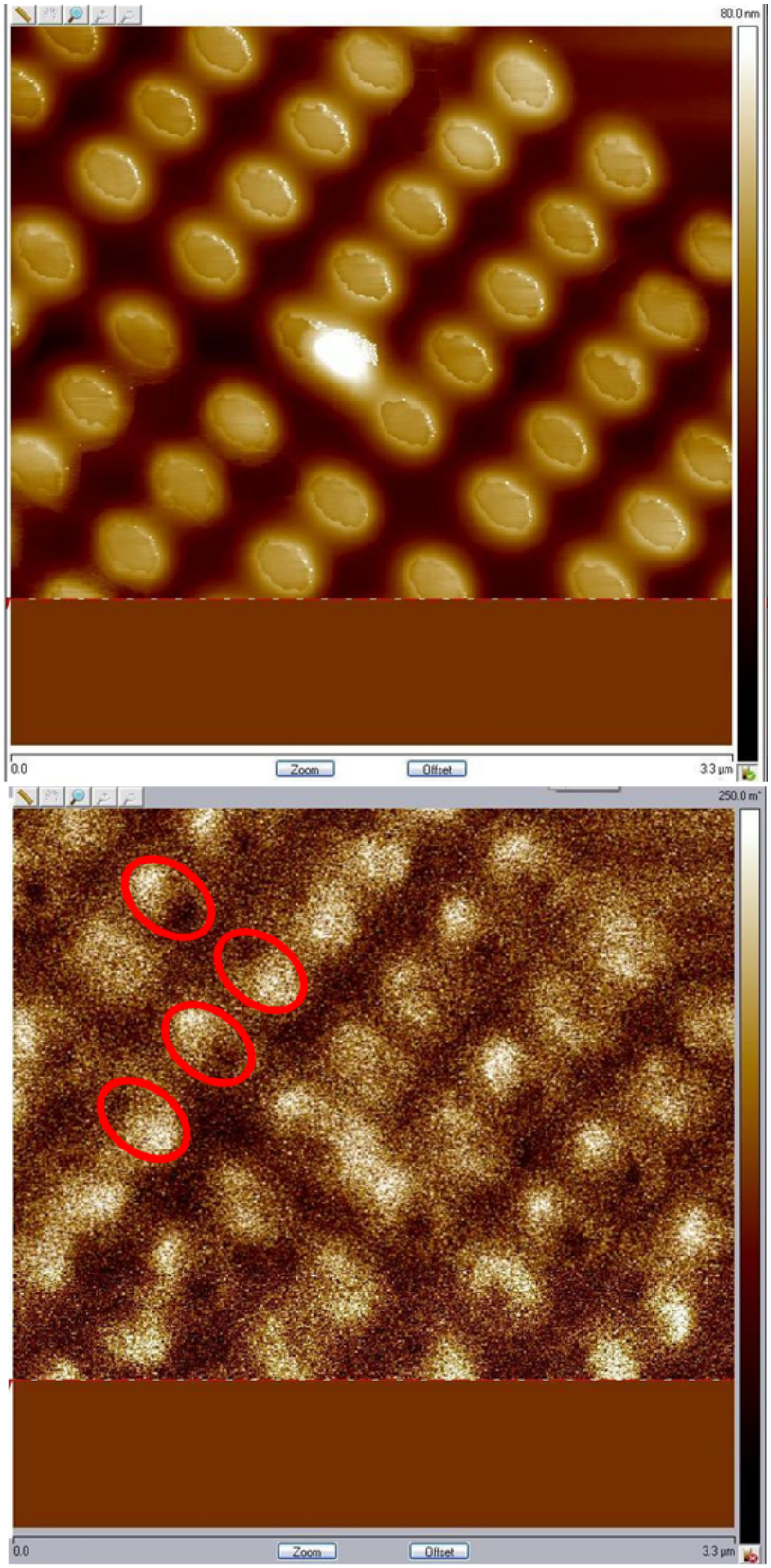

Figure 5.5: Magnetic Force Microscopy (MFM) image of nickel nanomagnets after electron-beam lithography, deposition by e-beam evaporation, and lift-off.

Chapter 6

Discussions and Conclusions

In this chapter, we will first describe the intriguing consequences of the theoretical formulations and simulation results presented in this dissertation. Finally, conclusions will be drawn based on our study.

6.1 Discussions

There can be intriguing consequences because of out-of-plane excursion of magnetization in magnet's full three-dimensional potential landscape. We will discuss in this section such consequences and how they differ from the general perceptions on binary switching and magnetization dynamics.

6.1.1 Binary switching in a "symmetric" potential landscape

Switching between the two stable states of a bistable switch (represented by a symmetric double well potential profile) is usually accomplished by lowering the energy barrier between the wells while tilting the profile towards the desired well, causing an *asymmetry* [1, 2, 3, 4] in the potential landscape. It is necessary to lower the energy barrier and make the monostable well deep enough to resist thermal fluctuations. But, it is the *tilt* in energy profile that is responsible for switching towards the desired direction when the potential landscape is turned back to bistable. The amount of tilt or asymmetry should be large enough to dissuade thermal noise such that switching takes place to the desired direction, however, with a permissible small

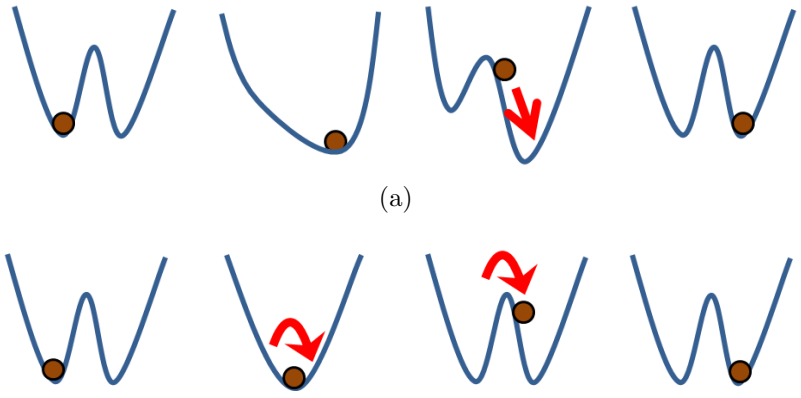

(a)

(b)

Figure 6.1: (a) The potential profile of a bistable switch at various stages of switching from one state to another. This is the usual methodology. Note that the potential landscape is tilted towards the direction of switching alongwith the lowering of energy barrier. (b) In the proposed scheme, the potential profile remains always *symmetric*, i.e., energy barrier is lowered but the potential landscape is *not* tilted to favor the final state. Switching occurs due to *internal* dynamics considering full three-dimensional potential landscape and full three-dimensional motion.

error probability. This well-established methodology is depicted in Fig. 6.1(a).

However, we have seen that the tilt or asymmetry in potential landscape is not necessary for switching for the magnetization in a magnetostrictive nanomagnet, even in the presence of thermal noise. Such intriguing possibility is depicted in Fig. 6.1(b). The potential energy landscape is never tilted to facilitate switching towards the desired direction. Basically, the *internal* dynamics of the system provides an equivalent *asymmetry* to cause error-resilient switching.

This differs from the general perception on binary switching that in a "symmetric" potential landscape, in the presence of thermal fluctuations, the successful switching probability is only 50%. However, such methodology does not consider the full three-dimensional potential landscape and internal dynamics due to out-of-plane excursion. In fact, the out-of-plane dynamics plays the crucial role to ensure such error-resilient switching. The built-in non-equilibrium dynamics of magnetization in full three-dimensional potential landscape as depicted in the Fig. 6.2 makes such intriguing phenomenon feasible. Also, magnetization's motion is aided because of its out-of-plane excursion, which can reduce switching delay by a couple of orders in magnitude (see Fig. 6.3).

We have theoretically demonstrated such possibility in successful magnetization reversal of

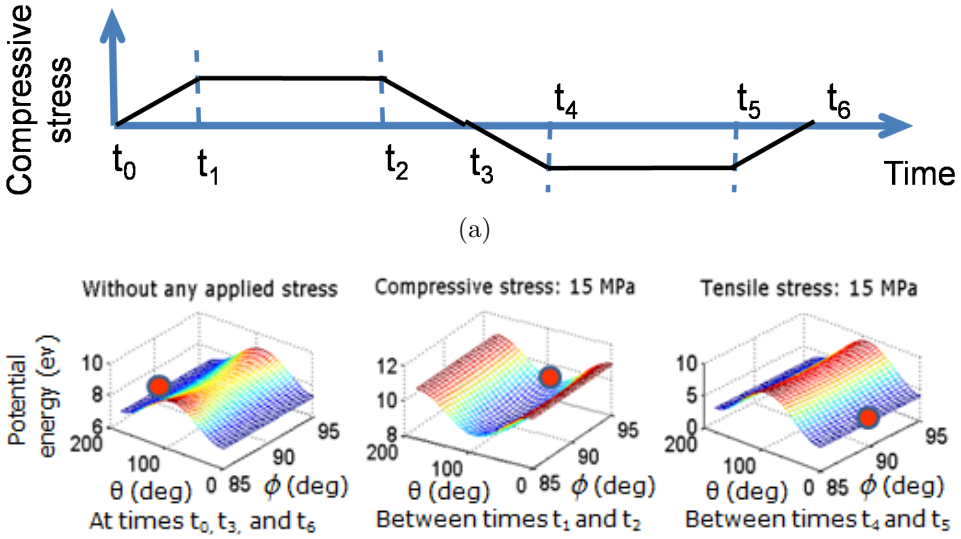

Figure 6.2: Built-in non-equilibrium dynamics makes the switching feasible. (a) Stress-cycle on the magnetostrictive nanomagnet. (b) Potential landscapes of the magnetostrictive nanomagnet in relaxed, compressively stressed, and expansively stressed conditions. Note that the three-dimensional potential landscape has never been made asymmetric to favor the final state during switching. But the magnetization stays out-of-plane, which is nonetheless not a minimum-energy position in the potential landscape, but magnetization has got already shifted out-of-plane due to applied stress and this out-of-plane excursion eventually helps magnetization to switch in its desired direction even in the presence of room temperature thermal noise provided we put up a sufficiently high stress alongwith a fast ramp rate of stress.

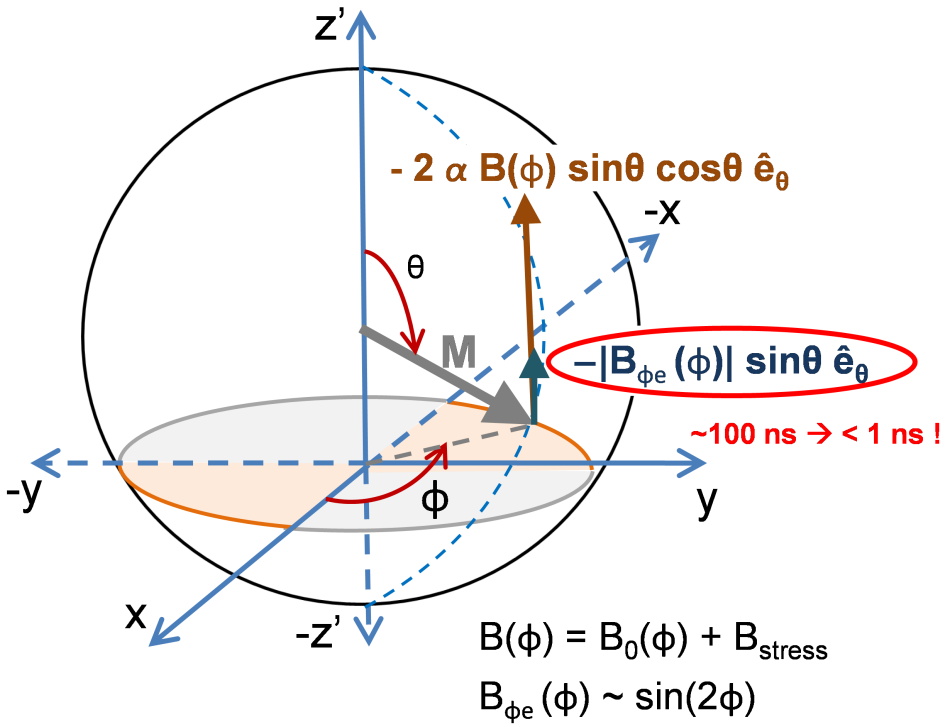

Figure 6.3: Magnetization's motion is aided and switching delay is tremendously decreased because of its out-of-plane excursion. As we have explained earlier, stress rotates magnetization out-of-plane in a "good" quadrant [(90°, 180°) or (270°, 360°)] while switching from $\theta \simeq 180°$ towards $\theta \simeq 0°$. This can decrease the switching time by a couple of orders in magnitude. The quadrant $\phi \in (90°, 180°)$ is chosen for illustration; choice of the other "good" quadrant $\phi \in (270°, 360°)$ is analogous.

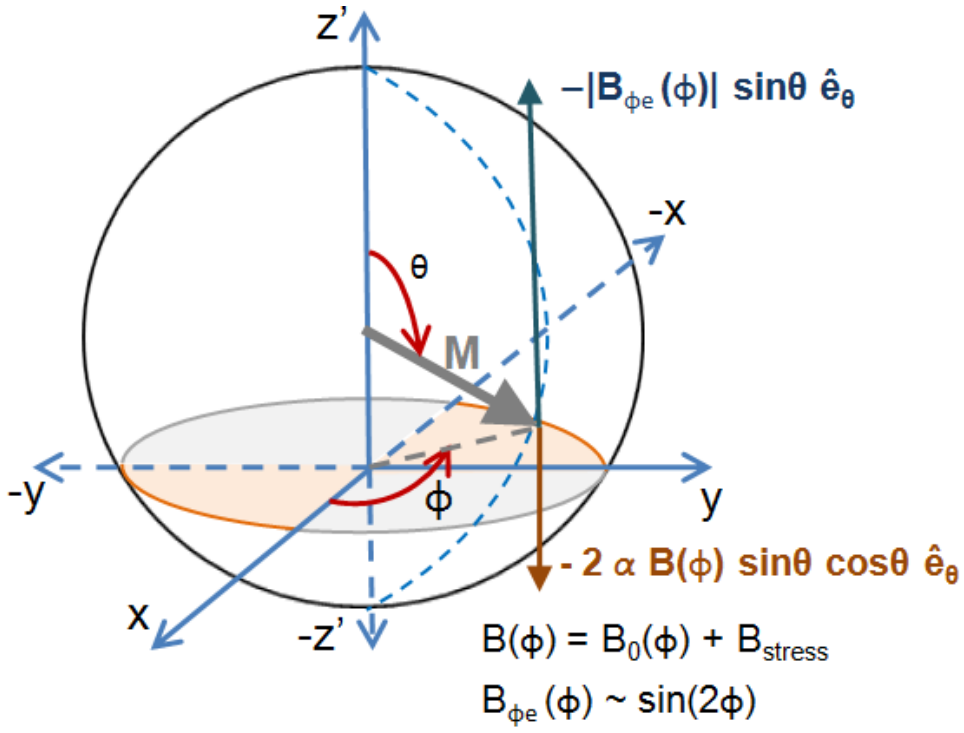

Figure 6.4: Magnetization can rotate towards its correct direction even if stress is withdrawn ahead of time. Magnetization has not yet reached at $\theta = 90°$ but stress is withdrawn/reversed. Magnetization can still switch to the correct direction because magnetization is in a "good" quadrant and there is a motion of magnetization $-|B_{\phi e}(\phi)|sin\theta\,\hat{\mathbf{e}}_\theta$ in its desired direction. The other magnetization's motion $-2\alpha B(\phi)sin\theta cos\theta\,\hat{\mathbf{e}}_\theta$ is counteracting the magnetization since stress has already been withdrawn/reversed. Mathematically, note that $B(\phi)$ has become positive and $cos\theta$ is negative for $\theta \in (90°, 180°)$. The quadrant $\phi \in (90°, 180°)$ is chosen for illustration; choice of the other "good" quadrant $\phi \in (270°, 360°)$ is analogous.

a single magnetostrictive particle, however, the ramification of our study is not limited to the field of nanomagnetism or to the particular shape or material used for the specimen. This can open up a new methodology of binary switching since tilting the potential landscape would not be necessary and we hope that our findings would stimulate experimental research to establish the proposed methodology of binary switching.

6.1.2 Tolerance when magnetization reaches $\theta = 90°$ and stress is ramped down

We point out here that we do need a sensing circuitry to detect when θ reaches around 90° so that stress can be ramped down, which is possible to achieve via the read-line measuring magnetoresistance of the complete MTJ structure. Such sensing circuitry is not uncommon in electronic circuits [211]. Some tolerance is nonetheless required since the sensing circuitry can-

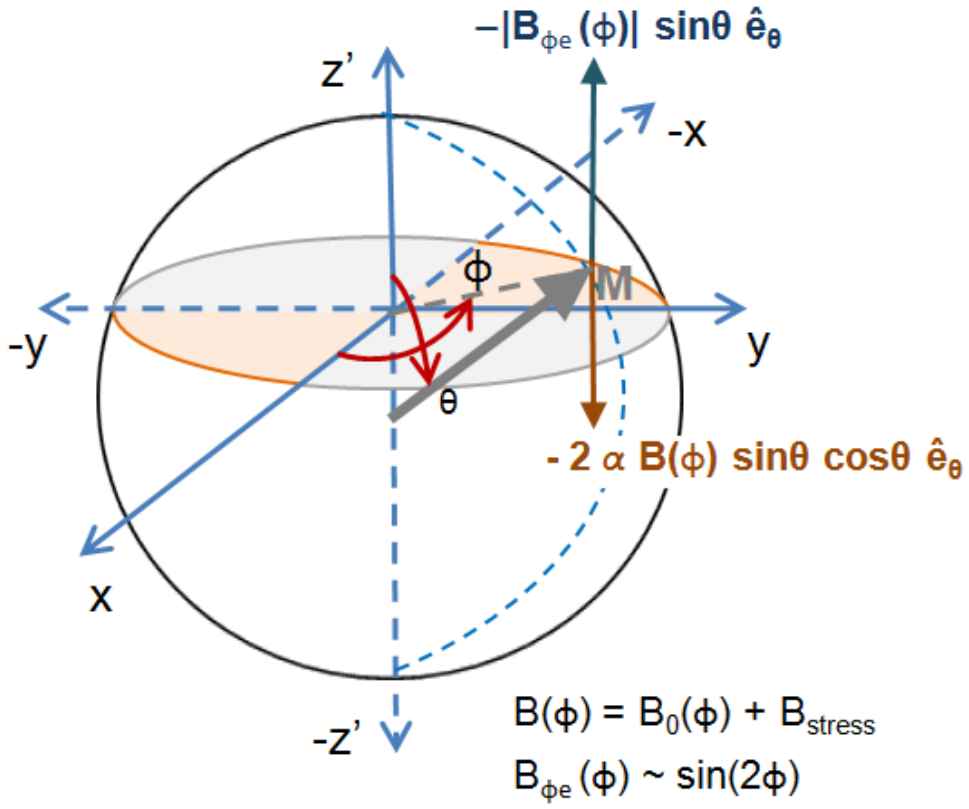

Figure 6.5: Magnetization can rotate towards its correct direction even if stress is withdrawn at a later time. Magnetization has already reached at $\theta = 90°$ but stress is not withdrawn/reversed yet. Magnetization can still switch to the correct direction because magnetization is in a "good" quadrant and there is a motion of magnetization $-|B_{\phi e}(\phi)|sin\theta\,\hat{\mathbf{e}}_\theta$ in its desired direction. The other magnetization's motion $-2\alpha B(\phi)sin\theta cos\theta\,\hat{\mathbf{e}}_\theta$ is counteracting the magnetization since stress has not been withdrawn/reversed yet even magnetization has crossed $\theta = 90°$ towards $\theta \simeq 0°$. Mathematically, note that $B(\phi)$ is still negative and $cos\theta$ is positive for $\theta \in (0°, 90°)$. The quadrant $\phi \in (90°, 180°)$ is chosen for illustration; choice of the other "good" quadrant $\phi \in (270°, 360°)$ is analogous.

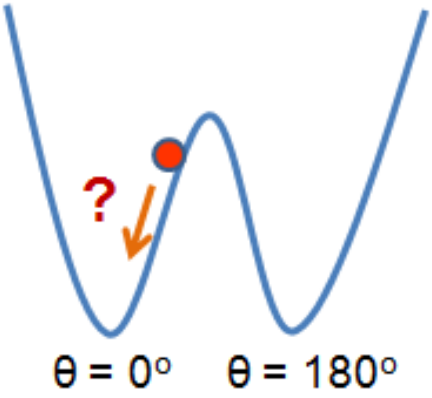

Figure 6.6: Magnetization can backtrack even after it has crossed the hard axis towards its destination. Looking at the two-dimensional plane and considering two-dimensional motion of magnetization, this seems unreasonable in the absence of thermal fluctuations. But, considering full-three dimensional potential landscape and full three-dimensional motion, this would be plausible even in the absence of thermal fluctuations.

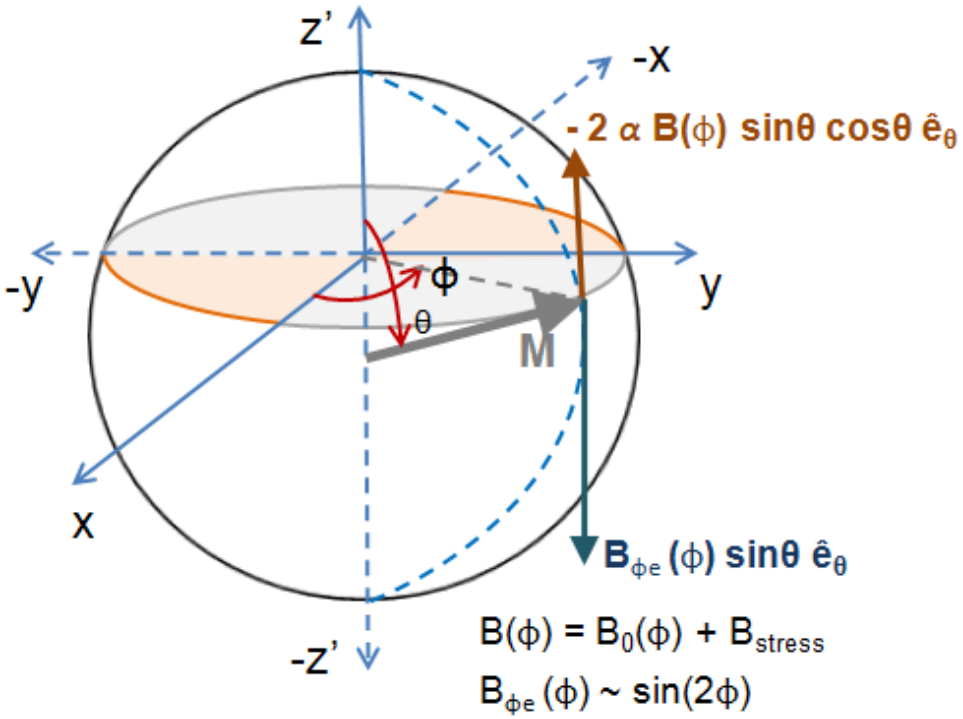

Figure 6.7: Magnetization can backtrack even after it has crossed the hard axis towards its destination. Magnetization can switch to the incorrect direction because magnetization is in a "bad" quadrant and there is a motion of magnetization $B_{\phi e}(\phi)\, sin\theta\, \hat{\mathbf{e}}_\theta$ in the unintended direction. The other magnetization's motion $-2\alpha B(\phi) sin\theta cos\theta\, \hat{\mathbf{e}}_\theta$ is in the intended direction but it may be quite small compared to the other motion and thus magnetization may well backtrack. The quadrant $\phi \in (0°, 90°)$ is chosen for illustration; choice of the other "bad" quadrant $\phi \in (180°, 270°)$ is analogous.

not be perfect. The simulation results (for 10 MPa stress with Terfenol-D as magnetostrictive layer) show that the internal dynamics works correctly as long as the stress is ramped down when θ is in the interval [75°, 125°], i.e. it does not have to be exactly 90°. Such scenarios are depicted in the Figs. 6.4 and 6.5. The main reasoning behind such happening is the out-of-plane excursion of magnetization in the "good" quadrants.

6.1.3 Backtracking of magnetization even after it crosses the hard axis

This is one more intriguing phenomenon that apears while considering the out-of-plane excursion of magnetization. Fig. 6.6 shows that magnetization has crossed the hard axis ($\theta = 90°$) towards its destination ($\theta \simeq 0°$). The question is whether magnetization can successfully traverse towards its destination (discarding thermal fluctuations to point out the phenomenon). Considering just in-plane magnetization dynamics, this seems unreasonable but considering full

three-dimensional magnetization dynamics, the switching may fail. This happens due to the internal torque generated due to out-of-plane excursion of magnetization in a "bad" quadrant as depicted in the Fig. 6.7.

6.2 Conclusions

Multiferroic devices are intriguing in respect to both basic physics and applied physics. Some intriguing basic physical phenomena, which differ from the general perceptions on binary switching and magnetization dynamics, have been observed and explained by carefully formulating the theory and analyzing the simulation results. The dynamics show rich and complex behaviors. On the applied physics arena, utilizing multiferroic composites for the purpose of room-temperature computing can be so energy-efficient that it can be powered solely by energy harvested from the environment. Therefore, they are ideal for medically implanted devices which draw energy solely from the patient's body movements, or even energy radiated by 3G networks and television stations. Also, the switching dynamics is adequately fast for general-purpose computing. This is an unprecedented opportunity in ultra-low-energy computing and can perpetuate Moore's law to beyond the year 2020. Successful experimental demonstration will pave the way for our future nanoelectronics.

Bibliography

[1] R. Landauer. Irreversibility and heat generation in the computing process. *IBM J. Res. Dev.*, 5(3):183–191, 1961.

[2] R. W. Keyes and R. Landauer. Minimal energy dissipation in logic. *IBM J. Res. Dev.*, 14(2):152–157, 1970.

[3] C. H. Bennett. The thermodynamics of computation - a review. *Int. J. Theor. Phys.*, 21(12):905–940, 1982.

[4] E. C. Stoner and E. P. Wohlfarth. A mechanism of magnetic hysteresis in heterogeneous alloys. *Phil. Trans. Roy. Soc. A (London)*, 240:599–642, 1948.

[5] R. Landauer. Uncertainty principle and minimal energy dissipation in the computer. *Int. J. Theor. Phys.*, 21(3):283–297, 1982.

[6] C. Shannon. The mathematical theory of communication. *The Bell System Technical Journal*, 27(7):379–423, 1948.

[7] R. Landauer. Minimal energy requirements in communication. *Science*, 272(5270):1914, 1996.

[8] J. D. Meindl and J. A. Davis. The fundamental limit on binary switching energy for terascale integration (tsi). *IEEE J. Solid-State Cir.*, 35(10):1515–1516, 2000.

[9] R. M. Swanson and J. D. Meindl. Ion-implanted complementary mos transistors in low-voltage circuits. *IEEE J. Solid-State Cir.*, 7(2):146–153, 1972.

[10] V. V. Zhirnov, R. K. Cavin, J. A. Hutchby, and G. I. Bourianoff. Limits to binary logic switch scaling-a gedanken model. *Proc. IEEE*, 9(11):1934–1939, 2003.

[11] R. K. Cavin, V. V. Zhirnov, J. A. Hutchby, and G. I. Bourianoff. Energy barriers, demons, and minimum energy operation of electronic devices (plenary paper). In *Proceedings of SPIE*, volume 5844, page 1, 2005.

[12] K. K. Likharev. Classical and quantum limitations on energy consumption in computation. *Int. J. Theor. Phys.*, 21(3):311–326, 1982.

[13] K. K. Likharev and A. N. Korotkov. "single-electron parametron": Reversible computation in a discrete-state system. *Science*, 273(5276):763, 1996.

[14] C. H. Bennett. Logical reversibility of computation. *IBM J. Res. Dev.*, 17(6):525–532, 1973.

[15] T. Toffoli. Reversible computing. *Automata, Languages and Programming*, pages 632–644, 1980.

[16] E. Fredkin and T. Toffoli. Conservative logic. *Int. J. Theor. Phys.*, 21(3):219–253, 1982.

[17] D. B. Tuckerman and R. F. W. Pease. Implications of high performance heat sinking for electron devices. *IEEE Trans. Electron. Dev.*, 28(10):1230–1231, 1981.

[18] G. E. Moore. Cramming More Components onto Integrated Circuits. *Proc. IEEE*, 86(1):82–85, January 1998.

[19] G. E. Moore. Progress in Digital Integrated Electronics. *International Electron Devices Meeting, IEEE*, pages 11–13, 1975.

[20] R. D. Isaac. The future of CMOS technology. *IBM J. Res. Dev.*, 44(3):369–378, May 2000.

[21] P. Chaparro, J. Gonzlez, G. Magklis, Q. Cai, and A. Gonzlez. Understanding the thermal implications of multi-core architectures. *IEEE Transactions on Parallel and Distributed Systems*, pages 1055–1065, 2007.

[22] S. Bandyopadhyay, B. Das, and A. E. Miller. Supercomputing with spin-polarized single electrons in a quantum coupled architecture. *Nanotechnology*, 5:113, 1994.

[23] S. A. Wolf, D. D. Awschalom, R. A. Buhrman, J. M. Daughton, S. Von Molnar, M. L. Roukes, A. Y. Chtchelkanova, and D. M. Treger. Spintronics: A spin-based electronics vision for the future. *Science*, 294(5546):1488, 2001.

[24] S. Bandyopadhyay and M. Cahay. *Introduction to spintronics*. CRC Press, 2008.

[25] S. Bandyopadhyay. Power dissipation in spintronic devices: A general perspective. *Journal of Nanoscience and Nanotechnology*, 7(1):168–180, 2007.

[26] M. Cahay and S. Bandyopadhyay. An electron's spin—Part I. *Potentials, IEEE*, 28(3):31–35, 2009.

[27] S. Pramanik, C. G. Stefanita, S. Patibandla, S. Bandyopadhyay, K. Garre, N. Harth, and M. Cahay. Observation of extremely long spin relaxation times in an organic nanowire spin valve. *Nature Nanotech.*, 2(4):216–219, 2007.

[28] D. E. Nikonov, G. I. Bourianoff, and P. A. Gargini. Power dissipation in spintronic devices out of thermodynamic equilibrium. *J. Supercond. Novel Magn.*, 19(6):497–513, 2006.

[29] S. Datta and B. Das. Electronic analog of the electro-optic modulator. *Appl. Phys. Lett.*, 56(7):665–667, 1990.

[30] S. Bandyopadhyay. Computing with spins: from classical to quantum computing. *Superlatt. Miscrostruct.*, 37(2):77–86, 2005.

[31] S. Bandyopadhyay and M. Cahay. Electron spin for classical information processing: a brief survey of spin-based logic devices, gates and circuits. *Nanotechnology*, 20:412001, 2009.

[32] S. Sugahara and J. Nitta. Spin-transistor electronics: An overview and outlook. *Proc. IEEE*, 98(12):2124–2154, 2010.

[33] E. C. Stoner and E. P. Wohlfarth. A mechanism of magnetic hysteresis in heterogeneous alloys. *IEEE Trans. Magn.*, 27(4):3475–3518, 2005.

[34] S. Chikazumi. *Physics of Magnetism*. Wiley New York, 1964.

[35] R. P. Cowburn, D. K. Koltsov, A. O. Adeyeye, M. E. Welland, and D. M. Tricker. Single-domain circular nanomagnets. *Phys. Rev. Lett.*, 83(5):1042–1045, 1999.

[36] W. F. Brown. The fundamental theorem of fine ferromagnetic particle theory. *J. Appl. Phys.*, 39:993, 1968.

[37] R. P. Cowburn and M. E. Welland. Phase transitions in planar magnetic nanostructures. *Appl. Phys. Lett.*, 72:2041, 1998.

[38] R. P. Cowburn and M. E. Welland. Micromagnetics of the single-domain state of square ferromagnetic nanostructures. *Phys. Rev. B*, 58(14):9217, 1998.

[39] G. A. Prinz. Magnetoelectronics. *Science*, 282(5394):1660–1663, Nov 27 1998.

[40] C. Chappert, A. Fert, and F. N. Van Dau. The emergence of spin electronics in data storage. *Nature Mater.*, 6(11):813–823, 2007.

[41] S. A. Wolf, J. Lu, M. R. Stan, E. Chen, and D. M. Treger. The promise of nanomagnetics and spintronics for future logic and universal memory. *Proc. IEEE*, 98(12):2155–2168, 2010.

[42] S. Salahuddin and S. Datta. Interacting systems for self-correcting low power switching. *Appl. Phys. Lett.*, 90:093503, 2007.

[43] K. B. Hathaway and A. E. Clark. Magnetostrictive materials. *MRS Bulletin*, 18(4):34–41, 1993.

[44] http://aml.seas.ucla.edu/research/areas/magnetostrictive/overview.htm.

[45] M. N. Baibich, J. M. Broto, A. Fert, F. N. Van Dau, F. Petroff, P. Etienne, G. Creuzet, A. Friederich, and J. Chazelas. Giant magnetoresistance of (001) Fe/(001) Cr magnetic superlattices. *Phys. Rev. Lett.*, 61(21):2472–2475, 1988.

[46] J. Barnaś, A. Fuss, R. E. Camley, P. Grünberg, and W. Zinn. Novel magnetoresistance effect in layered magnetic structures: Theory and experiment. *Phys. Rev. B*, 42(13):8110, 1990.

[47] P. Grünberg, R. Schreiber, Y. Pang, M. B. Brodsky, and H. Sowers. Layered magnetic structures: Evidence for antiferromagnetic coupling of fe layers across cr interlayers. *Phys. Rev. Lett.*, 57(19):2442–2445, 1986.

[48] S. S. P. Parkin, N. More, and K. P. Roche. Oscillations in exchange coupling and magnetoresistance in metallic superlattice structures: Co/Ru, Co/Cr, and Fe/Cr. *Phys. Rev. Lett.*, 64(19):2304–2307, 1990.

[49] S. S. P. Parkin, R. Bhadra, and K. P. Roche. Oscillatory magnetic exchange coupling through thin copper layers. *Phys. Rev. Lett.*, 66(16):2152–2155, 1991.

[50] A. Fert. Nobel lecture: Origin, development, and future of spintronics. *Rev. Mod. Phys.*, 80(4):1517, 2008.

[51] M. Julliere. Tunneling between ferromagnetic films. *Phys. Lett. A*, 54(3):225–226, 1975.

[52] R. Meservey and P. M. Tedrow. Spin-polarized electron tunneling. *Physics reports*, 238:173–243, 1994.

[53] J. S. Moodera and L. R. Kinder. Ferromagnetic-insulator-ferromagnetic tunneling: Spin-dependent tunneling and large magnetoresistance in trilayer junctions (invited). *J. Appl. Phys.*, 79(8):4724–4729, 2009.

[54] W. H. Butler. Tunneling magnetoresistance from a symmetry filtering effect. *Sci. Technol. Adv. Mater.*, 9:014106, 2008.

[55] J. S. Moodera, G. X. Miao, and T. S. Santos. Frontiers in spin-polarized tunneling. *Physics Today*, 63:46, 2010.

[56] W. H. Butler, X. G. Zhang, T. C. Schulthess, and J. M. MacLaren. Spin-dependent tunneling conductance of Fe|MgO|Fe sandwiches. *Phys. Rev. B*, 63(5):54416, 2001.

[57] J. Mathon and A. Umerski. Theory of tunneling magnetoresistance of an epitaxial Fe/MgO/Fe (001) junction. *Phys. Rev. B*, 63(22):220403, 2001.

[58] W. H. Butler, X. G. Zhang, T. C. Schulthess, and J. M. MacLaren. Reduction of electron tunneling current due to lateral variation of the wave function. *Phys. Rev. B*, 63(9):092402, 2001.

[59] J. Mathon and A. Umerski. Theory of tunneling magnetoresistance in a junction with a nonmagnetic metallic interlayer. *Phys. Rev. B*, 60(2):1117, 1999.

[60] X. G. Zhang and W. H. Butler. Large magnetoresistance in bcc Co/MgO/Co and FeCo/MgO/FeCo tunnel junctions. *Phys. Rev. B*, 70(17):172407, 2004.

[61] X. G. Zhang, W. H. Butler, and A. Bandyopadhyay. Effects of the iron-oxide layer in Fe-FeO-MgO-Fe tunneling junctions. *Phys. Rev. B*, 68(9):092402, 2003.

[62] C. Zhang, X. G. Zhang, P. S. Krstić, H. Cheng, W. H. Butler, and J. M. MacLaren. Electronic structure and spin-dependent tunneling conductance under a finite bias. *Phys. Rev. B*, 69(13):134406, 2004.

[63] S. S. P. Parkin, C. Kaiser, A. Panchula, P. M. Rice, B. Hughes, M. G. Samant, and S. H. Yang. Giant tunnelling magnetoresistance at room temperature with MgO (100) tunnel barriers. *Nature Mater.*, 3(12):862–867, 2004.

[64] S. Yuasa, T. Nagahama, A. Fukushima, Y. Suzuki, and K. Ando. Giant room-temperature magnetoresistance in single-crystal Fe/MgO/Fe magnetic tunnel junctions. *Nature Mater.*, 3(12):868–871, 2004.

[65] R. A. De Groot, F. M. Mueller, P. G. Van Engen, and K. H. J. Buschow. New class of materials: Half-metallic ferromagnets. *Phys. Rev. Lett.*, 50(25):2024–2027, 1983.

[66] H. Van Leuken and R. A. De Groot. Half-metallic antiferromagnets. *Phys. Rev. Lett.*, 74(7):1171–1173, 1995.

[67] H. Akai and M. Ogura. Half-metallic diluted antiferromagnetic semiconductors. *Phys. Rev. Lett.*, 97(2):26401, 2006.

[68] M. I. Katsnelson, V. Y. Irkhin, L. Chioncel, A. I. Lichtenstein, and R. A. De Groot. Half-metallic ferromagnets: From band structure to many-body effects. *Rev. Mod. Phys.*, 80(2):315, 2008.

[69] W. E. Pickett and J. S. Moodera. Half metallic magnets. *Physics Today*, 54:39, 2001.

[70] T. Graf, S. S. P. Parkin, and C. Felser. Heusler compounds–a material class with exceptional properties. *IEEE Trans. Magn.*, 47(2):367–373, 2011.

[71] T. Graf, C. Felser, and S. S. P. Parkin. Simple rules for the understanding of heusler compounds. *Prog. Solid State Chem.*, 2011.

[72] J. H. Park, E. Vescovo, H. J. Kim, C. Kwon, R. Ramesh, and T. Venkatesan. Direct evidence for a half-metallic ferromagnet. *Nature*, 392(6678):794–796, 1998.

[73] D. Xiao, Y. Yao, W. Feng, J. Wen, W. Zhu, X. Q. Chen, G. M. Stocks, and Z. Zhang. Half-heusler compounds as a new class of three-dimensional topological insulators. *Phys. Rev. Lett.*, 105(9):96404, 2010.

[74] P. Mavropoulos, K. Sato, R. Zeller, P. H. Dederichs, V. Popescu, and H. Ebert. Effect of the spin-orbit interaction on the band gap of half metals. *Phys. Rev. B*, 69(5):054424, 2004.

[75] P. Mavropoulos, I. Galanakis, V. Popescu, and P. H. Dederichs. The influence of spin-orbit coupling on the band gap of heusler alloys. *J. Phys. D: Cons. Mat.*, 16:S5759, 2004.

[76] S. S. P. Parkin, K. P. Roche, M. G. Samant, P. M. Rice, R. B. Beyers, R. E. Scheuerlein, E. J. O'Sullivan, S. L. Brown, J. Bucchigano, and D. W. Abraham. Exchange-biased magnetic tunnel junctions and application to nonvolatile magnetic random access memory (invited). *J. Appl. Phys.*, 85:5828, 1999.

[77] S. S. P. Parkin, X. Jiang, C. Kaiser, A. Panchula, K. P. Roche, and M. G. Samant. Magnetically engineered spintronic sensors and memory. *Proc. IEEE*, 91(5):661–680, 2003.

[78] W. J. Gallagher and S. S. P. Parkin. Development of the magnetic tunnel junction mram at ibm: from first junctions to a 16-Mb MRAM demonstrator chip. *IBM J. Res. Dev.*, 50(1):5–23, 2006.

[79] B. Behin-Aein, S. Salahuddin, and S. Datta. Switching energy of ferromagnetic logic bits. *IEEE Trans. Nanotech.*, 8(4):505–514, 2009.

[80] M. T. Alam, M. J. Siddiq, G. H. Bernstein, M. T. Niemier, W. Porod, and X. S. Hu. On-chip clocking for nanomagnet logic devices. *IEEE Trans. Nanotech.*, 9(3):348–351, 2010.

[81] G. H. Bernstein, A. Imre, V. Metlushko, A. Orlov, L. Zhou, L. Ji, G. Csaba, and W. Porod. Magnetic QCA systems. *Microelectron. J.*, 36(7):619–624, 2005.

[82] A. O. Orlov, I. Amlani, G. H. Bernstein, C. S. Lent, and G. L. Snider. Realization of a functional cell for quantum-dot cellular automata. *Science*, 277(5328):928, 1997.

[83] G. Csaba, A. Imre, G. H. Bernstein, W. Porod, and V. Metlushko. Nanocomputing by field-coupled nanomagnets. *IEEE Trans. Nanotech.*, 1(4):209–213, 2002.

[84] G. Csaba and W. Porod. Simulation of field coupled computing architectures based on magnetic dot arrays. *J. Comput. Electron.*, 1(1):87–91, 2002.

[85] A. Imre, G. Csaba, L. Ji, A. Orlov, G. H. Bernstein, and W. Porod. Majority logic gate for magnetic quantum-dot cellular automata. *Science*, 311(5758):205–208, 2006.

[86] R. K. Kummamuru, A. O. Orlov, R. Ramasubramaniam, C. S. Lent, G. H. Bernstein, and G. L. Snider. Operation of a quantum-dot cellular automata (QCA) shift register and analysis of errors. *IEEE Trans. Electron. Dev.*, 50(9):1906–1913, 2003.

[87] M. T. Niemier, M. T. Alam, X. S. Hu, G. H. Bernstein, W. Porod, M. Putney, and J. DeAngelis. Clocking structures and power analysis for nanomagnet-based logic devices. In *Proceedings of the 2007 international symposium on Low power electronics and design*, pages 26–31. ACM New York, NY, USA, 2007.

[88] G. Csaba, W. Porod, P. Lugli, and A. I. Csurgay. Activity in field-coupled nanomagnet arrays. *Int. J. Cir. Th. Appl.*, 35(3):281–293, 2007.

[89] G. Csaba, P. Lugli, and W. Porod. Power dissipation in nanomagnetic logic devices. In *Nanotechnology, 2004. 4th IEEE Conference on*, pages 346–348. IEEE, 2005.

[90] M. T. Niemier, X. S. Hu, M. Alam, G. Bernstein, W. Porod, M. Putney, and J. DeAngelis. Clocking structures and power analysis for nanomagnet-based logic devices. In *Low Power Electronics and Design (ISLPED), 2007 ACM/IEEE International Symposium on*, pages 26–31. IEEE, 2007.

[91] A. O. Orlov, I. Amlani, G. Toth, C. S. Lent, G. H. Bernstein, and G. L. Snider. Experimental demonstration of a binary wire for quantum-dot cellular automata. *Appl. Phys. Lett.*, 74(19):2875–2877, 2009.

[92] STMicroelectronics. *CORE9GPLL_HCMOS9_TEC_4.0 Databook UNICAD2.4*, June 2003.

[93] J. C. Slonczewski. Current-driven excitation of magnetic multilayers. *J. Magn. Magn. Mater.*, 159(1-2):L1–L7, 1996.

[94] L. Berger. Emission of spin waves by a magnetic multilayer traversed by a current. *Phys. Rev. B*, 54(13):9353–9358, 1996.

[95] J. Z. Sun. Spin-current interaction with a monodomain magnetic body: A model study. *Phys. Rev. B*, 62(1):570–578, 2000.

[96] D. E. Nikonov, G. I. Bourianoff, G. E. Rowlands, and I. N. Krivorotov. Strategies and tolerances of spin transfer torque switching. *J. Appl. Phys.*, 107(11):113910, 2010.

[97] J. Z. Sun. Spin angular momentum transfer in current-perpendicular nanomagnetic junctions. *IBM J. Res. Dev.*, 50(1):81–100, 2006.

[98] J. A. Katine, F. J. Albert, R. A. Buhrman, E. B. Myers, and D. C. Ralph. Current-driven magnetization reversal and spin-wave excitations in Co/Cu/Co pillars. *Phys. Rev. Lett.*, 84(14):3149–3152, 2000.

[99] G. D. Fuchs, J. A. Katine, S. I. Kiselev, D. Mauri, K. S. Wooley, D. C. Ralph, and R. A. Buhrman. Spin torque, tunnel-current spin polarization, and magnetoresistance in mgo magnetic tunnel junctions. *Phys. Rev. Lett.*, 96(18):186603, 2006.

[100] I. Theodonis, N. Kioussis, A. Kalitsov, M. Chshiev, and W. H. Butler. Anomalous bias dependence of spin torque in magnetic tunnel junctions. *Phys. Rev. Lett.*, 97(23):237205, 2006.

[101] A. Kalitsov, I. Theodonis, N. Kioussis, M. Chshiev, W. H. Butler, and A. Vedyayev. Spin-polarized current-induced torque in magnetic tunnel junctions. *J. Appl. Phys.*, 99:08G501, 2006.

[102] A. Kalitsov, M. Chshiev, I. Theodonis, N. Kioussis, and W. H. Butler. Spin-transfer torque in magnetic tunnel junctions. *Phys. Rev. B*, 79(17):174416, 2009.

[103] Y. H. Tang, N. Kioussis, A. Kalitsov, W. H. Butler, and R. Car. Influence of asymmetry on bias behavior of spin torque. *Phys. Rev. B*, 81(5):054437, 2010.

[104] J. C. Slonczewski and J. Z. Sun. Theory of voltage-driven current and torque in magnetic tunnel junctions. *J. Magn. Magn. Mater.*, 310(2):169–175, 2007.

[105] C. Heiliger and M. D. Stiles. Ab initio studies of the spin-transfer torque in magnetic tunnel junctions. *Phys. Rev. Lett.*, 100(18):186805, 2008.

[106] P. M. Haney, R. A. Duine, A. S. Nunez, and A. H. MacDonald. Current-induced torques in magnetic metals: Beyond spin-transfer. *J. Magn. Magn. Mater.*, 320(7):1300–1311, 2008.

[107] S. Salahuddin, D. Datta, and S. Datta. Spin transfer torque as a non-conservative pseudo-field. *arXiv:0811.3472*, 2008.

[108] D. Datta, B. Behin-Aein, S. Salahuddin, and S. Datta. Voltage asymmetry of spin-transfer torques. *IEEE Trans. Nanotech.*, (99):1–1, 2009.

[109] K. Roy, S. Bandyopadhyay, and J. Atulasimha. Metastable state in a shape-anisotropic single-domain nanomagnet subjected to spin transfer torque. *arXiv:1106.1215*, 2011.

[110] H. Kubota, A. Fukushima, K. Yakushiji, T. Nagahama, S. Yuasa, K. Ando, H. Maehara, Y. Nagamine, K. Tsunekawa, and D. D. Djayaprawira. Quantitative measurement

of voltage dependence of spin-transfer torque in mgo-based magnetic tunnel junctions. *Nature Phys.*, 4(1):37–41, 2008.

[111] J. C. Sankey, Y. T. Cui, J. Z. Sun, J. C. Slonczewski, R. A. Buhrman, and D. C. Ralph. Measurement of the spin-transfer-torque vector in magnetic tunnel junctions. *Nature Phys.*, 4(1):67–71, 2008.

[112] A. M. Deac, A. Fukushima, H. Kubota, H. Maehara, Y. Suzuki, S. Yuasa, Y. Nagamine, K. Tsunekawa, D. D. Djayaprawira, and N. Watanabe. Bias-driven high-power microwave emission from mgo-based tunnel magnetoresistance devices. *Nature Phys.*, 4(10):803–809, 2008.

[113] D. C. Ralph and M. D. Stiles. Spin transfer torques. *J. Magn. Magn. Mater.*, 320(7):1190–1216, 2008.

[114] K. Yagami, A. A. Tulapurkar, A. Fukushima, and Y. Suzuki. Low-current spin-transfer switching and its thermal durability in a low-saturation-magnetization nanomagnet. *Appl. Phys. Lett.*, 85(23):5634–5636, 2004.

[115] H. Kubota, A. Fukushima, K. Yakushiji, S. Yakata, S. Yuasa, K. Ando, M. Ogane, Y. Ando, and T. Miyazaki. Reduction in switching current using a low-saturation magnetization Co-Fe-(Cr, V)-B free layer in MgO-based magnetic tunnel junctions. *J. Appl. Phys.*, 105(7):07D117–07D117–3, 2009.

[116] K. Roy, S. Bandyopadhyay, J. Atulasimha, K. Munira, and A. Ghosh. Energy dissipation and switching delay in spin-transfer-torque switching of nanomagnets with low-saturation magnetization in the presence of thermal fluctuations. *arXiv:1107.0387*, 2011.

[117] O. Wessely, A. Umerski, and J. Mathon. Theory of spin-transfer torque in the current-in-plane geometries. *Phys. Rev. B*, 80(1):14419, 2009.

[118] T. Yang, T. Kimura, and Y. Otani. Giant spin-accumulation signal and pure spin-current-induced reversible magnetization switching. *Nature Phys.*, 4(11):851–854, 2008.

[119] J. Z. Sun, M. C. Gaidis, E. J. O'Sullivan, E. A. Joseph, G. Hu, D. W. Abraham, J. J. Nowak, P. L. Trouilloud, Y. Lu, and S. L. Brown. A three-terminal spin-torque-driven magnetic switch. *Appl. Phys. Lett.*, 95:083506, 2009.

[120] A. Ney, C. Pampuch, R. H. Koch, and K. H. Ploog. Programmable computing with a single magnetoresistive element. *Nature*, 425(6957):485–487, 2003.

[121] H. Dery, P. Dalal, L. Cywinski, and L. J. Sham. Spin-based logic in semiconductors for reconfigurable large-scale circuits. *Nature*, 447(7144):573–576, 2007.

[122] B. Behin-Aein, D. Datta, S. Salahuddin, and S. Datta. Proposal for an all-spin logic device with built-in memory. *Nature Nanotech.*, 5(4):266–270, 2010.

[123] H. Meng, J. Wang, and J. P. Wang. A spintronics full adder for magnetic cpu. *IEEE Elec. Dev. Lett.*, 26(6):360–362, 2005.

[124] J. Wang, H. Meng, and J. P. Wang. Programmable spintronics logic device based on a magnetic tunnel junction element. *J. Appl. Phys.*, 97:10D509, 2005.

[125] S. Matsunaga, J. Hayakawa, S. Ikeda, K. Miura, H. Hasegawa, T. Endoh, H. Ohno, and T. Hanyu. Fabrication of a nonvolatile full adder based on logic-in-memory architecture using magnetic tunnel junctions. *Appl. Phys. Exp.*, 1(9):1301, 2008.

[126] F. Ren and D. Markovic. True energy-performance analysis of the MTJ-based logic-in-memory architecture (1-bit full adder). *IEEE Trans. Elec. Dev.*, 57(5):1023–1028, 2010.

[127] D. E. Nikonov, G. I. Bourianoff, and T. Ghani. Nanomagnetic circuits with spin torque majority gates. In *Nanotechnology (IEEE-NANO), 2011 11th IEEE Conference on*, pages 1384–1388. IEEE, 2011.

[128] G. Tatara and H. Kohno. Theory of current-driven domain wall motion: Spin transfer versus momentum transfer. *Phys. Rev. Lett.*, 92(8):86601, 2004.

[129] G. Tatara, H. Kohno, and J. Shibata. Microscopic approach to current-driven domain wall dynamics. *Phys. Rep.*, 468(6):213–301, 2008.

[130] H. Akinaga and H. Ohno. Semiconductor spintronics. *IEEE Trans. Nanotech.*, 1(1):19–31, 2002.

[131] D. D. Awschalom and M. E. Flatte. Challenges for semiconductor spintronics. *Nature Phys.*, 3(3):153–159, 2007.

[132] H. Ohno. Making nonmagnetic semiconductors ferromagnetic. *Science*, 281(5379):951, 1998.

[133] H. Ohno, A. Shen, F. Matsukura, A. Oiwa, A. Endo, S. Katsumoto, and Y. Iye. (Ga, Mn) As: A new diluted magnetic semiconductor based on GaAs. *Appl. Phys. Lett.*, 69:363, 1996.

[134] B. K. Rao and P. Jena. Giant magnetic moments of nitrogen-doped Mn clusters and their relevance to ferromagnetism in Mn-Doped GaN. *Phys. Rev. Lett.*, 89(18):185504, 2002.

[135] M. Yamanouchi, D. Chiba, F. Matsukura, and H. Ohno. Current-induced domain-wall switching in a ferromagnetic semiconductor structure. *Nature*, 428(6982):539–542, 2004.

[136] S. Fukami, T. Suzuki, K. Nagahara, N. Ohshima, Y. Ozaki, S. Saito, R. Nebashi, N. Sakimura, H. Honjo, K. Mori, C. Igarashi, S. Miura, N. Ishiwata, and T. Sugibayashi. Low-current perpendicular domain wall motion cell for scalable high-speed MRAM. In *VLSI Technology, 2009 Symposium on*, pages 230–231. IEEE, 2009.

[137] Y. Ohno, D. K. Young, B. Beschoten, F. Matsukura, H. Ohno, and D. D. Awschalom. Electrical spin injection in a ferromagnetic semiconductor heterostructure. *Nature*, 402(6763):790–792, 1999.

[138] S. Mark, P. Durrenfeld, K. Pappert, L. Ebel, K. Brunner, C. Gould, and L. W. Molenkamp. Fully electrical read-write device out of a ferromagnetic semiconductor. *Phys. Rev. Lett.*, 106(5):57204, 2011.

[139] G. Schmidt, D. Ferrand, L. W. Molenkamp, A. T. Filip, and B. J. Van Wees. Fundamental obstacle for electrical spin injection from a ferromagnetic metal into a diffusive semiconductor. *Phys. Rev. B*, 62(8):4790–4793, 2000.

[140] E. I. Rashba. Theory of electrical spin injection: Tunnel contacts as a solution of the conductivity mismatch problem. *Phys. Rev. B*, 62(24):16267–16270, 2000.

[141] B. T. Jonker, G. Kioseoglou, A. T. Hanbicki, C. H. Li, and P. E. Thompson. Electrical spin-injection into silicon from a ferromagnetic metal/tunnel barrier contact. *Nature Phys.*, 3(8):542–546, 2007.

[142] S. S. P. Parkin, M. Hayashi, and L. Thomas. Magnetic domain-wall racetrack memory. *Science*, 320(5873):190, 2008.

[143] L. Thomas, M. Hayashi, X. Jiang, R. Moriya, C. Rettner, and S. S. P. Parkin. Resonant amplification of magnetic domain-wall motion by a train of current pulses. *Science*, 315(5818):1553, 2007.

[144] M. Hayashi, L. Thomas, R. Moriya, C. Rettner, and S. S. P. Parkin. Current-controlled magnetic domain-wall nanowire shift register. *Science*, 320(5873):209, 2008.

[145] L. Thomas, R. Moriya, C. Rettner, and S. S. P. Parkin. Dynamics of magnetic domain walls under their own inertia. *Science*, 330(6012):1810, 2010.

[146] R. P. Cowburn and D. Petit. Spintronics: turbulence ahead. *Nature Mater.*, 4(10):721–722, 2005.

[147] P. Xu, K. Xia, C. Gu, L. Tang, H. Yang, and J. Li. An all-metallic logic gate based on current-driven domain wall motion. *Nature Nanotech.*, 3(2):97–100, 2008.

[148] D. A. Allwood, G. Xiong, C. C. Faulkner, D. Atkinson, D. Petit, and R. P. Cowburn. Magnetic domain-wall logic. *Science*, 309(5741):1688, 2005.

[149] M. Dawber, K. M. Rabe, and J. F. Scott. Physics of thin-film ferroelectric oxides. *Rev. Mod. Phys.*, 77(4):1083, 2005.

[150] J. Li, B. Nagaraj, H. Liang, W. Cao, C. Lee, and R. Ramesh. Ultrafast polarization switching in thin-film ferroelectrics. *Appl. Phys. Lett.*, 84(7):1174–1176, 2004.

[151] V. Garcia, M. Bibes, L. Bocher, S. Valencia, F. Kronast, A. Crassous, X. Moya, S. Enouz-Vedrenne, A. Gloter, and D. Imhoff. Ferroelectric control of spin polarization. *Science*, 327(5969):1106, 2010.

[152] H. Kohlstedt, N. A. Pertsev, J. R. Contreras, and R. Waser. Theoretical current-voltage characteristics of ferroelectric tunnel junctions. *Phys. Rev. B*, 72(12):125341, 2005.

[153] V. Garcia, S. Fusil, K. Bouzehouane, S. Enouz-Vedrenne, N. D. Mathur, A. Barthélémy, and M. Bibes. Giant tunnel electroresistance for non-destructive readout of ferroelectric states. *Nature*, 460(7251):81–84, 2009.

[154] N. A. Hill. Density functional studies of multiferroic magnetoelectrics. *Annual Review of Materials Research*, 32(1):1–37, 2002.

[155] P. Baettig and N. A. Spaldin. Ab initio prediction of a multiferroic with large polarization and magnetization. *Appl. Phys. Lett.*, 86:012505, 2005.

[156] J. B. Neaton, C. Ederer, U. V. Waghmare, N. A. Spaldin, and K. M. Rabe. First-principles study of spontaneous polarization in multiferroic $BiFeO_3$. *Phys. Rev. B*, 71(1):014113, 2005.

[157] A. P. Levanyuk and D. G. Sannikov. Improper ferroelectrics. *Physics-Uspekhi*, 17(2):199–214, 1974.

[158] N. A. Benedek and C. J. Fennie. Hybrid improper ferroelectricity: a mechanism for controllable polarization-magnetization coupling. *Phys. Rev. Lett.*, 106(10):107204, 2011.

[159] C. W. Nan, M. I. Bichurin, S. Dong, D. Viehland, and G. Srinivasan. Multiferroic magnetoelectric composites: Historical perspective, status, and future directions. *J. Appl. Phys.*, 103:031101, 2008.

[160] W. Eerenstein, N. D. Mathur, and J. F. Scott. Multiferroic and magnetoelectric materials. *Nature*, 442(7104):759–765, 2006.

[161] Ü. Özgür, Y. Alivov, and H. Morkoç. Microwave ferrites, part 2: passive components and electrical tuning. *Journal of Materials Science: Materials in Electronics*, 20(10):911–952, 2009.

[162] F. Zavaliche, H. Zheng, L. Mohaddes-Ardabili, S. Y. Yang, Q. Zhan, P. Shafer, E. Reilly, R. Chopdekar, Y. Jia, and P. Wright. Electric field-induced magnetization switching in epitaxial columnar nanostructures. *Nano Lett.*, 5(9):1793–1796, 2005.

[163] F. Zavaliche, T. Zhao, H. Zheng, F. Straub, M. P. Cruz, P. L. Yang, D. Hao, and R. Ramesh. Electrically assisted magnetic recording in multiferroic nanostructures. *Nano Lett.*, 7(6):1586–1590, 2007.

[164] R. Ramesh and N. A. Spaldin. Multiferroics: progress and prospects in thin films. *Nature Mater.*, 6(1):21–29, 2007.

[165] T. Brintlinger, S. H. Lim, K. H. Baloch, P. Alexander, Y. Qi, J. Barry, J. Melngailis, L. Salamanca-Riba, I. Takeuchi, and J. Cumings. In situ observation of reversible nanomagnetic switching induced by electric fields. *Nano Lett.*, 10(4):1219–1223, 2010.

[166] T. K. Chung, S. Keller, and G. P. Carman. Electric-field-induced reversible magnetic single-domain evolution in a magnetoelectric thin film. *Appl. Phys. Lett.*, 94:132501, 2009.

[167] T. Wu, A. Bur, K. Wong, P. Zhao, C. S. Lynch, P. K. Amiri, K. L. Wang, and G. P. Carman. Electrical control of reversible and permanent magnetization reorientation for magnetoelectric memory devices. *Appl. Phys. Lett.*, 98:262504, 2011.

[168] K. Roy, S. Bandyopadhyay, and J. Atulasimha. Hybrid spintronics and straintronics: A magnetic technology for ultra low energy computing and signal processing. *Appl. Phys. Lett.*, 99(063108):063108, 2011.

[169] K. Roy, S. Bandyopadhyay, and J. Atulasimha. Switching dynamics of a magnetostrictive single-domain nanomagnet subjected to stress. *Phys. Rev. B*, 83(1-15):224412, 2011.

[170] K. Roy, S. Bandyopadhyay, and J. Atulasimha. Binary switching in a symmetric potential landscape. *arXiv:1111.5390*, 2011.

[171] K. Roy, S. Bandyopadhyay, and J. Atulasimha. Energy dissipation and switching delay in stress-induced switching of multiferroic devices in the presence of thermal fluctuations. *arXiv:1111.6129, J. Appl. Phys. (accepted)*, 2012.

[172] J. Atulasimha and S. Bandyopadhyay. Bennett clocking of nanomagnetic logic using multiferroic single-domain nanomagnets. *Appl. Phys. Lett.*, 97(173105):1–3, 2010.

[173] M. S. Fashami, K. Roy, J. Atulasimha, and S. Bandyopadhyay. Magnetization dynamics, bennett clocking and associated energy dissipation in multiferroic logic. *Nanotechnology*, 22(1-10):155201, 2011.

[174] M. S. Fashami, J. Atulasimha, and S. Bandyopadhyay. Magnetization dynamics, throughput and energy dissipation in a universal multiferroic nanomagnetic logic gate with fan-in and fan-out. *Nanotechnology*, 23(1-10):105201, 2012.

[175] A. Khitun, D. E. Nikonov, and K. L. Wang. Magnetoelectric spin wave amplifier for spin wave logic circuits. *J. Appl. Phys.*, 106:123909, 2009.

[176] N. A. Pertsev. Giant magnetoelectric effect via strain-induced spin reorientation transitions in ferromagnetic films. *Phys. Rev. B*, 78(21):212102, 2008.

[177] N. A. Pertsev and H. Kohlstedt. Magnetic tunnel junction on a ferroelectric substrate. *Appl. Phys. Lett.*, 95(16):163503, 2009.

[178] N. A. Pertsev and H. Kohlstedt. Resistive switching via the converse magnetoelectric effect in ferromagnetic multilayers on ferroelectric substrates. *Nanotechnology*, 21:475202, 2010.

[179] N. D'Souza, J. Atulasimha, and S. Bandyopadhyay. Four-state nanomagnetic logic using multiferroics. *J. Phys. D: Appl. Phys.*, 44(1-7):265001, 2011.

[180] N. D'Souza, J. Atulasimha, and S. Bandyopadhyay. Energy-efficient bennett clocking scheme for four-state multiferroic logic. *IEEE Trans. Nanotech.*, 11(2):418–425, 2012.

[181] N. D'Souza, J. Atulasimha, and S. Bandyopadhyay. An ultrafast image recovery and recognition system implemented with nanomagnets possessing biaxial magnetocrystalline anisotropy. *arXiv:1109.6932, IEEE Trans. Nanotech. (accepted)*, 2012.

[182] S. Roundy. *Energy scavenging for wireless sensor nodes with a focus on vibration to electricity conversion.* PhD thesis, Mech. Engr., UC-Berkeley, 2003.

[183] S. R. Anton and H. A. Sodano. A review of power harvesting using piezoelectric materials (2003-2006). *Smart Mater. Struct.*, 16:R1, 2007.

[184] F. Lu, H. P. Lee, and S. P. Lim. Modeling and analysis of micro piezoelectric power generators for micro-electromechanical-systems applications. *Smart Mater. Struct.*, 13:57, 2004.

[185] Y. B. Jeon, R. Sood, J. Jeong, and S. G. Kim. Mems power generator with transverse mode thin film pzt. *Sens. Act. A: Phys.*, 122(1):16–22, 2005.

[186] D. V. Berkov and J. Miltat. Spin-torque driven magnetization dynamics: Micromagnetic modeling. *J. Magn. Magn. Mater.*, 320(7):1238–1259, 2008.

[187] J. Fidler and T. Schrefl. Micromagnetic modelling-the current state of the art. *J. Phys. D: Appl. Phys.*, 33:R135, 2000.

[188] D. Bedau, H. Liu, J. Z. Sun, J. A. Katine, E. E. Fullerton, S. Mangin, and A. D. Kent. Spin-transfer pulse switching: From the dynamic to the thermally activated regime. *Appl. Phys. Lett.*, 97:262502, 2010.

[189] J. P. Strachan, V. Chembrolu, Y. Acremann, X. W. Yu, A. A. Tulapurkar, T. Tyliszczak, J. A. Katine, M. J. Carey, M. R. Scheinfein, and H. C. Siegmann. Direct observation of spin-torque driven magnetization reversal through nonuniform modes. *Phys. Rev. Lett.*, 100(24):247201, 2008.

[190] L. Landau and E. Lifshitz. On the theory of the dispersion of magnetic permeability in ferromagnetic bodies. *Phys. Z. Sowjet.*, 8(153):101–114, 1935.

[191] T. L. Gilbert. A phenomenological theory of damping in ferromagnetic materials. *IEEE Trans. Magn.*, 40(6):3443–3449, 2004.

[192] M. Beleggia, M. D. Graef, Y. T. Millev, D. A. Goode, and G. E. Rowlands. Demagnetization factors for elliptic cylinders. *J. Phys. D: Appl. Phys.*, 38:3333, 2005.

[193] W. F. Brown. Thermal fluctuations of a single-domain particle. *Phys. Rev.*, 130(5):1677–1686, 1963.

[194] G. Brown, M. A. Novotny, and P. A. Rikvold. Langevin simulation of thermally activated magnetization reversal in nanoscale pillars. *Phys. Rev. B*, 64(13):134422, 2001.

[195] A. Brataas, G. E. W. Bauer, and P. J. Kelly. Non-collinear magnetoelectronics. *Phys. Rep.*, 427(4):157–255, 2006.

[196] Z. Z. Sun and X. R. Wang. Strategy to reduce minimal magnetization switching field for stoner particles. *Phys. Rev. B*, 73(9):092416, 2006.

[197] L. B. Kish. End of moore's law: thermal (noise) death of integration in micro and nano electronics. *Phys. Lett. A*, 305(3-4):144–149, 2002.

[198] *http://www.itrs.net/Links/2009ITRS/2009Chapters_2009Tables/2009_Interconnect.pdf.*

[199] Z. Z. Sun and X. R. Wang. Fast magnetization switching of stoner particles: A nonlinear dynamics picture. *Phys. Rev. B*, 71(17):174430, 2005.

[200] R. Abbundi and A. E. Clark. Anomalous thermal expansion and magnetostriction of single crystal $Tb_{.27}Dy_{.73}Fe_2$. *IEEE Trans. Magn.*, 13(5):1519–1520, 1977.

[201] K. Ried, M. Schnell, F. Schatz, M. Hirscher, B. Ludescher, W. Sigle, and H. Kronmüller. Crystallization behaviour and magnetic properties of magnetostrictive TbDyFe films. *Phys. Stat. Sol. (a)*, 167(1):195–208, 1998.

[202] R. Kellogg and A. Flatau. Experimental investigation of Terfenol-D's elastic modulus. *J. Intell. Mater. Sys. Struc.*, 19(5):583, 2008.

[203] J. Walowski, M. D. Kaufmann, B. Lenk, C. Hamann, J. McCord, and M. Münzenberg. Intrinsic and non-local Gilbert damping in polycrystalline nickel studied by Ti: sapphire laser fs spectroscopy. *J. Phys. D: Appl. Phys.*, 41:164016, 2008.

[204] *http://www.allmeasures.com/Formulae/static/materials/.*

[205] M. Lisca, L. Pintilie, M. Alexe, and C. M. Teodorescu. Thickness effect in $Pb(Zr_{0.2}Ti_{0.8})O_3$ ferroelectric thin films grown by pulsed laser deposition. *Appl. Surf. Sci.*, 252(13):4549–4552, 2006.

[206] *http://www.memsnet.org/material/leadzirconatetitanatepzt/.*

[207] *http://www.itrs.net.*

[208] S. R. Anton and H. A. Sodano. A review of power harvesting using piezoelectric materials (2003-2006). *Smart Mater. Struct.*, 16:R1, 2007.

[209] F. Lu, H. P. Lee, and S. P. Lim. Modeling and analysis of micro piezoelectric power generators for micro-electromechanical-systems applications. *Smart Mater. Struct.*, 13:57, 2004.

[210] Y. B. Jeon, R. Sood, J. Jeong, and S. G. Kim. MEMS power generator with transverse mode thin film pzt. *Sens. Act. A: Phys.*, 122(1):16–22, 2005.

[211] B. Yu and M. L. Bushnell. A Novel Dynamic Power Cutoff Technique (DPCT) for Active Leakage Reduction in Deep Submicron CMOS Circuits. In *International Symposium on Low Power Electronics and Design 2006 (ISLPED'06)*, pages 214–219, Tegernsee, Germany, 4-6 October 2006.

[212] A. J. Masys, W. Ren, G. Yang, and B. K. Mukherjee. Piezoelectric strain in lead zirconate titante ceramics as a function of electric field, frequency, and dc bias. *J. Appl. Phys.*, 94:1155, 2003.

[213] S. Chikazumi. *Physics of Ferromagnetism.* Oxford University Press, USA, 1997.

[214] D. B. Carlton, N. C. Emley, E. Tuchfeld, and J. Bokor. Simulation studies of nanomagnet-based logic architecture. *Nano Lett.*, 8(12):4173–4178, 2008.

[215] F. M. Spedalieri, A. P. Jacob, D. E. Nikonov, and V. P. Roychowdhury. Performance of magnetic quantum cellular automata and limitations due to thermal noise. *IEEE Trans. Nanotech.*, 10(3):537–546, 2011.

[216] I. Amlani, A. O. Orlov, G. Toth, G. H. Bernstein, C. S. Lent, and G. L. Snider. Digital logic gate using quantum-dot cellular automata. *Science*, 284(5412):289, 1999.

[217] N. D'Souza, K. Roy, M. S. Fashami, J. Atulasimha, and S. Bandyopadhyay. Preliminary experiments on multiferroic nanomagnetic logic devices for ultralow power computing. In

ASME 2012 Conference on Smart Materials, Adaptive Structures and Intelligent Systems, Stone Mountain, Georgia, September 19-21, 2012, 2012.

[218] W. Zhou and Z. L. Wang, editors. *Scanning microscopy for nanotechnology: techniques and applications*. Springer, 2007.

[219] *http://www.jcnabity.com/*.

[220] Q. Hang, D. A. Hill, and G. H. Bernstein. Efficient removers for poly (methylmethacrylate). *Journal of Vacuum Science and Technology B: Microelectronics and Nanometer Structures*, 21:91, 2003.

[221] *http://www.veeco.com/*.

List of Publications

Works on Multiferroic Devices

Journals

1. **K. Roy**, S. Bandyopadhyay, and J. Atulasimha, "Hybrid spintronics and straintronics: A magnetic technology for ultra low energy computing and signal processing," ***Appl. Phys. Lett., 99, 063108 (1-3), 2011.*** **Chapter 3, Section 3.1**
   Highlighted in *Nature*, *AIP news*, *PhysicsWorld*, *NanoTechWeb* etc. and selected by *Virtual Journal of Nanoscale Science and Technology.*

2. **K. Roy**, S. Bandyopadhyay, and J. Atulasimha, "Switching dynamics of a magnetostrictive single-domain nanomagnet subjected to stress," ***Phys. Rev. B, 83, 224412 (1-15), 2011.*** **Chapter 3, Section 3.2**

3. **K. Roy**, S. Bandyopadhyay, and J. Atulasimha, "Binary switching in a symmetric potential landscape," ***arXiv:1111.5390, Under Review.*** **Chapter 3, Section 3.3**

4. **K. Roy**, S. Bandyopadhyay, and J. Atulasimha, "Energy dissipation and switching delay in stress-induced switching of multiferroic devices in the presence of thermal fluctuations," ***arXiv:1111.6129, J. of Appl. Phys. [Accepted].*** **Chapter 3, Section 3.4**

5. M. S. Fashami, **K. Roy**, J. Atulasimha, and S. Bandyopadhyay, "Magnetization dynamics, Bennett clocking and associated energy dissipation in multiferroic logic," ***Nanotechnology, 22, 155201 (1-10), 2011.*** **Chapter 4**

Conferences

1. N. D'Souza, **K. Roy**, M. S. Fashami, J. Atulasimha, and S. Bandyopadhyay, "Preliminary experiments on multiferroic nanomagnetic logic devices for ultralow power computing," ***ASME 2012 Conference on Smart Materials, Adaptive Structures and Intelligent Systems, Stone Mountain, Georgia, September 19-21, 2012.*** **Chapter 5**

Presentations

1. **K. Roy**, S. Bandyopadhyay, and J. Atulasimha, "Hybrid spintronics and straintronics: An ultra-low energy computing paradigm," ***presented at American Physical Society (APS) March 2012 Meeting, Boston, Massachusetts, 2012.***

News: Strain and spin could drive ultralow energy computers.

* Nature: ***http://www.nature.com/nature/journal/v476/n7361/full/476375c.html***
* AIP News: ***http://www.aip.org/aip/research/PNH-8-15-2011.html***
* PhysicsWorld: ***http://physicsworld.com/cws/article/news/44910***
* NanoTechweb: ***http://nanotechweb.org/cws/article/tech/44911***
* Virtual Journal of Nanoscale Science and Technology: ***http://www.vjnano.org/dbt/dbt.jsp?KEY=VIRT01&Volume=24&Issue=8#MAJOR4***

Funding Acknowledgement: US National Science Foundation grant ECCS–1124714, which was one out of twelve grants awarded in the *Nanoelectronics for 2020 and Beyond (NEB)* competition.

Works on Spin-Transfer-Torque [**not included in this dissertation**]

Journals

1. **K. Roy**, S. Bandyopadhyay, and J. Atulasimha, "Metastable state in a shape-anisotropic single-domain nanomagnet subjected to spin-transfer-torque," ***arXiv:1106.1215, Under Review.***
2. **K. Roy**, S. Bandyopadhyay, J. Atulasimha, K. Munira, and A. Ghosh, "Energy dissipation and switching delay in spin-transfer-torque switching of nanomagnets with low-saturation magnetization in the presence of thermal fluctuations," ***arXiv:1107.0387, Under Review.***

Vita

Kuntal Roy was born on February 23rd, 1983 in the state West Bengal, India. He graduated from Krishnanagar Collegiate High School, West Bengal, India in 1999. He received his Bachelor of Engineering in Electronics and Tele-Communication Engineering from Jadavpur University, West Bengal, India (1999-2003). He held technical positions on information technologies in industries like Interra-IT, TCS, and IBM all in India during 2003-2006. He received his Master of Science in Embedded Systems Design from Advanced Learning and Research Institute (ALaRI), Switzerland (2006-2008). He spent two years (2008-2010) as a PhD student at Purdue University, USA, where he passed his PhD written qualifying examination. He joined VCU as a transfer PhD student in Fall 2010.